Structure/Property Relationships in Elastomers Filled with Graphite Nanoplatelets

A thesis submitted to

The University of Manchester

for the degree of

Doctor of Philosophy

in the

Faculty of Science and Engineering

2017

Suhao Li

School of Materials

Content

Word count: 47776

List of Abbreviation

MC	Mechanical Cleavage
SEM	Scanning Electron Microsope
HOPE	Highly Oriented Pyrolytic Graphite
AFM	Atomic Force Microscope
LPE	Liquid-phase Exfoliation
NMP	N-methyl-pyrrolidone
TEM	Transmission Electron Microscope
CVD	Chemical Vapour Deposition
PECVD	Plasma Enhanced Chemical Vapor Deposition
LBL	Layer-by-layer
GO	Graphene Oxide
CO	Carbon Monoxide
CO_2	Carbon Dioxide
HI	Hydrogenated Iodine
HBr	Hydrogenated Bromine
NaOH	Sodium Hydroxide
$NaBH_4$	Hydrogen Boride
Al	Aluminum
HCl	Hydrogen Chloride
GNP(s)	Expanded Graphite Nanoplatelets
GIC	Graphite Intercalation Compound
ESEM	Environmental Scanning Electron Microscope
Si	Silicon
SiO_2	Silicon Oxide
PMMA	Polymethyl Methacrylate
XRD	X-ray Diffraction
H_2O	Water
DFPT	Density Function Perturbation Theory
GPa	Giga Pascal (unit of stress)
MPa	Mega Pascal (unit of stress)
MD	Molecular Dynamics Simulation
-OH	Hydroxyl
-O-	Ketonic Bond
LM	Longitudinal Mode
TM	Transverse Mode

W/mK	Watts per meter-Kelvin (unit of thermal conductivity)
WKB	Wentzel-Kramers-Brillouin
BR	Butadiene Rubber
SBR	Styrene-butadiene Rubber
IIR	Isobutylene-isoprene Rubber
NBR	Nitrile Butadiene Rubber
BHT	2,6-di-t-butyl-p-cresol
NDPA	N-nitrosodiphenylamine
CBS	N-Cyclohexyl-2-benzothiazole sulfenamide
CTP	N-(cyclohexylthio) phthalimide
ZDMA	Zinc dimethacrylate
TEGO	Thermally-exfoliated Graphene Oxide
FGS	Few-layer Sheets
NR	Natural Rubber
TGA	Thermogravimetric Analysis
PDMS	Dimethylsiloxane
MLGS	Multi-layer Graphene Sheets
NRL	Natural Rubber Latex
SDS	Sodium Dodecyl Sulfate
NRGO	Natural Rubber/ Graphene Oxide Nanocomposite
C≡N	Cyano Bond
FTIR	Fourier Transform Infrared Spectroscopy
FESEM	Field Emission Scanning Electron Microscope
HRTEM	High-resolution Transmission Electron Microscopy
PC-rGO	Proanthocyanidin-reduced Graphene Oxide
GE	Chemically-reduced Graphene Oxide
PHR or phr	Part per Hundred Rubber
CCD	Charge Coupled Device
CT	Computed Tomography
EPDM	Ethylene-Propylene-Diene Monomer Rubber
CB	Carbon black
FLG	Few-layer Graphene
HAF	High Abrasion Furnace

SMR	Standard Malaysian Rubber
CV	Constant Viscosity
ML	Minimum Torque
TMTD	Tetramethylthiuram Disulfide
VPSEM	Variable Pressure Scanning Electron Microscope
kV	Kilovolt (unit of voltage)
FEG	Field Emission Gun
ODF	Orientation Distribution Function
ASTM	American Society of Testing Materials

List of Tables

List of Figures

Abstract

Structure/Property Relationships in Elastomers Filled with Graphite Nanoplatelets

The University of Manchester
Suhao Li
Doctor of Philosophy
27 September 2017

The microstructure and properties have been investigated in nanocomposites consisting of graphite nanoplatelets (GNPs) in natural rubber (NR) and nitrile butadiene rubber (NBR). Nanocomposites with four different loadings of three different sized GNPs (nominal lateral dimension of 5, 15 and 25 microns) were prepared that were bench-marked against nanocomposites loaded with N330 carbon black. The materials were processed using conventional melt-processing methods in a two-roll mill and the composition of the nanocomposites was confirmed by thermogravimetric analysis. The microstructure of the nanocomposites was characterised though a combination of scanning electron microscopy, polarised Raman spectroscopy and X-ray computer tomography (CT) scanning, where it was shown that the GNPs were well dispersed with a preferred orientation parallel to the surface of the nanocomposite sheets.

The mechanical properties of the nanocomposites were evaluated through tensile testing, Shore A hardness testing and tear testing. It was shown that, for a given loading, there was a three times greater increase in stiffness for the GNPs than for the carbon black. The size effect of the particles is significant in the mechanical properties. Stress transfer from the NR and the NBR to the GNPs was evaluated from stress-induced Raman bands shifts indicating that the effective Young's modulus of the GNPs in the NR was only of the order of 100 MPa, similar to the value evaluated using *the rule of mixtures* from the stress-strain data. A comprehensive theory was developed to explain the deficiency of the stress transfer in soft matrix systems.

Transport properties including solvent diffusion and thermal conductivity were investigated. Anisotropic swelling was observed for all the GNPs composites due to the orientation of the GNP flakes. The diffusion coefficient decreases with the increasing loading of the fillers and the increasing particle size. Thermal conductivity was enhanced with the addition of the fillers and the largest particle gives rise to the highest enhancement.

Declaration

No portion of the work referred to in the thesis has been submitted in support of an application for another degree or qualification of this or any other university or other institute of learning

Copyright statement

i. The author of this thesis (including any appendices and/or schedules to this thesis) owns certain copyright or related rights in it (the “Copyright”) and s/he has given The University of Manchester certain rights to use such Copyright, including for administrative purposes.

ii. Copies of this thesis, either in full or in extracts and whether in hard or electronic copy, may be made only in accordance with the Copyright, Designs and Patents Act 1988 (as amended) and regulations issued under it or, where appropriate, in accordance with licensing agreements which the University has from time to time. This page must form part of any such copies made.

iii. The ownership of certain Copyright, patents, designs, trade marks and other intellectual property (the “Intellectual Property”) and any reproductions of copyright works in the thesis, for example graphs and tables (“Reproductions”), which may be described in this thesis, may not be owned by the author and may be owned by third parties. Such Intellectual Property and Reproductions cannot and must not be made available for use without the prior written permission of the owner(s) of the relevant Intellectual Property and/or Reproductions.

iv. Further information on the conditions under which disclosure, publication and commercialisation of this thesis, the Copyright and any Intellectual Property and/or Reproductions described in it may take place is available in the University IP Policy (see http://www.campus.manchester.ac.uk/medialibrary/policies/intellectual-property.pdf), in any relevant Thesis restriction declarations deposited in the University Library, The University Library’s regulations (see http://www.manchester.ac.uk/library/aboutus/regulations) and in The University’s policy on presentation of Theses.

Acknowledgement

First, I would like to express my appreciation to Professor Robert J. Young for his enthusiastic supervision and encouragement throughout this project. Second, my gratitude also goes to Professor Ian A. Kinloch for his helpful suggestions and also providing me the nice samples.

I would also like to thank Dr. Zheling Li for the calculation of the polarized Raman data, Dr. Dimitrios Papageorgiou, Mr. Fang Wang, Mr. Mufeng Liu, of our group, for their invaluable suggestions in the project.

I would also like to acknowledge Mr. Andrij Zadoroshnyj for his kind support on Raman spectroscopy and to acknowledge Dr. Timothy Burnett and Mr. Thomas Slater for their kind support on CT-scanning My thanks also go to the staff in School of Materials for their invaluable support.

I would also like to thank all the colleagues in the Raman group for their fruitful discussions. They are not only good colleagues but also faithful friends.

At last but not least, I would express my gratitude to my wife, Yingning Li, my family and all the friends for their constant support and encouragement.

1. Graphene

1.1. Introduction

Graphene, a new material that triggered a 'gold rush' in reality has been a subject of theoretical investigation for more than half a century.[1-2] Nevertheless, this intriguing material that was long investigated was thought not to exist owing to the theoretical demonstration of its thermodynamically-unstable lattice structure.[3-4] Subsequently, continuous successors and supporters of this conclusion kept supporting this authoritative theory,[5-8] which was terminated by the reality of graphene monolayers being prepared by Geim and Novoselov in 2004.[9]

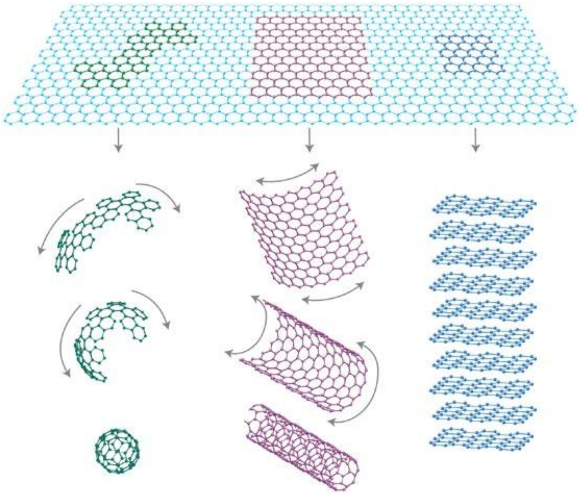

Figure 1.1 Formation of the graphitic materials based on the 2D graphene structural unit[10]

Basically, graphene is structured in a honeycomb lattice pattern bonded by sp^2-hybridised carbon atoms which are the integral basis of all forms of graphtic materials, including 0D fullerene, 1D carbon nanotubes and 3D graphite etc (see in Figure 1.1).[10] The graphene monolayer is a one atom thick sheet, which is 0.335 nm in thickness.[11] However, there is a necessity for clarification before defining 2D graphene with respect to thickness. Normally, it is thought to be graphite from above 10 layers, due to the electronic characteristics starting to exhibit 3D features for this thickness.[12]

Since its discovery, graphene has demonstrated its own exceptional properties in several fields, including a high intrinsic mobility, preeminent stiffness and strength, high thermal conductivity and outstanding barrier properties etc. However, fabrication of graphene nanocomposites has also appealed to numerous academic and industrial researchers, as it is capable of imparting the excellent properties of graphene into a wide range of matrices at a low level of incorporation. This has led to a large number of research groups and institutions that are seeking ways to produce and use graphene with different characteristics along with the corresponding nanocomposites.

1.2. Preparation technology

Normally, a long time is needed for a new technique or material to experience the transformation from research to industrial application, and surely graphene cannot skip this step. Although in the situation of lacking a mature downstream production, the development of scale-up production of graphene has no reason to remain stagnant. Intelligence from different fields has been mobilized to attempt to produce high yields of un-damaged graphene platelets by cost-effective methods. Nevertheless, graphene flakes derived from different methods possess various structural features and hence diverse properties. The preparation methods currently employed are reviewed next.

1.2.1. Mechanical cleavage (MC)

Over decades, a number of efforts were made to achieve the thickness reduction of graphite. In 1964, Hennig et al.[13] prepared thin graphite films by pre-cleavage between glass slides covered by Duco cement and further thinning by scotch tape. In 1999, Lu et al.[14] fabricated individual graphite islands by oxygen plasma etching of lithographically patterned substrates (see in Figure 1.2a), subsequently rubbed by a silicon (001) substrate to obtained thinner separated graphite plates (see in Figure 1.2b). The thinnest graphite island produced by Lu et al.[14] was of 200 nm thick, and a repeating transferring method was implied as a potential exfoliation way for monolayer.[14-15]

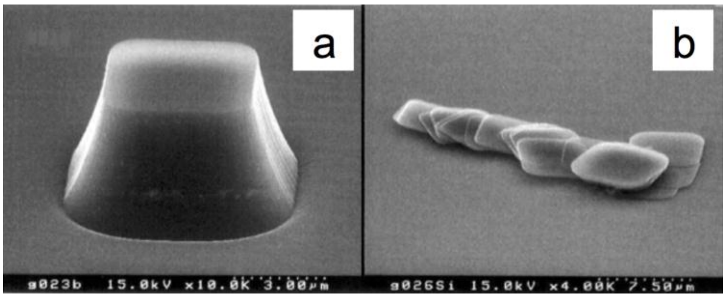

Figure 1.2 SEM images (a) single graphite island obtained from oxygen plasma etching on an HOPG substrate; (b) delaminated graphite plates after transferring[14]

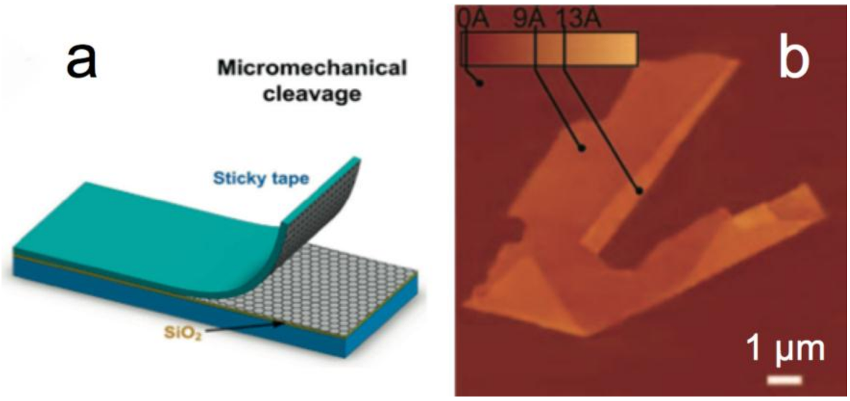

Figure 1.3 (a) Schematic sketch of mechanical cleavage of graphite on silica substrate[16] (b) AFM image of graphene flakes on 300 nm Si wafer[17]

The well-known separation of graphene in 2004 and following works revealed that the simple mechanical exfoliation (see in Figure 1.3a) by using scotch tape produces high-quality graphene flakes (see in Figure 1.3b) with large areas starting from graphite.[9, 17] Nevertheless, the cleaved flakes are normally free of defects along with uncontrollability of lateral sizes, shapes, and azimuthal orientations, for which the aforementioned synthesis method mainly targets at supply for research purposes rather than a scale-up of production.

1.2.2. Liquid-phase exfoliation (LPE)

The mechanism of liquid-phase exfoliation is based on the breaking of the van der Waals interaction between the graphene interlayers by liquid invasion.[18-19] Ferrari et al.[20] demonstrated a high-yielding defect-free production of graphene dispersion (0.01 mg ml^{-1}) through exfoliation by four solvents (including N-methyl-pyrrolidone, NMP), with an actual and potential single layer yield of 1 wt% and 7-12 wt%, respectively. This was followed by the individual flakes being characterized using Raman spectroscopy, transmission electron microscopy (Figure 1.4 shows the image and the distribution of layer number) and electron diffraction. They surmised that solvent molecules with surface energies comparable to that of graphene provided the graphene-solvent interaction to delaminate the layers.

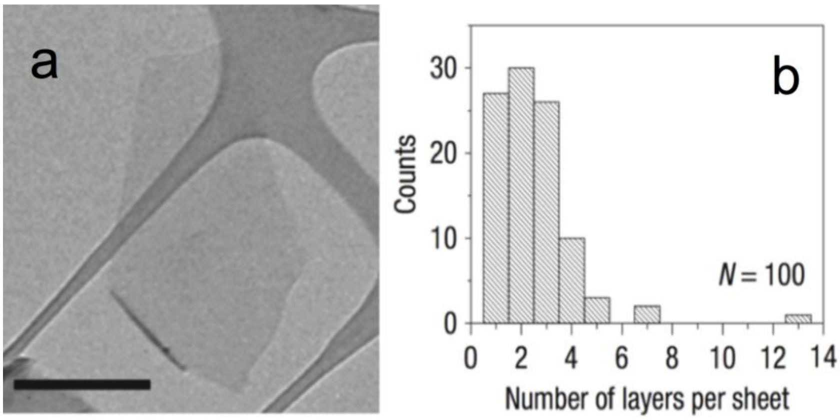

Figure 1.4 (a) Bright-field TEM image of NMP-exfoliated graphene flakes (scale bar: 500 nm); (b) histogram of the flake layer number in NMP dispersion[20]

Xu et al. [21] introduced an increased yield of graphene (as high as 0.15 mg ml^{-1} in NMP, see comparison in Figure 1.5A) through sonication by the addition of naphthalene, which played a role during the exfoliation as a “molecular wedge”. Defects were detected by Raman spectroscopy from the intensity ratio of D band to G band (I_D/I_G) of around 0.5 (see in Figure 1.5B), and this is much lower than the values from chemically- and thermally-reduced graphene oxide.[22-23]

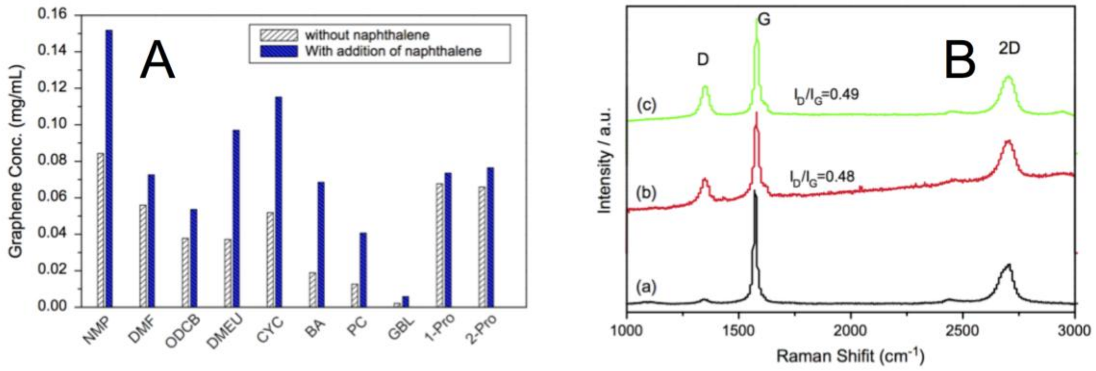

Figure 1.5 (A) Graphene concentration produced with and without addition of naphthalene; (B) Raman spectra of (a) original graphite; liquid-phase exfoliated graphene (a) with and (b) without addition of naphthalene (laser excitation: 532 nm).[21]

A theoretical study by Monajjemi[24] indicated that surfactants or stabilizers containing sulfonic group exhibit highest efficiency in liquid phase exfoliation using any solvent, and suggested a ranking of the functional groups according to their exfoliating capacity as cation > anion > zwitterion > nonionic.

1.2.3. Chemical vapour deposition

With the advantages of low cost, scale-up capacity and large flake area, chemical vapour deposition is an attractive technique by which graphene films can be grown epitaxially at high temperature on a range of metals. The accomplishment of graphene preparation through CVD on polycrystalline Ni was firstly reported by Yu et al.[25] in 2008. The graphene can be lithographically patterned and remained high quality after transfer to other substrates by wet etching.[25-26] They pointed out the cooling rate highly affects the thickness of the graphene film produced, and concluded an optimum at a wide range of medium cooling rates. The graphene flakes synthesized (<10 layers) were characterized by Raman spectroscopy and proved to be consistent with the aforementioned conclusion indicated by the graphene fabricated under a medium cooling rate showing a negligible D band and a lower G band intensity compared with that of the 2D band (see in Figure 1.6).

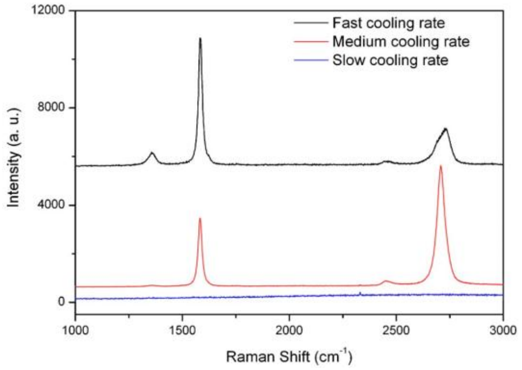

Figure 1.6 Raman spectra of CVD-made graphene on Ni at different cooling rates (laser excitation: 514 nm).[25]

Further research indicated that the features (layer number, area and continuity around the metal grain boundaries) of the CVD-derived graphene films were also affected by the CVD parameters such as the thickness of the metals, size, location and boundaries of the metal crystalline grains, and concentration/flow rate of the precursor gases.[27-29] Methodologically, this promising preparation method was exploited widely with adoption of low-temperature plasma enhanced chemical vapor deposition (PECVD) and layer-by-layer (LBL) growth targeting at tuning the area size, thickness and continuity of the graphene films for specific practical demands. The substrates were broadened to Cu (now the most widely used), Co, Ta, and SiO_2/Si, and more feed gas species were employed, such as methane, ethylene, carbon dioxide and arbitrary transfer substrates.[26-38]

1.2.4. Reduction from graphene oxide (GO)

Graphene oxide (GO), a derivative from graphene, is normally prepared by oxidation through modified Hummers methods,[39-44] the structure of which has been revealed as graphene-like sheets decorated with oxidative debris (see in Figure 1.7) by Rourke et al. [45] in 2011. This material has attracted tremendous attentions due to its high yield potential and dispersion superiority to graphene in a wide range of matrices, although with less impressive properties. In addition, the strong intention to reduce GO to high quality graphene arose from numerous researchers concerned about graphene scale-up production, including mainly thermal and chemical reduction.

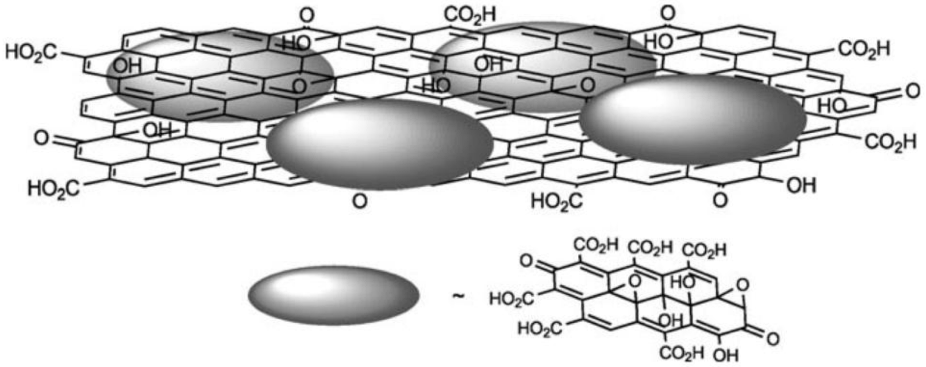

Figure 1.7 Localized schematic illustration of GO: highly oxidized graphene-like sheets with surface-bound debris.[45]

Specifically, several heating resources have been employed for purposes of thermal reduction, such as annealing,[46-48] arc discharge,[49] microwave[50-51] and photo-irradiation.[52-53] The mechanism of thermal reduction consists of two steps: firstly, the rapid heating decomposes the oxidatively functionalized groups attached to the graphene frame emitting CO/ CO_2 gases; secondly, the gases suddenly being released expand between interlayers to exfoliate GO to graphene.[46-49] This dual-effect approach for preparing graphene provides high yield yet with small sizes and ripples due to the loss of carbon atoms that fragmentates the continuous graphene planes during gases generation.[48] As another strategy to reduce GO, chemical reduction has the advantage of less strict experimental conditions (room or moderate temperature), and a more straightforward procedure compared with thermal routes. Although there are several reaction choices for the reduction of the oxidative functional groups on GO, direct reaction with chemical reagents is the most popular. A number of groups have tried different types of reagents, which can be broadly classified as "mechanism known" reagents and "mechanism unknown" reagents. The former have well understood mechanisms, such as hydrohalic acid (e.g. HI[54] and HBr[55]), sulphur-containing reagents (e.g. thiourea dioxide/NaOH[56]), borohydrides (e.g. $NaBH_4$[57]) etc., whereas the latter are ambiguous in mechanism, such as nitrogen-containing reagents (e.g. hydrazine[58-59]), metal acids (e.g. Al/HCl[60]), amino acids (e.g. glycine[61]) and vitamin C[62] etc. Moreover, the C/O ratio can be used as a criterion to evaluate the reducing capacity of the reagents. This was reviewed in detail in 2014 and the findings were tabulated by Chua and Pumera[63] in 2014.

1.2.5. Synthesis of expanded graphite nanoplatelets (GNP)

The synthesis of expanded graphite nanoplatelets (GNP) were developed by Drzal's group[64-69] and reported as a new reinforcement to replace carbon nanotubes in polymers due to its cost efficiency, promising mechanical properties and thermal properties. The synthesis started from a sulfuric acid/ nitric acid graphite intercalation compound (GIC), which was prepared through chemical oxidation of natural graphite in acids. The structure of the GIC is tightly-bonded nano-scale layers of graphite (see in Figure 1.8a). Subsequently, the GIC experiences a rapid heating by microwave leading to the coupling of the conductive graphite to the radiation, which expels the intercalants between the interlayers and expands the flakes by ~500 times. The products from the microwave expansion have a worm-like structure as seen in Figure 1.8b. Afterwards, the expanded graphite flakes are pulverized though ultrasonication to produce individual graphite nanoplatelets that have a thickness less than 10 nm and a diameter of microns (see in Figure 1.8c). The flakes can be further broken by vibratory mill resulting into flakes of the same thickness and a diameter less than 1 μm. The TEM images of the interlayer structure provided an estimation of the thickness of GNP from 5 – 10 nm given the thickness of 0.335 nm[11] for a monolayer (see an example of two adjacent GNP in Figure 1.8d). Since the thickness of GNP is normally over 10 layers, it is essentially graphite nanoplatelets. However, some researchers prefer to term them “graphene nanoplatelets”. According to the National Physical Laboratory’s new ISO standard on graphene nomenclature, “graphene nanoplatelets” usually have thickness of between 1 nm to 3 nm and lateral dimensions ranging from 100 nm to 100 μm,[70] GNPs will refer to “graphite nanoplatelets” in this study.

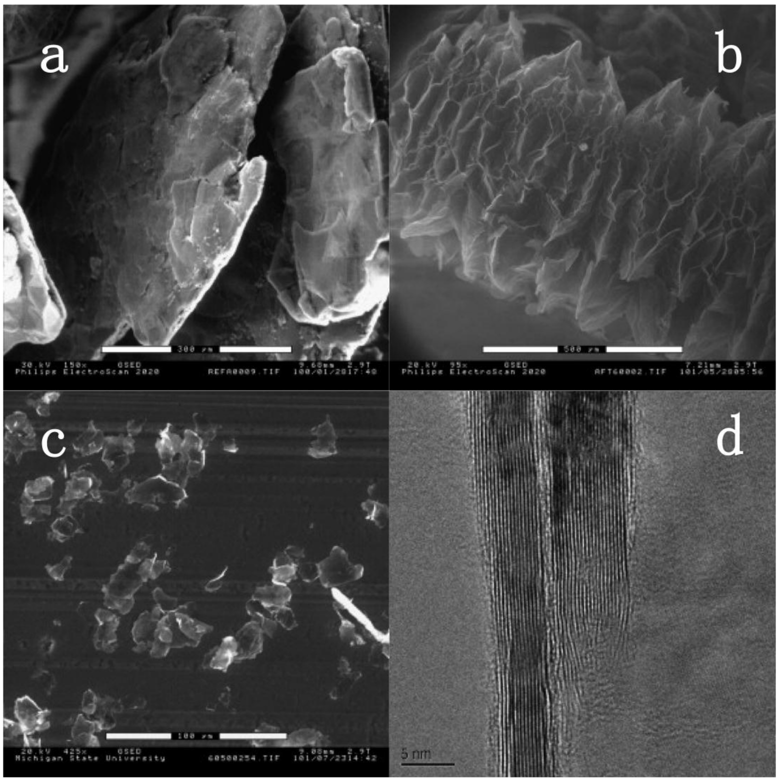

Figure 1.8 ESEM images of (a) intercalated graphite (scale bar 300 μm); (b) microwave expanded graphite (scale bar 500 μm); (c) exfoliated graphite nanoplatelets (scale bar 100 μm). (d) TEM image of two adjacent xGnP flakes (scale bar 5 nm).[68]

1.3. Characterization

1.3.1. Microscopy

Optical microscopy has been employed as a feasible and efficient technique to detect graphene monolayers especially fabricated from micromechanical cleavage. However, as an absorbance-based technique, it is difficult to resolve a one atom thick layer as the absorbance of visible light increases with graphene layer number at a rate of 2.3 % per layer.[71] Experimentally, the selection of a proper wavelength of the light employed makes the contrast fluctuate, which can be possibly diminished by utility of proper filters. Furthermore, a Si/SiO_2 wafer was chosen as a limited substrate to facilitate the cleavage and observation of the monolayers due to its preponderance of visualization of graphene species in an optical microscope[72] and partially due to its lack of Raman bands between 1000 cm^{-1} and 3000 cm^{-1}.[73] In addition, the thickness of the SiO_2 layer controls the distinguishability of monolayers from other thicker layers even with a small variation.[72]

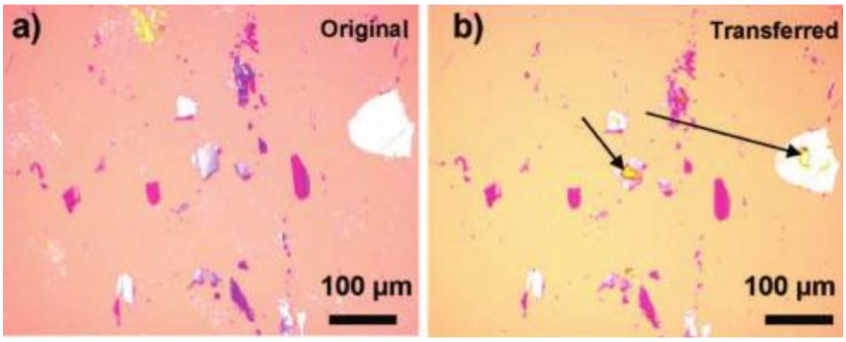

Figure 1.9 Optical images of the graphene flakes (a) before and (b) after transfer (Arrows point to PMMA residues spin coated before transfer).[74]

Generally, there are needs for identification and localization of a graphene area of interest after transferred to another substrate for further investigation, which can be efficiently achieved by a meticulous transferring and comparison of the optical images before and after (see in Figure 1.9).[74] Additionally, optical microscopy can also be used to observe the growth,[75] identify graphene layer numbers,[76-78] and probe defects, quality[79] and grain boundaries[80] of CVD graphene.

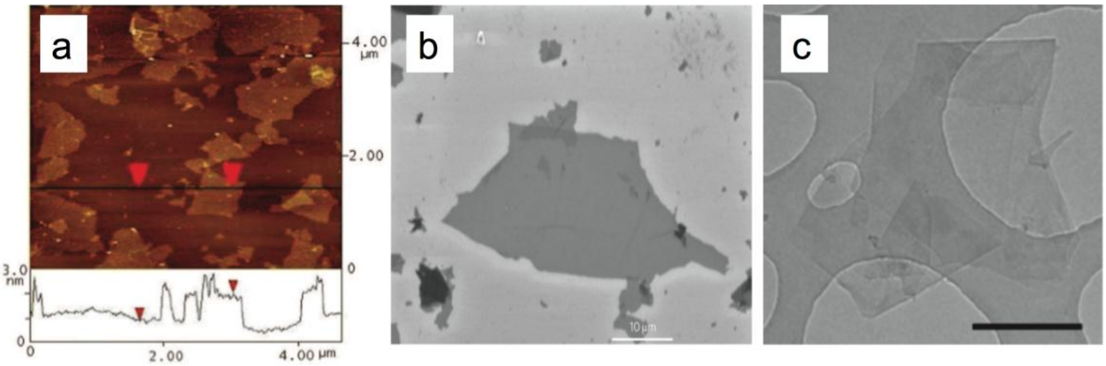

Figure 1.10 (a) AFM image of water-soluble graphene on freshly cleaved mica; the height difference between two red arrows is 1.2 nm.[81] (b) SEM image of a single chemically derived graphene flake on Si/SiO2 substrate (scale bar 10 μm).[82] (c) Bright-field TEM images of a folded multilayer graphene sheet, deposited from NMP (scale bar 500 nm).[20]

Although it is possible to get basic information of graphene flakes from optical microscopy, deeper observation requires other microscopies with higher resolution. Atomic force microscopy (AFM) has become a fundamental scanning probe microscopy to characterize graphene sheets, which not only shows the morphology of the flakes but also determines the flake thickness along certain profiles (see an example in Figure 1.10a[81]). Scanning electron microscopy (SEM) is also thought as a routinely used technique to characterize graphene flakes[82-94] down to single layer (see an example in Figure 1.10b[82]). It can be utilized to observe the morphology, compare the thickness contrast, calculate the mean lateral size, and primarily characterize the quality of the graphene flakes by rapid visualization. The only disadvantage of SEM is that for high quality images, the specimens need to be deposited on electronically conductive substrates. Finally, transmission electron microscopy (TEM) images (see an example in Figure 1.10c[20]) can give highest resolution, which enables the detection of local structural details down to the atomic scale, although it has a low-throughput of information compared with SEM.

1.3.2. Raman spectroscopy

Owing to ambiguity produced by optical microscopy and the low throughput from AFM, the identification of graphene layer number needed a new characterization method to proceed. In this case, Raman spectroscopy has manifested its superiority of non-destruction, high efficiency, and relatively high precision characterization to satisfy the demand. Specifically, an intensive G peak at around 1580 cm^{-1} (see in Figure 1.11a) invariably appears in a Raman spectrum of graphene stemming from the doubly degenerate zone center E_{2g} vibrational mode, while a D peak around 1350 cm^{-1} derived from zone-boundary phonons can be observed on a graphene flake with defects or in the vicinity of edges.[95-97] Additionally, there is a G' peak around 2700 cm^{-1} (see in Figure 1.11a) involved with second order of zone-boundary phonons. This is also termed the 2D peak, being the second order overtone of the D peak.[98]

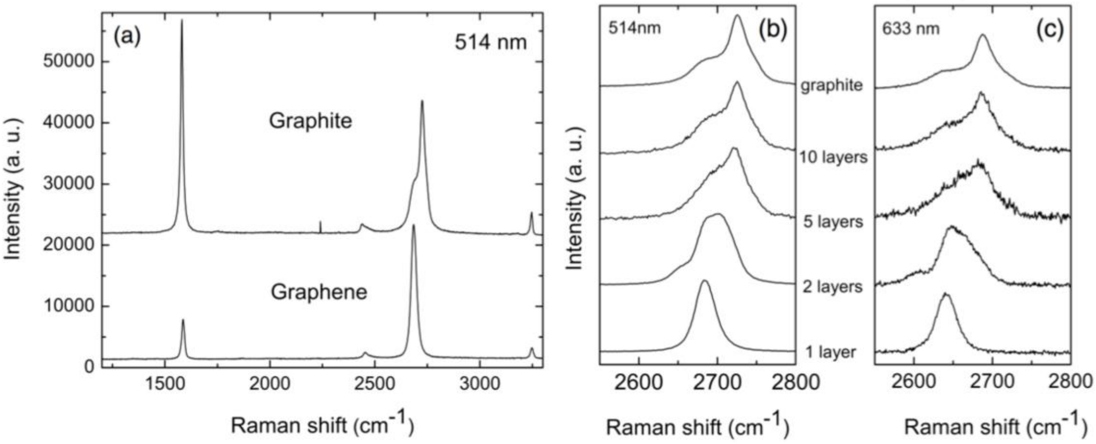

Figure 1.11 (a) Raman spectra of prestine graphite and graphene monolayer; Evolution of 2D peak with increasing layer number detected by laser with wavelength (b) 514 nm and (c) 644 nm.[97]

As seen in Figure 1.11b and 1.11c, the G' peak evolves with the layer number of graphene. Specifically, the G' (2D) peak upshifts with the increasing layer number, with more peak components appearing leading to the loss of symmetry.[97] In terms of GNP, the Raman spectrum (see in Figure 1.12) shows a tiny D band, a sharp G band and a moderate high 2D band, which confirms the sp^2-hybridised carbon atoms, a small quantity of defects and a good crystallographic structure. This implies that there is negligible damage introduced in the graphite flakes by the chemical intercalation, rapid heating and pulverization during the preparation.[66]

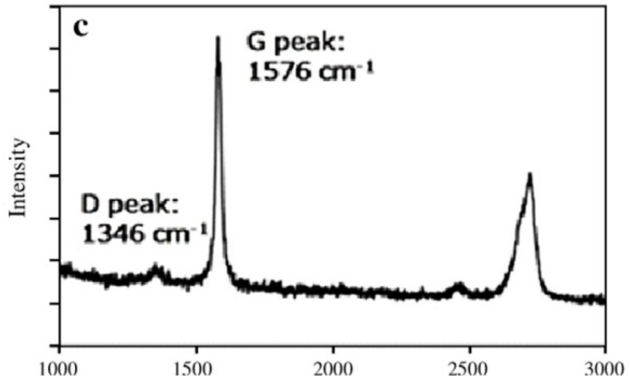

Figure 1.12 Typical Raman spectrum of xGnP.[66]

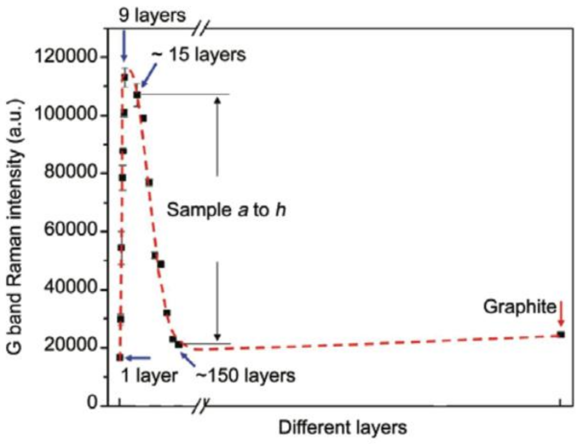

Figure 1.13. The G peak intensity vs layer number of graphene obtained from combination of Raman spectroscopy and contrast spectroscopy. The dashed curve is a guide to eyes.[99]

With an increasing layer number, the 2D peak appears to upshift along with broadening, transforming asymmetrically owing to splitting of the electronic band structure.[97] Unfortunately, the distinction of the 2D peak between bilayer and few layers becomes less obvious and the shape approximates to graphite over five layers. Nevertheless, the intensity of the G peak basically rises linearly with the increasing layer number thinner than 10 layers and gradually decreases above that (see in Figure 1.13),[99] which enables the determination of the layer number combined with other features obtained from the 2D peak.

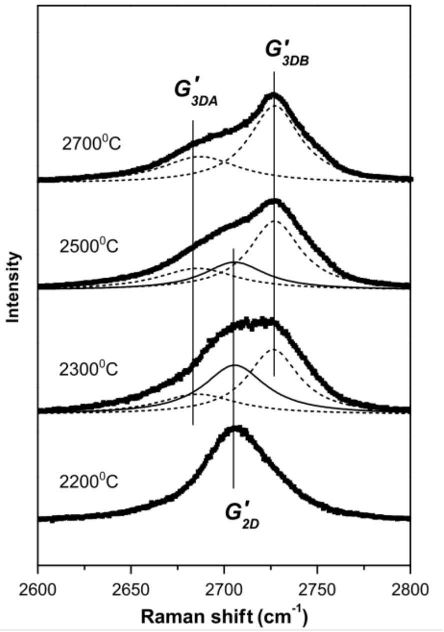

Figure 1.14 Raman G’ peaks of graphite nanosheets obtained by heating at different temperatures showing 1 to 3 fitted components. Laser length: 514.5 nm.[100]

Apart from the very popular utility in layer number detection, it is feasible to acquire the stacking order of graphitic materials using Raman spectroscopy. The 2D peak is thought to be involved with the structural change along the out-of plane c-axis of the lattices.[101] Specifically, Cançado et al.[100] elucidated a method to quantitatively determine the coexistence of 2D and 3D phases of graphitic materials using a combination of Raman spectroscopy and X-ray diffraction. Experimentally, samples of disordered graphite were thermally annealed at different temperatures to produce graphite nanosheets in different degrees of crystallinity. In detail, as seen in Figure 1.14, only one component (referred to as G'_{2D}) shows up in the 2D peak of the 2D graphite produced at 2200 °C, whereas two components (refer to G'_{3DA} and G'_{3DB}) emerge in the 3D graphite produced at 2700 ℃. Moreover, in the other two spectra consisting of both 2D and 3D phases, three components (G'_{2D}, G'_{3DA} and G'_{3DB}) appear simultaneously, while the intensity ratio of G'_{3DB}/G'_{2D} (refers to R) can be utilized to evaluate the volume fraction of the 2D and 3D phases.

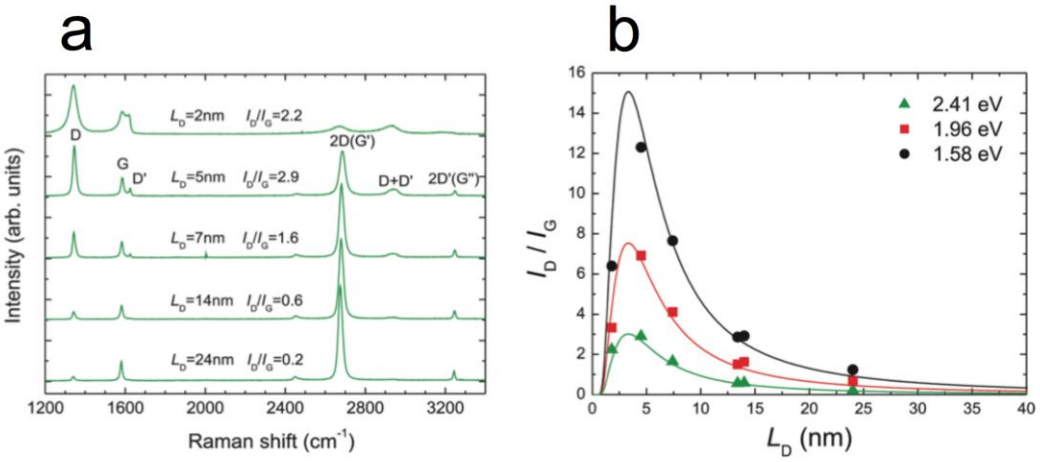

Figure 1.15 (a) Raman spectrum evolution of single layer graphene produced by increasing ion bombardment resulting in a series of defect density. L_D refers to the distance between two point defects. Laser excitation: 514 nm. (b) I_D/I_G of single layer graphene against defect density (represented by L_D) detected by different laser excitation. (Reproduced)[102]

Furthermore, a number of researchers have devoted efforts to studying the relation between the disorder/defects and the Raman spectra in graphitic materials.[95, 103-105] In most research, the intensity ratio of D peak to G peak (I_D/I_G) is the most widely utilized to quantify the extent of the disorder which varies inversely with the in-plane crystallite size L_a.[95] When the disorder density increases, the Raman spectrum of the graphene-based material experiences evolution (see in Figure 1.15a) including several phenomena: (a) I_D/I_G rises reaching the maximum at L_D = 3 nm and sharply decreases to zero as the Tuinstra and Koenig relation fails (plotted in Figure 1.15b); (b) all peaks become broadened; (c) the D’ peak (origins from the double resonance connecting two points belonging to the same cone around **K** or **K**’[106]) arises and gradually overlaps with the G peak; (d) the D+D’ peak and the 2D’(or G”) peak show up with the 2D peak becomes weakened trending to a broad feature from 2300 to 3200 cm^{-1}.[107-109] In addition to the layer number determination and disorder quantification, it is possible to extract other information from the Raman spectrum of graphene, including the exploitation of doping[110] and the visualization of crystallographic stacking order[111] etc.

1.3.3. X-ray Diffraction

Generally, information acquired from XRD is capable of determining the lattice parameter, molecular size, layer size and stacking order of a substance.[112-115] In the detailed exploration into the nanostructure of carbon based substances, X-ray diffraction (XRD) has made a time-honored contribution compared with microscopy and Raman spectroscopy since over 70 years ago when Warren et al.[116] first researched the atomic structure of carbon black.

In terms of graphene, XRD patterns are most commonly facilitated to determine the spacing of the layers. Specifically, over the course of oxidation, the interlayers of graphene or graphite usually undergo expansion, which can be monitored by XRD at different stages. As seen in Figure 1.16A and black curves in Figure 1.16B, the intensity of the (002) peak (related to the d-spacing = 3.4 Å) in graphene or graphite around 26 ° fades away gradually when oxidation proceeds whereas the (001) peak around 11.8 ° (corresponding to 7.49 Å) arises in the meantime (see Figure 1.16B), which is in accordance with the layer expansion by the introduction of the oxygen-containing functional groups and H_2O molecules into the interlayers.[117-118]

Also, the c-curve from a thermally exfoliated graphene nanosheets sample in Figure 1.16A shows the disappearance of the (002) and (001) peaks probably due to the exfoliation or the augmented degree of disorder generated during the annealing.[119-120] Moreover, the analysis of the (002) peak of XRD patterns using the Scherrer equation[121-122] and Laue function model[123] has been commonly utilized to determine the average number of the graphene layers, while the former works better with uniform thickness system and the latter functions well both with uniform and non-uniform thickness systems.

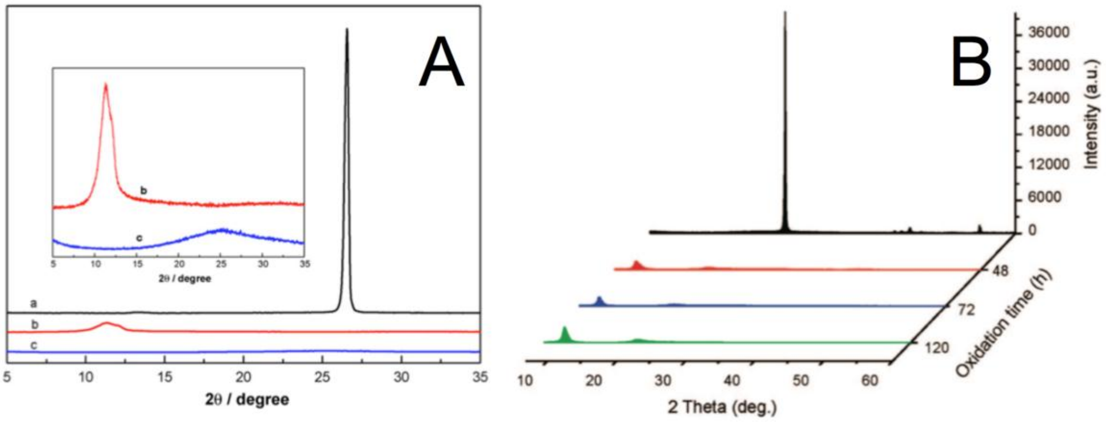

Figure 1.16 (A) XRD pattern of (a) graphite powder, (b) graphite oxide and (c) thermally exfoliated graphene nanosheets;[119] (B) XRD patterns of graphite to GO over a range of oxidation durations.[117]

1.4. Properties

1.4.1. Mechanical properties

The actual mechanical properties of graphene monolayers were firstly measured by Lee et al.[124] using nanoindentation with an atomic force microscopy (AFM), in which mechanically-exfoliated graphene membranes were suspended and tensioned over nano-scale lithographically patterned holes. Optical microscopy and Raman spectroscopy were employed to find the monolayers and confirm the thickness respectively. The value of in-plane Young' modulus and breaking strength were determined to be 1.0 ± 0.1 TPa and 130 ± 10 GPa, respectively, which correlated to the estimation of $\sigma = E/9$ by Griffith[125] where materials fracture at intrinsic strength of atomic bonds without defects and flaws involved. On the basis that the atomic motions are the relatively macroscopic expression of the phonon modes, Liu et al.[126] performed an ab initio calculation on the Brillouin zones and unit cells of graphene lattices through density functional perturbation theory (DFPT) to evaluate the uniaxial stiffness and the ideal breaking strength of graphene monolayers. Values of Young's modulus E = 1050 GPa at small strains and strengths σ_f = 107.4 to 121 GPa were determined. This not only provided the similar values to those measured by Lee et al. [124] but also was consistent with the conclusion drawn by Griffith.[125]

On the other hand, the derivative made through the oxidation of graphene, graphene oxide, appears to be different from graphene regarding its structure and properties. In 2007, Dikin et al.[83] firstly measured the Young's modulus and strength of graphene oxide paper, with low values of ~30 GPa and ~130 MPa, respectively. With the improvement of techniques to impart thickness narrowing to the GO flakes, these values have been raised significantly. Experimentally, a modulus of 250 ± 150 GPa was reported by Gómez-Navarro et al.[127] using AFM measurements whereas Suk et al.[128] utilized AFM with finite element analysis to provide a value of 207.6 ± 23.4 GPa under the premise of 0.7 nm as the thickness. Theoretically, Paci et al.[129] employed molecular dynamics simulation (MD) to probe the mechanical properties of GO, reporting a modulus of ~670 GPa and a strength of ~63 GPa based on a thickness of 0.34 nm, along with a modulus of ~325 GPa and a strength of ~31 GPa based on a thickness of 0.7 nm. The inferiority of mechanical properties of GO compared to those of graphene was supposed to be due to the coverage of the oxygen-containing functional groups (-OH and -O-) and the fraction of the amorphous region (sp^3-bonded carbon atoms).[130]

In addition, Liu et al.[126] and Fan et al.[131] both employed density functional perturbation theory (DFPT) to find the anisotropic features of graphene under uniaxial tensile at large strains which was attributed to the hexagonal nature of the lattice units, while Fan et al. also investigated the dependence of Stone-Wales defects formation on the stress directions. Similar points were made by Ni et al.[132] using a molecular dynamics (MD) simulation. They concluded that the stiffness and strength in LM showed a slight superiority to those in TM (see in Figure 1.17), which was in correlation with the work by Liu et al.[126] Additionally, the deformation process of graphene was analysed as reversible elastic behavior before the fracture point confirmed by the overlapped loading and unloading load-displacement or stress-strain curves.[132-133]

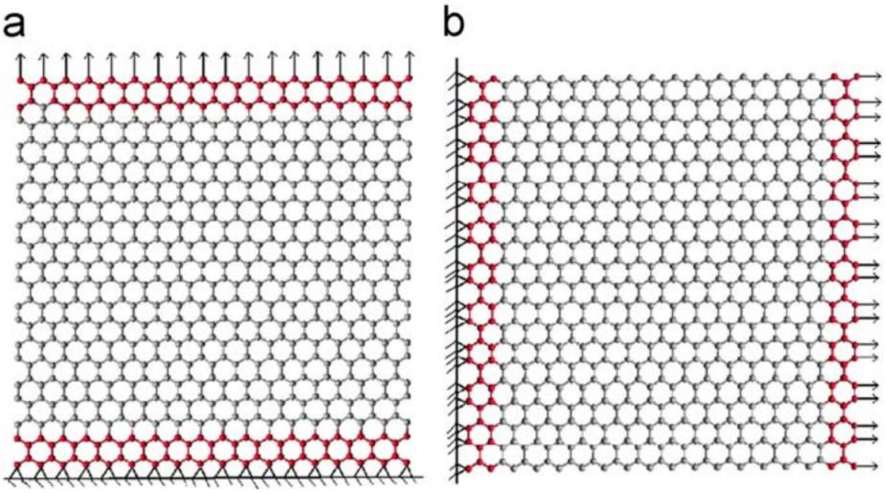

Figure 1.17 Schematic illustration of tensile model for (a) longitudinal mode (LM) and (b) transverse mode (TM).[132]

Nevertheless, despite the theoretical and experimental studies on monolayers, evidence shows that thickness plays a crucial role in the mechanical properties of multilayer graphene flakes. Zhang and coworker[134] operated a nano-indentation on graphene deposited on SiO_2 films to detect the relation between the layer number and mechanical behavior with the assistance of optical microscopy and AFM to confirm the layer numbers of the subject flakes. It implied that with increment of graphene layer number, the hardness and elastic modulus exhibited a linear decrease over a certain range of strains (see in Figure 1.18 and 1.19).

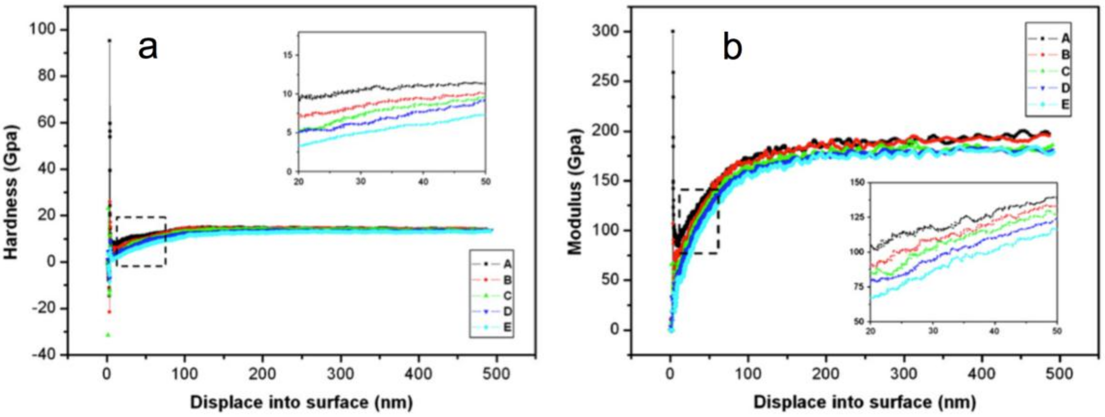

Figure 1.18 (a) The hardness-displacement curves and (b) the elastic modulus-displacement curves of graphene with different layers in the range of 0 - 500nm. Insets show the magnification in the range of 20 - 50 nm. A, B, C, D, and E are the notations for layer number of 1, 2, 3, 4 and above 4.[134]

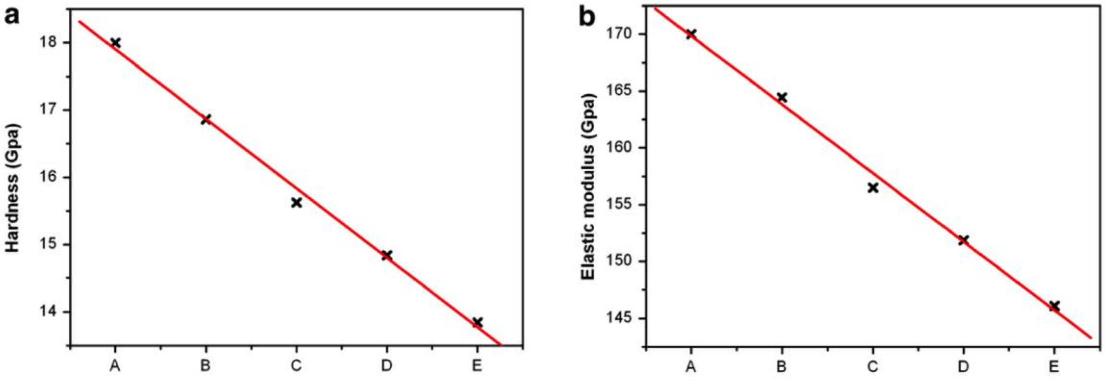

Figure 1.19 The mechanical properties variational trend of different layers graphene (a) hardness and (b) elastic modulus linearly decreases as the number of layers of graphene increase in the range of 10–500 nm.[134] (It should be pointed out that the units are GPa not Gpa)

1.4.2. Raman spectroscopy and deformation

In fact, any strain applied to a crystal will result in a change in the atomic structure (lattice distortion and bond stretching etc.), leading to the variation of the phonon modes, which is reflected in the mechanical and thermal properties. Specifically, isotropic compression and tension can bring up an increase (phonon hardening) and a decrease (phonon softening) in the frequency of the vibrational mode, respectively.[135] Therefore, by directly conducting the deformation of the material and spectrum collection simultaneously under a Raman spectrometer, can be a convenient approach for the stiffness estimation of a certain crystal. The stress-induced band shift can be directly obtained from the slope of the plots of peak position versus strain, the value of which was found to be proportional to the modulus of the lattice.[136]

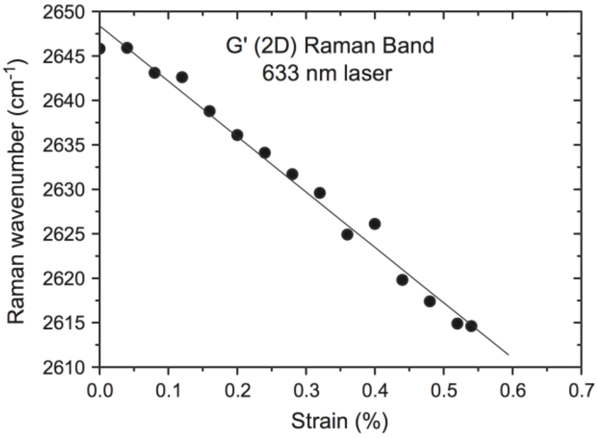

Figure 1.20 Raman G’ (2D) band shift of a graphene monolayer under strains[137]

In terms of graphene, the G band and 2D band shift of graphene shows a linear dependence on strain. The simplest way to detect the modulus of a graphene monolayer is to deposit the flake on a poly(methyl methacrylate) beam clamped in a four-point bending rig, followed by applying stress and plotting the peak position at each strain.[138] As seen in Figure 1.20, the 2D band shift rate of a graphene monolayer on PMMA beams gives a high value of -60 ± 5 cm^{-1}/% strain.[137] According to the universal calibration of -5 cm^{-1}/% strain for the 2D band all graphitic forms concluded from carbon fibres by Cooper et al.[139], the monolayer possesses a Young’s modulus of 1200 ± 100 GPa, which basically coincides with the values determined from the indentation by Lee et al.[124] and the ab initio calculation by Liu et al.[126] Additionally, while band shifts can be observed under strains, splitting and broadening of the G band and 2D band occur as well, which can enable determining the crystallographic orientation of the graphene lattice under strain.[140-141]

1.4.3. Thermal properties

The in-plane thermal conductivity of graphene has been found to be the highest amongst all the existed materials ever, whereas the conductivity is much lower between the interlayers that are bonded by week van der Waals interaction.[142] Specifically, at room temperature, the conductivity of pyrolytic graphite[143] (≈ 2000 W/mK) in the basal plane represents the 3D limit as the layer number of grahene approaches infinity, while the cross-plane show a value[143-144] (≈ 6W/mK) more than two orders of magnitude smaller. However, suspended graphene without the poor interaction between the interlayers can exhibit a superior conductivity of ~ 2000 to 5000 W/mK depending on the grain size and quality.[145-149] Additionally, it has been proved that the increasing layer number leads to the reduction of thermal conductivity of graphene due to the cross-plane coupling of the low-energy phonons and corresponding changes in the phonon Umklapp scattering.[150] Moreover, compared with suspended graphene, the conductivity of a supported thin graphene film decreases due to more phonon vibration modes aroused by the substrates.[151]

1.4.4. Gas barrier properties

The permeability of graphene flakes to gases was firstly direct measured by Bunch et al.[152] in 2008. They employed a graphene-sealed microchamber (as seen in Figure 1.21a) with pressure difference across the graphene drumhead and tested the gas leak rates through the membranes. As seen in Figure 1.21b, for the same species of gas, there is no dependence of the gas leak rate on the thickness of the graphene membranes, which implied that a leak did not occur upon the graphene flakes or through the defects on the flakes. They confirmed that any leak was from the SiO_2 walls on the microchamber by comparing the values of helium in the Figure 1.21b and the helium diffusion through glass calculated by Fick's law of diffusion. After a further estimation based on WKB tunneling along with the assumption of regarding helium atoms as point particles, they confirmed the perfection of a graphene layer and its impermeability to all standard gases. Apart from perfect graphene, porous graphene flakes were also studied by Jiang et al.[153] using density functional theory calculation in an attempt to achieve gas selectivity whereas Drahushuk et al.[154] built a model for porous graphene to give consideration of the manipulation of permeation rate.

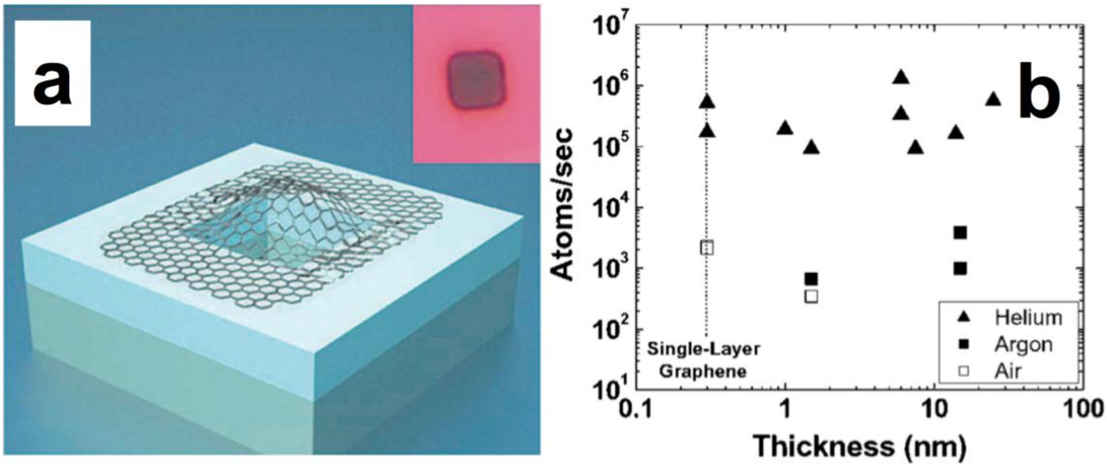

Figure 1.21 (a) Schematic sketch of the microchamber (440 nm SiO_2 walls on the top) sealed by a suspended graphene membrane (Inset shows the optical image of a graphene monolayer drumhead). (b) Scatter plot of the gas leak rates against graphene membrane thickness.[152]

References

1. Slonczewski, J. C.; Weiss, P. R., Band Structure of Graphite. *Phys. Rev.* **1958,** *109*, 272-279.

2. Wallace, P. R., The Band Theory of Graphite. *Phys. Rev.* **1947,** *71*, 622-634.

3. Quelques, R. E., Quelques proprietes typiques des corps solides. *Ann. I. H. Poincare* **1935,** *5*, 177-222.

4. Landau, L. D., Zur Theorie der phasenumwandlungen II. *Phys. Z. Sowjetunion* **1937,** *11*.

5. Evans, J. W.; Thiel, P. A.; Bartelt, M. C., Morphological evolution during epitaxial thin film growth: Formation of 2D islands and 3D mounds. *Surf. Sci. Rep.* **2006,** *61*, 1-128.

6. Venable, J. A.; Spiller, G. D. T.; Hanbucken, M., Nucleation and growth of thin films. *Rep. Prog. Phys.* **1984,** *47*, 399-459.

7. Mermin, N. D., Crystalline order in two dimensions. *Phys. Rev.* **1968,** *176*, 250-254.

8. Fradkin, E., Critical behavior of disordered degenerate semiconductors. II. Spectrum and transport properties in mean-field theory. *Phys. Rev. B* **1986,** *33*, 3263-3268.

9. Novoselov, K. S.; Geim, A. K.; Morozov, S. V.; Jiang, D.; Zhang, Y., Electric field effect in atomically thin carbon films. *Science* **2004,** *306*, 666-669.

10. Geim, A. K.; Novoselov, K. S., The rise of graphene. *Nat. Mater.* **2007,** *6*, 183-191.

11. Al-Jishi, R.; Dresselhaus, G., Lattice-dynamical model for graphite. *Phys. Rev. B* **1982,** *26*, 4514-4522.

12. Partoens, B.; Peeters, F. M., From graphene to graphite: Electronic structure around the K point. *Phys. Rev. B* **2006,** *74*, 075404.

13. Hennig, G. R., Determination of Lattice Vacancies in Graphite. *J. Chem. Phys.* **1964,** *40*, 2877-2882.

14. Lu, X. K.; Yu, M. F.; Huang, H.; Ruoff, R. S., Tailoring graphite with the goal of achieving single sheets. *Nanotechnology* **1999,** *10*, 269-272.

15. Lu, X. K.; Huang, H.; Nemchuk, N.; Ruoff, R. S., Patterning of highly oriented pyrolytic graphite by oxygen plasma etching. *Appl. Phys. Lett.* **1999,** *75*, 193-195.

16. Bonaccorso, F.; Lombardo, A.; Hasan, T.; Sun, Z.; Colombo, L.; Ferrari, A., Production and processing of graphene and 2d crystals. *Mater. Today* **2012,** *15*,

564-589.

17. Novoselov, K. S.; Jiang, D.; Schedin, F.; Booth, T. J.; Khotkevich, V. V.; Morozov, S. V.; Geim, A. K., Two-dimensional atomic crystals. *Proc. Natl. Acad. Sci. USA* **2005,** *102,* 10451-3.

18. Liu, X.; Hu, B.; Cui, B.; Han, H. J.; Ma, Q.; Wang, B. H., Liquid-phase exfoliation of graphite to produce high-quality graphene. *J. Appl. Sci. Eng. Inno.* **2015,** *2,* 240-244.

19. Wei, Y.; Sun, Z., Liquid-phase exfoliation of graphite for mass production of pristine few-layer graphene. *Curr. Opin. Colloid In.* **2015,** *20,* 311-321.

20. Hernandez, Y.; Nicolosi, V.; Lotya, M.; Blighe, F. M.; Sun, Z.; De, S.; McGovern, I. T.; Holland, B.; Byrne, M.; Gun'Ko, Y. K.; Boland, J. J.; Niraj, P.; Duesberg, G.; Krishnamurthy, S.; Goodhue, R.; Hutchison, J.; Scardaci, V.; Ferrari, A. C.; Coleman, J. N., High-yield production of graphene by liquid-phase exfoliation of graphite. *Nat. Nanotechnol* **2008,** *3,* 563-8.

21. Xu, J.; Dang, D. K.; Tran, V. T.; Liu, X.; Chung, J. S.; Hur, S. H.; Choi, W. M.; Kim, E. J.; Kohl, P. A., Liquid-phase exfoliation of graphene in organic solvents with addition of naphthalene. *J. Colloid Interf. Sci.* **2014,** *418*, 37-42.

22. Mattevi, C.; Eda, G.; Agnoli, S.; Miller, S.; Mkhoyan, K. A.; Celik, O.; Mastrogiovanni, D.; Granozzi, G.; Garfunkel, E.; Chhowalla, M., Evolution of electrical, chemical, and structural properties of transparent and conducting chemically derived graphene thin films. *Adv. Funct. Mater.* **2009,** *19*, 2577-2583.

23. López, V.; Sundaram, R. S.; Gómez-Navarro, C.; Olea, D.; Burghard, M.; Gómez-Herrero, J.; Zamora, F.; Kern, K., Chemical vapor deposition repair of graphene oxide: a route to highly-conductive graphene monolayers. *Adv. Mater.* **2009,** *21*, 4683-4686.

24. Monajjemi, M., Liquid-phase exfoliation (LPE) of graphite towards graphene: an ab initio study. *J. Mol. Liq.* **2017,** *230*, 461-472.

25. Yu, Q.; Lian, J.; Siriponglert, S.; Li, H.; Chen, Y. P.; Pei, S.-S., Graphene

segregated on Ni surfaces and transferred to insulators. *Appl. Phys. Lett.* **2008,** *93*, 113103.

26. Kim, K. S.; Zhao, Y.; Jang, H.; Lee, S. Y.; Kim, J. M.; Kim, K. S.; Ahn, J. H.; Kim, P.; Choi, J. Y.; Hong, B. H., Large-scale pattern growth of graphene films for stretchable transparent electrodes. *Nature* **2009,** *457*, 706-10.

27. Strudwick, A. J.; Weber, N. E.; Schwab, M. G.; Kettner, M.; Weitz, R. T.; Wunsch, J. R.; Mullen, K.; Sachdev, H., Chemical vapor deposition of high quality graphene films from carbon dioxide atmospheres. *ACS Nano* **2015,** *9*, 31-42.

28. Reina, A.; Jia, X.; Ho, J.; Nezich, D.; Son, H.; Bulovic, V.; Dresselhaus, M. S.; Kong, J., Large area, few-Layer graphene films on arbitrary substrates by chemical vapor deposition. *Nano. Lett.* **2009,** *9*, 30-35.

29. De Arco, L. G.; Yi, Z.; Kumar, A.; Chongwu, Z., Synthesis, transfer, and devices of single- and few-Layer graphene by chemical vapor deposition. *IEEE T. Nanotechnol.* **2009,** *8*, 135-138.

30. Chugh, S.; Mehta, R.; Lu, N.; Dios, F. D.; Kim, M. J.; Chen, Z., Comparison of graphene growth on arbitrary non-catalytic substrates using low-temperature PECVD. *Carbon* **2015,** *93*, 393-399.

31. Losurdo, M.; Giangregorio, M. M.; Capezzuto, P.; Bruno, G., Graphene CVD growth on copper and nickel: role of hydrogen in kinetics and structure. *Phys. Chem. Chem. Phys.* **2011,** *13*, 20836-43.

32. Drieschner, S.; Weber, M.; Wohlketzetter, J.; Vieten, J.; Makrygiannis, E.; Blaschke, B. M.; Morandi, V.; Colombo, L.; Bonaccorso, F.; Garrido, J. A., High surface area graphene foams by chemical vapor deposition. *2D Mater.* **2016,** *3*, 045013.

33. Chen, C. Y.; Dai, D.; Chen, G. X.; Yu, J. H.; Nishimura, K.; Lin, C. T.; Jiang, N.; Zhan, Z. L., Rapid growth of single-layer graphene on the insulating substrates by thermal CVD. *Appl. Surf. Sci.* **2015,** *346*, 41-45.

34. Park, J.; An, H.; Choi, D. C.; Hussain, S.; Song, W.; An, K. S.; Lee, W. J.; Lee, N.;

Lee, W. G.; Jung, J., Selective growth of graphene in layer-by-layer via chemical vapor deposition. *Nanoscale* **2016,** *8*, 14633-42.

35. Li, M.; Guo, W.; Li, H.; Xu, S.; Qu, C.; Yang, B., Synthesis of chemical vapor deposition graphene on tantalum wire for supercapacitor applications. *Appl. Surf. Sci.* **2014,** *317*, 1100-1106.

36. Mehedi, H. A.; Baudrillart, B.; Alloyeau, D.; Mouhoub, O.; Ricolleau, C.; Pham, V. D.; Chacon, C.; Gicquel, A.; Lagoute, J.; Farhat, S., Synthesis of graphene by cobalt-catalyzed decomposition of methane in plasma-enhanced CVD: Optimization of experimental parameters with Taguchi method. *J. Appl. Phys.* **2016,** *120*, 065304.

37. Kaindl, R.; Jakopic, G.; Resel, R.; Pichler, J.; Fian, A.; Fisslthaler, E.; Grogger, W.; Bayer, B. C.; Fischer, R.; Waldhauser, W., Synthesis of graphene-layer nanosheet coatings by PECVD. *Mater. Today* **2015,** *2*, 4247-4255.

38. Cabrero-Vilatela, A.; Weatherup, R. S.; Braeuninger-Weimer, P.; Caneva, S.; Hofmann, S., Towards a general growth model for graphene CVD on transition metal catalysts. *Nanoscale* **2016,** *8*, 2149-58.

39. Zhao, J.; Pei, S.; Ren, W.; Gao, L.; Cheng, H., Efficient preparation of large-area graphene oxide sheets for transparent conductive films. *ACS Nano* **2010,** *4*, 5245-5252.

40. Kovtyukhova, N. I.; Ollivier, P. J.; Martin, B. R., Layer-by-layer assembly of ultrathin composite films from micron-sized graphite oxide sheets and polycations. *Chem. Mater.* **1999,** *11*, 771-778.

41. Song, J.; Wang, X.; Chang, C.-T., Preparation and Characterization of Graphene Oxide. *J. Nanomater.* **2014,** *2014*, 1-6.

42. Rattana; Chaiyakun, S.; Witit-anun, N.; Nuntawong, N.; Chindaudom, P.; Oaew, S.; Kedkeaw, C.; Limsuwan, P., Preparation and characterization of graphene oxide nanosheets. *Procedia Eng.* **2012,** *32*, 759-764.

43. Hummers, W. S.; Offeman, R. E., Preparation of graphitic xxide. *J. Am. Chem. Soc.* **1958,** *80*, 1339.

44. Hirata, M.; Gotou, T.; Horiuchi, S.; Fujiwara, M.; Ohba, M., Thin-film particles of graphite oxide 1: high-yield synthesis and flexibility of the particles. *Carbon* **2004,** *42*, 2929-2937.

45. Rourke, J. P.; Pandey, P. A.; Moore, J. J.; Bates, M.; Kinloch, I. A.; Young, R. J.; Wilson, N. R., The real graphene oxide revealed: stripping the oxidative debris from the graphene-like sheets. *Angew. Chem. Int. Ed.* **2011,** *50*, 3173-7.

46. Wu, Z.-S.; Ren, W.; Gao, L.; Liu, B.; Jiang, C.; Cheng, H.-M., Synthesis of high-quality graphene with a pre-determined number of layers. *Carbon* **2009,** *47*, 493-499.

47. McAllister, M. J.; Li, J.; Adamson, D. H.; Schniepp, H. C., Single sheet functionalized graphene by oxidation and thermal expansion of graphite. *Chem. Mater.* **2007,** *19*, 4396-4404.

48. Schniepp, H. C.; Li, J.; McAllister, M. J.; Sai, H.; Herrera-Alonso, M.; Admson, H.; Prud'homme, R. K.; Car, R.; Saville, D. A.; Aksay, I. A., Functionalized single graphene sheets derived from splitting graphite oxide. *J. Phys. Chem. B* **2006,** *110*, 8535-8539.

49. Wu, Z.; Ren, W.; Gao, L., Synthesis of graphene sheets with high electrical conductivity and good thermal stablility by hydrogen arc discharge exfoliation. *ACS Nano* **2009,** *3*, 411-417.

50. Hassan, H. M. A.; Abdelsayed, V.; Khder, A. E. R. S.; AbouZeid, K. M.; Terner, J.; El-Shall, M. S.; Al-Resayes, S. I.; El-Azhary, A. A., Microwave synthesis of graphene sheets supporting metal nanocrystals in aqueous and organic media. *J. Mater. Chem.* **2009,** *19*, 3832.

51. Chu, Z.; He, R.; Zhang, X.; Jiang, Z.; Cheng, H.; Wang, Y.; Li, X., Fabrication of porous SiCy (core)/C (shell) fibres using a hybrid precursor of polycarbosilane and pitch. *Carbon* **2010,** *48*, 2115-2118.

52. Cote, L. J.; Cruz-Silva, R.; Huang, J., Flash reduction and patterning of graphite oxide and its polymer composite. *J. Am. Chem. Soc.* **2009,** *131*, 11027-11032.

53. Zhang, Y.; Guo, L.; Wei, S.; He, Y.; Xia, H.; Chen, Q.; Sun, H.-B.; Xiao, F.-S., Direct imprinting of microcircuits on graphene oxides film by femtosecond laser reduction. *Nano Today* **2010,** *5*, 15-20.

54. Pei, S.; Zhao, J.; Du, J.; Ren, W.; Cheng, H.-M., Direct reduction of graphene oxide films into highly conductive and flexible graphene films by hydrohalic acids. *Carbon* **2010,** *48*, 4466-4474.

55. Chen, Y.; Zhang, X.; Zhang, D.; Yu, P.; Ma, Y., High performance supercapacitors based on reduced graphene oxide in aqueous and ionic liquid electrolytes. *Carbon* **2011,** *49*, 573-580.

56. Chua, C. K.; Ambrosi, A.; Pumera, M., Graphene oxide reduction by standard industrial reducing agent: thiourea dioxide. *J. Mater. Chem.* **2012,** *22*, 11054.

57. Gao, W.; Alemany, L. B.; Ci, L.; Ajayan, P. M., New insights into the structure and reduction of graphite oxide. *Nat Chem* **2009,** *1*, 403-8.

58. Stankovich, S.; Dikin, D. A.; Piner, R. D.; Kohlhaas, K. A.; Kleinhammes, A.; Jia, Y.; Wu, Y.; Nguyen, S. T.; Ruoff, R. S., Synthesis of graphene-based nanosheets via chemical reduction of exfoliated graphite oxide. *Carbon* **2007,** *45*, 1558-1565.

59. Park, S.; An, J.; Potts, J. R.; Velamakanni, A.; Murali, S.; Ruoff, R. S., Hydrazine-reduction of graphite- and graphene oxide. *Carbon* **2011,** *49*, 3019-3023.

60. Fan, Z.; Wang, K.; Wei, T.; Yan, J.; Song, L.; Shao, B., An environmentally friendly and efficient route for the reduction of graphene oxide by aluminum powder. *Carbon* **2010,** *48*, 1686-1689.

61. Bose, S.; Kuila, T.; Mishra, A. K.; Kim, N. H.; Lee, J. H., Dual role of glycine as a chemical functionalizer and a reducing agent in the preparation of graphene: an environmentally friendly method. *J. Mater. Chem.* **2012,** *22*, 9696.

62. Fernández-Merino, M. J.; Guardia, L.; Paredes, J. I.; Villar-Rodil, S.; Solís-Fernández, P.; Martínez-Alonso, A.; Tascón, J. M. D., Vitamin C is an ideal substitute for hydrazine in the reduction of graphene oxide suspensions. *J. Phys. Chem. C* **2010,** *114*, 6426-6432.

63. Chua, C. K.; Pumera, M., Chemical reduction of graphene oxide: a synthetic chemistry viewpoint. *Chem. Soc. Rev.* **2014,** *43*, 291-312.

64. Fukushima, H. Graphite nanoreinforcements in polymer nanocomposites. Ph.D Thesis, Michigan State University, East Lansing, MI, USA, 2003

65. Kim, S.; Do, I.; Drzal, L. T., Thermal stability and dynamic mechanical behavior of exfoliated graphite nanoplatelets-LLDPE nanocomposites. *Polym. Composite.* **2009,** *31*, 755-761.

66. Xiang, J.; Drzal, L. T., Thermal conductivity of exfoliated graphite nanoplatelet paper. *Carbon* **2011,** *49*, 773-778.

67. Cho, D.; Lee, S.; Yang, G.; Fukushima, H.; Drzal, L. T., Dynamic Mechanical and Thermal Properties of Phenylethynyl-Terminated Polyimide Composites Reinforced With Expanded Graphite Nanoplatelets. *Macromol. Mater. Eng.* **2005,** *290*, 179-187.

68. Kalaitzidou, K.; Fukushima, H.; Drzal, L. T., Mechanical properties and morphological characterization of exfoliated graphite – polypropylene nanocomposites. *Compos. Part A - Appl. S.* **2007,** *38*, 1675-1682.

69. Kim, S.; Drzal, L. T., High latent heat storage and high thermal conductive phase change materials using exfoliated graphite nanoplatelets. *Sol. Energ. Mater. Sol. C.* **2009,** *93*, 136-142.

70. ISO/TS 80004-13:2017: Nanotechnologies - Vocabulary. Part 13: Graphene and related two-dimensional (2D) materials.

71. Nair, R. R.; Blake, P.; Grigorenko, A. N.; Novoselov, K. S.; Booth, T. J.; Stauber, T.; Peres, N. M.; Geim, A. K., Fine structure constant defines visual transparency of graphene. *Science* **2008,** *320*, 1308.

72. Blake, P.; Hill, E. W.; Castro Neto, A. H.; Novoselov, K. S.; Jiang, D.; Yang, R.; Booth, T. J.; Geim, A. K., Making graphene visible. *Appl. Phys. Lett.* **2007,** *91*, 063124.

73. Wang, Y.; Ni, Z.; Yu, T.; Shen, Z.; Wang, H.; Wu, Y.; Chen, W.; Wee, A., Raman Studies of Monolayer Graphene- The Substrate Effect. *J. Phys. Chem. C* **2008,** *112*,

10637–10640.

74. Reina, A.; Son, H.; Jiao, L.; Fan, B.; Dresselhaus, M. S.; Liu, Z.; ong, J., Transferring and Identification of Single- and Few-Layer Graphene on Arbitrary Substrates. *J. Phys. Chem. C* **2008,** *112*, 17741–17744.

75. Terasawa, T. O.; Saiki, K., Radiation-mode optical microscopy on the growth of graphene. *Nat. Commun.* **2015,** *6*, 6834.

76. Cheng, Y.; Song, Y.; Zhao, D.; Zhang, X.; Yin, S.; Wang, P.; Wang, M.; Xia, Y.; Maruyama, S.; Zhao, P.; Wang, H., Direct identification of multilayer graphene stacks on copper by optical microscopy. *Chem. Mater.* **2016,** *28,* 2165-2171.

77. Obelenis, F.; Champi, A., Determination of the number of graphene layers on different substrates by optical microscopy Technique. *Braz. J. Phys.* **2014,** *44*, 682-686.

78. Gaskell, P. E.; Skulason, H. S.; Rodenchuk, C.; Szkopek, T., Counting graphene layers on glass via optical reflection microscopy. *Appl. Phys. Lett.* **2009,** *94,* 143101.

79. Lai, S.; Kyu Jang, S.; Jae Song, Y.; Lee, S., Probing graphene defects and estimating graphene quality with optical microscopy. *Appl. Phys. Lett.* **2014,** *104*, 043101.

80. Duong, D. L.; Han, G. H.; Lee, S. M.; Gunes, F.; Kim, E. S.; Kim, S. T.; Kim, H.; Ta, Q. H.; So, K. P.; Yoon, S. J.; Chae, S. J.; Jo, Y. W.; Park, M. H.; Chae, S. H.; Lim, S. C.; Choi, J. Y.; Lee, Y. H., Probing graphene grain boundaries with optical microscopy. *Nature* **2012,** *490,* 235-9.

81. Si, Y.; Samulski, E. T., Synthesis of water soluble graphene. *Nano Lett.* **2008,** *8*, 1679-1682.

82. Tung, V. C.; Allen, M. J.; Yang, Y.; Kaner, R. B., High-throughput solution processing of large-scale graphene. *Nat. Nanotechnol.* **2009,** *4*, 25-9.

83. Dikin, D. A.; Stankovich, S.; Zimney, E. J.; Piner, R. D.; Dommett, G. H.; Evmenenko, G.; Nguyen, S. T.; Ruoff, R. S., Preparation and characterization of graphene oxide paper. *Nature* **2007,** *448,* 457-60.

84. Wang, Z.-J.; Weinberg, G.; Zhang, Q.; Lunkenbein, T.; Klein-Hoffmann, A.; Kurnastowska, M.; Plodinec, M.; Li, Q.; Chi, L.; Schloegl, R.; Willinger, M.-G., Direct observation of graphene growth and associated copper substrate dynamics by in situ scanning electron microscopy. *ASC Nano* **2015,** *9*, 1506-1519.

85. Ilyin, A.; Guseinov, N.; Nikitin, A.; Tsyganov, I., Characterization of thin graphite layers and graphene by energy dispersive X-ray analysis. *Physica. E Low-dimens. syst. nanostruct.* **2010,** *42*, 2078-2080.

86. Wang, H.; Yamada, C.; Homma, Y., Scanning electron microscopy imaging mechanisms of CVD-grown graphene on Cu substrate revealed by in situ observation. *Jan. J. Appl. Phys.* **2015,** *54*, 050301.

87. Jia, C.; Jiang, J.; Gan, L.; Guo, X., Direct optical characterization of graphene growth and domains on growth substrates. *Sci. Rep.* **2012,** *2*, 707.

88. Park, M.-H.; Kim, T.-H.; Yang, C.-W., Thickness contrast of few-layered graphene in SEM. *Surf. Interface Anal.* **2012,** *44*, 1538-1541.

89. Takahashi, K.; Yamada, K.; Kato, H.; Hibino, H.; Homma, Y., In situ scanning electron microscopy of graphene growth on polycrystalline Ni substrate. *Surf. Sci.* **2012,** *606*, 728-732.

90. Grodecki, K.; Jozwik, I.; Baranowski, J. M.; Teklinska, D.; Strupinski, W., SEM and Raman analysis of graphene on SiC(0001). *Micron* **2016,** *80*, 20-3.

91. Park, J. B.; Kim, Y.-J.; Kim, S.-M.; Yoo, J. M.; Kim, Y.; Gorbachev, R.; Barbolina, I. I.; Kim, S. J.; Kang, S.; Yoon, M.-H.; Cho, S.-P.; Novoselov, K. S.; Hong, B. H., Non-destructive electron microscopy imaging and analysis of biological samples with graphene coating. *2D Mater.* **2016,** *3*, 045004.

92. Lee, J.; Zheng, X.; Roberts, R. C.; Feng, P. X. L., Scanning electron microscopy characterization of structural features in suspended and non-suspended graphene by customized CVD growth. *Diam. Relat. Mater.* **2015,** *54*, 64-73.

93. Wojcik, M.; Hauser, M.; Li, W.; Moon, S.; Xu, K., Graphene-enabled electron microscopy and correlated super-resolution microscopy of wet cells. *Nat. Commun.*

2015, *6*, 7384.

94. Fox, D.; O'Neill, A.; Zhou, D.; Boese, M.; Coleman, J. N.; Zhang, H. Z., Nitrogen assisted etching of graphene layers in a scanning electron microscope. *Appl. Phys. Lett.* **2011,** *98*, 243117.

95. Tuinstra, F.; Koenig, J. L., Raman Spectrum of Graphite. *J. Chem. Phys.* **1970,** *53*, 1126-1130.

96. Nemanich, R. J.; Solin, S. A., First- and second-order Raman scattering from finite-size crystals of graphite. *Phys. Rev. B* **1979,** *20*, 392-401.

97. Ferrari, A. C.; Meyer, J. C.; Scardaci, V.; Casiraghi, C.; Lazzeri, M.; Mauri, F.; Piscanec, S.; Jiang, D.; Novoselov, K. S.; Roth, S.; Geim, A. K., Raman spectrum of graphene and graphene layers. *Phys. Rev. Lett.* **2006,** *97*, 187401.

98. Vidano, R. P.; Fischbach, D. B., Observation of Raman band shifting with excitation wavelength for carbons and graphites. *Solid State Commun.* **1981,** *39*, 341-344.

99. Wang, Y. Y.; Ni, Z. H.; Shen, Z. X.; Wang, H. M.; Wu, Y. H., Interference enhancement of Raman signal of graphene. *Appl. Phys. Lett.* **2008,** *92* (4), 043121.

100. Cançado, L. G.; Takai, K.; Enoki, T.; Endo, M.; Kim, Y. A.; Mizusaki, H.; Speziali, N. L.; Jorio, A.; Pimenta, M. A., Measuring the degree of stacking order in graphite by Raman spectroscopy. *Carbon* **2008,** *46*, 272-275.

101. Wilhelm, H.; Lelaurain, M.; McRae, E.; Humbert, B., Raman spectroscopic studies on well-defined carbonaceous materials of strong two-dimensional character. *J. Appl. Phys.* **1998,** *84*, 6552-6558.

102. Cançado, L. G.; Jorio, A.; Ferreira, E. H.; Stavale, F.; Achete, C. A.; Capaz, R. B.; Moutinho, M. V.; Lombardo, A.; Kulmala, T. S.; Ferrari, A. C., Quantifying defects in graphene via Raman spectroscopy at different excitation energies. *Nano. Lett.* **2011,** *11* (8), 3190-6.

103. Matthews, M. J.; Pimenta, M. A., Origin of dispersive effects of the Raman D band in carbon materials. *Phys. Rev. B* **1999,** *59*, R6585–R6588.

104. Ferrari, A. C., Raman spectroscopy of graphene and graphite: Disorder, electron–phonon coupling, doping and nonadiabatic effects. *Solid State Commun.* **2007,** *143*, 47-57.

105. Pimenta, M. A.; Dresselhaus, G.; Dresselhaus, M. S.; Cancado, L. G.; Jorio, A.; Saito, R., Studying disorder in graphite-based systems by Raman spectroscopy. *Phys. Chem. Chem. Phys.* **2007,** *9*, 1276-91.

106. Ferrari, A. C.; Basko, D. M., Raman spectroscopy as a versatile tool for studying the properties of graphene. *Nat. Nanotechnol.* **2013,** *8*, 235-46.

107. Ferrari, A. C.; Robertson, J., Interpretation of Raman spectra of disordered and amorphous carbon. *Phys. Rev. B* **2000,** *61*, 14095–14107.

108. Lucchese, M. M.; Stavale, F.; Ferreira, E. H. M.; Vilani, C.; Moutinho, M. V. O.; Capaz, R. B.; Achete, C. A.; Jorio, A., Quantifying ion-induced defects and Raman relaxation length in graphene. *Carbon* **2010,** *48*, 1592-1597.

109. Martins Ferreira, E. H.; Moutinho, M. V. O.; Stavale, F.; Lucchese, M. M.; Capaz, R. B.; Achete, C. A.; Jorio, A., Evolution of the Raman spectra from single-, few-, and many-layer graphene with increasing disorder. *Phys. Rev. B* **2010,** *82*.

110. Beams, R.; Gustavo Cancado, L.; Novotny, L., Raman characterization of defects and dopants in graphene. *J. Phys. Condens. Matter.* **2015,** *27*, 083002.

111. Lui, C. H.; Li, Z.; Chen, Z.; Klimov, P. V.; Brus, L. E.; Heinz, T. F., Imaging stacking order in few-layer graphene. *Nano. Lett.* **2011,** *11* (1), 164-9.

112. Warren, B. E., X-Ray diffraction in random layer lattices. *Phys.l Rev.* **1941,** *59*, 693-698.

113. Wilson, A. J. C., X-Raydiffraction by random layers: ideal line profiles and determination of structure amplitudes from observed line profiles. *Acta Cryst.* **1949,** *2*, 245.

114. Fujimoto, H.; Shiraishi, M., Characterization of unordered carbon using Warren–Bodenstein’s equation. *Carbon* **2001,** *39*, 1753-1761.

115. Fujimoto, H., Theoretical X-ray scattering intensity of carbons with turbostratic

stacking and AB stacking structures. *Carbon* **2003,** *41*, 1585-1592.

116.Warren, B. E., X‐Ray diffraction study of carbon black. *J. Chem. Phys.* **1934,** *2*, 551-555.

117.Wang, G.; Yang, J.; Park, J.; Gou, X.; Wang, B.; Liu, H.; Yao, J., Facile synthesis and characterization of graphene nanosheets. *J. Phys. Chem. C* **2008,** *112*, 8192-8195.

118.Pan, D.; Wang, S.; Zhao, B.; Wu, M.; Zhang, H.; Wang, Y.; Jiao, Z., Li Storage Properties of Disordered Graphene Nanosheets. *Chem. Mater.* **2009,** *21*, 3136-3142.

119.Lian, P.; Zhu, X.; Liang, S.; Li, Z.; Yang, W.; Wang, H., Large reversible capacity of high quality graphene sheets as an anode material for lithium-ion batteries. *Electrochim. Acta* **2010,** *55*, 3909-3914.

120. Chen, Y.; Xie, B.; Ren, Y.; Yu, M.; Qu, Y.; Xie, T.; Zhang, Y.; Wu, Y., Designed nitrogen doping of few-layer graphene functionalized by selective oxygenic groups. *Nanoscale Res. Lett.* **2014,** *9*, 646.

121. Saikia, B. K.; Boruah, R. K.; Gogoi, P. K., A X-ray diffraction analysis on graphene. *J. Chem. Sci.* **2009,** *121*, 103-106.

122. Manoj, B.; Kunjomana, A. G., Study of stacking structure of amorphous carbon by X-Ray diffraction technique. *Int. J. Electrochem. Sci.* **2012,** *7*, 3127-3134.

123. Andonovic, B.; Grozdanov, A.; Paunović, P.; Dimitrov, A. T., X-ray diffraction analysis on layers in graphene samples obtained by electrolysis in molten salts: a new perspective. *Micro Nano Lett.* **2015,** *10*, 683-685.

124. Lee, C.; Wei, X.; Kysar, J. W.; Hone, J., Measurement of the elastic properties and intrinsic strength of monolayer graphene. *Science* **2008,** *321*, 385-8.

125. Griffith, A. A., The phenomena of rupture and flow in solids. *Philos. Trans. R. Soc. London Ser. A* **1921,** *221*, 163-198.

126. Liu, F.; Ming, P.; Li, J., Ab initiocalculation of ideal strength and phonon instability of graphene under tension. *Phys. Rev. B* **2007,** *76*.

127. Gómez-Navarro, C.; Burghard, M.; Kern, K., Elastic Properties of Chemically Derived Single Graphene Sheets. *Nano Lett.* **2008,** *8*, 2045-2049.

128. Suk, J. W.; Piner, R. D.; An, J.; Ruoff, R. S., Mechanical properties of monolayer graphene oxide. *ACS Nano* **2010,** *4*, 6557–6564.

129. Paci, J. T.; Belytschko, T.; Schatz, G. C., Computational studies of the structure, behavior upon heating, and mechanical properties of graphite oxide. *J. Phys. Chem. C* **2008,** *111*, 18099-18111.

130. Liu, L.; Zhang, J.; Zhao, J.; Liu, F., Mechanical properties of graphene oxides. *Nanoscale* **2012,** *4*, 5910-6.

131. Fan, B. B.; Yang, X. B.; Zhang, R., Anisotropic mechanical properties and Stone–Wales defects in graphene monolayer: A theoretical study. *Phys. Lett. A* **2010,** *374*, 2781-2784.

132. Ni, Z.; Bu, H.; Zou, M.; Yi, H.; Bi, K.; Chen, Y., Anisotropic mechanical properties of graphene sheets from molecular dynamics. *Physica B* **2010,** *405*, 1301-1306.

133. Nardelli, M. B.; Yakobson, B. I.; Bernholc, J., Brittle and ductile behavior in carbon nanotubes. *Phys. Rev. Lett.* **1998,** *81*, 4656-4659.

134. Zhang, Y.; Pan, C., Measurements of mechanical properties and number of layers of graphene from nano-indentation. *Diam. Relat. Mater.* **2012,** *24*, 1-5.

135. Ferralis, N., Probing mechanical properties of graphene with Raman spectroscopy. *J. Mater. Sci.* **2010,** *45*, 5135-5149.

136. Andrews, M. C.; Young, R. J., Analysis of the deformation of aramid fibres and composites using Raman spectroscopy. *J. Raman Spectrosc.* **1993,** *24*, 539-544.

137. Young, R. J.; Kinloch, I. A.; Gong, L.; Novoselov, K. S., The mechanics of graphene nanocomposites: A review. *Compos. Sci. Technol.* **2012,** *72*, 1459-1476.

138. Gong, L.; Kinloch, I. A.; Young, R. J.; Riaz, I.; Jalil, R.; Novoselov, K. S., Interfacial stress transfer in a graphene monolayer nanocomposite. *Adv. Mater.* **2010,** *22*, 2694-7.

139. Cooper, C. A.; Young, R. J.; Halsall, M., Investigation into the deformation of carbon nanotubes and their composites through the use of Raman spectroscopy.

Compos. Part A **2001,** *32*, 401-411.

140. Huang, M.; Yan, H.; Chen, C.; Song, D.; Heinz, T. F.; Hone, J., Phonon softening and crystallographic orientation of strained graphene studied by Raman spectroscopy. *Proc. Natl. Acad. Sci.* **2009,** *106*, 7304-8.

141. Mohiuddin, T. M. G.; Lombardo, A.; Nair, R. R.; Bonetti, A.; Savini, G.; Jalil, R.; Bonini, N.; Basko, D. M.; Galiotis, C.; Marzari, N.; Novoselov, K. S.; Geim, A. K.; Ferrari, A. C., Uniaxial strain in graphene by Raman spectroscopy:Gpeak splitting, Grüneisen parameters, and sample orientation. *Phys. Rev. B* **2009,** *79*.

142. Schabel, M. C.; Martins, J. L., Energetics of interplanar binding in graphite. *Phys. Rev. B* **1992,** *46*, 7185-7188.

143. Ho, C. Y.; Powell, R. W.; Liley, P. E., Thermal conductivity of the elements: a comprehensive review. *J. Phys. Chem. Ref. Data* **1974,** *3*, 1.

144. Sun, K.; Stroscio, M. A.; Dutta, M., Graphite C-axis thermal conductivity. *Superlattice. Microst.* **2009,** *45*, 60-64.

145. Chen, S.; Moore, A. L.; Cai, W.; Suk, J. W.; An, J.; Mishra, C.; Amos, C.; Magnuson, C. W.; Kang, J.; Shi, L.; Ruoff, R. S., Raman measurements of thermal transport in suspended monolayer graphene of variable sizes in vacuum and gaseous environments. *ACS Nano* **2011,** *5*, 321-328.

146. Chen, S.; Wu, Q.; Mishra, C.; Kang, J.; Zhang, H.; Cho, K.; Cai, W.; Balandin, A. A.; Ruoff, R. S., Thermal conductivity of isotopically modified graphene. *Nat. Mater.* **2012,** *11*, 203-7.

147. Balandin, A. A.; Ghosh, S.; Bao, W.; Calizo, I.; Teweldebrhan, D.; Miao, F.; Lau, C. N., Superior thermal conductivity of single-layer graphene. *Nano Lett.* **2008,** *8*, 902-907.

148. Ghosh, S.; Calizo, I.; Teweldebrhan, D.; Pokatilov, E. P.; Nika, D. L.; Balandin, A. A.; Bao, W.; Miao, F.; Lau, C. N., Extremely high thermal conductivity of graphene: Prospects for thermal management applications in nanoelectronic circuits. *Appl. Phys. Lett.* **2008,** *92*, 151911.

149. Nika, D. L.; Pokatilov, E. P.; Askerov, A. S.; Balandin, A. A., Phonon thermal conduction in graphene: Role of Umklapp and edge roughness scattering. *Phys. Rev. B* **2009,** *79*, 155413.

150. Ghosh, S.; Bao, W.; Nika, D. L.; Subrina, S.; Pokatilov, E. P.; Lau, C. N.; Balandin, A. A., Dimensional crossover of thermal transport in few-layer graphene. *Nat. Mater.* **2010,** *9*, 555-8.

151. Seol, J. H.; Jo, I.; Moore, A. L.; Lindsay, L.; Aitken, Z. H.; Pettes, M. T.; Li, X.; Yao, Z.; Huang, R.; Broido, D.; Mingo, N.; Ruoff, R. S.; Shi, L., Two-dimensional phonon transport in supported graphene. *Science* **2010,** *328*, 213-217.

152. Bunch, J. S.; Verbridge, S. S.; Alden, J. S.; van der Zande, A. M.; Parpia, J. M.; Craighead, H. G.; McEuen, P. L., Impermeable atomic membranes from graphene sheets. *Nano Lett.* **2008,** *8*, 2458-2462.

153. Jiang, D.; Cooper, V. R.; Dai, S., Porous graphene as the ultimate membrane for gas separation. *Nano Lett.* **2009,** *9*, 4019-4024.

154. Drahushuk, L. W.; Strano, M. S., Mechanisms of gas permeation through single layer graphene membranes. *Langmuir* **2012,** *28*, 16671-8.

2. Graphene elastomer composites

2.1. Introduction

Elastomers are used widely for various applications in many engineering sectors including automotive, aerospace, packaging and healthcare among others. This is based upon their wide range of attributes that include their ease of deformation at ambient temperatures, heat resistance and exceptional elongation and flexibility before breaking. Carbon-based nanomaterials such as carbon black have been used to reinforce elastomers such as natural rubber for more than 100 years, giving rise to improvements in properties such as stiffness, strength and wear resistance.[1-3] More recently, high-performance elastomeric nanocomposites have been produced through the incorporation of other different types of inorganic fillers such as silica nanoparticles, layered silicates, multi-walled carbon nanotubes, nanoclays and other nanomaterials.[4-23]

There is currently a great deal of interest in the properties of graphene and other 2D materials.[24-26] It is therefore not surprising that once graphene-based materials, such as graphene oxide and graphene nanoplatelets, became available in bulk they would be considered for use in nanocomposites,[27-31] with elastomers being obvious candidates as matrix materials. Actually, graphene oxide or functionalized graphene are often preferred rather than pristine graphene or graphene nanoplatelets in the fabrication of composites in current research[32-52] due to their strong adhesion to the rubber molecules, as will be discussed later.

2.2. Brief introduction to natural and synthetic rubbers

Among various materials, elastomers or rubbers owe their uniqueness to a combination of high deformability and excellent resilience to allow them spring back to their original shape even after strains up to 1000 %.[53] This makes them a non-alternative in many applications.

Raw rubbers can be formulated with designed compositions of additives to improve the processability and manipulate the vulcanization. Sulfur has been the predominant vulcanizing agent since its use by Charles Goodyear and Thomas Hancock.[53] The crosslinking forms a network structure in the whole vulcanisate, and the segments between crosslinking determine the mechanical properties of the rubber. Specifically, the localized segments are coiled randomly under no stress and deform in the direction of the stress axis. Although the structure is too complicated to visualise, *the theory of rubber elasticity* based on a statistic analysis of the local segments and entropy change during deformation can be employed to model the mechanical behaviours of the rubbers.[54]

In terms of source, rubbers can be normally classified into natural rubber and synthetic rubbers. Natural rubber is found in form of latex in the natural state, usually extracted from certain plant species, which is colloidal polymer dispersion usually in an aqueous liquid. The latex is processed through preservation and concentration for the purpose of prevention bacterial attack, stability enhancement and a high production of dry rubber content.[53] The main composition of natural rubber is *cis*-1,4 polyisoprene (as shown in Figure 2.1), and the intrinsic structure defines the connection pattern of the monomers that results in linear long chains of a range of molecular weights.[55] The properties of natural rubber are however highly impacted by the crosslinking, fillers and additives. Specifically, for mechanical properties, natural rubber exhibits remarkable tensile strength compared with most of synthetic rubbers even without reinforcement by fillers, which is attributed to the stress-induced crystallization at high strains. On the other hand, the reinforcement effect of strength of natural rubber by addition of fillers is much less than that in non-crystallizing rubbers.[53] Moreover, the high tensile strength of natural rubber caused by stress-induced crystallization is dependent significantly on temperature. Basically, over 100 ℃, crystallization will be suppressed, which leads to a dramatic reduction of the tensile strength. However, the temperature dependence on tensile strength can be minimised with the incorporation of fillers.[53]

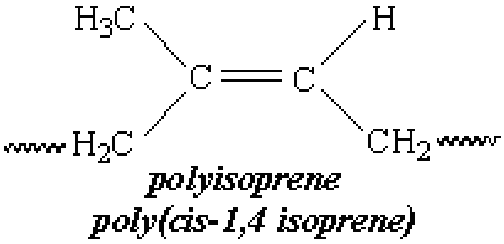

Figure 2.1 Chemical structure of natural rubber[55]

For dynamic mechanical properties, the stress-induced crystallization effect also imparts good performance upon natural rubber compared with the non-crystallizing elastomers. The crystallization can elevate the threshold energy to initiate a crack tip and decrease the propagation rate of the cracks. Fillers of fine particle size are found to improve the threshold energy due to their ability to blunt the crack tip.[53] The features above grant natural rubber excellent tear strength and fatigue resistance. With such outstanding properties, natural rubber is widely used in many applications, 55 % of which are targeted at tyres. It also exhibits excellent performance in products including beltings, hoses, footwear and latex products etc.[53, 55]

Even though natural rubber shows superiority in mechanical properties, there are some drawbacks making it disappointing in some areas. To be specific, natural rubber has poor resistance to heat and chemicals, including organic solvents and oxygen-containing gases, along with degradation when exposed to light. In that context, synthetic rubbers made through polymerization aroused intent to substitute for natural rubber to supplement its deficiencies in particular applications.[53] For instance in tyre use, butadiene rubber (BR) exhibits lower rolling resistance for sidewalls whereas styrene-butadiene rubber (SBR) offers a longer service life for treads compared with natural rubber.[53] Saturated elastomers such as isobutylene-isoprene rubber (IIR) and its derivatives are highly impermeable to gases and are resistant to light due to the saturated backbones and minimal pendant groups.[53] In addition, nitrile butadiene rubber (NBR) is a well-known elastomer for its good solvent resistance due to its chemical structure (see in Figure 2.2). NBR is a copolymer that is connected by the monomers of butadiene and acrylonitrile, and the linearity or branching of the chains can vary depending on the conditions of polymerization. In fact, the composition of the polar unit, acrylonitrile, greatly affects the properties of NBR.[53] Normally, with a higher content of acrylonitrile in NBR, a higher repellency to solvent and a higher glass transition temperature will be obtained. The applications for NBR are mainly focused on its chemical resistance, in applications including seals, gaskets, gloves and footwear etc.[53, 55]

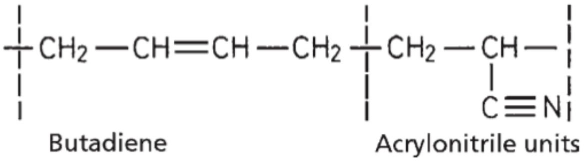

Figure 2.2 Chemical structure of nitrile rubber[53]

2.3. Preparation of graphene elastomer composites

There are a number of synthesis methods reported in literature to prepare graphene elastomer composites, each of which shows particular influence on the properties of the resultant composites. Differences can emerge during the mixing process including the filler-filler interaction, filler-matrix interaction, filler dispersion in the matrix, content of impurity and consistency of the formula composition. Each of the factors mentioned above leads to a composite with distinct characteristic properties. Sometimes, a combination of different methods (such as liquid-phase mixing followed by two roll mill mixing)[33, 36, 39, 44, 47, 56-60] is employed to achieve a proper dispersion and well-controlled vulcanization based on the objective to tailor the properties for specific research or a commercial product. Apart from the effects on the properties, cost, time efficiency and impact on environmental also need to be taken into consideration in the selection of synthesis methods.

2.3.1. Additives[53, 55]

The compounding of the graphene rubber composites is a process to incorporate the rubber matrix with fillers or additives with a good dispersion for the expectation of reinforcement, facilitation of the crosslinking or improvement of the processability. Designed formulas with different additives can lead to highly-distinct properties of the rubbers. The sources of additives used in the rubber compounding are massively various to satisfy different requirements, and the most common additives can be simply classified and explained as below.

Specifically, vulcanizing agents (e.g. sulphur) are usually added to form crosslinks between the polymers chains. Vulcanization accelerators (e.g. sulphenamide, CBS accelerator) are used to speed up the vulcanization as a full vulcanization of a pure rubber and sulphur can require hours to accomplish. Vulcanization activators are normally employed to improve the crosslinking efficiency of the vulcanizate (e.g. increased by 60% by Zinc Oxide in natural rubber). Lubricants (e.g. stearic acid) are basically utilized to improve the processability by increasing the flowability of the rubber compounds. Antidegradants (e.g. 2,6-di-t-butyl-p-cresol, BHT, for oxidative degradation) are employed to improve the ageing properties in the situation where the rubbers are frequently subject to exposure to oxygen-containing gases, heat and light and mechanical deformation. Retarders (e.g. N-nitrosodiphenylamine, NDPA) and inhibitors (e.g. N-(cyclohexylthio) phthalimide, CTP) of vulcanization are incorporated in rubbers to ensure the safety of processing, with the former decreasing the rate of vulcanization and the latter exhibiting no effect on the vulcanization. Plasticizers and softeners (e.g. petroleum waxes) are usually added to decrease the temperature and viscosity of the rubber compounds to promote the workability during processing, along with a cost reduction.

2.3.2. Compounding methods

2.3.2.1.Melt mixing

Melt mixing has been a conventional method to compound formulated rubbers in industry, owing to the advantages of low cost, high time efficiency and large-scale production. The mechanism is to apply a shear force for mixing while the materials are in the molten state. Internal mixers and two-roll mills are the most common instruments employed to conduct this procedure. Internal mixers are able to ensure the consistency of the composites of the recipes and without manual operation while open two-roll mills usually need efforts to prevent the loss of flying powders and the manual operation can also bring an influence on the resultant compound. Sometimes, these two instruments may be combined to conduct multiple-stage mixing of the ingredients, for example, with pre-mixing of the rubbers, fillers and additives without the vulcanizing agents (e.g. sulphur) in an internal mixer, followed by the addition of the vulcanizing agents and further mixing in a two-roll mill.[61]

Melt mixing can be used to mix the additives and basically all kinds of graphene flakes in the solid phase with the rubber at given temperatures. The resultant composites show a range of dispersion performance depending on the characteristics of the particular filler-matrix systems. Basically, the aggregation of flakes can occur and can be affected by the loading, size, thickness and chemical modification (such as doping or functionalization) of the graphene used. Specifically, thermally-reduced graphene oxide usually shows a fine dispersion (see in Figure 2.3b-c) with some areas of aggregation (see in Figure 2.3a) of graphene flakes in diene or phenolic rubbers,[41, 62-63] which can be attributed to the chemical π-π interaction between the interlayers and the rubbers confirmed by FT-IR and Raman spectroscopy analysis.[62] In contrast, chemically-reduced graphene oxide was reported to form a good dispersion in rubbers.[64] Apart from that, the chemical modification on graphene flakes can greatly affect the dispersion as well. For example, zinc oxide doping was proven to achieve a uniform dispersion of graphene (chemically-reduced graphene oxide) in rubber as the metallic oxide shells isolate the flakes from a tendency to interact [45, 65] whereas zinc dimethacrylate (ZDMA) functionalized graphene was found to form a well-dispersed structure meanwhile causing the aggregation of poly-ZDMA covering the graphene particles that form during the functionalization.[66-67] With the featured thickness, GNP particles normally show wrinkled shapes in the rubber matrix while the dispersion or aggregation is difficult to define since the particles are essentially bundles of layers on the microscale.[61, 68] What is more, small loadings of the graphene flakes can also lead to a good dispersion (see in Figure 2.4) due to the reduction of the possibility of the flake-flake interaction.[47, 69] Basically, all the studies show that the graphene flakes may have a good dispersion with a certain degree of aggregation.

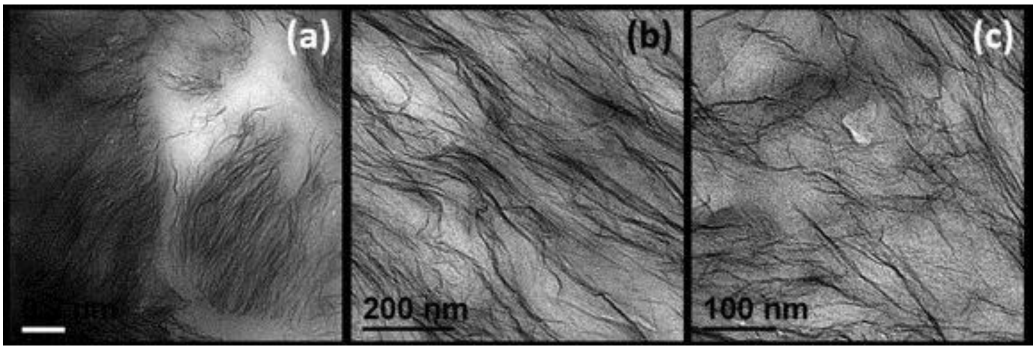

Figure 2.3 TEM images show the cross-section of the melt processed TEGO/ NR composites. Scar bar in image (a) is 200 nm.[41]

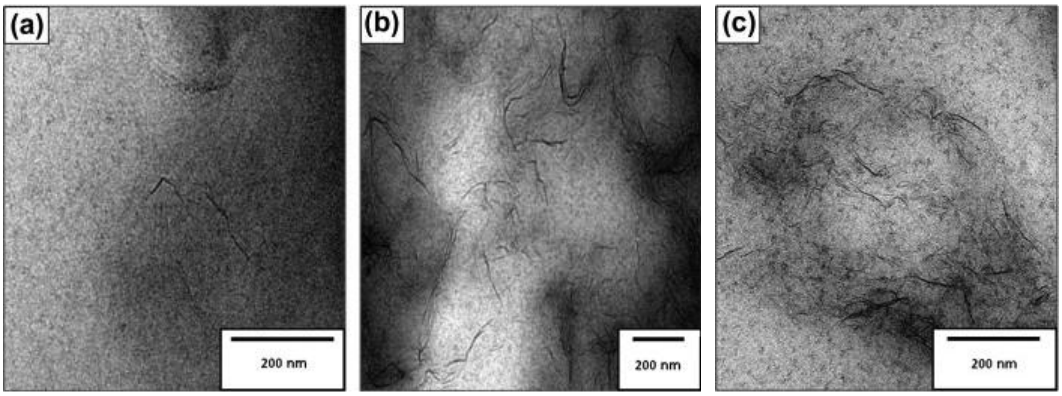

Figure 2.4 TEM graphs of FGS/NR composites. (a) 0.1 phr; (b) 0.5 phr; (c) 1 phr.[69]

On the other hand, even with its advantages favoured by industry, there are some problems that limit the use of melt mixing. The lateral dimension of the particles can undergo a shortening due to the shear force generating by the rubber flow of high viscosity.[41, 68] It is also difficult to achieve an excellent dispersion of fillers at relatively high loadings with the highly viscous matrix exhibiting a limited incorporation ability of the fillers compared with liquid phase mixing.[41, 70] Even though the dispersion of the composites fabricated by melt mixing does not give the best homogeneity, the mechanical properties show a great improvement, which can be attributed to the strong interfaces between the graphene flakes and the rubber polymers. This has been proven either by both the reinforcement or the tensile failure images showing the flakes embedded tightly in the rough fracture surfaces of the composites.[64-65]

2.3.2.2.Liquid-phase mixing

Liquid-phase mixing of elastomer composites, including solution mixing[48-50, 71-78] and latex mixing[33, 35-44, 56-60, 79-87], has been employed widely due to the production of well-dispersed filler-rubber systems, the ability of conducting small-scale research and using a rapid procedure. Basically, the method is to blend the ingredients of the rubber composites in liquid phase, with solution mixing in organic solvents and latex mixing in aqueous emulsion, followed by the phase change of the compounds from liquid to solid. Specifically, the organic solvents in solution mixing provide high solubility to graphene flakes to avoid aggregation while latex mixing needs co-coagulation of the composites by acids that sometimes leads to re-aggregation of graphene flakes depending on the kinetic conditions.

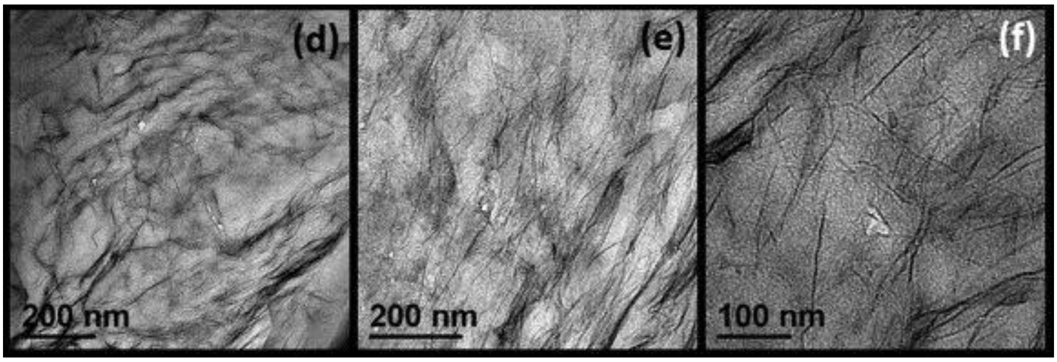

Figure 2.5 TEM images show the cross-section of the latex-produced TEGO/NR composites[41]

Compared with melting mixing, liquid-phase mixing generally facilitates a better dispersion, which can be seen in the comparison with melt mixing (see in Figure 2.3 and 2.5) reported by Potts et al.[41] Although showing the advantage of dispersion, procedure briefness, liquid-phase mixing has inevitable shortcomings, including residue of solvents, cost, low time efficiency and the difficulty in the scale-up of production.

2.3.2.3.Infusion of graphene

An innovative method to produce graphene rubber composites for sensors was developed by Boland et al.[88] by using pre-swollen rubber bands soaking in graphene suspension. Specifically, the toluene-treated rubber bands were soaked in a suspension of graphene in a mixture of NMP and water of designed composition that facilitated the energetic favourability of graphene penetrating into the swollen rubber. Finally, the graphene-infused rubber was dried in the oven to eliminate the solvents. The resultant composites showed a distributive dispersion of graphene in the rubber band and exhibited high electrical conductivity sensitive to strain change. The aim of this method is to employ the vulcanized rubbers as the starting materials, which opens up an easy path to produce wearable, low-cost sensors for body motion. However, the type of the graphene was not given, which makes it very difficult to replicate the experiment as the size of the graphene should be comparable with the size of the penetration holes of the swollen rubber network.

2.4. Characterization

2.4.1. Thermogravimetric analyses

Thermogravimetric analysis (TGA) has been a conventional technique to characterize the thermal properties of rubber composites incorporated with silica,[89-90] carbon black,[91] graphite,[92] carbon nanotubes[93-95] and graphene.[32, 35, 46, 51-52, 75, 80, 95-110] The most common property of interest obtained by a TGA thermogram is thermal stability. The thermal degradation curves of graphene elastomers composites can show a variety of stages, depending on the atmosphere and the chemical structures of the filler and the rubber species. Normally, for the most widely used atmosphere, nitrogen, graphene oxide can undergo an initial degradation at low temperature (see the green dashed line in Figure 2.6d), which sometimes creates a false impression that the addition of graphene oxide weakens the thermal stability of the composites.[52] In terms of the rubber matrix, silicone rubber such as dimethylsiloxane (PDMS) usually exhibits a two-stage depolymerization (see the solid line annotated by SR0 in Figure 2.6b) due to the different temperatures to initiate the bond breaking of the siloxane chains (410 to 440 ℃) and the polymer backbones,[52, 103] whereas NBR,[51, 100] NR[32] (see in Figure 2.6c) and SBR[97, 99] (see in Figure 2.6a) normally degrade in a one-stage process. On the other hand, in an oxidative atmosphere such as air, NR can perform a multiple-stage degradation (see in Figure 2.6d), which can be involved with a more complicated reaction including oxidation, chain splitting, decrosslinking, and chain decomposition occurring at different temperatures.[106]

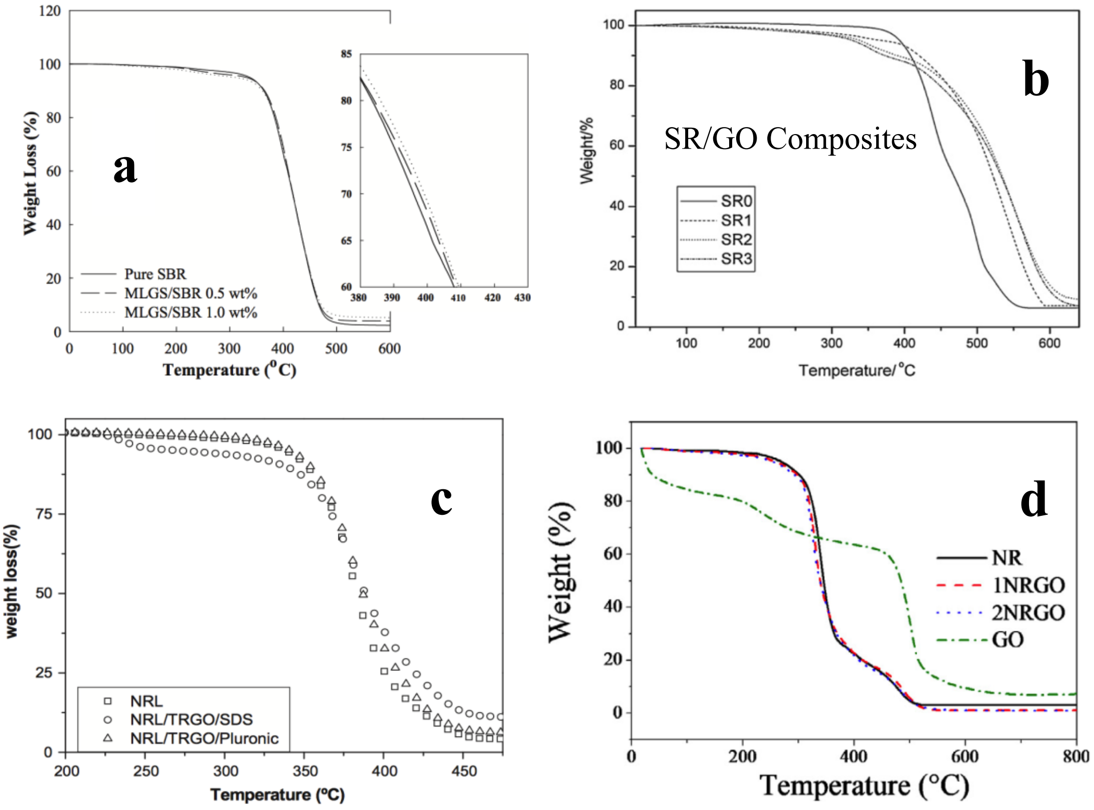

Figure 2.6 TGA curves of graphene composites. (a) MLGS (thermally-exfoliated GO)/ SBR[99] (SR0, SR1, SR2 and SR3 denote pure silicone rubber, silicone rubber filled with 0.6, 1.8 and 3 wt% GO, respectively), (b) GO/ silicone rubber[52] and (c) TRGO/ NR[32] in nitrogen; (d) GO/ NR[106] in air.

Basically, for most of the graphene filled composites, the thermal stability was enhanced (see the right shift in Figure 2.6a inset). Two predominant explanations were proposed to explain including (i) the graphene flakes of high aspect ratios hinder the diffusion of the gas and the volatile decomposition products (barrier effect);[46, 96, 102-103, 109] (ii) strong adhesion (such as π-π interaction or bonding between polar groups) between the graphene flakes and the rubber polymers decrease the thermal motion and degradation probability.[51-52, 75, 99-100, 103, 108-110] However, in some studies, the thermal stability was found to be reduced after the incorporation of graphene at very low contents, and it was explained that the dilute graphene flakes were unable to form a barrier but enhance the thermal conductivity of the whole composites, which facilitated the degradation.[96] Finally, from the analysis of degradation, TGA is also employed to determine the actual composition of the fillers by subtraction of the final weight residues of the composites from that of the pure rubber.[91] This has been used in the present study to check the actually filler loadings in the elastomers studied, compared with the nominal loadings that may be incorrect due to the loss of ingredients during processing.

2.4.2. Raman spectroscopy

2.4.2.1.Raman spectra of rubbers and graphene/rubber composites

Since only natural rubber and nitrile rubber were used in this project, the following sections will focus only on NR and NBR. The study of Raman spectra of elastomers has encountered the significant problem of fluorescence, which may be further amplified by impurities, heating and crosslinking.[111-112] As can be seen in Figure 2.7, natural rubber shows a predominant peak at 1665 cm^{-1}, which can be attributed to the C=C stretch. A range of minor peaks from 1000 to 1500 cm^{-1} and a broad peak at around 2900 cm^{-1} also show up depending on the chemical modifications.[112] On the other hand, the Raman spectrum of nitrile rubber (see in Figure 2.8) shows similar features to that of NR, with the exception of a sharp peak at 2241 cm^{-1}, which can be attributed to the C≡N stretch.[111] As mentioned above, the pure rubbers can show a strong fluorescence background, and there are many solutions to reduce that effect, such as employing near-IR excitation and a modified FTIR spectrometer, and the addition of fillers (such as silica or calcium carbonate as seen in Figure 2.7). Although the mechanism is not properly understood, the Raman peaks of rubbers can become more clear and sharp due to the addition of the fillers.[112]

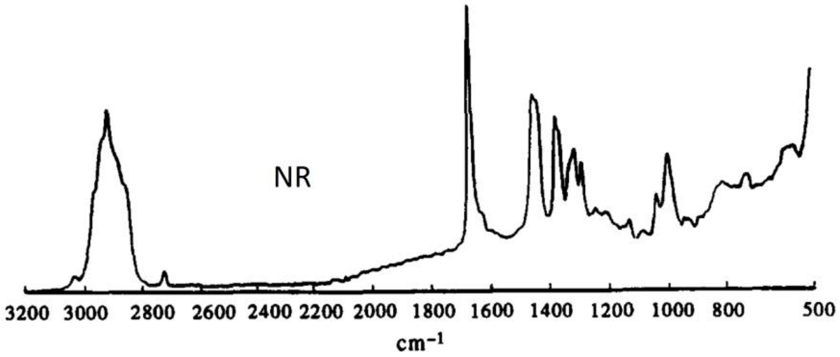

Figure 2.7 Raman spectrum of cured natural rubber filled with calcium carbonate (50% by weight)[112]

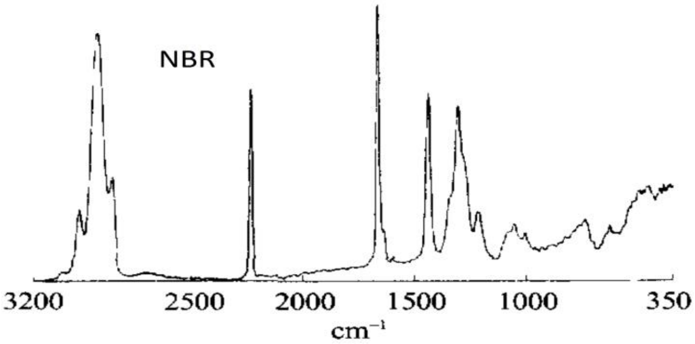

Figure 2.8 Raman spectrum of raw nitrile rubber[111]

Unfortunately, due to the significant fluorescence effect, it is not easy to obtain well-defined Raman spectra upon the full range of graphene rubber composites, which is why most of the literature either only shows the spectrum of graphene synthesized by the specific methods[40, 45, 47, 61, 69, 113] or a small range of the spectra of GO/elastomers exhibiting only the intensive D and G peaks.[32-34, 62] A good example of the Raman spectra of graphene rubber composites can be seen in Figure 2.9, which exposes all the feature peaks of graphene as well as the rubber fluorescence background, although the annotation of the 2D peak position is probably incorrect.[63]

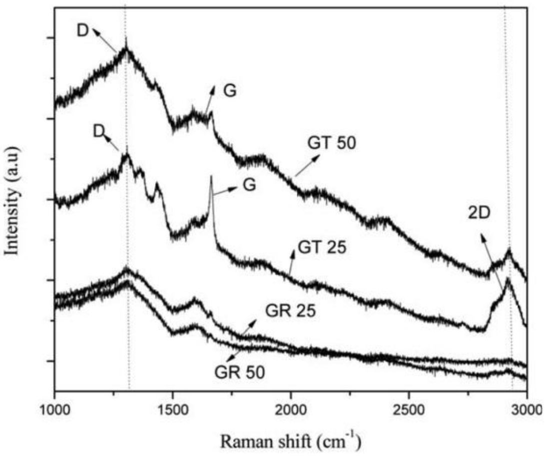

Figure 2.9 Raman spectra of epoxidized natural rubber composites filled with graphite (GT) and reduced graphene oxide (GR). [63] (Note that the annotation for the 2D peak is probably incorrect)

2.4.2.2. Raman spectroscopy for quantification of the dispersion of graphene flakes

Technically for the graphene nanocomposites, the Raman peak intensity ratio of the graphene to the matrix can be used to quantify the dispersion of graphene flakes, which was achieved by employing the following equation,[114]

$$D = \sqrt{\frac{\sum(r_i - \bar{r})^2}{N}} \tag{2.1}$$

where

D is the dispersion parameter,

r_i is the intensity ratio of graphene peak (D peak) to the epoxy peak (1454 cm^{-1}),

$\bar{r}$ is the average ratio,

N is the number of total unit measurements.

A higher value of D means a larger variation on the intensity ratio, which indicates a less homogeneous dispersion of the flakes.

2.4.2.3. Polarized Raman spectroscopy for the orientation of graphene flakes

Polarized Raman spectroscopy can be a convenient technique to quantify the orientation of the graphene flakes in a matrix, due to the peak intensity depending on the angle of the flake relative to the laser polarization, which was developed by Li et al.[115-117] They demonstrated the angular dependence of the Intensity as

$$I_{sample}^{VV}(\Phi) = I_0 \cdot \left\{ \frac{8}{15} + \langle P_2(\cos\theta)\rangle \left(-\frac{16}{21} + \frac{8}{7}\cos^2\Phi \right) + \langle P_4(\cos\theta)\rangle \left(\frac{8}{35} - \frac{8}{7} cos^2\Phi + cos^4\Phi \right) \right\} \qquad (2.2)$$

where

the constant I_0 is the amplitude,

Φ is the angle how the specimens were rotated regard to the laser polarization direction,

$\langle P_2(\cos\theta)\rangle$ and $\langle P_4(\cos\theta)\rangle$ are the mean values of the Legendre polynomials in the Orientation Distribution Function (ODF)[116], which can be used to quantify the orientation. $\langle P_2(\cos\theta)\rangle$ is the primary parameter and a randomly aligned can be determined when $\langle P_2(\cos\theta)\rangle$ =0 (whereas $\langle P_2(\cos\theta)\rangle$ =1 means perfect alignment).

2.4.3. SEM images

In terms of the dispersion and orientation of the graphene flakes in the rubber matrix, scanning electron microscopy can be utilized as a fast visualization technique to characterize. The materials described in most of the literature are a homogeneous dispersion or a certain degree of aggregation from freeze fractured or tensile failed specimens, whereas only a few papers pointed out any orientation of the flakes.[35-39, 41, 43, 45-47, 59, 64-65, 67, 72, 78, 82, 84, 86, 118]

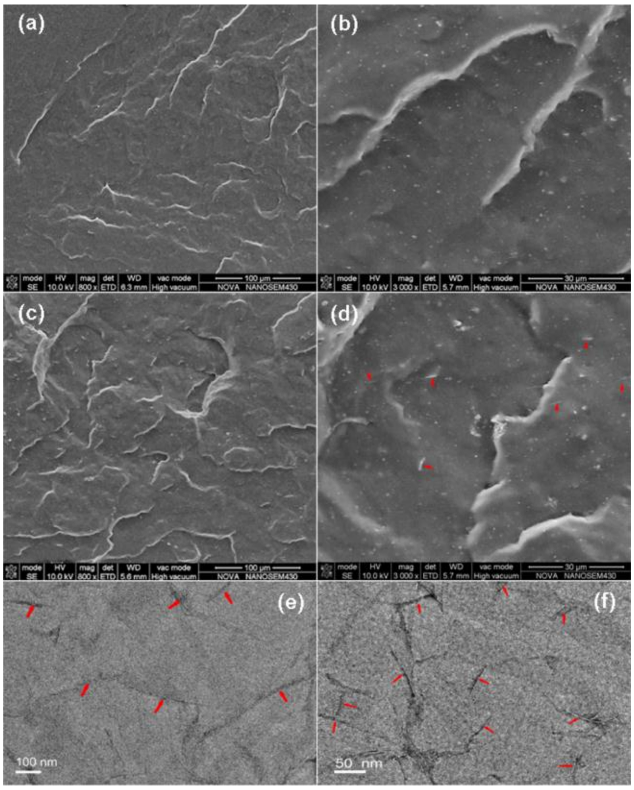

Figure 2.10 (a, b) FESEM images of neat NR, (c, d) FESEM images of NR/PC-rGO-0.9 composite, (e, f) HRTEM images of NR/PC-rGO-0.9 composite. Composites were prepared by latex mixing followed by two-roll mill mixing. PC-rGO sheets are highlighted by the red arrows. FESEM: field-emission scanning electron microscopy[47]

Basically, few trends of flake alignment have been reported, and random orientations were mostly described. A good example of the orientation can be seen in the work by Wu et al. [47] As presented in Figure 2.10a-d, the neat rubber shows a smooth fractured surface, whereas the graphene (proanthocyanidin-reduced graphene oxide, PC-rGO) rubber composites exhibit a rough surface. The random orientation of the flakes can be clearly seen in Figure 2.10e-f, as annotated by the red arrows.

2.4.4. X-ray diffraction

When graphene and rubbers are fabricated into composites, there are some questions of interest, such as any structural change of the flakes and the rubbers. X-ray diffraction can be a powerful technique to determine any changes before and after fabrication.[10, 33-34, 46, 50, 62, 70-71, 74-76, 81, 100, 102, 119-121] As presented in Figure 2.11, the rubber exhibits a broad peak, implying the amorphous structure of the rubber polymers. After the incorporation of graphene, the characteristic graphitic peak at around 26.5 ° shows up indicating that the exfoliation of graphene was incomplete after the fabrication.[71]

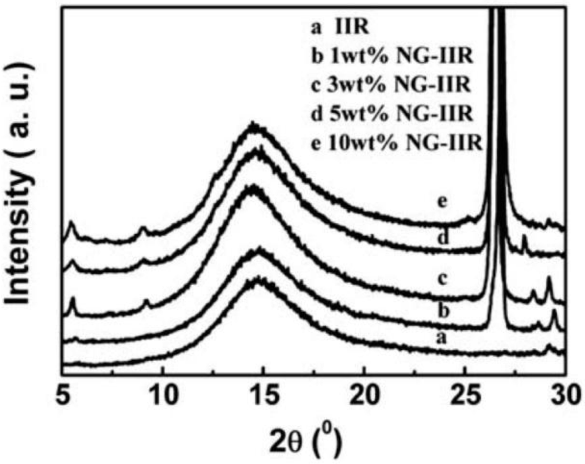

Figure 2.11 The XRD patterns of natural graphite (NG)/ butyl rubber composites[71]

In contrast, complete exfoliation of graphene (monolayer) in NR can be seen in Figure 2.12a, with the characteristic peak of graphite vanishing.[33] For NBR composites presented in Figure 2.12b, similar to the NR composites and butyl rubber composites in Figure 2.11, the broad peak also can be seen for pure NBR for the same reason, and the complete exfoliation can be observed as well. Hence, the crystallization of the rubber and graphene flakes, and the extent of exfoliation of the flakes can be determined by XRD.

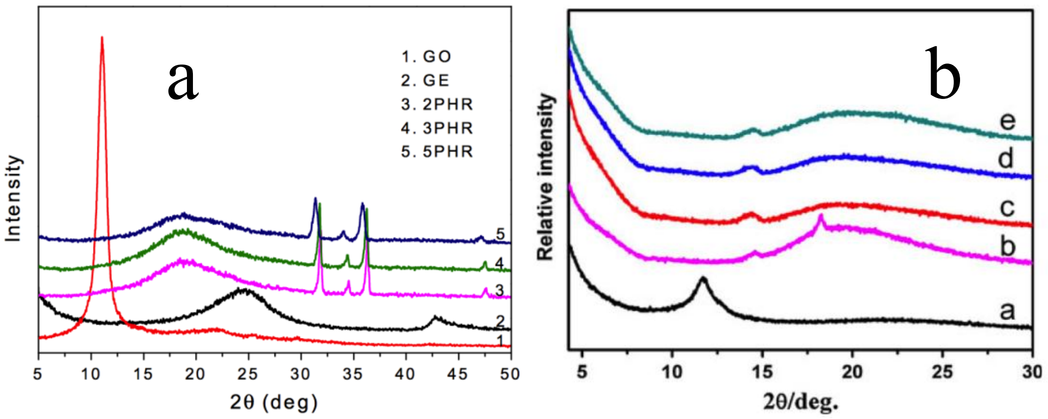

Figure 2.12 The XRD patterns of (a) graphite oxide, chemically reduced graphene oxide (GE) and GE/NR composites;[33] (b) a GO; b NBR; c 0.5 wt%; d 1.5 wt%; e 3 wt% GO/NBR composites.[50]

For crystalline rubber, such as NR, the stress-induced crystallinity can be quantified as seen in Figure 2.13.[70] The unstretched rubber composites show a broad amorphous peak (Figure 2.13a), while two crystalline peaks appear at 14.12 ° and 20.65 ° for the deformed rubber (Figure 2.13b).

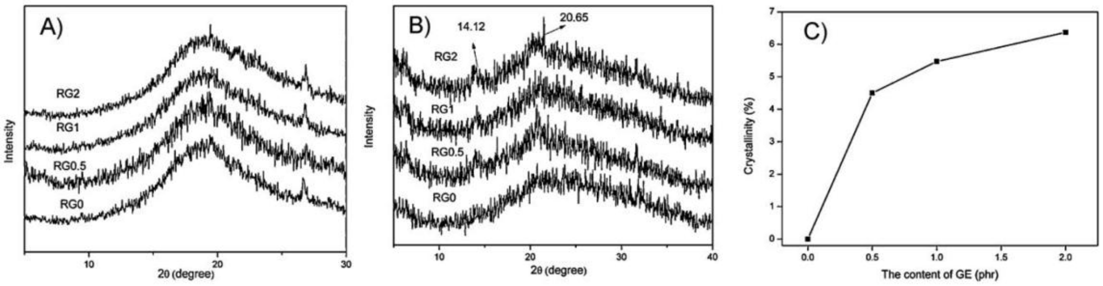

Figure 2.13 XRD patterns of NR/GE (chemically-reduced graphene oxide) composites at different extension ratio of α=1 (A) and α=3 and crystallinity (C) of NR/GE composites with different GE content at α=3.[70]

The degree of the crystallinity can be quantified by the areas ratio of the crystalline peaks and the amorphous peaks as shown in Figure 2.13c. Overall, any change in the crystallinity or stacking order of the composites can be characterized by XRD.

2.4.5. X-ray tomography

Apart from the 2D imaging methods such as SEM or TEM, X-ray tomography is a non-destructive technique capable of rendering the 3D imaging of the materials at the scale down to 1 micron, which enables the investigation of the relationship between the microstructure and the properties of the materials.[122-124] The brief principle of X-ray tomography is schematically illustrated in Figure 2.14.[123] Specifically, the specimen is placed on a rotating stage where the X-ray beam emits through. The X-ray is partially absorbed and the transmitted emission can be converted into a visible light and recorded by a CCD camera. The recorded images are related to a bundle of projection (hundreds of sets) of the specimens, which can be used to reconstruct the 3D image of the specimen. The contrast in the image is aroused by the difference of the X-ray absorption coefficient in the localized regions of the specimens, which is affected by the density of the materials, atomic number and the energy of the X-rays.

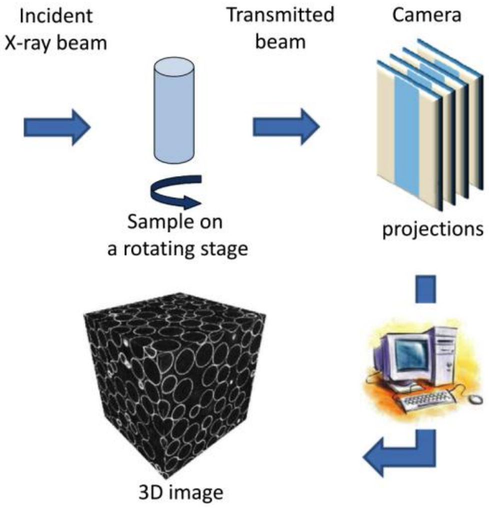

Figure 2.14 Principle of tomography[123]

Unfortunately, there are few well-defined CT-images reported for graphene elastomers. In the study of the properties of SBR composites filled with carbon materials, Schopp et al.[125] exhibited an illustration of the dispersion of three types of graphene in SBR by CT scanning as can be seen in Figure 2.15. Although the graphene flakes were reported to be of good dispersion the SBR matrix from the CT-images, the resolution is too limited to provide more details about the agglomerates, shapes, position, and interaction of the graphene flakes.

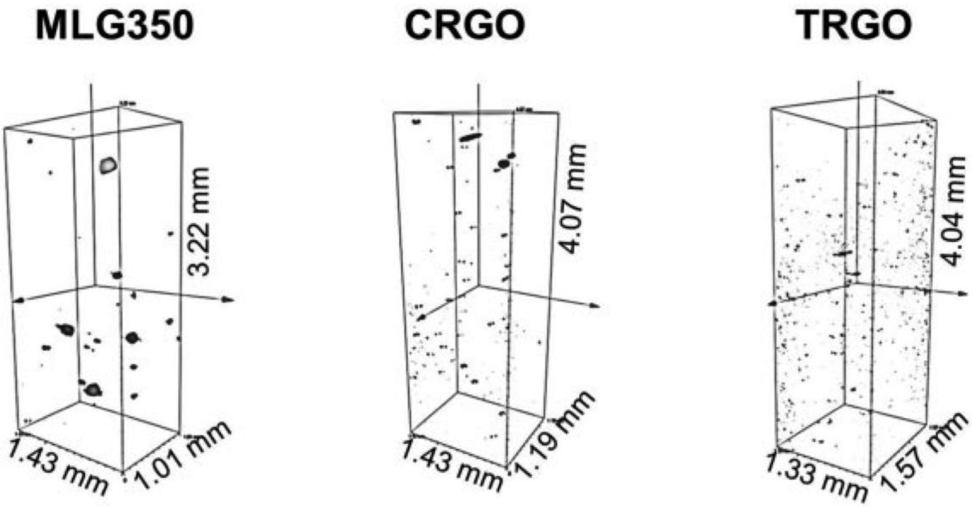

Figure 2.15 Micro-CT images of SBR composites with 25 phr of MLG350 (multiple layer graphene, 350 m^2 g^{-1}), CRGO (chemically reduced graphene oxide) and TRGO (thermally reduced graphene oxide)[125]

Another study on EPDM composites filled with GNP (an intermediate grade between graphene and graphite) and carbon black (N330) by Valentini et al.[126] also showed the microstructure of the graphene flakes in the elastomer matrix. As presented in Figure 2.16, a higher resolution was obtained compared with the work by Schopp et al.[125] The carbon black was found in forms of aggregation whereas the graphene flakes were dispersed uniformly in the matrix. Overall, the previous studies of X-ray tomography have not shown the satisfied details of the microstructure of the graphene elastomer composites compared with those obtained by SEM and TEM.

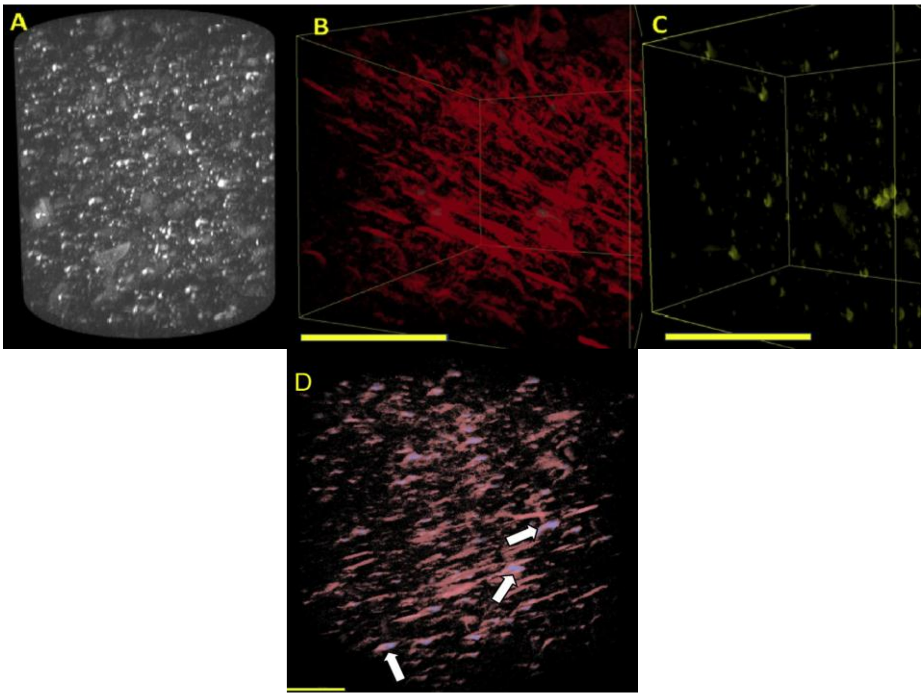

Figure 2.16 Micro-CT images of the (A) EPDM composites (2 wt% GNP and 24 wt% CB); (B) and (C) Detail of the segmented micro-CT images showing the distribution of the GNP and CB aggregates, respectively. (scale bar is 50 μm); (D) Detail of segmented m-CT images showing the whole distribution of the GNP (in red) and CB aggregates (in blue indicated by the arrows) (scale bar is 50 mm).[126]

2.5. Mechanical properties

2.5.1. Theoretical studies on rubber elasticity

As mentioned in section 2.2, the deformation of an individual chain, a polymer network or a bulk elastomer can be statistically modeled by *the theory of rubber elasticity*.[54] As the network is stretched the entropy will reduce. The statistic theory demonstrates how to determine the entropy change on deforming an elastomeric polymer network and how to relate the entropy change to the extension ratio and the chain number per unit volume. The theory is based on the assumption that the junction points are regarded as fixed at the mean position and the segments between the points behave as freely-jointed chains. With further assumption that the elastomer deforms at constant volume, the stress-strain curves can be predicted as shown in Figure 2.17.[54, 127] As can be seen in Figure 2.17a, the theoretically predicted curve for tensile behavior shows a great agreement at small extension ratio (λ < 1.5). With increasing elongation, the experimental curve rises above the theoretical curve, which can probably be attributed to that the Gaussian function will not be applicable and the occurrence of the stress-induced crystallization of natural rubber. In contrast, for compression (λ < 1) in Figure 2.17b, the theoretical prediction is in great consistence with experimental data, which is due to that the Gaussian function is expected to provide a good approximation and that the stress-induced crystallization does not take place.[54, 127]

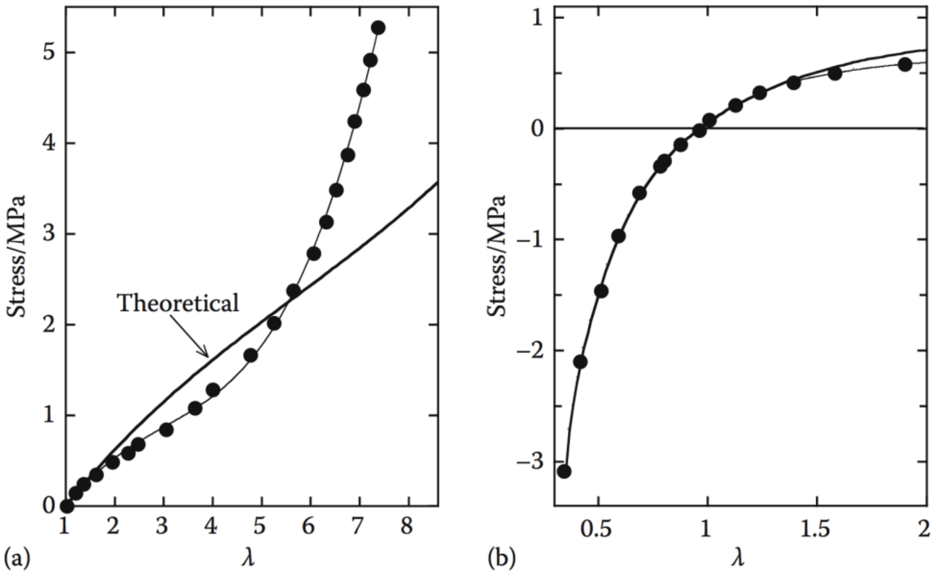

Figure 2.17 Relationship between nominal stress σ_n and extension ratio λ for vulcanized natural rubber. The theoretical curves for a value of shear modulus G = 0.4MPa are given as heavy lines: (a) extension and (b) compressive deformation. (Referred from the adaption by Young, R. J.; Lovell, P. A., *Introduction to polymers*. 3rd ed.; CRC Press: Boca Raton, 2011.[127] Original data was taken from Treloar, L. R. G., *The physics of rubber elasticity*. Clarendon Press: Oxford, UK, 1975.[54])

2.5.2. Mechanical properties of graphene rubber composites

There are a number of studies with regards to the tensile properties of graphene NR composites[36, 38-39, 41-42, 47, 59, 62, 64, 66, 69-70, 76-78, 81, 85, 128-129] and graphene NBR composites.[51, 74, 78, 100, 121, 130] The tensile properties of the composites can be influenced by the preparation methods, types of graphene and dispersion of the flakes. Compared with graphene, graphene oxide is more popular due to its strong interfaces with the rubber polymers.

In terms of NR, Potts et al.[41] compared the tensile properties of thermally-reduced graphene oxide composites synthesized by latex mixing and two-roll mill processing. As presented in Figure 2.18, the reinforcement achieved by addition of graphene was seen from the stress-strain curves. The the latex mixed composites exhibited a larger increase in both modulus and strength and less strain at break compared with those processed by the two-roll mill. The better reinforcement of the former was explained by the TEM images showing a better dispersion of the flakes with less aggregation (see in Figure 2.3 and 2.5). However, the vulcanization of the composites was prolonged which led to scorch that removed the stress-induced crystallinity from the natural rubbers. A better example that retained the stress-induced crystallinity of the natural rubber which was properly cured can be seen in Figure 2.19.[39]

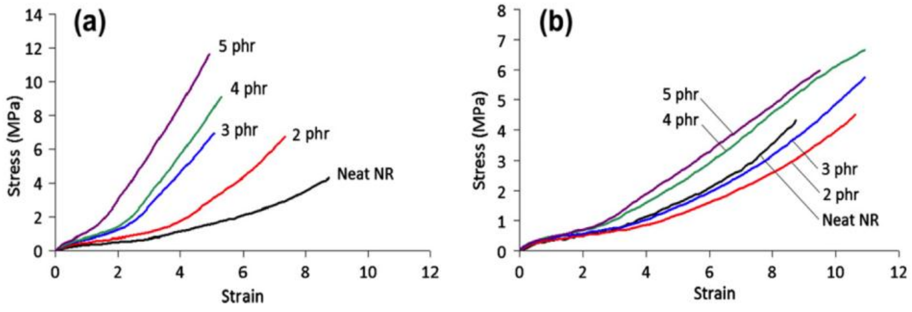

Figure 2.18 Stress-strain curves of the thermally reduced graphene oxide NR composites synthesized by (a) latex mixing and (b) two-roll mill mixing.[41]

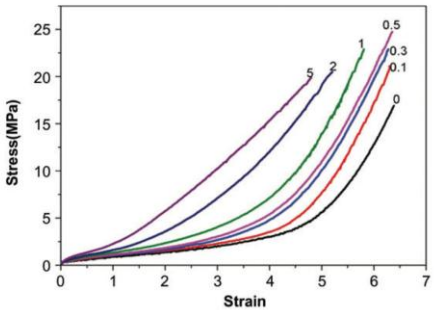

Figure 2.19 Stress-strain curves of the graphene oxide/natural rubber nanocomposites.[39]

Unlike NR composites, NBR composites show a completely different behavior. As can be seen in Figure 2.20, there is no stress-induced crystallinity of graphene NBR composites due to the own characteristics of NBR chemical structure. Apart from that, with differences of the graphene resources and preparation methods, the composites can exhibit a variety of degrees of reinforcement and improvement of the ultimate strain.[100, 130]

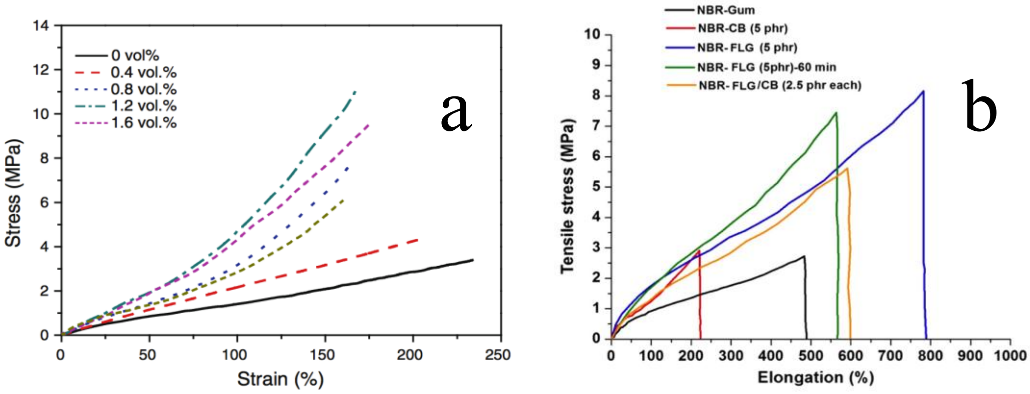

Figure 2.20 Stress-strain curves of (a) GO/ xNBR composites[100] and (b) NBR composites filled with few layer graphene (FLG), carbon black (CB, N550) and both fillers.[130]

The hardness of rubber composites was also investigated in a number of studies, in most of which a range of enhancement were obtained by the addition of graphene flakes.[44, 46, 120, 125, 130-134] However, the hardness of silicone rubber was found to be reduced with the incorporation of GNPs by Song et al.,[109] which was not explained clearly in the study. In addition, the enhancement effect on hardness by graphene (thermally- and chemically- reduced graphene oxide) was reported to be higher than that by carbon black (Corax N 234) by Schopp et al.[125] whereas Varghese et al.[130] found the opposite (GNPs and N550 carbon black). Moreover, for dynamic mechanical properties, the tear resistance was found to substantially improve with the incorporation of graphene flakes.[44-46, 59, 70, 73, 121, 135] The mechanism is illustrated that the crack propagation is restrained by the physical barriers generating from the large interfaces between the rubber matrix and the 2-dimensional graphene flakes of high aspect ratio. Thus, the processing history can also leave an impact on the tear behavior of the composites. Especially for comparison between melting mixing and solution mixing, the two methods both exfoliate or intercalate the flakes while the former shortens the length of the particles and the latter exfoliates or intercalates the flakes more, which results in different areas of the interfaces between the fillers and the matrix as schematically sketched in Figure 2.21.[73] Based on the mechanism aforementioned, solution mixing is expected to produce the composites of higher tear resistance compared with melting mixing as can be seen in Figure 2.22 (it should be pointed out that the pure rubbers synthesized by both methods showed no difference).[73]

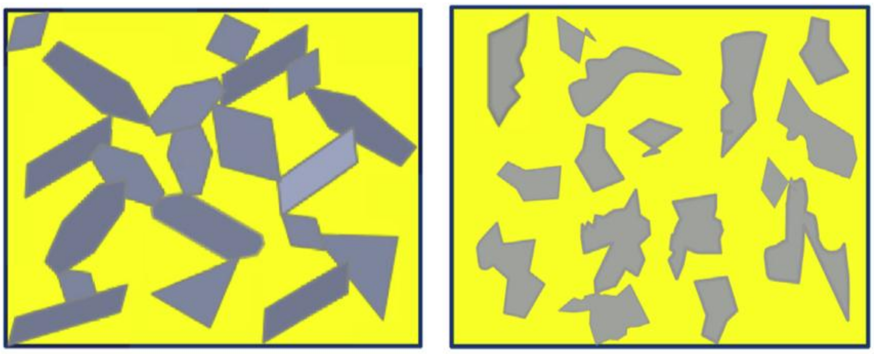

Figure 2.21 Schematics of nanocomposites by solution compounding (left) and melt mixing (right)[73]

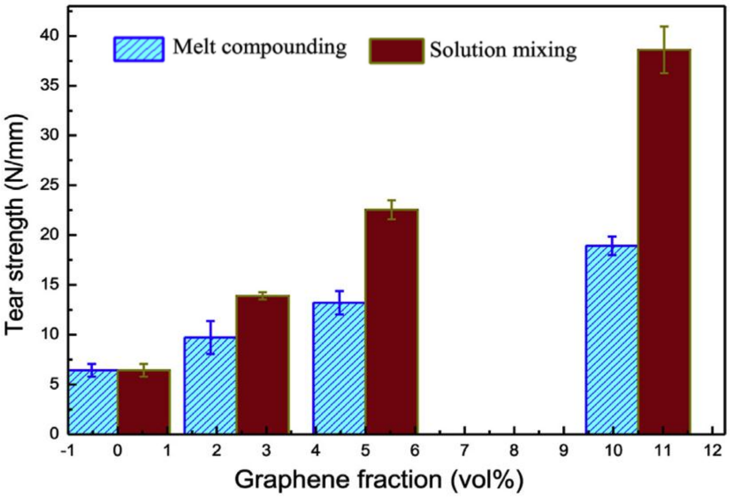

Figure 2.22 Tear strength of the GNPs/ SBR composites prepared by melt compounding and solution mixing.[73]

2.6. Thermal conductivities

Graphene addition has been found to enhance the thermal conductivity of a range of rubbers by many studies due to its intrinsic extraordinary high in-plane thermal conductivity.[10, 68, 70, 73, 81, 100, 102, 109, 136] However, the processing history of the composites, resulting in the microstructure of the composites including the dispersion, shape, dimension of the fillers, pores and interfaces etc., can play a crucial role in optimizing the thermal conducting path of the composites. Basically, the graphene elastomer composites prepared through melt compounding and solution mixing can exhibit different tendencies to form a conducting path network. Specifically, the graphene flakes can be shortened by the shear forced during melt mixing while solution mixing retains the surface-to-volume ratio of the flakes or even exfoliate/intercalate the flakes to create more surfaces similarly to that presented in Figure 2.21. As a consequence, it is easier for the solution mixed composites to produce more larger particles with a higher possibility of filler interaction to form a conducting network at even small contents of the fillers while melt mixed composites requires a high loading of the fillers to build a conducting network. The higher conductivity of the composites obtained by solution methods compared with those made by melt mixing can be seen in Figure 2.23.[81, 136]

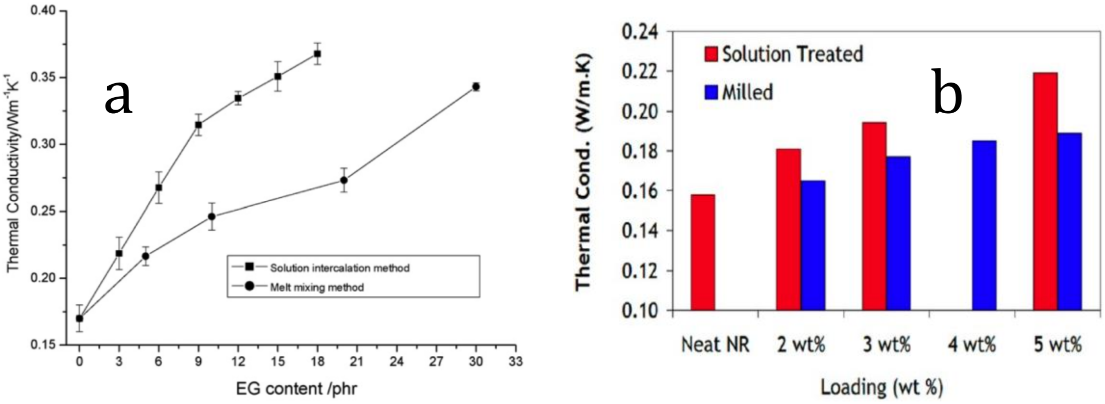

Figure 2.23 Thermal conductivities of (a) expanded graphite/ silicone composites prepared by solution intercalation method (toluene) and melting mixing method;[136] (b) milled and solution-treated RGO (hydrazine monohydrate reduced GO)/NR nanocomposites at various loadings.[81]

2.7. Diffusion and swelling at equilibrium

As demonstrated in the previous chapter, graphene has a strong barrier effect on molecular penetration.[137] Hence, it is reasonable to expect graphene elastomer composites to exhibit better solvent and gas resistance than pure elastomers. Unfortunately, there are few studies that have shown interests in the diffusion kinetics of the elastomer composites modified by graphene. Nevertheless, studies on the solvent diffusion into graphene non-elastomers composites or elastomer composites filled with other fillers have been undertaken for a number of years,[138-144] the analysis of which can be employed in this project in later chapters. Different from diffusion that is involved with the penetration of the solvent molecules, swelling at equilibrium is often employed for the calculation of crosslink density in elastomer composites using the Flory-Rehner equation in many studies.[33, 38-39, 56, 62, 64, 66, 68, 73] The calculated crosslinking density was found to dramatically increase with the addition of graphene flakes, the essence of which is the additional entanglement (namely physical crosslinking) caused by the filler-rubber interaction such as π-π interaction and more chemical crosslinking created during the vulcanization. However, despite the lack of existed publications on the barrier properties or swelling behaviours of graphene elastomer composites, it is still possible to find some research on the barrier properties for elastomer composites filled with other 2D nano-fillers such as nanoclays.[12-23] The increase in the crosslink density and the suppression of the permability by the addition of the 2D nano-fillers were widely reported.

2.8. Objective of this work

This present study aims to investigate the relationship between the structure and the properties of the GNP elastomer composites in a way that was rarely used in the previous literature. Specifically, the morphology and the orientation of the flakes inside the rubbery matrix was determined by multiple techniques and the effect of the structure was discussed while analysing the properties of different composites in different directions. GNPs were selected as the main fillers to compare with the carbon black and the reasons can be clarified as follow: (i) GNPs are of 2-dimensional structure with relatively high aspect ratios which can highlight the effect of the morphology and the orientation of the fillers; (ii) GNPs have proven their high quality in numerous studies concerning various properties such as mechanical, electronic, thermal and barrier properties, which implies their application potential in various fields; (iii) this study requires a high usage of fillers and GNPs are comparatively accessible compared with other graphene-related materials.

References

1. Donnet, J. B.; Voet, A., *Carbon black: physics, chemistry and elastomer reinforcement*. Marcel Dekker: New York, 1976.

2. Edwards, D. C., Polymer-filler interactions in rubber reinforcement. *J. Mater. Sci.* **1990,** *25*, 4175-4185.

3. Boonstra, B. B., Role of particulate fillers in elastomer reinforcement- a review. *Polymer* **1979,** *20*, 691-704.

4. Koerner, H.; Price, G.; Pearce, N. A.; Alexander, M.; Vaia, R. A., Remotely

actuated polymer nanocomposites—stress-recovery of carbon-nanotube-filled thermoplastic elastomers. *Nat. Mater.* **2004,** *3*, 115-120.

5. Leblanc, J. L., Rubber–filler interactions and rheological properties in filled compounds. *Prog. Polym. Sci.* **2002,** *27*, 627-687.

6. Frogley, M. D.; Ravich, D.; Wagner, H. D., Mechanical properties of carbon nanoparticle-reinforced elastomers. *Compos. Sci. Technol.* **2003,** *63*, 1647-1654.

7. Donnet, J. B., Nano and microcomposites of polymers elastomers and their reinforcement. *Compos. Sci. Technol.* **2003,** *63*, 1085-1088.

8. Joly, S.; Garnaud, G.; Ollitrault, R.; Bokobza, L., Organically modified layered silicates as reinforcing fillers for natural rubber. *Chem. Mater.* **2002,** *14*, 4202-4208.

9. Ponnamma, D.; Sadasivuni, K. K.; Grohens, Y.; Guo, Q.; Thomas, S., Carbon nanotube based elastomer composites – an approach towards multifunctional materials. *J. Mater. Chem. C* **2014,** *2*, 8446-8485.

10. Araby, S.; Zaman, I.; Meng, Q.; Kawashima, N.; Michelmore, A.; Kuan, H. C.; Majewski, P.; Ma, J.; Zhang, L., Melt compounding with graphene to develop functional, high-performance elastomers. *Nanotechnology* **2013,** *24*, 165601.

11. Basu, D.; Das, A.; Stöckelhuber, K. W.; Wagenknecht, U.; Heinrich, G., Advances in layered double hydroxide (LDH)-based elastomer composites. *Prog. Polym. Sci.* **2014,** *39*, 594-626.

12. Wu, Y.-P.; Jia, Q.-X.; Yu, D.-S.; Zhang, L.-Q., Structure and properties of nitrile rubber (NBR)–clay nanocomposites by co-coagulating NBR latex and clay aqueous suspension. *J. Appl. Polym. Sci.* **2003,** *89*, 3855-3858.

13. Kim, J.-t.; Oh, T.-s.; Lee, D.-h., Curing and barrier properties of NBR/organo-clay nanocomposite. *Polym. Int.* **2004,** *53*, 406-411.

14. Koo, J. H., *Polymer nanocomposites: Processing, characterization, and applications*. McGraw-Hill: 2006.

15. Sridhar, V.; Tripathy, D. K., Barrier properties of chlorobutyl nanoclay composites. *J. Appl. Polym. Sci.* **2006,** *101*, 3630-3637.

16. Zhu, L.; Wool, R. P., Nanoclay reinforced bio-based elastomers- Synthesis and characterization. *Polymer* **2006,** *47*, 8106-8115.

17. Maiti, M.; Bhowmick, A. K., Effect of polymer–clay interaction on solvent transport behavior of fluoroelastomer–clay nanocomposites and prediction of aspect ratio of nanoclay. *J. Appl. Polym. Sci.* **2007,** *105*, 435-445.

18. Subramaniyan, A. K.; Sun, C. T., Toughening polymeric composites using nanoclay- Crack tip scale effects on fracture toughness. *Compos. Part A - Appl. S.* **2007,** *38*, 34-43.

19. Das, A.; Costa, F. R.; Wagenknecht, U.; Heinrich, G., Nanocomposites based on chloroprene rubber: Effect of chemical nature and organic modification of nanoclay on the vulcanizate properties. *Eur. Polym. J.* **2008,** *44*, 3456-3465.

20. Fritzsche, J.; Das, A.; Jurk, R.; Stoeckelhuber, K. W.; Heinrich, G.; Klueppel, M., Relaxation dynamics of carboxylated nitrile rubber filled with organomodified nanoclay. *Express Polym. Lett.* **2008,** *2*, 373-381.

21. Ghassemieh, E., Enhancement of the properties of EPDM/NBR elastomers using nanoclay for seal applications. *Polym. Composites* **2009,** *30*, 1657-1667.

22. Herrera-Alonso, J. M.; Marand, E.; Little, J. C.; Cox, S. S., Transport properties in polyurethane/clay nanocomposites as barrier materials: Effect of processing conditions. *J. Membrane Sci.* **2009,** *337*, 208-214.

23. Zarei, M.; Naderi, G.; Bakhshandeh, G. R.; Shokoohi, S., Ternary elastomer nanocomposites based on NR/BR/SBR: Effect of nanoclay composition. *J. Appl. Polym. Sci.* **2013,** *127*, 2038-2045.

24. Novoselov, A. K.; S., G. K.; Morozov, S.; Jiang, D.; Zhang, Y.; Dubonos, S.; Grigorieva, I.; Firsov, A., Electric field effect in atomically thin carbon films. *Science* **2004,** *306*, 666-669.

25. Novoselov, K. S.; Geim, A. K.; Morozov, S. V.; Jiang, D.; Katsnelson, M. I.; Grigorieva, I. V.; Dubonos, S. V.; Firsov, A. A., Two-dimensional gas of massless Dirac fermions in graphene. *Nature* **2005,** *438*, 197-200.

26. Geim, A. K.; Novoselov, K. S., The rise of graphene. *Nat. Mater.* **2007,** *6*, 183-191.

27. Young, R. J.; Kinloch, I. A., Graphene and graphene-based nanocomposites. *Nanosci.-Spec. Per. Rep.* **2013,** *1*, 145-179.

28. Young, R. J.; Kinloch, I. A.; Gong, L.; Novoselov, K. S., The mechanics of graphene nanocomposites: A review. *Compos. Sci. Technol.* **2012,** *72*, 1459-1476.

29. Young, R. J.; Liu, M., The microstructure of a graphene-reinforced tennis racquet. *J. Mater. Scie.* **2016,** *51*, 3861-3867.

30. Boland, C. S.; Khan, U.; Ryan, G.; Barwich, S.; Charifou, R.; Harvey, A.; Backes, C.; Li, Z.; Ferreira, M. S.; Möbius, M. E.; Young, R. J.; Coleman, J. N., Sensitive electromechanical sensors using viscoelastic graphene-polymer nanocomposites. *Science* **2016,** *35*, 1257-1260.

31. Papageorgiou, D. G.; Kinloch, I. A.; Young, R. J., Hybrid multifunctional graphene/glass-fibre polypropylene composites. *Compos. Sci. Technol.* **2016,** *137*, 44-51.

32. Aguilar-Bolados, H.; Brasero, J.; Lopez-Manchado, M. A.; Yazdani-Pedram, M., High performance natural rubber/thermally reduced graphite oxide nanocomposites by latex technology. *Compos. Part B - Eng.* **2014,** *67*, 449-454.

33. Wu, J.; Xing, W.; Huang, G.; Li, H.; Tang, M.; Wu, S.; Liu, Y., Vulcanization kinetics of graphene/natural rubber nanocomposites. *Polymer* **2013,** *54*, 3314-3323.

34. Xing, W.; Tang, M.; Wu, J.; Huang, G.; Li, H.; Lei, Z.; Fu, X.; Li, H., Multifunctional properties of graphene/rubber nanocomposites fabricated by a modified latex compounding method. *Compos. Sci. Technol.* **2014,** *99*, 67-74.

35. Suriani, A. B.; Nurhafizah, M. D.; Mohamed, A.; Zainol, I.; Masrom, A. K., A facile one-step method for graphene oxide/natural rubber latex nanocomposite production for supercapacitor applications. *Mater. Lett.* **2015,** *161,* 665-668.

36. Zhang, X.; Wang, J.; Jia, H.; Yin, B.; Ding, L.; Xu, Z.; Ji, Q., Polyvinyl pyrrolidone modified graphene oxide for improving the mechanical, thermal

conductivity and solvent resistance properties of natural rubber. *RSC Adv.* **2016,** *6*, 54668-54678.

37. Suriani, A. B.; Nurhafizah, M. D.; Mohamed, A.; Masrom, A. K.; Sahajwalla, V.; Joshi, R. K., Highly conductive electrodes of graphene oxide/natural rubber latex-based electrodes by using a hyper-branched surfactant. *Mater. Design* **2016,** *99*, 174-181.

38. Yang, G.; Liao, Z.; Yang, Z.; Tang, Z.; Guo, B., Effects of substitution for carbon black with graphene oxide or graphene on the morphology and performance of natural rubber/carbon black composites. *J. Appl. Polym. Sci.* **2015,** *132*, 41832.

39. Xing, W.; Wu, J.; Huang, G.; Li, H.; Tang, M.; Fu, X., Enhanced mechanical properties of graphene/natural rubber nanocomposites at low content. *Polym. Int.* **2014,** *63*, 1674-1681.

40. Aguilar-Bolados, H.; Lopez-Manchado, M. A.; Brasero, J.; Avilés, F.; Yazdani-Pedram, M., Effect of the morphology of thermally reduced graphite oxide on the mechanical and electrical properties of natural rubber nanocomposites. *Compos. Part B - Eng.* **2016,** *87*, 350-356.

41. Potts, J. R.; Shankar, O.; Murali, S.; Du, L.; Ruoff, R. S., Latex and two-roll mill processing of thermally-exfoliated graphite oxide/natural rubber nanocomposites. *Compos. Sci. Technol.* **2013,** *74*, 166-172.

42. Zhao, L.; Sun, X.; Liu, Q.; Zhao, J.; Xing, W., Natural rubber/graphene oxide nanocomposites prepared by latex mixing. *J. Macromol. Sci. B* **2015,** *54*, 581-592.

43. Mao, Y.; Wen, S.; Chen, Y.; Zhang, F.; Panine, P.; Chan, T. W.; Zhang, L.; Liang, Y.; Liu, L., High performance graphene oxide based rubber composites. *Sci. Rep.* **2013,** *3*, 2508.

44. Dong, B.; Liu, C.; Zhang, L.; Wu, Y., Preparation, fracture, and fatigue of exfoliated graphene oxide/natural rubber composites. *RSC Adv.* **2015,** *5*, 17140-17148.

45. Lin, Y.; Chen, Y.; Zeng, Z.; Zhu, J.; Wei, Y.; Li, F.; Liu, L., Effect of ZnO

nanoparticles doped graphene on static and dynamic mechanical properties of natural rubber composites. *Compos. Part A - Appl. S.* **2015,** *70,* 35-44.

46. Liu, X.; Kuang, W.; Guo, B., Preparation of rubber/graphene oxide composites with in-situ interfacial design. *Polymer* **2015,** *56*, 553-562.

47. Wu, L.; Qu, P.; Zhou, R.; Wang, B.; Liao, S., Green synthesis of reduced graphene oxide and its reinforcing effect on natural rubber composites. *High Perform. Polym.* **2014,** *27*, 486-496.

48. Singh, V. K.; Shukla, A.; Patra, M. K.; Saini, L.; Jani, R. K.; Vadera, S. R.; Kumar, N., Microwave absorbing properties of a thermally reduced graphene oxide/nitrile butadiene rubber composite. *Carbon* **2012,** *50,* 2202-2208.

49. Ha, H.; Park, J.; Ha, K.; Freeman, B. D.; Ellison, C. J., Synthesis and gas permeability of highly elastic poly(dimethylsiloxane)/graphene oxide composite elastomers using telechelic polymers. *Polymer* **2016,** *93*, 53-60.

50. Li, Y.; Wang, Q.; Wang, T.; Pan, G., Preparation and tribological properties of graphene oxide/nitrile rubber nanocomposites. *J. Mater. Sci.* **2011,** *47*, 730-738.

51. Mensah, B.; Kim, S.; Arepalli, S.; Nah, C., A study of graphene oxide-reinforced rubber nanocomposite. *J. Appl. Polym. Sci.* **2014,** *131*, 40640.

52. Wang, X.; Dou, W., Preparation of graphite oxide (GO) and the thermal stability of silicone rubber/GO nanocomposites. *Thermochim. Acta* **2012,** *529*, 25-28.

53. De, S. K.; White, J. R., *Rubber technologist's handbook*. Rapra Technology Ltd.: UK, 2001.

54. Treloar, L. R. G., *The physics of rubber elasticity*. Clarendon Press: Oxford, UK, 1975.

55. Boczkowska, A., *Advanced elastomers - technology, properties and applications*. InTech: 2012.

56. Zhang, X.; Xue, X.; Yin, Q.; Jia, H.; Wang, J.; Ji, Q.; Xu, Z., Enhanced compatibility and mechanical properties of carboxylated acrylonitrile butadiene rubber/styrene butadiene rubber by using graphene oxide as reinforcing filler. *Compos.*

Part B - Eng. **2017,** *111*, 243-250.

57. Lin, Y.; Liu, S.; Liu, L., A new approach to construct three dimensional segregated graphene structures in rubber composites for enhanced conductive, mechanical and barrier properties. *J. Mater. Chem. C* **2016,** *4*, 2353-2358.

58. Huang, J.; Tang, Z.; Yang, Z.; Guo, B., Bioinspired interface engineering in elastomer/graphene composites by constructing sacrificial metal-ligand bonds. *Macromol. Rapid Comm.* **2016,** *37*, 1040-5.

59. Zhang, X.; Wang, J.; Jia, H.; You, S.; Xiong, X.; Ding, L.; Xu, Z., Multifunctional nanocomposites between natural rubber and polyvinyl pyrrolidone modified graphene. *Compos. Part B - Eng.* **2016,** *84*, 121-129.

60. Yang, Z.; Liu, J.; Liao, R.; Yang, G.; Wu, X.; Tang, Z.; Guo, B.; Zhang, L.; Ma, Y.; Nie, Q.; Wang, F., Rational design of covalent interfaces for graphene/elastomer nanocomposites. *Compos. Sci. Technol.* **2016,** *132*, 68-75.

61. Das, A.; Kasaliwal, G. R.; Jurk, R.; Boldt, R.; Fischer, D.; Stöckelhuber, K. W.; Heinrich, G., Rubber composites based on graphene nanoplatelets, expanded graphite, carbon nanotubes and their combination: A comparative study. *Compos. Sci. Technol.* **2012,** *72*, 1961-1967.

62. Yaragalla, S.; A.P, M.; Kalarikkal, N.; Thomas, S., Chemistry associated with natural rubber–graphene nanocomposites and its effect on physical and structural properties. *Ind. Crop. Prod.* **2015,** *74*, 792-802.

63. Yaragalla, S.; Chandran, C. S.; Kalarikkal, N.; Subban, R. H. Y.; Chan, C. H.; Thomas, S., Effect of reinforcement on the barrier and dielectric properties of epoxidized natural rubber–graphene nanocomposites. *Polym. Eng. Sci.* **2015,** *55*, 2439-2447.

64. Kang, H.; Tang, Y.; Yao, L.; Yang, F.; Fang, Q.; Hui, D., Fabrication of graphene/natural rubber nanocomposites with high dynamic properties through convenient mechanical mixing. *Compos. Part B- Eng.* **2017,** *112*, 1-7.

65. Lin, Y.; Zeng, Z.; Zhu, J.; Chen, S.; Yuan, X.; Liu, L., Graphene nanosheets

decorated with ZnO nanoparticles: facile synthesis and promising application for enhancing the mechanical and gas barrier properties of rubber nanocomposites. *RSC Adv.* **2015,** *5* (71), 57771-57780.

66. Lin, Y.; Liu, K.; Chen, Y.; Liu, L., Influence of graphene functionalized with zinc dimethacrylate on the mechanical and thermal properties of natural rubber nanocomposites. *Polym. Composite.* **2015,** *36*, 1775-1785.

67. Lin, Y.; Chen, Y.; Zhang, Y.; Jia, D.; Luo, Y.; Liu, L., The use of zinc dimethacrylate functionalized graphene as a reinforcement in rubber composites. *Polym. Advan. Technol.* **2015,** *26*, 423-431.

68. Araby, S.; Zhang, L.; Kuan, H.-C.; Dai, J.-B.; Majewski, P.; Ma, J., A novel approach to electrically and thermally conductive elastomers using graphene. *Polymer* **2013,** *54*, 3663-3670.

69. Hernández, M.; Bernal, M. d. M.; Verdejo, R.; Ezquerra, T. A.; López-Manchado, M. A., Overall performance of natural rubber/graphene nanocomposites. *Compos. Sci. Technol.* **2012,** *73*, 40-46.

70. Zhan, Y.; Wu, J.; Xia, H.; Yan, N.; Fei, G.; Yuan, G., Dispersion and exfoliation of graphene in rubber by an ultrasonically-assisted katex mixing and in situ reduction process. *Macromol. Mater. Eng.* **2011,** *296*, 590-602.

71. Lian, H.; Li, S.; Liu, K.; Xu, L.; Wang, K.; Guo, W., Study on modified graphene/butyl rubber nanocomposites. I. Preparation and characterization. *Polym. Eng. Sci.* **2011,** *51*, 2254-2260.

72. Ozbas, B.; O'Neill, C. D.; Register, R. A.; Aksay, I. A.; Prud'homme, R. K.; Adamson, D. H., Multifunctional elastomer nanocomposites with functionalized graphene single sheets. *J. Polym. Sci. Pol. Phys.* **2012,** *50*, 910-916.

73. Araby, S.; Meng, Q.; Zhang, L.; Kang, H.; Majewski, P.; Tang, Y.; Ma, J., Electrically and thermally conductive elastomer/graphene nanocomposites by solution mixing. *Polymer* **2014,** *55*, 201-210.

74. Bai, X.; Wan, C.; Zhang, Y.; Zhai, Y., Reinforcement of hydrogenated

carboxylated nitrile–butadiene rubber with exfoliated graphene oxide. *Carbon* **2011,** *49*, 1608-1613.

75. Gan, L.; Shang, S.; Yuen, C. W. M.; Jiang, S.-x.; Luo, N. M., Facile preparation of graphene nanoribbon filled silicone rubber nanocomposite with improved thermal and mechanical properties. *Compos. Part B - Eng.* **2015,** *69*, 237-242.

76. Wu, J.; Huang, G.; Li, H.; Wu, S.; Liu, Y.; Zheng, J., Enhanced mechanical and gas barrier properties of rubber nanocomposites with surface functionalized graphene oxide at low content. *Polymer* **2013,** *54*, 1930-1937.

77. Ozbas, B.; Toki, S.; Hsiao, B. S.; Chu, B.; Register, R. A.; Aksay, I. A.; Prud'homme, R. K.; Adamson, D. H., Strain-induced crystallization and mechanical properties of functionalized graphene sheet-filled natural rubber. *J. of Polym. Sci. Pol. Phys.* **2012,** *50*, 718-723.

78. Frasca, D.; Schulze, D.; Wachtendorf, V.; Huth, C.; Schartel, B., Multifunctional multilayer graphene/elastomer nanocomposites. *Eur. Polym. J.* **2015,** *71*, 99-113.

79. He, C.; She, X.; Peng, Z.; Zhong, J.; Liao, S.; Gong, W.; Liao, J.; Kong, L., Graphene networks and their influence on free-volume properties of graphene-epoxidized natural rubber composites with a segregated structure: rheological and positron annihilation studies. *Phys. Chem. Chem. Phys.* **2015,** *17*, 12175-84.

80. Wang, L.; Wang, W.; Fu, Y.; Wang, J.; Lvov, Y.; Liu, J.; Lu, Y.; Zhang, L., Enhanced electrical and mechanical properties of rubber/graphene film through layer-by-layer electrostatic assembly. *Compos. Part B - Eng.* **2016,** *90*, 457-464.

81. Potts, J. R.; Shankar, O.; Du, L.; Ruoff, R. S., Processing–morphology–property relationships and composite theory analysis of reduced graphene oxide/natural rubber nanocomposites. *Macromolecules* **2012,** *45,* 6045-6055.

82. Lin, Y.; Liu, S.; Peng, J.; Liu, L., Constructing a segregated graphene network in rubber composites towards improved electrically conductive and barrier properties. *Compos. Sci. Technol.* **2016,** *131*, 40-47.

83. Song, S. H.; Kim, J. M.; Park, K. H.; Lee, D. J.; Kwon, O. S.; Kim, J.; Yoon, H.; Chen, X., High performance graphene embedded rubber composites. *RSC Adv.* **2015,** *5,* 81707-81712.

84. Lin, Y.; Liu, S.; Chen, S.; Wei, Y.; Dong, X.; Liu, L., A highly stretchable and sensitive strain sensor based on graphene–elastomer composites with a novel double-interconnected network. *J. Mater. Chem. C* **2016,** *4,* 6345-6352.

85. Cao, J.; Zhang, X.; Wu, X.; Wang, S.; Lu, C., Cellulose nanocrystals mediated assembly of graphene in rubber composites for chemical sensing applications. *Carbohydr. Polym.* **2016,** *140,* 88-95.

86. Zhou, Z.; Zhang, X.; Wu, X.; Lu, C., Self-stabilized polyaniline@graphene aqueous colloids for the construction of assembled conductive network in rubber matrix and its chemical sensing application. *Compos. Sci. Technol.* **2016,** *125,* 1-8.

87. Tang, M.; Xing, W.; Wu, J.; Huang, G.; Xiang, K.; Guo, L.; Li, G., Graphene as a prominent antioxidant for diolefin elastomers. *J. Mater. Chem. A* **2015,** *3,* 5942-5948.

88. Boland, C. S.; Khan, U.; Backes, C.; O'Neill, A.; McCauley, J.; Duane, S.; Shanker, R.; Liu, Y.; Jurewicz, I.; Dalton, A. B.; Coleman, J. N., Sensitive, high-strain, high-rate bodily motion sensors based on graphene–rubber composites. *ACS Nano* **2014,** *8,* 8819-8830.

89. Bandyopadhyay, A.; Bhowmick, A. K.; De Sarkar, M., Synthesis and characterization of acrylic rubber/silica hybrid composites prepared by sol-gel technique. *J. Appl. Polym. Sci.* **2004,** *93,* 2579-2589.

90. Liang, Y.-R.; Ma, J.; Lu, Y.-L.; Wu, Y.-P.; Zhang, L.-Q.; Mai, Y.-W., Effects of heat and pressure on intercalation structures of isobutylene-isoprene rubber/clay nanocomposites. I. Prepared by melt blending. *J. Polym. Sci. Pol. Phys.* **2005,** *43,* 2653-2664.

91. Bieliński, D. M.; Dobrowolski, O.; Przybytniak, G., Morphological aspects of rubber fracture and wear. *J. Appl. Polym. Sci.* **2008,** *110,* 55-60.

92. Li, J.; Lin, H.; Zhao, W.; Chen, G., Instant modification of graphite nanosheets by

the grafting of a styrene oligomer under microwave radiation. *J. Appl. Polym. Sci.* **2008,** *109*, 1377-1380.

93. Verdejo, R.; Saiz-Arroyo, C.; Carretero-Gonzalez, J.; Barroso-Bujans, F.; Rodriguez-Perez, M. A.; Lopez-Manchado, M. A., Physical properties of silicone foams filled with carbon nanotubes and functionalized graphene sheets. *Eur. Polym. J.* **2008,** *44*, 2790-2797.

94. De Falco, A.; Marzocca, A. J.; Corcuera, M. A.; Eceiza, A.; Mondragon, I.; Rubiolo, G. H.; Goyanes, S., Accelerator adsorption onto carbon nanotubes surface affects the vulcanization process of styrene-butadiene rubber composites. *J. Appl. Polym. Sci.* **2009,** *113*, 2851-2857.

95. Matos, C. F.; Galembeck, F.; Zarbin, A. J. G., Multifunctional materials based on iron/iron oxide-filled carbon nanotubes/natural rubber composites. *Carbon* **2012,** *50,* 4685-4695.

96. Raghu, A. V.; Lee, Y. R.; Jeong, H. M.; Shin, C. M., Preparation and physical properties of waterborne polyurethane/functionalized graphene sheet nanocomposites. *Macromol. Chem. Phys.* **2008,** *209*, 2487-2493.

97. Kim, J. S.; Hong, S.; Park, D. W.; Shim, S. E., Water-borne graphene-derived conductive SBR prepared by latex heterocoagulation. *Macromol. Res.* **2010,** *18,* 558-565.

98. Kim, J. S.; Yun, J. H.; Kim, I.; Shim, S. E., Dielectric properties of electrospun barium titanate fibers:graphene:silicone rubber composites. *J. Ind. Eng. Chem.* **2011,** *17*, 325-330.

99. Kim, J. S.; Yun, J. H.; Kim, I.; Shim, S. E., Electrical properties of graphene/SBR nanocomposite prepared by latex heterocoagulation process at room temperature. *J. Ind. Eng. Chem.* **2011,** *17*, 325-330.

100. Wang, J.; Jia, H.; Tang, Y.; Ji, D.; Sun, Y.; Gong, X.; Ding, L., Enhancements of the mechanical properties and thermal conductivity of carboxylated acrylonitrile butadiene rubber with the addition of graphene oxide. *J. Mater. Sci.* **2013,** *48,*

1571-1577.

101. Dao, T. D.; Lee, H. I.; Jeong, H. M., Alumina-coated graphene nanosheet and its composite of acrylic rubber. *J. Colloid. Interface Sci.* **2014,** *416*, 38-43.

102. Xiong, X.; Wang, J.; Jia, H.; Fang, E.; Ding, L., Structure, thermal conductivity, and thermal stability of bromobutyl rubber nanocomposites with ionic liquid modified graphene oxide. *Polym. Degrad. Stabil.* **2013,** *98*, 2208-2214.

103. Pradhan, B.; Srivastava, S. K., Synergistic effect of three-dimensional multi-walled carbon nanotube-graphene nanofiller in enhancing the mechanical and thermal properties of high-performance silicone rubber. *Polym. Int.* **2014,** *63*, 1219-1228.

104. Tian, M.; Zhang, J.; Zhang, L.; Liu, S.; Zan, X.; Nishi, T.; Ning, N., Graphene encapsulated rubber latex composites with high dielectric constant, low dielectric loss and low percolation threshold. *J. Colloid. Interface Sci.* **2014,** *430*, 249-56.

105. Zhang, Y.; Mark, J. E.; Zhu, Y.; Ruoff, R. S.; Schaefer, D. W., Mechanical properties of polybutadiene reinforced with octadecylamine modified graphene oxide. *Polymer* **2014,** *55*, 5389-5395.

106. Matos, C. F.; Galembeck, F.; Zarbin, A. J. G., Multifunctional and environmentally friendly nanocomposites between natural rubber and graphene or graphene oxide. *Carbon* **2014,** *78*, 469-479.

107. Zhang, H.; Wang, C.; Zhang, Y., Preparation and properties of styrene-butadiene rubber nanocomposites blended with carbon black-graphene hybrid filler. *J. Appl. Polym. Sci.* **2015,** *132*, 41309.

108. Malas, A.; Pal, P.; Giri, S.; Mandal, A.; Das, C. K., Synthesis and characterizations of modified expanded graphite/emulsion styrene butadiene rubber nanocomposites: Mechanical, dynamic mechanical and morphological properties. *Compos. Part B - Eng.* **2014,** *58*, 267-274.

109. Song, Y.; Yu, J.; Yu, L.; Alam, F. E.; Dai, W.; Li, C.; Jiang, N., Enhancing the

thermal, electrical, and mechanical properties of silicone rubber by addition of graphene nanoplatelets. *Mater. Design* **2015,** *88*, 950-957.

110. Gan, L.; Shang, S.; Jiang, S.-x., Impact of vinyl concentration of a silicone rubber on the properties of the graphene oxide filled silicone rubber composites. *Compos. Part B - Eng.* **2016,** *84*, 294-300.

111. Jackson, K. D. O.; Loadman, M. J. R.; Jones, C. H.; Ellis, G., Fourier transform raman spectroscopy of elastomers, an overview. *J. Nat. Rubb. Res.* **1991,** *6*, 230-240.

112. Hendra, P. J.; Jackson, K. D. O., Applications of Raman spectroscopy to the analysis of natural rubber. *Spectrochim. Acta A* **1994,** *50*, 1987-1997.

113. Sadasivuni, K. K.; Ponnamma, D.; Thomas, S.; Grohens, Y., Evolution from graphite to graphene elastomer composites. *Prog. Polym. Sci.* **2014,** *39*, 749-780.

114. Li, Z.; Young, R. J.; Wang, R.; Yang, F.; Hao, L.; Jiao, W.; Liu, W., The role of functional groups on graphene oxide in epoxy nanocomposites. *Polymer* **2013,** *54*, 5821-5829.

115. Li, Z.; Young, R. J.; Kinloch, I. A., Interfacial stress transfer in graphene oxide nanocomposites. *ACS Appl. Mater. Inter.* **2013,** *5*, 456-63.

116. Li, Z.; Young, R. J.; Kinloch, I. A.; Wilson, N. R.; Marsden, A. J.; Raju, A. P. A., Quantitative determination of the spatial orientation of graphene by polarized Raman spectroscopy. *Carbon* **2015,** *88*, 215-224.

117. Li, Z.; Young, R. J.; Wilson, N. R.; Kinloch, I. A.; Vallés, C.; Li, Z., Effect of the orientation of graphene-based nanoplatelets upon the Young's modulus of nanocomposites. *Compos. Sci. Technol.* **2016,** *123*, 125-133.

118. Dao, T. D.; Jeong, H. M., Novel stearic acid/graphene core–shell composite microcapsule as a phase change material exhibiting high shape stability and performance. *Sol. Energ. Mat. Sol. C.* **2015,** *137*, 227-234.

119. Kumar, S. K.; Castro, M.; Saiter, A.; Delbreilh, L.; Feller, J. F.; Thomas, S.; Grohens, Y., Development of poly(isobutylene-co-isoprene)/reduced graphene oxide nanocomposites for barrier, dielectric and sensingapplications. *Mater. Lett.* **2013,** *96*,

109-112.

120. Ponnamma, D.; Sadasivuni, K. K.; Strankowski, M.; Guo, Q.; Thomas, S., Synergistic effect of multi walled carbon nanotubes and reduced graphene oxides in natural rubber for sensing application. *Soft Matter.* **2013,** *9*, 10343.

121. Kang, H.; Zuo, K.; Wang, Z.; Zhang, L.; Liu, L.; Guo, B., Using a green method to develop graphene oxide/elastomers nanocomposites with combination of high barrier and mechanical performance. *Compos. Sci. Technol.* **2014,** *92*, 1-8.

122. Salvo, L.; Cloetens, P.; Maire, E.; Zabler, S.; Blandin, J. J.; Buffière, J. Y.; Ludwig, W.; Boller, E.; Bellet, D.; Josserond, C., X-ray micro-tomography an attractive characterisation technique in materials science. *Nucl. Instrum. Methods Phys. Res., Sect. B* **2003,** *200*, 273-286.

123. Salvo, L.; Suéry, M.; Marmottant, A.; Limodin, N.; Bernard, D., 3D imaging in material science: Application of X-ray tomography. *CR. Phys.* **2010,** *11*, 641-649.

124. Mitri, F. G.; Garzon, F. H.; Sinha, D. N., Characterization of acoustically engineered polymer nanocomposite metamaterials using x-ray microcomputed tomography. *Rev. Sci. Instrum.* **2011,** *82*, 034903.

125. Schopp, S.; Thomann, R.; Ratzsch, K.-F.; Kerling, S.; Altstädt, V.; Mülhaupt, R., Functionalized Graphene and Carbon Materials as Components of Styrene-Butadiene Rubber Nanocomposites Prepared by Aqueous Dispersion Blending. *Macromol. Mater. Eng.* **2014,** *299*, 319-329.

126. Valentini, L.; Bittolo Bon, S.; Lopez-Manchado, M. A.; Verdejo, R.; Pappalardo, L.; Bolognini, A.; Alvino, A.; Borsini, S.; Berardo, A.; Pugno, N. M., Synergistic effect of graphene nanoplatelets and carbon black in multifunctional EPDM nanocomposites. *Compos. Sci. Technol.* **2016,** *128*, 123-130.

127. Young, R. J.; Lovell, P. A., *Introduction to polymers*. 3rd ed.; CRC Press: Boca Raton, 2011.

128. She, X.; He, C.; Peng, Z.; Kong, L., Molecular-level dispersion of graphene into epoxidized natural rubber: Morphology, interfacial interaction and mechanical

reinforcement. *Polymer* **2014,** *55*, 6803-6810.

129. Stanier, D. C.; Patil, A. J.; Sriwong, C.; Rahatekar, S. S.; Ciambella, J., The reinforcement effect of exfoliated graphene oxide nanoplatelets on the mechanical and viscoelastic properties of natural rubber. *Compos. Sci. Technol.* **2014,** *95*, 59-66.

130. Varghese, T. V.; Ajith Kumar, H.; Anitha, S.; Ratheesh, S.; Rajeev, R. S.; Lakshmana Rao, V., Reinforcement of acrylonitrile butadiene rubber using pristine few layer graphene and its hybrid fillers. *Carbon* **2013,** *61*, 476-486.

131. Li, C.; Feng, C.; Peng, Z.; Gong, W.; Kong, L., Ammonium-assisted green fabrication of graphene/natural rubber latex composite. *Polym. Composite.* **2013,** *34*, 88-95.

132. Jagielski, J.; Ostaszewska, U.; Kozinski, R.; Hassa-Zaloba, A.; Romaniec, M.; Kurpaska, L.; Kosinska, A.; Grambole, D.; Jozwik, I., Structural and functional properties of ion-irradiated graphene-reinforced elastomers. *Surf. Coat. Technol.* **2016,** *306*, 176-180.

133. Mensah, B.; Kumar, D.; Lim, D.-K.; Kim, S. G.; Jeong, B.-H.; Nah, C., Preparation and properties of acrylonitrile-butadiene rubber-graphene nanocomposites. *J. Appl. Polym. Sci.* **2015,** *132*, 42457.

134. Tang, Z.; Wu, X.; Guo, B.; Zhang, L.; Jia, D., Preparation of butadiene–styrene–vinyl pyridine rubber–graphene oxide hybrids through co-coagulation process and in situ interface tailoring. *J. Mater. Chem.* **2012,** *22*, 7492.

135. Al-Ghamdi, A. A.; Al-Ghamdi, A. A.; Al-Turki, Y.; Yakuphanoglu, F.; El-Tantawy, F., Electromagnetic shielding properties of graphene/acrylonitrile butadiene rubber nanocomposites for portable and flexible electronic devices. *Composites Part B: Engineering* **2016,** *88*, 212-219.

136. Mu, Q.; Feng, S., Thermal conductivity of graphite/silicone rubber prepared by solution intercalation. *Thermochim. Acta* **2007,** *46*, 70-75.

137. Bunch, J. S.; Verbridge, S. S.; Alden, J. S.; van der Zande, A. M.; Parpia, J. M.; Craighead, H. G.; McEuen, P. L., Impermeable atomic membranes from graphene

sheets. *Nano Lett.* **2008,** *8*, 2458-2462.

138. Unnikrishnan, G.; Thomas, S., Diffusion and transport of aromatic hydrocarbons through natural rubber. *Polymer* **1994,** *35*, 5504-5510.

139. Wei, C., Thermal expansion and diffusion coefficients of carbon nanotube-polymer composites. *Nano Lett.* **2002,** *6*, 647-650.

140. Gwaily, S. E.; Badawy, M. M.; Hassan, H. H.; Madani, M., Influence of thermal aging on crosslinking density of boron carbide:natural rubber composites. *Polym. Test.* **2003,** *22*, 3-7.

141. Geethamma, V. G.; Thomas, S., Diffusion of water and artificial seawater through coir fiber reinforced natural rubber composites. *Polym. Composite.* **2005,** *26*, 136-143.

142. Yin, H.; Ma, Q.; Zhou, Y.; Ai, S.; Zhu, L., Electrochemical behavior and voltammetric determination of 4-aminophenol based on graphene–chitosan composite film modified glassy carbon electrode. *Electrochim. Acta* **2010,** *55*, 7102-7108.

143. Visakh, P. M.; Thomas, S.; Oksman, K.; Mathew, A. P., Cellulose nanofibres and cellulose nanowhiskers based natural rubber composites: Diffusion, sorption, and permeation of aromatic organic solvents. *J. Appl. Polym. Sci.* **2012,** *124*, 1614-1623.

144. Obasi, H. C.; Ogbobe, O.; Igwe, I. O., Diffusion Characteristics of Toluene into Natural Rubber/Linear Low Density Polyethylene Blends. *Int. J. Polym. Sci.* **2009,** *2009*, 1-6.

3. Experimental

3.1. Materials

The XG graphite nanoplatelets (termed GNP) were purchased from XG Sciences Inc. Lansing, Michigan, USA and used as received. Three types of XGNP Grade-M particles were employed with lateral diameters quoted by the supplier of 5 μm, 15 μm and 25 μm (designated as M5, M15 and M25, respectively). The thicknesses of all the flakes were quoted by the manufacturer to be in the range 6 to 8 nm (i.e. around 20 graphene layers). A carbon-based nanomaterial often used to reinforce elastomers, high abrasion furnace HAF N330 carbon black (CB) supplied by the Berwin Polymer Processing Group, Duckinfield, UK, was employed for comparison with the GNPs.

The grade of natural rubber (NR) used was SMR CV60 (Standard Malaysian Rubber, Mooney-Viscosity ML (1+4, 100 ℃) of 60). It was purchased from Astlett Rubber Inc., Oakville, Ontario, Canada and used as received. The source of the nitrile butadiene rubber (NBR) used is grade Nipol® 1052J, from Clwyd Compounders Ltd. All the additives involved in the rubber processing, zinc oxide, stearic acid, TMTD, CBS accelerator and sulfur, were of analytical grade and used as received. Toluene (anhydrous, 99.8%) was purchased from Sigma-Aldrich Co. Ltd. and used as received.

3.2. Preparation of GNP and CB rubber nanocomposites

The rubber mastication was conducted with a Bridge two-roll mill (manufactured by David Bridge & Co. Ltd) using the formulations listed in Table 3.1 and 3.2. Nominal loadings of 0, 5, 10, 15, 20 phr of the three different types of GNP (only M15 for NBR) and N330 CB were incorporated into the natural rubber or nitrile rubber matrix.

Before the mixing, pieces of the natural rubber were pre-heated at 60 ℃ in an oven for 30 minutes to enable decrystallization which was unnecessary for the nitrile rubber. The two-roll mill was set to a speed of 22 rpm with a friction ratio of 1.5:1 and a nip gap of 1 mm. For each batch of material, 200 g rubber was put in the two-roll mill and formed a sheet adhering to the surface of one of the rolls. When the rubber sheets became warm and sticky under rolling compaction, additives including zinc oxide, stearic acid, TMTD and CBS accelerator, in accordance with the formulation, were added on to the rubber sheet. This was followed by mixing for 10 minutes, during which time the rubber sheet was cut from one side and folded to the other side to achieve a good dispersion. Subsequently, the GNP or CB powder were gradually incorporated into the compound and followed by a similar mixing procedure for a time depending on the amount of additive. Finally, the sulfur was blended into the compound, with further mixing to achieve a uniform dispersion of all the additives in the natural rubber matrix and the mixing time was controlled to avoid the occurrence of premature vulcanization.

Table 3.1 Formulation of the NR compounds

Materials	Loading (phr*)
SMR CV60	100
Sulfur	3
CBS accelerator	1
Zinc Oxide	3
Stearic acid	2.5
GNP and N330	5, 10, 15, 20

*“phr” is a preferred used unit in the rubber industry, abbreviation for “parts per hundred rubber”.

Table 3.2 Formulation of the NBR compounds

Materials	Loading (phr*)
NBR Nipol® 1052J	100
Sulfur	2
CBS accelerator	0.5
Zinc Oxide	4
TMTD	0.25
GNP and N330	5, 10, 15, 20

The compounds were then cut into amounts corresponding to the designed mould dimensions and hot pressed in a metal mould into sheets (~ 1 or 2 mm thick) in a Collin Platen Press (Platen Press P 300 P/M). The vulcanization proceeded at a temperature of 160 ℃ for 10 minutes under a hydraulic pressure of 30 bar.

3.3. Thermogravimetric analysis (TGA)

The actual mass fractions of GNP and CB in all the nanocomposites were determined by thermogravimetric analysis (TGA) in a TA Instruments Q500 TGA. The temperature range was set from room temperature to 800 ℃ using a heating rate of 40 ℃/min in an atmosphere of nitrogen. The amounts of processing additives were presumed to be identical in the pure rubbers and all the nanocomposites in the determination of the mass fractions of the GNP and CB in the rubbers.

3.4. Scanning electron microscopy

The scanning electron microscopy (SEM) images of the GNP and rubber nanocomposites were acquired using EVO60 VPSEM (Zeiss) operated at 8-10 kV. The GNP particles and N330 CB were sprinkled on aluminium stubs before examination. SEM images of the carbon black were obtained using a higher resolution XL 30 FEG Philips operated at 10 kV, the samples being coated with gold/ palladium before analysis. The microstructure of the nanocomposites was evaluated from low temperature fracture surfaces. The samples of 1 mm thick were immersed into liquid nitrogen and broken by hand to produce well-defined brittle fracture surfaces. They were subsequently coated with gold/palladium to render them conductive before being examined in the SEM.

3.5. Raman spectroscopy

Raman spectra were obtained from the materials using a Renishaw 2000 of Raman spectrometer with a laser length of 633 nm and a ×50 objective lens in the microscope, giving a spot size of the order of 2 μm. The calibration of the wavenumber was conducted on a silicon wafer. A laser configuration without orientation (VN mode, incident light in vertical direction and scattered light in all direction, see the beam path in Figure 3.1 and the laser setting in Table 3.3) was employed. The GNPs and N330 CB particles were characterised from small clusters on glass slides. Raman spectra were also obtained from the low temperature fracture surfaces of the nanocomposites.

The spatial orientation of GNP flakes in rubber compound was determined as described else.[1-2] In the orientation test, the Raman laser was aligned perpendicular to one surface of the rubber (either along the X or the Z axis as in Figure 3.2), with the incident and scattered radiations polarized parallel to each other (VV mode, incident and scattered lights are both in vertical direction, see the beam path in Figure 3.1 and the laser setting in Table 3.3). The rotation angle in X and Z axis are denoted as Φ_X and Φ_Z, respectively. The Raman G band of GNP was recorded, and its intensity as the function of the rotation angle Φ_X or Φ_Z, as shown in Figure 3.2. On basis of the parameters determined from the orientation study, the orientation distribution function (ODF) of GNPs in the rubber can be estimated. The angle between the surface normal of each GNP flake, and the reference normal of the rubber piece is defined as θ, as illustrated in Figure 2 (ref [1]). For example, if a GNP flake is in the plane of the rubber sheet, then θ =0. The data was calculated by *Wolfram Mathematica 9* to obtain the values of the parameters for plotting the figures.

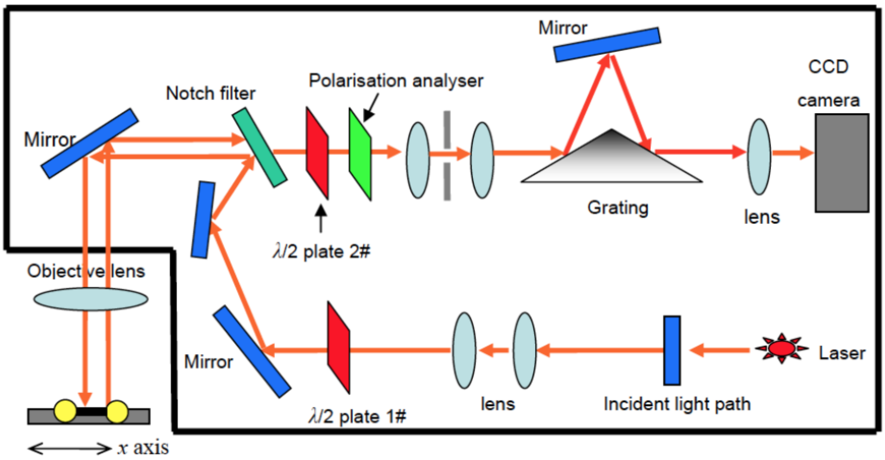

Figure 3.1 Schematic diagram of the Renishaw Raman spectrometer[3]

Table 3.3 the position of the optical components for different polarisation configurations

	VN	VV
λ/2 Plate 1#	In	In
λ/2 Plate 2#	Out	Out
Polarisation analyser	Out	In

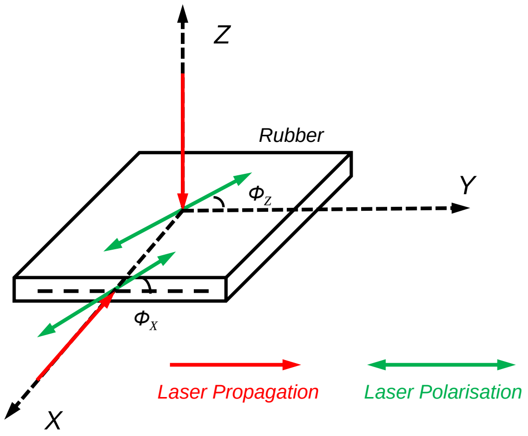

Figure 3.2 Experimental arrangement for the study of GNP orientation using Raman spectroscopy.

The shifts of the Raman 2D band in the GNP rubber nanocomposites with strain were determined for the highest loadings (20 phr) of each type of GNP. This was undertaken using a tensile rig to clamp the rubber strip specimens and provide a static tensile force. The strain was determined from the change in separation of the grips. A VN laser polarization configuration (vertically-polarized incident light and unpolarised scattered light) was used and the laser beam focused on the same marked individual flake exposed on the surface of each specimen. Spectra were obtained at static strains of 0, 30, 40, 60, 80, 90, 120 and 160%. At least 16 different specimens were tested for each of the GNP/NR materials.

3.6. X-ray diffraction

X-ray diffraction (XRD) patterns were obtained in a D8-Discover (Bruker Corp.) using Cu Kα radiation to determine the GNP layer spacing of the nanocomposites within the range of scattering angles (2h) of 5 °–45 ° at a scan rate of 3 °/min. The reflection mode was employed to scan the top surfaces of all the specimens (see Figure 3.3a, the red arrow indicates the reflection path and the projection of the X-ray is parallel to the *Y* axis). M15 NR composites at 10 and 20 phr were scanned on the edge surfaces as well (see in Figure 3.3b, the red arrow indicates the reflection path and the projection of the X-ray is perpendicular to the *Y* axis).

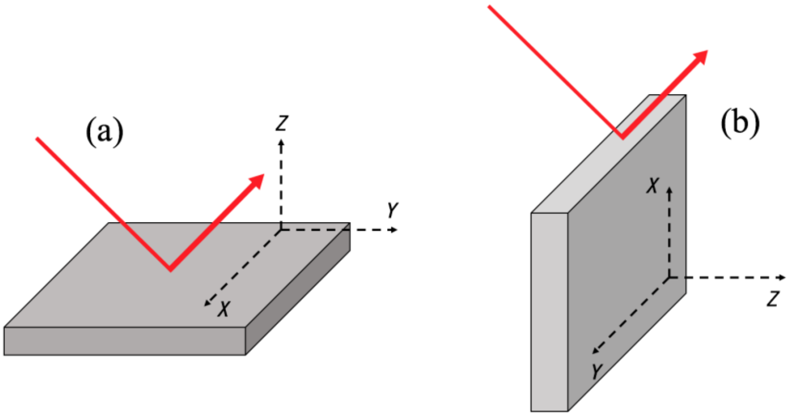

Figure 3.3 The setup of the XRD reflection experiment. (a) Reflection on the top surface; (b) reflection on the edge surface

3.7. X-ray computed tomography scanning

Samples for X-ray CT were prepared using a Leica Ultracut UC6 Ultramicrotome. Sections of the moulded sheets were sandwiched between two aluminium plates for cutting and were microtomed at an angle along three directions, leaving the moulded surface face intact.

Nanoscale X-ray CT data were acquired on a Zeiss Xradia Ultra 810 instrument of the Henry Moseley X-ray Imaging Facility. Projections for each sample were acquired in phase contrast and 'large field of view' mode with a 30 s exposure time, 801 projections and a pixel size of 128 nm. The series were reconstructed with a filtered back projection reconstruction through the Zeiss XMReconstructor software (version 9.1.12862).

All visualisation and thresholding was performed in the Avizo software package (version 9.1.1). Segmentation was performed through manual thresholding and removal of 'islands' of volume less than 500 pixels. The surface area and the orientation of each flake were calculated through use of the Avizo 'Label Measures'. To calculate the orientation of each flake, the angles corresponding to the 'length', the longest flake dimension (calculated over 91 angles in 3D), and the 'breadth', the longest flake dimension perpendicular to the 'length' (calculated over 90 angles in the plane perpendicular to the length), were first obtained. The polar angles of the direction perpendicular to the 'length' and 'breadth', corresponding to the direction normal to the flake' was calculated by taking the cross-product of unit vectors at the angles corresponding the 'length' and 'breadth' for each flake. The angle between the normal to the flake and the normal to the pressed surface was obtained by calculating the dot-product of the unit vector corresponding to each direction.

3.8. Mechanical testing

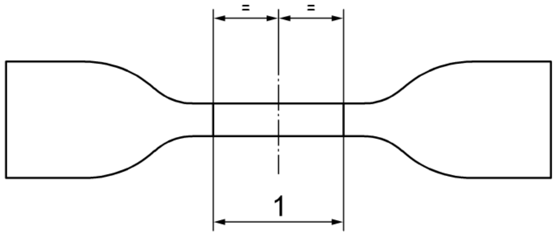

Figure 3.4 Shape of tensile testing specimens (Type 1)[4], gauge length 25 mm.

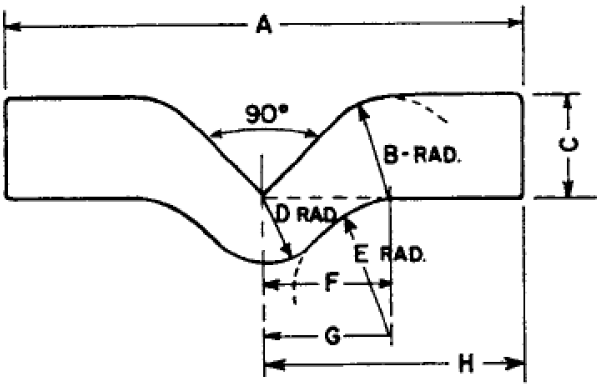

Figure 3.5 Shape of tear testing specimens (Die C)[5]

Tensile testing and tear testing were undertaken using an Instron-1122 universal testing machine. The tensile specimens and the tear specimens were prepared by cutting the 2 mm sheets by a stamping machine. The shapes of the specimens for both tests are shown (showing the designated types at the ends of the captions) in Figure 3.4 and 3.5, respectively, and more detail can be found in Standard ISO 37:2011(tensile test)[4] and ASTM D624 - 00:2012 (tear test).[5] The specimens were Prior to testing the specimens were conditions by being placed in a climate-controlled laboratory for 24 hours at a temperature of 23.0 ± 0.1 ℃ and a relative humidity of 50 ± 5%. For each formulation, 5 specimens were tested and deformed at a crosshead speed of 500 mm/min until fracture. The strain was measured from the crosshead displacement. The tear strength was calculated by the maximum forced divided by the specimen thickness.

3.9. Hardness testing

The hardness tests were conducted using a Shore A durometer (Duratool 59-500-000 Durometer Shore "A" Scale, manufactured to the standards DIN 53505/ ASTM D2240). The durometer was held in a vertical position with the indenter point at least 12 mm from the specimen edge, followed by the pressure foot being applied to the specimen as rapidly as possible, without shock. The hardness values were obtained from the stop hand retained at the hardness reading. The tests were undertaken at 23 ℃ ± 2 ℃, and 5 specimens were measured for each composition using the procedure detailed above.

3.10. Thermal conductivity testing

The thermal conductivity measurements of the nanocomposites were undertaken by a FOX 50 Heat Flow Meter as shown in Figure 3.6. The conditions were set at a mean temperature of 25 ℃ (upper platen: 35 ℃, bottom platen: 15 ℃). The specimens were cut into round sheets of a diameter of ~50 mm and a thickness of ~2 mm. 3 specimens were tested for each composite and each specimen was repeated twice to obtained a mean value of the conductivity.

Figure 3.6 FOX 50 Heat Flow Meter

3.11. Swelling testing

The swelling tests were conducted by soaking rubber sheets in toluene in glass petri dishes at room temperature until equilibrium. The specimens were of square shape and of a dimension of ~35 mm long and 2 mm thick, which were cut from the specimens used for thermal conductivity testing. Dimension measurement of the specimens was taken at the beginning and at the equilibrium. Mass measurement was undertaken at certain intervals by an analytical balance (Explorer Pro, Medel: EP114C) precise to ± 0.1 mg. The glass petri dishes were placed in a fume cupboard and were capped to prevent evaporation of the solvent.

References

1. Li, Z.; Young, R. J.; Wilson, N. R.; Kinloch, I. A.; Vallés, C.; Li, Z., Effect of the orientation of graphene-based nanoplatelets upon the Young's modulus of nanocomposites. *Compos. Sci. Technol.* **2016,** *123*, 125-133.

2. Li, Z.; Young, R. J.; Kinloch, I. A.; Wilson, N. R.; Marsden, A. J.; Raju, A. P. A., Quantitative determination of the spatial orientation of graphene by polarized Raman spectroscopy. *Carbon* **2015,** *88*, 215-224.

3. Kao, C. C. Study of the deformation of single-walled carbon nanotube (SWNT)/epoxy composites using Raman spectroscopy. Ph.D Thesis, University of Manchester, 2008.

4. ISO 37:2011: Rubber, vulcanized or thermoplastic - Determination of tensile stress-strain properties.

5. D624 - 00:2012: Standard test method for tear strength of conventional vulcanized rubber and thermoplastic elastomers.

4. NR GNP composites characterization and mechanical properties*

4.1. Introduction

This chapter will present the structure characterisation on the natural rubber filled with the three grades of GNPs and the N330 carbon black. The structure of the fillers will be seen through imaging provided by different techniques on the cross-sectional areas or the 3D domains of the specimens and the orientation of the flakes will be quantified by polarized Raman spectroscopy. Subsequently, the mechanical tests will be exhibited showing the reinforcement achieved by the addition of the fillers. The effects on the mechanical enhancement by the GNPs and the carbon black will be compared.

4.2. Characterisation of the GNPs and carbon black

4.2.1. Scanning electron microscopy (SEM)

Scanning electron micrographs of the three different types of GNP and of the N330 carbon black are shown in Figure 4.1. It can be seen that the GNP have a high aspect ratio with a systematic increase in flake size going from M5 to M15 to M25. The morphology of the N330 is however, quite different consisting of agglomerates of nano-sized particles of the order of 30-35 nm in diameter, near to the resolution limit of the scanning electron microscope. The fracture surfaces of pure NR in Figure 4.2 show the crack lines in random directions at low magnification and the relatively flat surface at high magnification.

*Based upon the paper "S. Li, Z. Li, T. L. Burnett, T. J. A. Slater, T. Hashimoto, R. J. Young. Nanocomposites of graphene nanoplatelets in natural rubber: microstructure and mechanism of reinforcement. *J Mater. Sci.* (2017) 52:9558-9572."

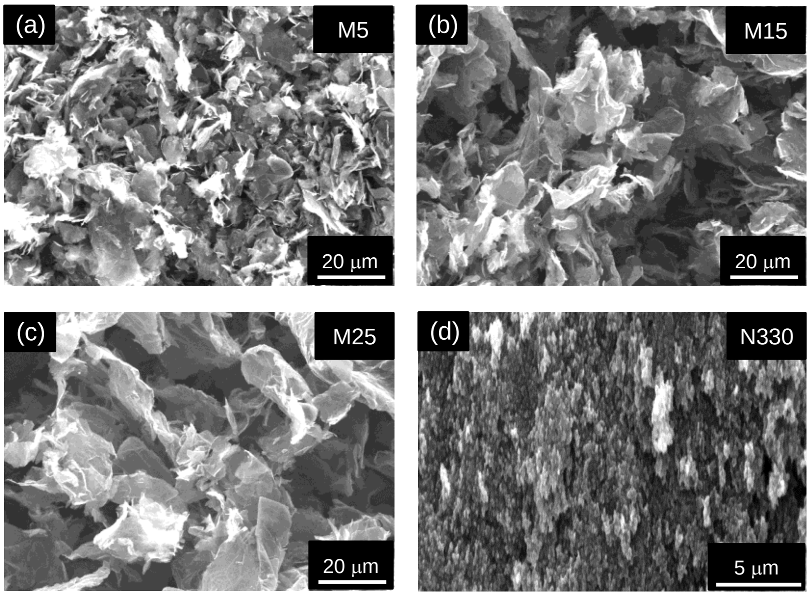

Figure 4.1 SEM micrographs of the particles, (a) M5, (b), M15, (c) M25 and (d) N330 carbon black.

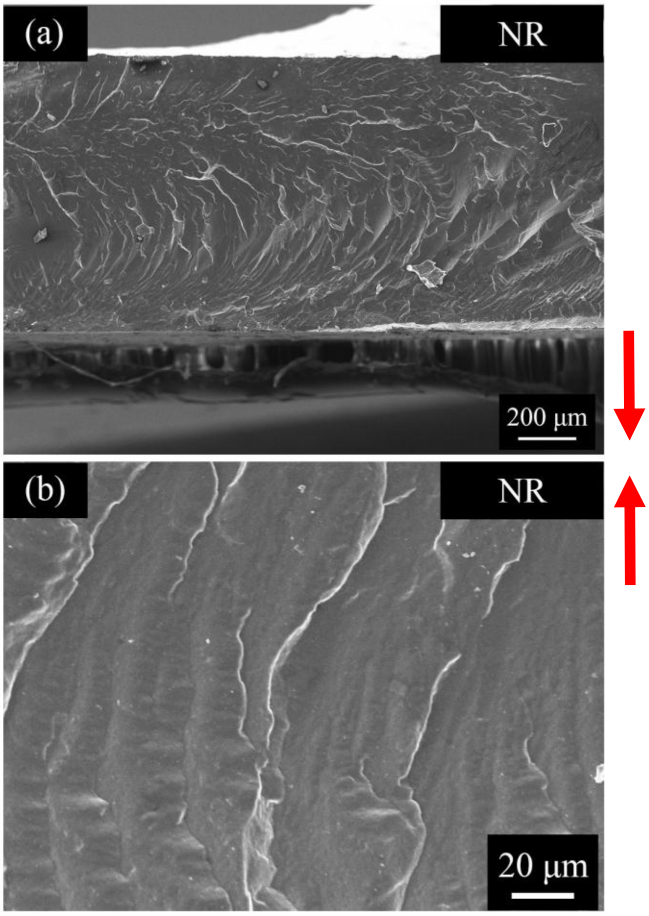

Figure 4.2 SEM micrographs of the matrix at (a) low and (b) high magnification. Specimen thickness: 1mm. The red arrows indicate the hydraulic pressure direction in the hot press.

4.2.2. Raman spectroscopy

Representative Raman spectra of the three types of GNP, carbon black and natural rubber are presented in Figure 4.3. It can be seen that the GNP all show a weak D band and well-defined G and 2D bands indicative of a graphitic structure. In contrast the N330 carbon black has two very broad and overlapping D and G bands and no 2D band, consistent with a highly-disordered amorphous carbon structure. No well-defined Raman spectrum can be obtained from the natural rubber and it shows only a very broad peak resulting from background fluorescence.

Raman spectra for the NR filled with 5, 10, 15 and 20 phr of the three different types of GNP and carbon blacks are shown in Figure 4.4. It can be seen that the GNP composites appear similar to the spectra for the GNP in Figure 4.3 but the relative intensity of the D band is slightly higher than in the spectra of the GNP before processing. There is also a fluorescent background from the rubber matrix. No particular changes of the peak shape are found in the carbon black composites to the carbon black in Figure 4.3, and the fluorescence background is less significant compared with those in the GNP composites spectra. It seems the fillers (GNPs and carbon black) can suppress the fluorescence background of the rubber, and expose the latent rubber peaks. The exposed NR peaks can be seen at around 1448, 1676, and 2930 cm^{-1}. The mechanism of fluorescence suppression in elastomers by adding fillers is not well understood, but the method was earlier employed by Hendra[1] in 1994 using silica and calcium carbonate (50% by weight) as fillers to make the Raman peaks of natural rubber sharp. The similar effect was also reported by Xie et al. to suppress the fluorescence background of fluorochrome by using graphene as a substrate.[2]

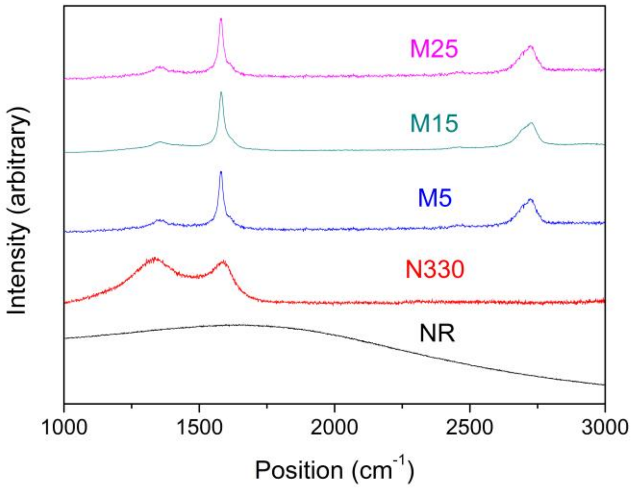

Figure 4.3 Raman spectra of the starting materials (laser excitation: 633 nm).

Once the fluorescence background is reduced, the rubber peaks can emerge to compare with those of the GNP. For example, upon the range of 1450 to 1750 cm^{-1} of the Raman spectra of the M5 NR composites as presented in Figure 4.5, it can be seen a G band from the M5 GNP and a peak around 1676 cm^{-1} from NR. The intensity ratio of the G band to the rubber peak is significantly increased from 5 to 20 phr loadings of GNP. The reason of the intensity ratio evolution is related to the concentration of the filler-matrix composites. It has been reported by Pakjamsai and Suwanprateeb[3] that in composites, the selected Raman band ratio can be linearly proportional to the volume fraction ratio the filler and the matrix. To be more specific, the scatted intensity of a Raman band is proportional to the intensity of the incident light, the volume of the sample illuminated by the laser beam and collected by the spectrometer, and the concentration of the scattering species.

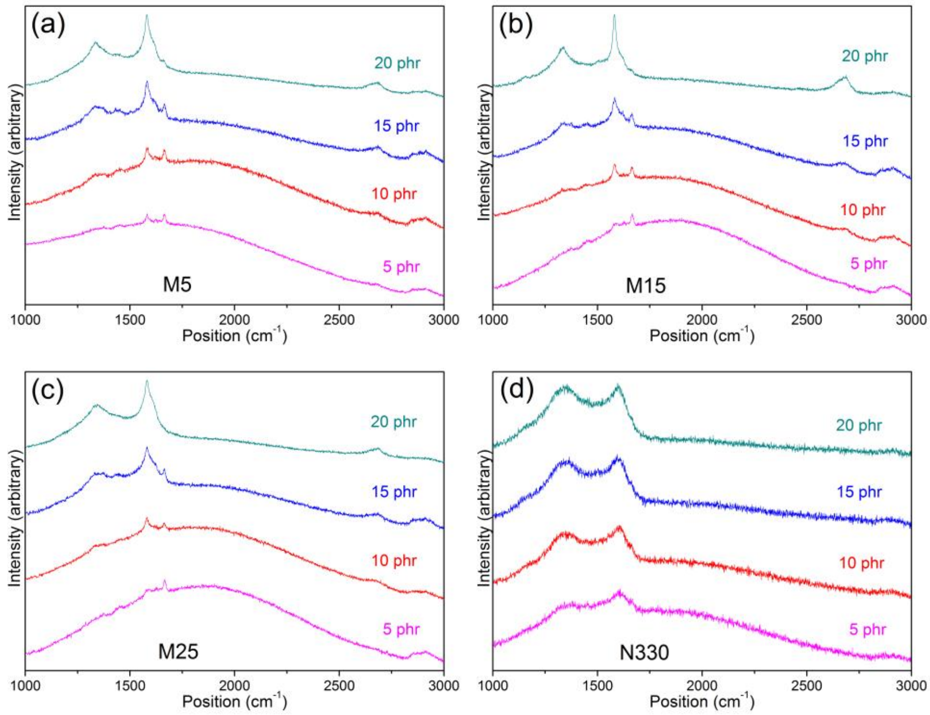

Figure 4.4 Raman spectra of the nanocomposites at 5, 10, 15, 20 phr loadings. (a) M5; (b) M15; (c) M25; (d) N330 (laser excitation: 633 nm).

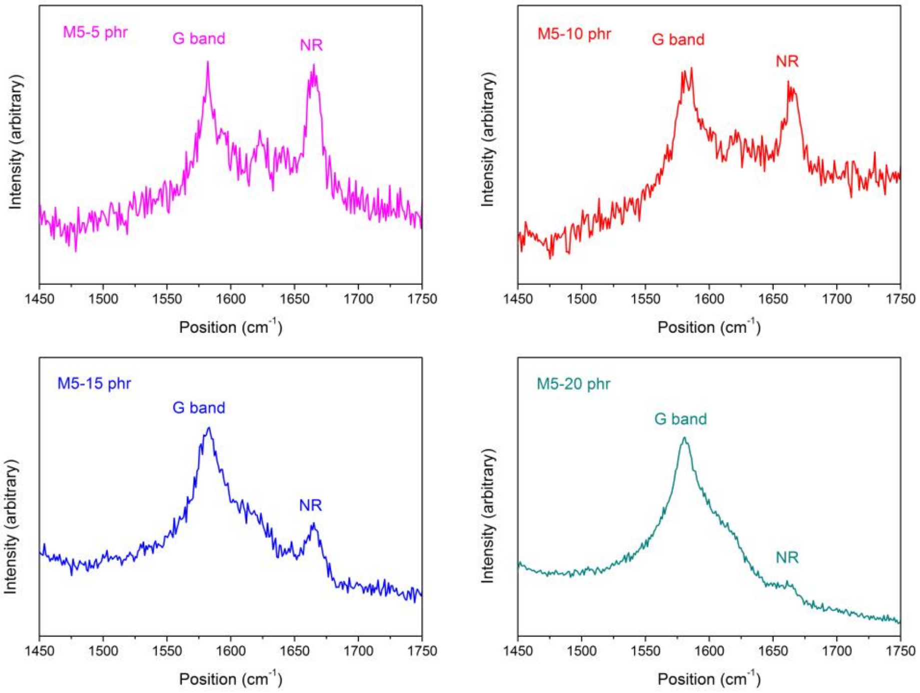

Figure 4.5 Raman spectra of the M5 GNP NR nanocomposites at 5, 10, 15, 20 phr loadings ranging from 1450 to 1750 cm^{-1} (laser excitation: 633 nm).

4.3. Characterisation of the nanocomposites

4.3.1. Thermogravimetric analysis (TGA)

Thermogravimetric analysis was undertaken to the thermal stability of the NR composites determine the actual compositions of the composites since the processing method employed inevitably involves some loss of filler material. The TGA curves of the M5 GNP composites and CB composites can be seen in Figure 4.6 and 4.7 and a small range of the curves is shown in the inset. As can been seen in the TGA curves, with the addition of GNP flakes, the T_{50} (temperature at 50% weight loss, indicated by the dash line in the inset) increases whereas the $T_{\max}$ (temperature of the maximum weight loss, indicated by the gradient dashed line at around 500 ℃) basically remain the same. The other two types of GNPs show the similar behaviours. It is clear that the thermal stability of the natural rubber is enhanced by the addition of the GNPs. The reason may be attributed to the strong interaction (such as π-π bonding) between the GNP flakes and the rubber matrix that delays the degradation of the rubber polymers.

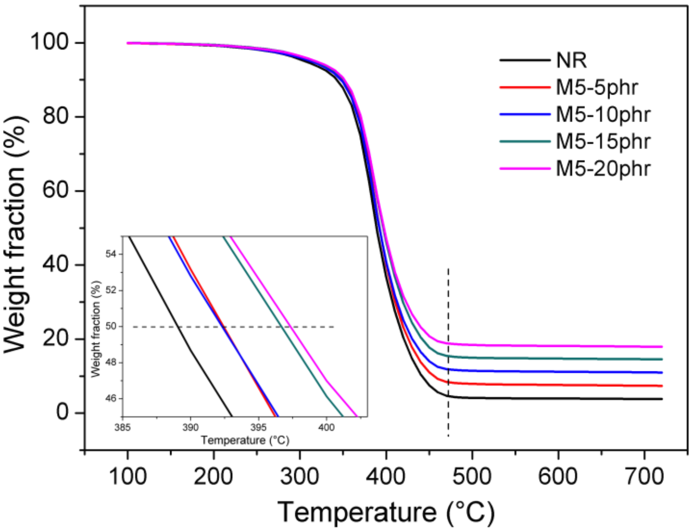

Figure 4.6 TGA curves of the M5 GNP NR composites. Each curve shows the typical one out of three results. (Inset shows the small range to highlight the T_{50})

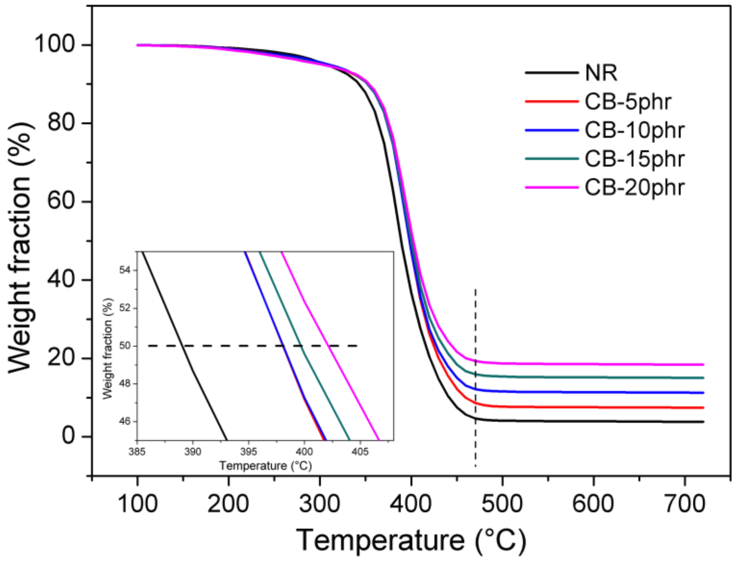

Figure 4.7 TGA curves of the M5 GNP NR composites. Each curve shows the typical one out of three results. (Inset shows the small range to highlight the T_{50})

Similar enhancement of thermal stability is also observed in CB NR composites as shown in Figure 4.7. The improvement by carbon black is even higher than that by the GNP. Specifically, the T_{50} of the CB composites at 20 phr is roughly 5 ℃ higher than that of the GNP composites. This can be explained by the strong interface bonding between the carbon black particles and the rubber matrix and the much poorer heat transfer of the carbon black compared with that of the GNP, which can be seen in detail in Chapter 6.

Apart from the thermal stability, the weight loss from the TGA curves can also be used to determine the actual composition of the composites. Basically, the filler mass fraction is calculated by deducting the residual mass in the pure rubber (contains the mass of the non-degraded rubber and the additives) from the composites residual mass. The mass fractions of the GNP and carbon black in the natural rubber determined from TGA are summarized in Table 4.1. The volume fractions, calculated using the appropriate densities of the rubber, filler and additives are also given in the Table.

Table 4.1 Mass fractions of the GNP and carbon black in the natural rubber determined from thermogravimetric analysis, along with the estimated volume fractions.

Material	Mass fraction (%)	Volume fraction (%)
NR	0	0
M5 5phr	3.55 ±0.35	1.58 ±0.15
M5 10phr	7.10 ±0.41	3.22 ±0.18
M5 15phr	10.64 ±0.35	4.94 ±0.15
M5 20phr	14.19 ±0.06	6.73 ±0.03
M15 5phr	3.18 ±0.19	1.41 ±0.08
M15 10phr	7.34 ±0.32	3.34 ±0.14
M15 15phr	10.76 ±0.17	5.00 ±0.07
M15 20 phr	13.31 ±0.58	6.28 ±0.25
M25 5phr	3.70 ±0.14	1.65 ±0.06
M25 10phr	6.88 ±0.30	3.12 ±0.13
M25 15phr	10.21 ±0.24	4.73 ±0.10
M25 20phr	13.21 ±0.09	6.21 ±0.04
CB 5phr	3.64 ±0.14	1.97 ±0.08
CB 10phr	7.44 ±0.18	4.11 ±0.10
CB 15phr	11.27 ±0.12	6.34 ±0.06
CB 20phr	14.67 ±0.08	8.40 ±0.04

*Density of the materials used for the calculation are, NR[4]: 0.92 g/cm^3, zinc oxide[5]: 5.61g/cm^3, stearic acid[6]: 0.95 g/cm^3, CBS accelerator[7]: 1.325 g/cm^3, sulphur[8]: 1.98 g/cm^3 and GNP[9]: 2.2 g/cm^3; CB[10]: 1.8 g/cm^3.

Assumptions were made for the calculation as follow: (*i*) there was no change of the intrinsic volumes of the materials before and after the processing; (*ii*) there was no loss of the rubber (due to the sticky body) and additives (very small amount and would be efficiently absorbed by the rubber) during the processing; (*iii*) the GNPs were assumed to be fully compressed by the high shear force in the two-roll mill and by the high hydraulic pressure in the hot press (given the slightly excessive amount of the compounds than the designed amount for the moulds). The volume fraction of the fillers can be calculated using the following equation:

$$V_\mathrm{f} = \frac{\frac{m_\mathrm{f}}{\rho_\mathrm{f}}}{\sum \frac{m_i}{\rho_i} + \frac{m_\mathrm{f}}{\rho_\mathrm{f}}} \tag{4.1}$$

where

V_f is the volume fraction of the filler;

m_f is the mass fraction of the filler determined from the TGA data as illustrated above;

ρ_f is the density of the filler;

m_i is each mass fraction of the rubber and the additives determined from "the designed mass fraction (using the formulation in Table 3.1, calculated without the filler loading) × (100% $-$ m_f) on the basis of the assumption (*ii*);

ρ_i represents the densities of the rubber and the additives.

4.3.2. Scanning electron microscopy

The distribution and orientation of the GNP and carbon black in the natural rubber was evaluated firstly using SEM of samples fractured rubber sheets after immersion in liquid nitrogen. Examples of the fracture surfaces for the materials with all loadings of the fillers are given in Figure 4.8 – 4.11. Flakes of the GNP can clearly be seen to be well distributed in the natural rubber matrix and protruding from the surfaces for the M5, M15 and M25 materials whereas the fracture surface for the sample containing the N330 NBR is much smoother and sub-micron-sized clusters of carbon black agglomerates can just about be resolved in the surface features. Preferred alignment of the GNP in the plane of the sheets (horizontal) can also be seen in Figures 4.8 – 4.10.

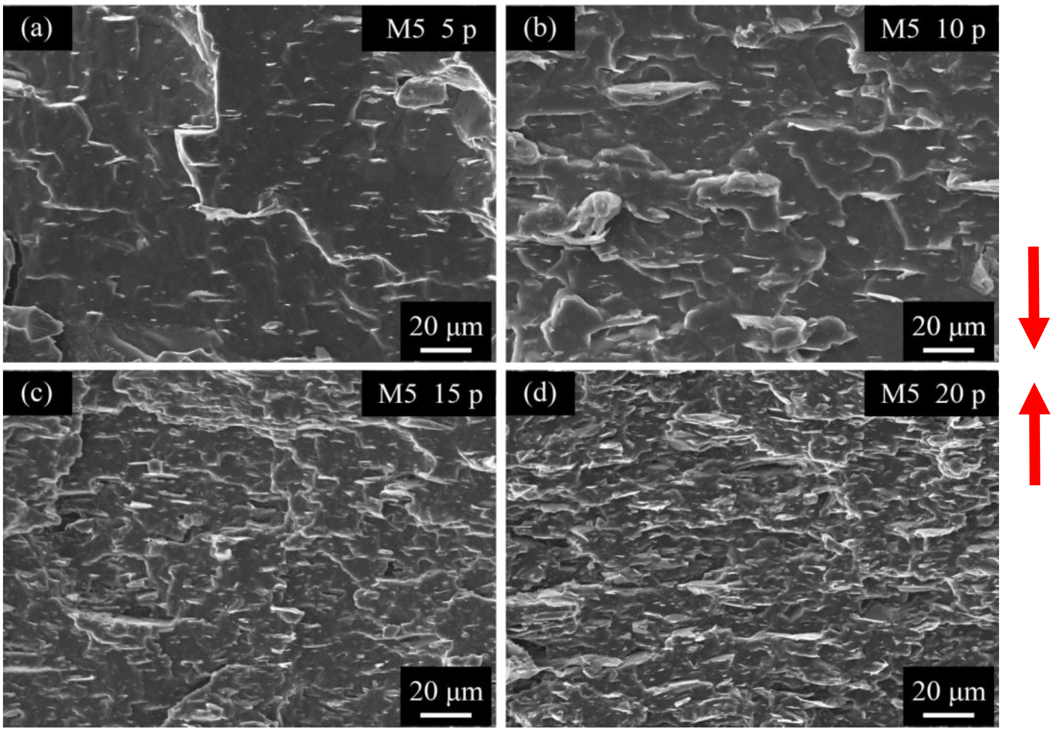

Figure 4.8 SEM micrographs of fracture surfaces of the M5 NR nanocomposites. Specimen thickness: 1mm. The red arrows indicate the hydraulic pressure direction in the hot press.

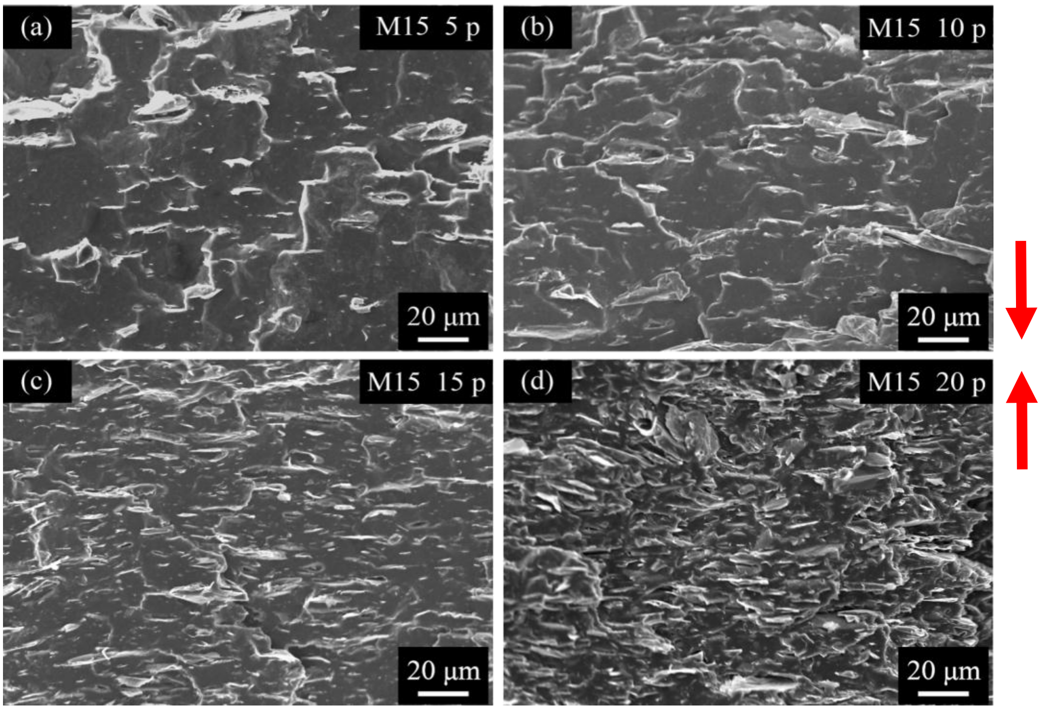

Figure 4.9 SEM micrographs of fracture surfaces of the M15 NR nanocomposites. Specimen thickness: 1mm. The red arrows indicate the hydraulic pressure direction in the hot press.

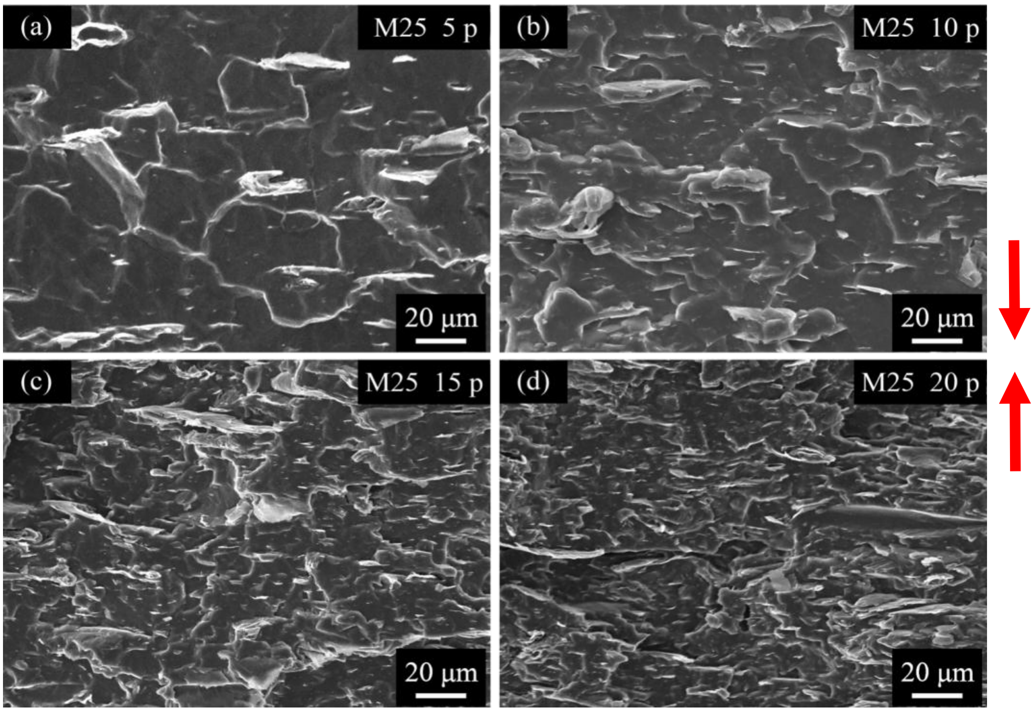

Figure 4.10 SEM micrographs of fracture surfaces of the M25 NR nanocomposites. Specimen thickness: 1mm. The red arrows indicate the hydraulic pressure direction in the hot press.

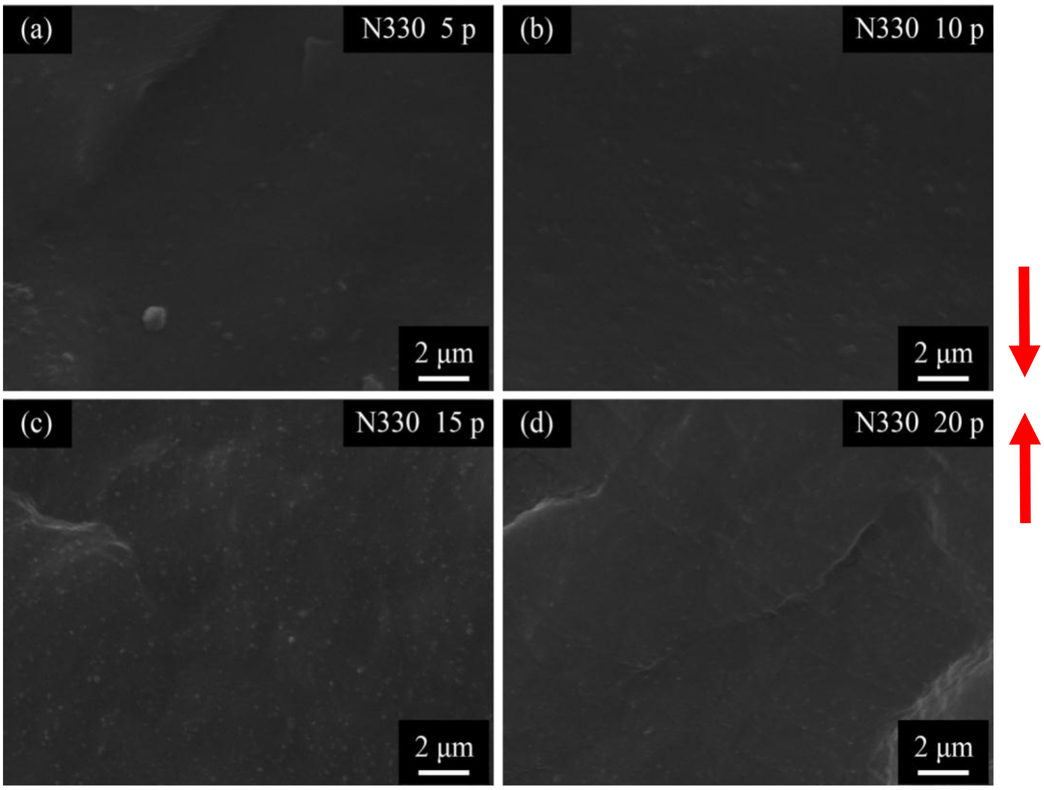

Figure 4.11 SEM micrographs of fracture surfaces of the M25 NR nanocomposites. Specimen thickness: 1mm. The red arrows indicate the hydraulic pressure direction in the hot press.

The individual GNP flakes can be most easily seen in the fracture surfaces of the composites with 5 phr loading, which appear as white straight lines parallel to horizontal direction. The lengths of straight lines, holes and pulled-out flakes are consistent with the lateral sizes of the GNP as given in Figure 4.1. What is more, the 15 phr carbon black NR composite shows the most visible particles, which can be attributed to the high loading of fillers but not high enough to generate aggregation of carbon black in the rubber matrix.

4.3.3. Polarized Raman spectroscopy

Since the fracture surfaces of the GNP nanocomposites showed preferred alignment of the GNP, polarized Raman spectroscopy was employed to quantify the level of orientation of the GNP in the nanocomposites. The results of this analysis are shown in Figure 4.12 – 4.14 where the measurements of the intensity of the G band as a function of orientation rotating each specimen around the *Z* and *X* axes are presented for the natural rubber with 5, 10, 15 and 20 phr of the three different GNP. It can be seen that in each case there is no change intensity (red dots in Figure 4.12 – 4.14) during rotation of the specimen about the *Z* axis (perpendicular to the sheet), implying no preferred orientation of the GNP in the *X* or *Y* directions. In contrast, it can be seen that in each case the intensity of the G band decreases (black dots in Figure 4.12 – 4.14) with increasing angle of rotation when the specimens were rotated about the *X* axis (similar behaviour was found for rotation about the *Y* axis). This implies that the GNP tends to be aligned in-plane within the natural rubber sheets.

It is possible to quantify the level of orientation from the values of $\langle P_2(\cos\theta)\rangle$ and $\langle P_4(\cos\theta)\rangle$[11] fitted to the data in Figure 4.12 – 4.14 and they are also given on the plots. It can be seen that with the highest loadings (GNP basically show up everywhere in the Raman laser spot on the fracture surfaces), $\langle P_2(\cos\theta)\rangle$ and $\langle P_4(\cos\theta)\rangle$ decrease going from M5 to M15 to M25 implying a lower degree of orientation for the highest loadings of the the larger GNP ($\langle P_2(\cos\theta)\rangle$ = 1 for perfect alignment and $\langle P_2(\cos\theta)\rangle$ = 0 for random orientation[12]). The value of $\langle P_2(\cos\theta)\rangle$ was found to be in the range 0.2-0.7 for the all the 12 GNP nanocomposite samples studied (5, 10, 15 and 20 phr of M5, M15 and M25 GNP), showing a general preferred in-plane alignment of the nanoplatelets.

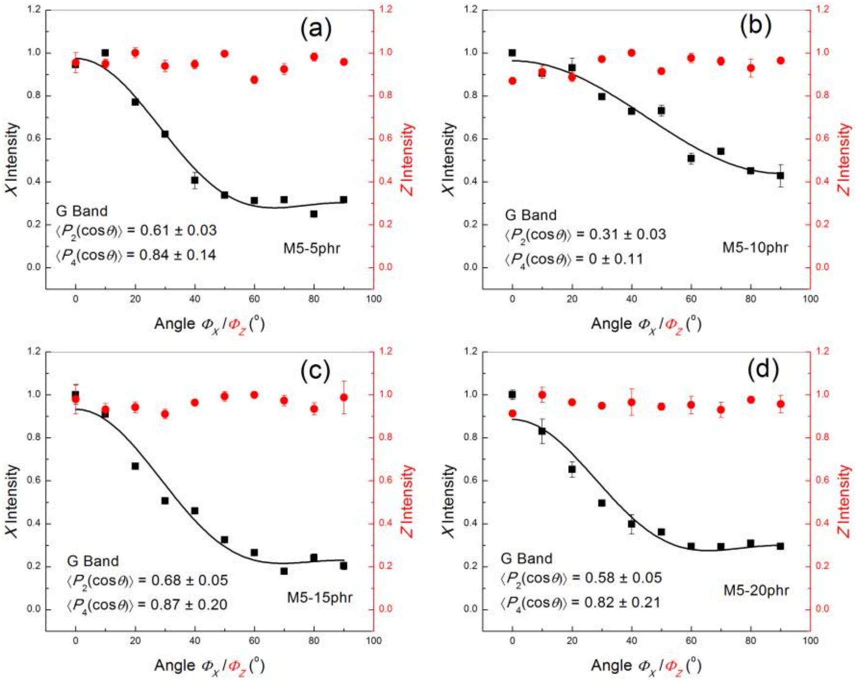

Figure 4.12 Polarized Raman measurements of the intensity of the G band as a function of orientation around the *Z* and *X* axes for the natural rubber with M5 GNP at (a) 5, (b) 10, (c)15 and (d) 20 phr loadings. Each curve set (black and red) are from one sample and each data point is from 3 scanning. Error bars represent the standard errors (laser excitation: 633 nm).

In general, no systematic trend could, however, be found with either the level of loading or particle size. This is most likely due to the fact that the size of the Raman laser spot (~2 μm) is or the same order of magnitude as the lateral size of the GNP. In this case, the laser spot could probably either cover a small number of flakes or a part of each flake, which results in a deviation to the actual situation. Hence, the composites at the highest loading which provide more flakes in the laser sport can be more convincing for quantitative calculation.

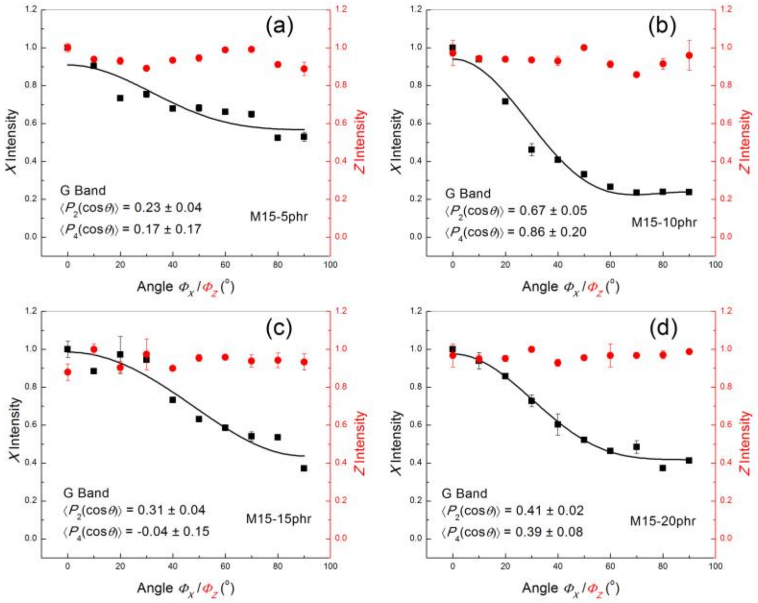

Figure 4.13 Polarized Raman measurements of the intensity of the G band as a function of orientation around the *Z* and *X* axes for NR with M15 GNP at (a) 5, (b) 10, (c)15 and (d) 20 phr loadings. Each curve set (black and red) are from one sample and each data point is from 3 scanning. Error bars represent the standard errors (laser excitation: 633 nm).

The reason to cause the in-plane alignment of the flakes in the rubber matrix can be attributed to the processing in the hot press. No matter how the masticated rubber compounds in any shape were put into the mould (one piece, multiple pieces, flat-like, sphere-like, folded or unfolded), it always shows the similar orientation of flakes. The orientation formation in the hot press can be affected by the viscosity (involved with the intrinsic viscosity of the rubber and the specie of the graphene) of the compound at the curing temperature, the time how long the compound can be in a fluid state and the how much the hydraulic pressure is from the hot press.

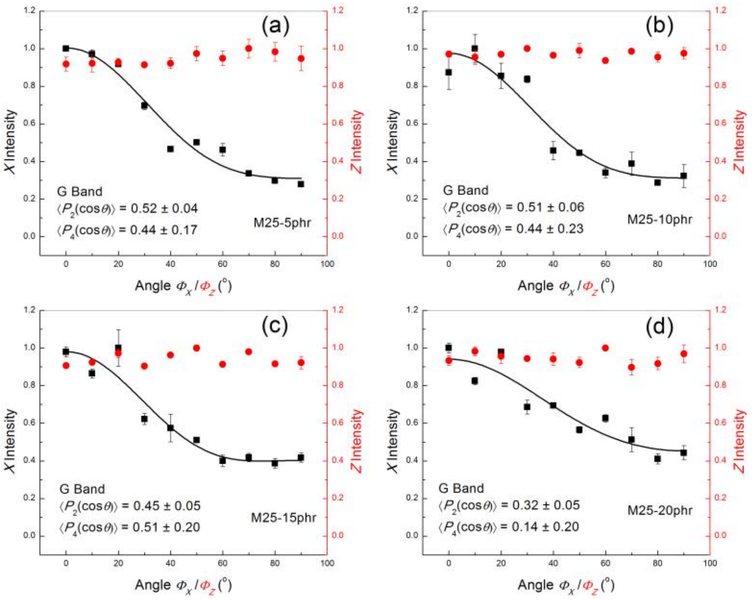

Figure 4.14 Polarized Raman measurements of the intensity of the G band as a function of orientation around the *Z* and *X* axes for NR with M25 GNP at (a) 5, (b) 10, (c)15 and (d) 20 phr loadings. Each curve set (black and red) are from one sample and each data point is from 3 scanning. Error bars represent the standard errors (laser excitation: 633 nm).

4.3.4. X-ray diffraction

The X-ray diffraction patterns of the GNPs and pure natural rubber can be seen Figure 4.15. Three types of GNPs basically exhibit the identical features in the patterns, showing the sharp typical graphitic peak at 26.4 °, which is corresponding to a lattice spacing of 0.334 nm. In contrast, the natural rubber only shows a broad peak at around 19.6 ° with several minor peaks that can be attributed to the additives incorporated during the mixing.

After the fabrication by adding GNPs into the natural rubber matrix, the XRD patterns of the composites show a combination of each component. As can be seen in Figure 4.16-4.18, the XRD patterns of the GNPs NR composites keep both the sharp typical graphitic peak and the short broad rubber peak. The positions of the graphitic peak are slightly shifted to 26.6 °, which can be considered as identical as those of the GNPs.

Apart from that, when the intensity of the graphitic is normalized, the intensity of the broad rubber peak shows an evolution of decrease upon increasing GNP loading. The reason of this evolution is similar to the change of the Raman peak intensity ratio with the GNP loading.

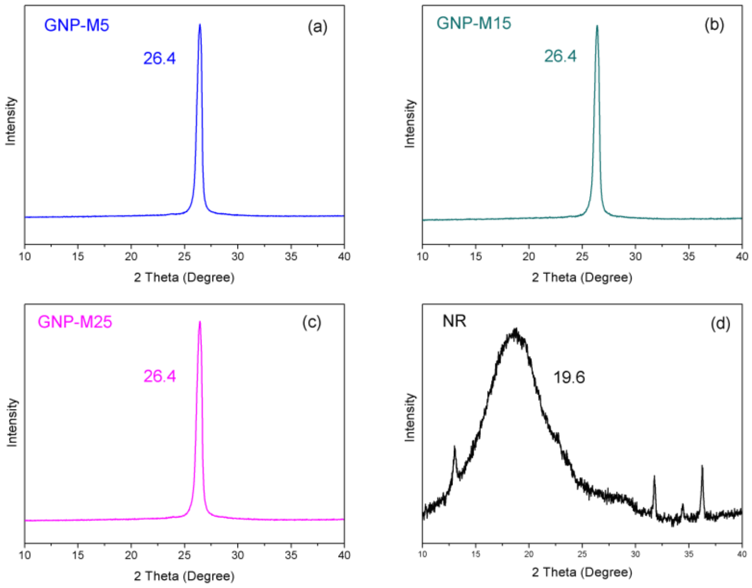

Figure 4.15 XRD patterns of the GNPs. (a) M5; (b) M15; (c) M25; (d) NR.

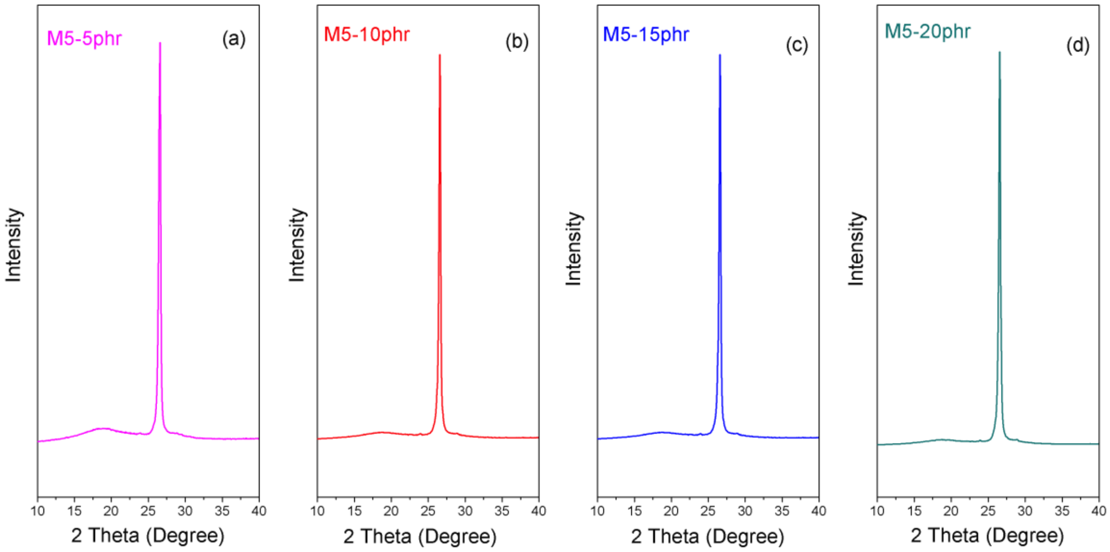

Figure 4.16 XRD patterns of the M5-GNP NR composites at 5 to 20 phr.

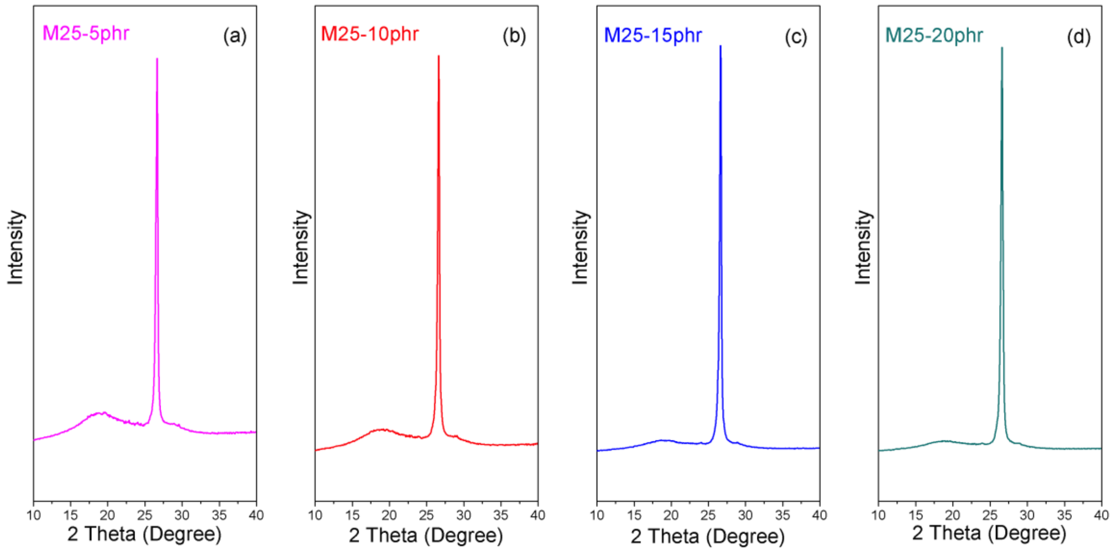

Figure 4.17 XRD patterns of the M15-GNP NR composites at 5 to 20 phr.

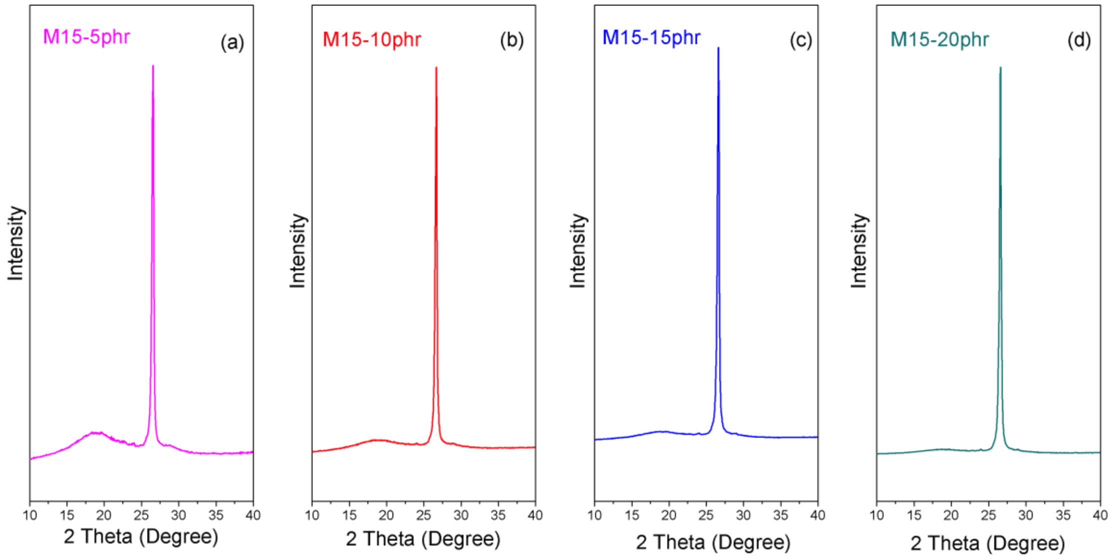

Figure 4.18 XRD patterns of the M25-GNP NR composites at 5 to 20 phr.

4.3.5. X-ray computed tomography scanning

X-ray computer nanotomography was also used to characterise the distribution and orientation of the GNP in the nanocomposites as shown in Figure 4.19 – 4.21. The contrast origins from the difference of the electron density of different phases (since the GNPs and rubber are mainly made of carbon atoms, the atomic number difference should be really small). It can be seen that the GNP are well distributed within the rubber matrix with the same preferential alignment as seen in the SEM micrographs. Moreover the nanotomography technique gives unprecedented detail of the morphology of the GNP showing that many are bent into loops, “U” shape or “S” shape (Figure 4.19), although their overall dimensions are consistent with their nominal size specifications.

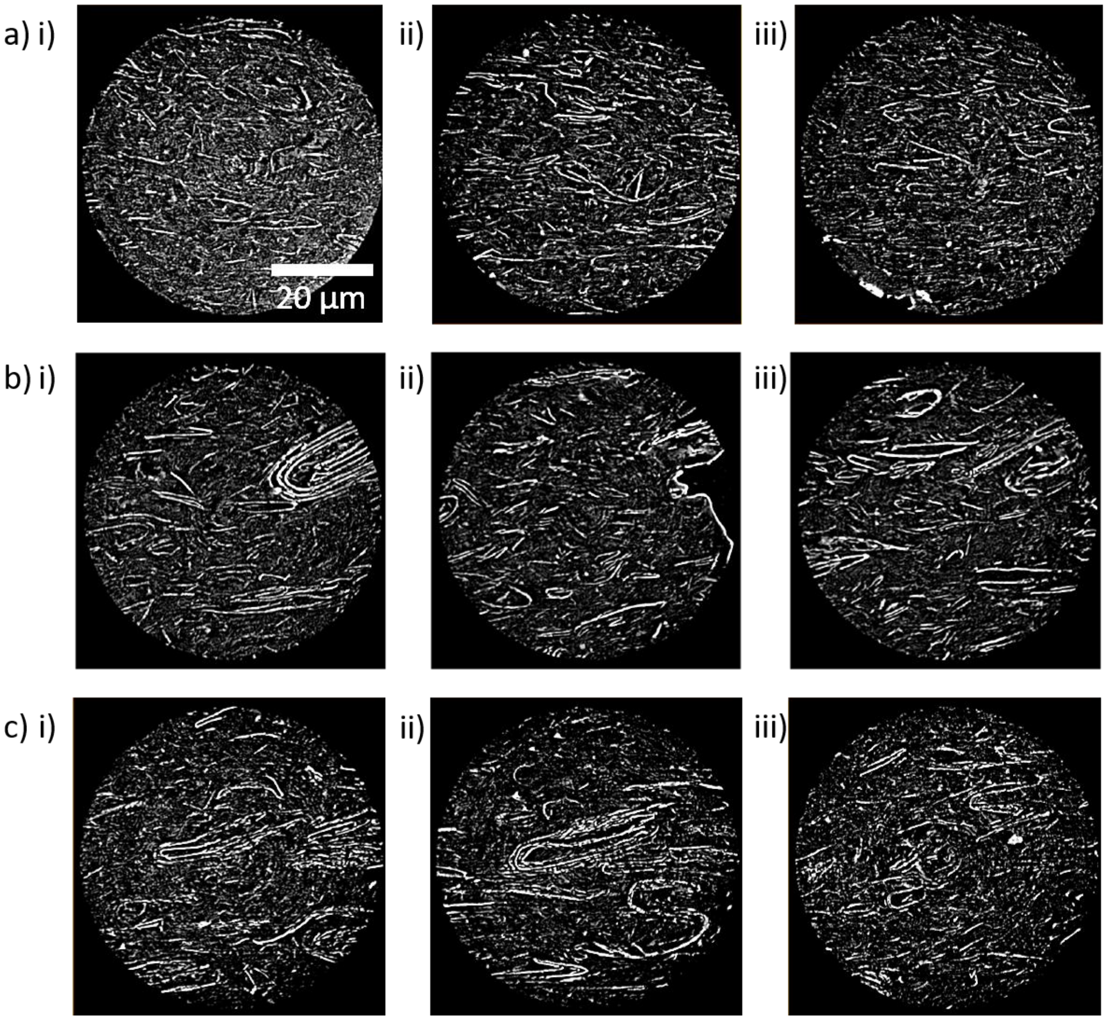

Figure 4.19 CT scans showing details of structure, distribution and orientation of the GNP in the natural rubber nanocomposites at 20 phr loading for (a) M5, (b), M15, (c) M25. (The surface of the sheet is horizontal and the small white spots in the micrographs are from the zinc oxide added to aid the vulcanization of the rubber)

More detail of the distributions of the GNP throughout the samples can be seen in screenshots of the movies (the movies are available in the supplementary material on https://link.springer.com/article/10.1007/s10853-017-1144-0) of the slices through the nanocomposites shown in Figure 4.20. The histogram of the angle of the flakes to the specimen surface is given in Figure 4.21. It can be seen that the majority of the flakes are at angles of less than 30 ° rather than a uniform distribution, implying the high tendency of the flakes to be parallel to the surface of the specimens.

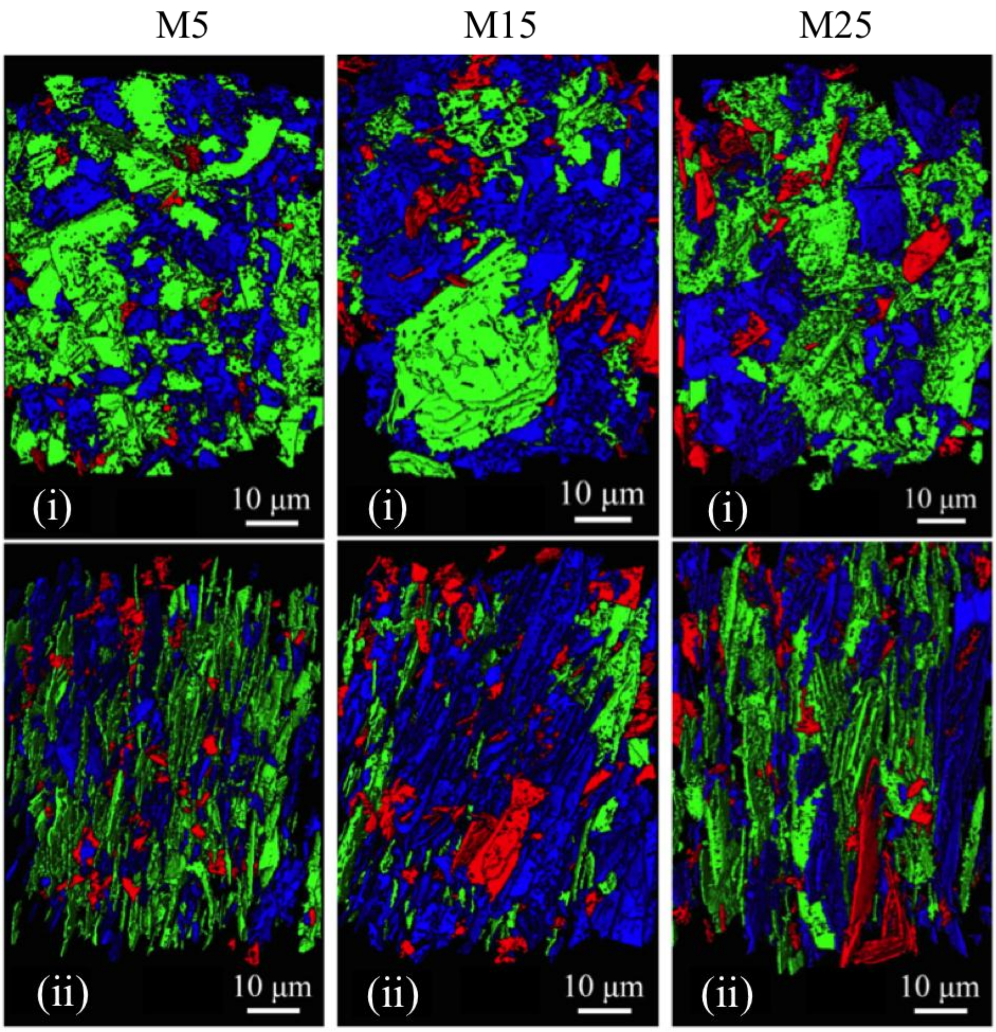

Figure 4.20 Artificially-coloured images of the individual GNP flakes from the CT scans. Images were taken by screenshot during the rotation of the specimens around X axis (parallel to the vertical direction) at (i) 0 ° and (ii) 90 ° showing the alignment of the GNP flakes.

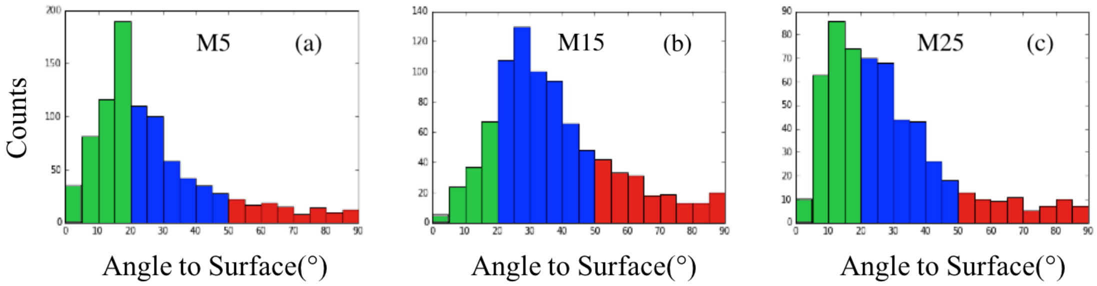

Figure 4.21 Histograms of the distributions of the angle of the individual flake to the surface of the GNP /NR nanocomposite sheets for (a) M5, (b), M15, (c) M25.

Apart from the orientation, the distribution of the surface area of the GNPs in the NR nanocomposites can be obtained by tomography as shown in Figure 4.22. It can be seen that there is a big portion of small flakes in all the types of GNPs whereas extremely large flakes only show up in M15 (~ 2500 μm^2) and M25 (~3500 μm^2) composites. It can be seen in Figure 4.19 that larger flakes give a higher possibility to distort or fold in the matrix, which may result in deficiency of the reinforcement in the preferred alignment direction.

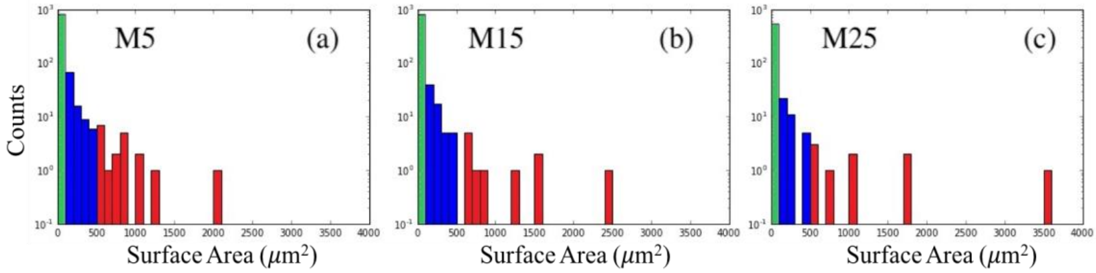

Figure 4.22 Histograms of the distribution of the surface area of the individual flake in the GNP/NR nanocomposites sheets for (a) M5, (b), M15, (c) M25.

4.4. Mechanical properties

4.4.1. Stress-strain behavior

Stress strain curves for all the materials studied are given in Figure 4.23. Five stress-strain curves were obtained for each loading level for each type of filler, and representative ones are presented.

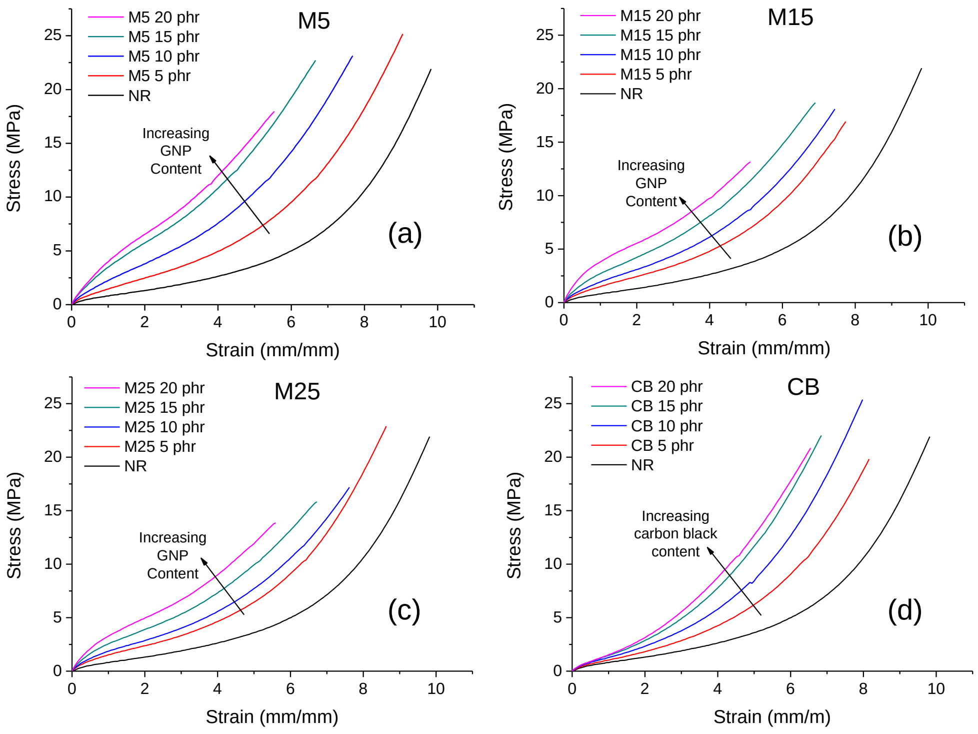

Figure 4.23 Stress-strain curves for the natural rubber containing 5, 10, 15 and 20 phr of (a) M5, (b), M15, (c) M25 and (d) N330 carbon black. Each curve is the typical one out of 5 results. Specimen thickness: 2 mm.

Overall the addition of the GNP and carbon black can be seen to increase the stiffness of the materials significantly. Natural rubber has a relatively high inherent strength because of its tendency to strain crystallise and none of the fillers appear to increase its strength. The strength of the natural rubber appears to be maintained for the M5 and CB fillers but decreases somewhat in the case of the addition of the larger M15 and M25 GNP. In all cases the strain at failure appears to be reduced by the addition of the different types of filler.

4.4.2. Modulus values

The effect of the addition of the different fillers upon the stiffness of the rubber is shown in detail in Figure 4.24. Although there does not appear to be large difference in the overall stress-strain curves between the GNP and CB fillers in Figure 4.23, Figure 4.24a shows that for the 20 phr loading the shapes of the stress-strain curves are quite different at low strain (<300%). The addition of the GNP leads to a significantly higher initial slope for the stress-strain curve than for the rubber reinforced with carbon black, so that the modulus at 100% strain is more than twice that of the carbon black loaded material. Similar behaviour was found for the other levels of filler loading.

The tensile moduli at 100% and 200% strain are plotted as a function of the volume fraction of fillers (Table 4.1) in Figures 4.24b and 4.24c respectively. Since the modulus appears linearly increasing upon the loading of the fillers, the significance analysis is conducted by comparing the slopes obtained from the linearly fitted data and the values are tabulated in Table 4.2. In Figure 4.24b and 4.24c as well as in Table 4.2, the higher levels of reinforcement achieved with the addition of the GNP compared with that obtained for the CB at a given volume fraction can be clearly seen. There also seems to be a slightly better reinforcement of the rubber for the M5 GNP compared with the M15 or M25 fillers, which can be more straightforwardly seen in Table 4.2. Another way of looking at the data in Figures 4.24b and 4.24c is in terms of the volume fraction of filler needed for a particular level of modulus. It can be seen that for a particular modulus value, up to six times the volume fraction of carbon black is needed to match that of natural rubber reinforced with the GNP materials.

Finally, the Shore hardness of sheets of the natural rubber and all materials with different filler loadings was determined as shown in Figure 4.24d. The significance analysis follows the same procedure for the modulus as tabulated in Table 4.2. It can be seen that the measured values of Shore hardness of GNPs composites exhibit nearly doubly increasing rates compared with the rubber filled with CB. However, in terms of the composites filled with the three types of GNPs, difference can be seldom concluded. This can be explained by the testing direction that was vertical to the preferred alignment plane of the flakes. In that case, the GNPs were subject to an out-of-plane indentation rather than an in-plane stretching, which weakens the difference of the reinforcement effect influenced by the aspect ratio difference.

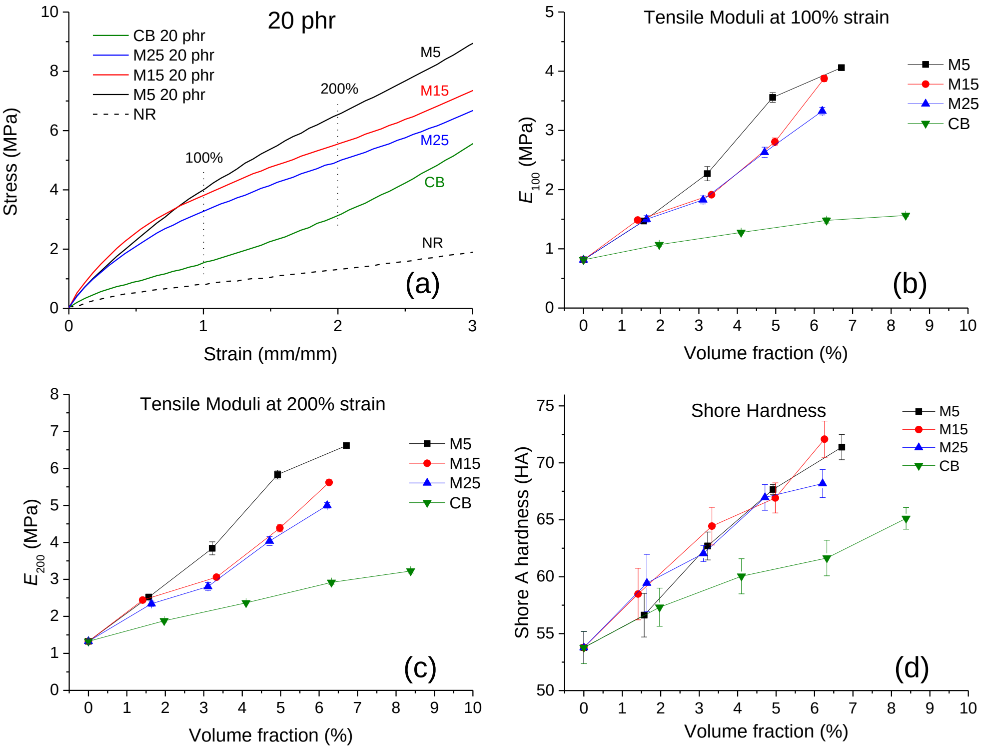

Figure.4.24 Mechanical properties of the nanocomposites. (a) Comparison of the stress-strain curves for the different nanofillers at 20 phr loading. (b) Tensile modulus at 100% strain as a function of filler volume fraction. (c) Tensile modulus at 200% strain as a function of filler volume fraction. (d) Shore A hardness as a function of filler volume fraction(5 specimens for each point). Error bars represent the standard deviation. Specimen thickness: 2 mm for tensile tests and 6 mm for hardness tests.

Table 4.2 Slope of the linear fitting of the curves in Figure 4.24b, c and d. (units: 10^{-2} MPa/vol% fillers for E_{100} and E_{200}; 10^{-2} HA/vol% fillers for hardness)

Sample	E_{100}	E_{200}	Hardness
NR-M5	49.2 ±0.7	79.4 ±0.9	277 ±23
NR-M15	41.9 ±0.7	63.6 ±1.2	279 ±30
NR-M25	38.2 ±0.9	56.5 ±1.4	234 ±27
NR-CB	8.5 ±0.3	23.0 ±0.8	130 ±18

4.4.3. Ultimate properties

It was pointed out earlier that since natural rubber crystallizes under stress, it is relatively strong. Figure 4.25a shows that the strength is unaffected by the addition of the carbon black but tends to decrease slightly on the addition of the GNP, with the largest particles giving rise to the highest level of strength reduction. Figure 4.25b show the effect of the addition of GNP and CB upon the ultimate failure strain of the natural rubber. It decreases with filler loading, with all three GNP materials showing the same behaviour. In contrast, the addition of carbon black causes rather less reduction in failure strain, particularly for the higher volume fractions. This is probably due to the fillers hindering the straightening and stress-induced crystallization of the NR polymer chains. Figure 4.26 exhibit the change of the tear strength of the rubber incorporated with GNP and CB. With small loadings of M5 GNP and CB, the tear strength shows an improvement and tends to flatten at higher loadings. On the other hand, the M15 and M25 GNP impart no enhancement to the tear strength of the rubber at all loadings, which is different with the clear improvement reported by most of the literature.[13-20]

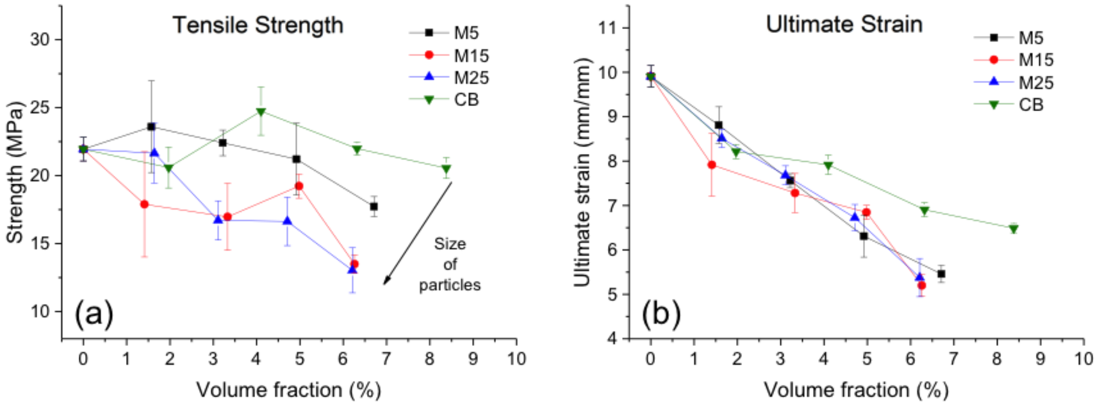

Figure 4.25 Mechanical properties of the nanocomposite as a function of filler volume fraction. (a) Tensile strength and (b) ultimate strain. Error bars represent the standard deviation.

The effect of the different nano-fillers upon the ultimate properties of the natural rubber appears to be related to the size of the particles. This implies that the particles act as defects in nucleating cracks. Hence, the largest GNP particles, M15 and M25 cause the highest decrease in tensile strength with increasing volume fraction (Figure 4.25a), whereas the tensile strength appears to be maintained upon the addition of the carbon black.

Analogously, smaller particles lead to higher tear strength. Since the bonding at the interfaces between the GNP flakes and the rubber matrix behaves as physical crosslinking, the blunt effect of GNP flakes on the crack tip initiation and the crack propagation that perform in tensile facture and tearing respectively can be involved with the degree of the physical crosslinking, which can be seen in detail in Chapter 6.

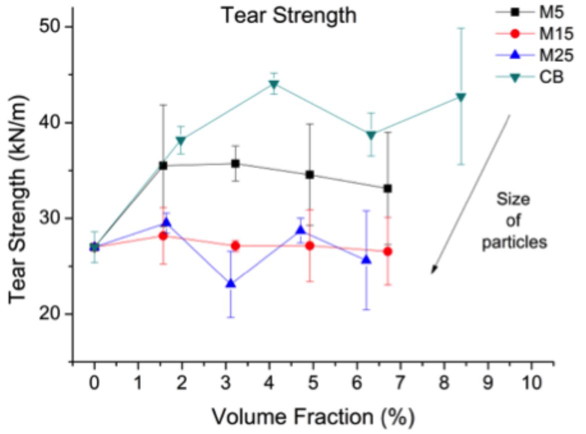

Figure 4.26 Tear strength of the nanocomposite as a function of filler volume fraction (5 specimens for each point). Error bars represent the standard deviation. Specimen thickness: 2 mm.

Overall, the parameters of the mechanical properties of the GNPs NR composites can be tabulated in Table 4.3 as below.

Table 4.3 Parameters of the mechanical properties

	E_{100}	E_{200}	σ_u	ε_u	H	σ_t
	(MPa)	(MPa)	(MPa)	(mm/mm)	(HA)	(MPa)
NR	0.81 ±0.02	1.33 ±0.05	22.0 ±0.9	9.90 ±0.24	53.8 ±1.4	27.0 ±1.6
M5-5phr	1.47 ±0.05	2.52 ±0.08	23.6 ±3.4	8.81 ±0.41	56.6 ±1.9	35.5 ±6.3
M5-10phr	2.27 ±0.12	3.83 ±0.18	22.4 ±0.9	7.56 ±0.16	62.7 ±1.2	35.7 ±1.8
M5-15phr	3.56 ±0.08	5.83 ±0.12	21.2 ±2.6	6.31 ±0.47	67.7 ±0.4	34.6 ±5.3
M5-20phr	4.06 ±0.04	6.62 ±0.04	17.7 ±0.7	5.46 ±0.19	71.4 ±1.1	33.1 ±5.9
M15-5phr	1.49 ±0.02	2.44 ±0.04	17.9 ±3.9	7.92 ±0.70	58.5 ±2.3	28.2 ±2.9
M15-10phr	1.91 ±0.03	3.06 ±0.06	17.0 ±2.5	7.28 ±0.44	64.4 ±1.7	27.1 ±0.6
M15-15phr	2.81 ±0.07	4.39 ±0.10	19.2 ±0.9	6.85 ±0.16	66.9 ±1.3	27.1 ±3.8
M15-20phr	3.88 ±0.06	5.62 ±0.07	13.5 ±0.7	5.20 ±0.25	72.1 ±1.6	27.0 ±1.6
M25-5phr	1.50 ±0.06	2.34 ±0.07	21.7 ±2.2	8.52 ±0.21	59.4 ±2.5	30.0 ±1.0
M25-10phr	1.83 ±0.07	2.81 ±0.10	16.7 ±1.4	7.68 ±0.21	62.0 ±0.7	23.1 ±3.5
M25-15phr	2.63 ±0.09	4.04 ±0.12	16.6 ±1.8	6.73 ±0.30	67.0 ±1.1	28.7 ±1.3
M25-20phr	3.33 ±0.06	5.00 ±0.08	13.0 ±1.7	5.38 ±0.43	68.2 ±1.2	25.6 ±5.2
CB-5phr	1.07 ±0.03	1.88 ±0.03	20.6 ±1.5	8.21 ±0.16	57.3 ±1.7	38.2 ±1.4
CB-10phr	1.28 ±0.02	2.37 ±0.01	24.7 ±1.8	7.92 ±0.21	60.0 ±1.5	44.1 ±1.1
CB-15phr	1.48 ±0.05	2.92 ±0.06	22.0 ±0.5	6.90 ±0.16	61.6 ±1.6	38.8 ±2.2
CB-20phr	1.56 ±0.02	3.23 ±0.06	20.6 ±0.8	6.49 ±0.10	65.1 ±1.0	42.7 ±7.1

* E_{100}, E_{200}, σ_u, ε_u, H and σ_t are the Young's modulus at 100% strain, Young's modulus at 200% strain, tensile strength, ultimate strain, Shore A hardness and tear strength, respectively.

4.4.4. Stress-induced Raman band shifts

Shifts in the position of the 2D Raman band with strain were determined for the NR filled with the three different GNP materials, as shown in Figure 4.27. This was a particularly difficult experiment to undertake as the 2D band is rather ill-defined in the spectrum as a result of fluorescence from the NR matrix, as found in Figure 4.4a-c, and the shifts were relatively small. Hence only the materials with the highest loading of 20 phr of GNP were employed as they had the strongest 2D band. Additionally, as the result of the small band shifts and scatter in the data, the experiments were undertaken upon at least 16 different specimens for each composition and the data points in Figure 4.27 represent the mean values for all the specimens used for each type of GNP.

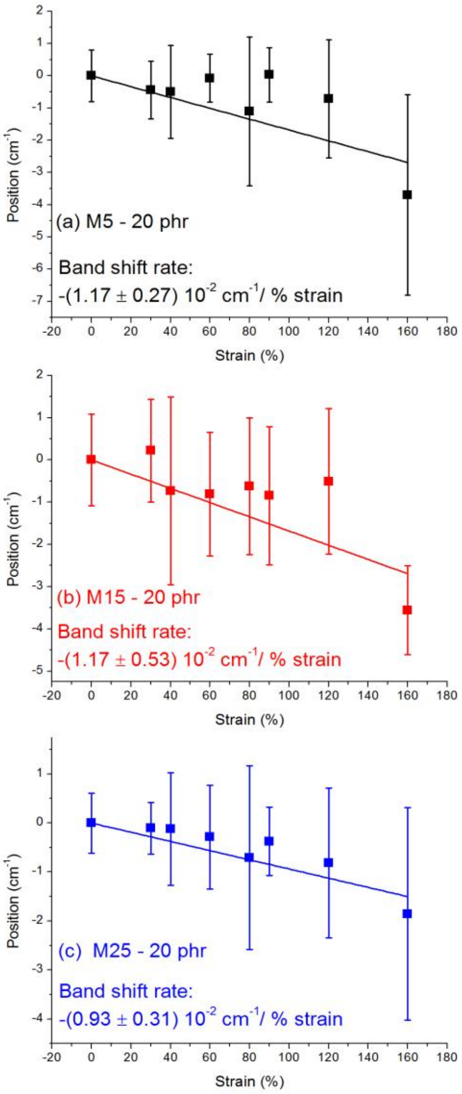

Figure 4.27 Shift of the 2D Raman band with strain for the nanocomposites with 20 phr of (a) M5, (b) M15 and (c) M25 (laser excitation: 633 nm). Each data point represents the average of 10 repeated scanning of 16 specimens at one particular strain. Error bars represent the standard deviation. Specimen thickness: 2 mm.

Although there is considerable scatter in the data in Figure 4.27 and relatively larger error bars than the energy error of the instrument (±1 cm^{-1}), but the data of each figure were obtained from numerous data points and it appears that there is a small but significant downshift in the position of the 2D band with tensile strain. For each type of filler, the data were linearly fitted that all show a band shift rate in an order of magnitude of 10^{-2} cm^{-1}/% strain. These band shift rates will be further discussed in Chapter 7.

4.5. Conclusion

From the SEM images and 3D restructuring by the CT scanning, the good dispersion of GNPs can be observed. The orientation of the flakes was determined to be in-plane alignment by the SEM images and CT scanning and was quantified by polarized Raman spectroscopy. The addition of GNPs was found to suppress the fluorescence background of the Raman spectrum of the natural rubber. The addition of the fillers was confirmed to enhance the thermal stability. The GNPs imparted a higher reinforcement to the natural rubber compared with the carbon black. The stiffness enhancement by the addition of GNPs has shown a size-dependent effect (M5 > M15 > M25), and this will be discussed further in Chapter 7. Small stress transfer between the GNPs and the rubber was detected by the deformation experiment under Raman spectroscopy.

References

1. Hendra, P. J.; Jackson, K. D. O., Applications of Raman spectroscopy to the analysis of natural rubber. *Spectrochim. Acta A* **1994,** *50*, 1987-1997.

2. Xie, L.; Ling, X.; Fang, Y.; Zhang, J.; Liu, Z., Graphene as a substrate to suppress fluorescence in resonance Raman spectroscopy. *J. Am. Chem. Soc.* **2009,** *131*, 9890-9891.

3. Pakjamsai, S.; Suwanprateeb, J., Using FT-Raman spectroscopy for quantitative determination of high filler content in particulated composites. *J. Appl. Polym. Sci.*

2000, *78*, 1947-1954.

4. Tunnicliffe, L. B.; Thomas, A. G.; Busfield, J. J. C., The free retraction of natural rubber: A momentum-based model. *Polym. Test.* **2015,** *47*, 36-41.

5. Derenzo, S. E.; Weber, M. J.; Klintenberg, M. K., Temperature dependence of the fast, near-band-edge scintillation from CuI, HgI2, PbI2, ZnO:Ga and CdS:In. *Nucl. Instr. Meth. Phys. Res. A* **2002,** *486*, 214-219.

6. Lodha, P.; Netravali, A. N., Characterization of stearic acid modified soy protein isolate resin and ramie fiber reinforced 'green' composites. *Compos. Sci. Technol.* **2005,** *65*, 1211-1225.

7. Janković, B.; Marinović-Cincović, M.; Jovanović, V.; Samaržija-Jovanović, S.; Marković, G., The comparative kinetic analysis of non-isothermal degradation process of acrylonitrile–butadiene/ethylene–propylene–diene rubber blends reinforced with carbon black/silica fillers. Part II. *Thermochim. Acta* **2012,** *543*, 304-312.

8. Dorfler, S.; Hagen, M.; Althues, H.; Tubke, J.; Kaskel, S.; Hoffmann, M. J., High capacity vertical aligned carbon nanotube/sulfur composite cathodes for lithium-sulfur batteries. *Chem. Commun.* **2012,** *48*, 4097-9.

9. Centeno, A.; Rocha, V. G.; Alonso, B.; Fernández, A.; Gutierrez-Gonzalez, C. F.; Torrecillas, R.; Zurutuza, A., Graphene for tough and electroconductive alumina ceramics. *J. Eur. Ceram. Soc.* **2013,** *33*, 3201-3210.

10. Tunnicliffe, L. B.; Kadlcak, J.; Morris, M. D.; Shi, Y.; Thomas, A. G.; Busfield, J. J. C., Flocculation and Viscoelastic Behaviour in Carbon Black-Filled Natural Rubber. *Macromol. Mater. Eng.* **2014,** *299*, 1474-1483.

11. Li, Z.; Young, R. J.; Kinloch, I. A.; Wilson, N. R.; Marsden, A. J.; Raju, A. P. A., Quantitative determination of the spatial orientation of graphene by polarized Raman spectroscopy. *Carbon* **2015,** *88*, 215-224.

12. Li, Z.; Young, R. J.; Wilson, N. R.; Kinloch, I. A.; Vallés, C.; Li, Z., Effect of the orientation of graphene-based nanoplatelets upon the Young's modulus of nanocomposites. *Compos. Sci. Technol.* **2016,** *123*, 125-133.

13. Araby, S.; Meng, Q.; Zhang, L.; Kang, H.; Majewski, P.; Tang, Y.; Ma, J., Electrically and thermally conductive elastomer/graphene nanocomposites by solution mixing. *Polymer* **2014,** *55*, 201-210.

14. Lin, Y.; Chen, Y.; Zeng, Z.; Zhu, J.; Wei, Y.; Li, F.; Liu, L., Effect of ZnO nanoparticles doped graphene on static and dynamic mechanical properties of natural rubber composites. *Compos. Part A - Appl. S.* **2015,** *70*, 35-44.

15. Liu, X.; Kuang, W.; Guo, B., Preparation of rubber/graphene oxide composites with in-situ interfacial design. *Polymer* **2015,** *56*, 553-562.

16. Kang, H.; Zuo, K.; Wang, Z.; Zhang, L.; Liu, L.; Guo, B., Using a green method to develop graphene oxide/elastomers nanocomposites with combination of high barrier and mechanical performance. *Compos. Sci. Technol.* **2014,** *92*, 1-8.

17. Zhan, Y.; Wu, J.; Xia, H.; Yan, N.; Fei, G.; Yuan, G., Dispersion and exfoliation of graphene in rubber by an ultrasonically-assisted katex mixing and in situ reduction process. *Macromol. Mater. Eng.* **2011,** *296*, 590-602.

18. Zhang, X.; Wang, J.; Jia, H.; You, S.; Xiong, X.; Ding, L.; Xu, Z., Multifunctional nanocomposites between natural rubber and polyvinyl pyrrolidone modified graphene. *Compos. Part B - Eng.* **2016,** *84*, 121-129.

19. Al-Ghamdi, A. A.; Al-Ghamdi, A. A.; Al-Turki, Y.; Yakuphanoglu, F.; El-Tantawy, F., Electromagnetic shielding properties of graphene/acrylonitrile butadiene rubber nanocomposites for portable and flexible electronic devices. *Composites Part B: Engineering* **2016,** *88*, 212-219.

20. Dong, B.; Liu, C.; Zhang, L.; Wu, Y., Preparation, fracture, and fatigue of exfoliated graphene oxide/natural rubber composites. *RSC Adv.* **2015,** *5*, 17140-17148.

5. NBR GNP composites characterization and mechanical properties

5.1. Introduction

Unlike NR composites, the fillers used in NBR composites were selected to be only M15 GNP and N330 carbon black. The reason is that the comparison of the GNPs of different dimensions has been basically accomplished among M5, M15 and M25 in NR, and M15 and N330 carbon black were chosen to be the fixed fillers for the comparison of the different matrices (NR and NBR). The two different rubber systems almost went through the same characterization and tests except that NBR composites were not X-ray CT-scanned. They show certain similarity in morphology but some appreciable distinction in mechanical properties.

5.2. Characterisation of the GNP and carbon black

5.2.1. Scanning electron microscopy (SEM)

Scanning electron micrographs of the M15 GNP and of the N330 carbon black can be seen in Figure 4.1b and d. It can be seen that the image of the free-standing M15 GNP shows an agglomerate of thin films in a state of random curliness, the lateral size of which are basically consistent with the given average value (15 μm). The morphology of the N330 is however, quite different consisting of clusters of nano-sized particles of the order of 30-35 nm in diameter, near to the resolution limit of the scanning electron microscope. The fracture surface of pure NBR in Figure 5.1a shows the radiated crack lines and where the crack initiated (from the radial center where there are no crack lines) at low magnification. At high magnification in Figure 5.1b, the fracture exhibits a smooth surface with vein-like crack lines on it, which is regarded as the baseline to compare with the fractured surfaces of composites.

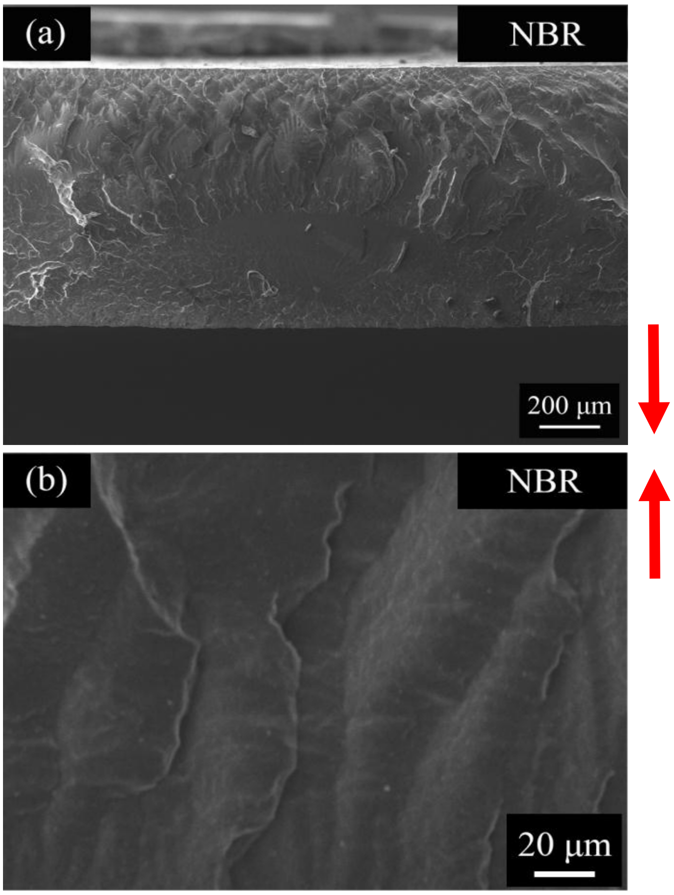

Figure 5.1 SEM micrographs of the matrix at (a) low and (b) high magnification. Specimen thickness: 1mm. The red arrows indicate the hydraulic pressure direction in the hot press.

5.2.2. Raman spectroscopy

Raman spectra of the M15 GNP, carbon black and nitrile butadiene rubber are presented in Figure 5.2. It can be seen that the M15 GNP shows a weak D band and a sharp G and well-defined 2D bands indicative of a graphitic structure. By comparison, the N330 carbon black has two very broad and overlapping D and G bands and no 2D band, consistent with a highly-disordered amorphous carbon structure. No well-defined Raman spectrum can be obtained from the nitrile butadiene rubber and it shows only a very broad peak resulting from background fluorescence.

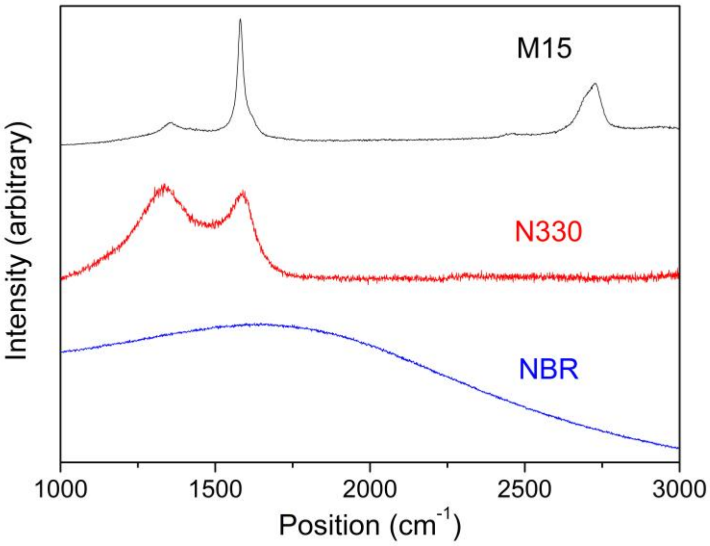

Figure 5.2 Raman spectra of the starting materials (laser excitation: 633 nm).

Raman spectra for the NBR filled with 5, 10, 15 and 20 phr of the M15 GNP and carbon black are shown in Figure 5.2. It can be seen that the GNP composites appear similar to the spectra for the GNP in Figure 5.2 but the relative intensity of the D band is slightly higher than in the spectra of the GNP before processing, which indicates possible damage and tearing of the flakes caused by the shear force during the mixing. Fluorescent background from the rubber matrix can still be seen in the spectra of composites, but it becomes less significant with increasing loadings of GNPs. No particular changes of the peak shape are found in the carbon black composites to the carbon black in Figure 5.2, and the fluorescence background decreases with more fillers similar to the GNP composites. It seems the fillers (GNPs and carbon black) can suppress the fluorescence background of the rubber, and expose the latent rubber peaks. The exposed NBR peaks can be seen at around 1448, 1676, 2241, 2874 and 2930 cm^{-1} as discussed in Section 2.4.2.1 The mechanism of fluorescence suppression by adding fillers is unknown, but the method was earlier employed by Hendra[1] in 1994 using silica and calcium carbonate (50% by weight) as fillers to make the

Raman peaks of natural rubber sharp. The similar effect was also reported by Xie et al. to suppress the fluorescence background of fluorochrome by using graphene as a substrate.[2]

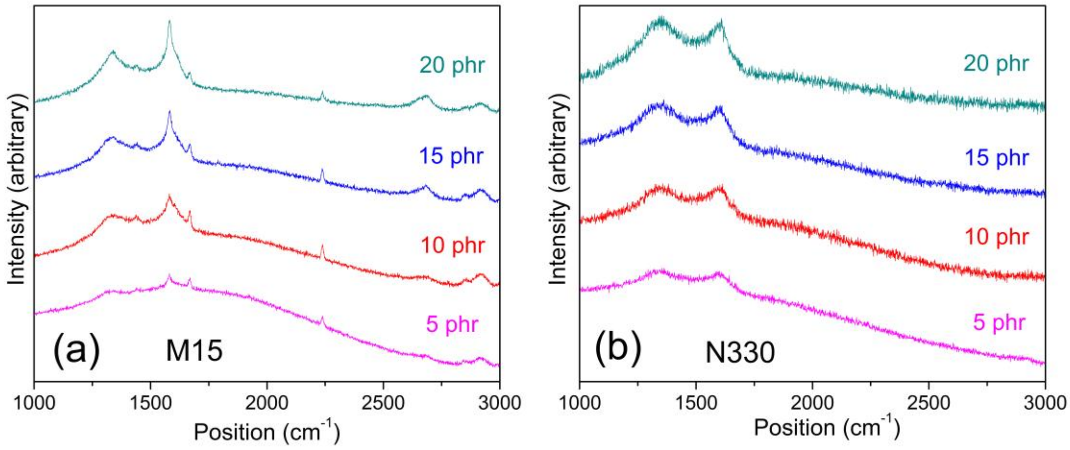

Figure.5.3 Raman spectra of the nanocomposites at 5, 10, 15, 20 phr loadings. (a) M15; (b) N330 (laser excitation: 633 nm).

Once the fluorescence background is reduced, the rubber peaks can emerge to compare with those of the GNP. Over the range of 1450 to 1750 cm^{-1} as presented in Figure 5.4, it can be seen a G band from the M15 GNP and a peak around 1676 cm^{-1} from NBR. The intensity ratio of the G band to the rubber peak is significantly increased from 5 to 20 phr loadings of GNP, which can be seen in the NR composites as discussed in Chapter 4 as well. The reason of the intensity ratio evolution is related to the concentration of the filler-matrix composites. It has been reported by Pakjamsai and Suwanprateeb[3] that in composites, the selected Raman band ratio can be linearly proportional to the volume fraction ratio the filler and the matrix. To be more specific, the scatted intensity of a Raman band is proportional to the intensity of the incident light, the volume of the sample illuminated by the laser beam and collected by the spectrometer, and the concentration of the scattering specie.

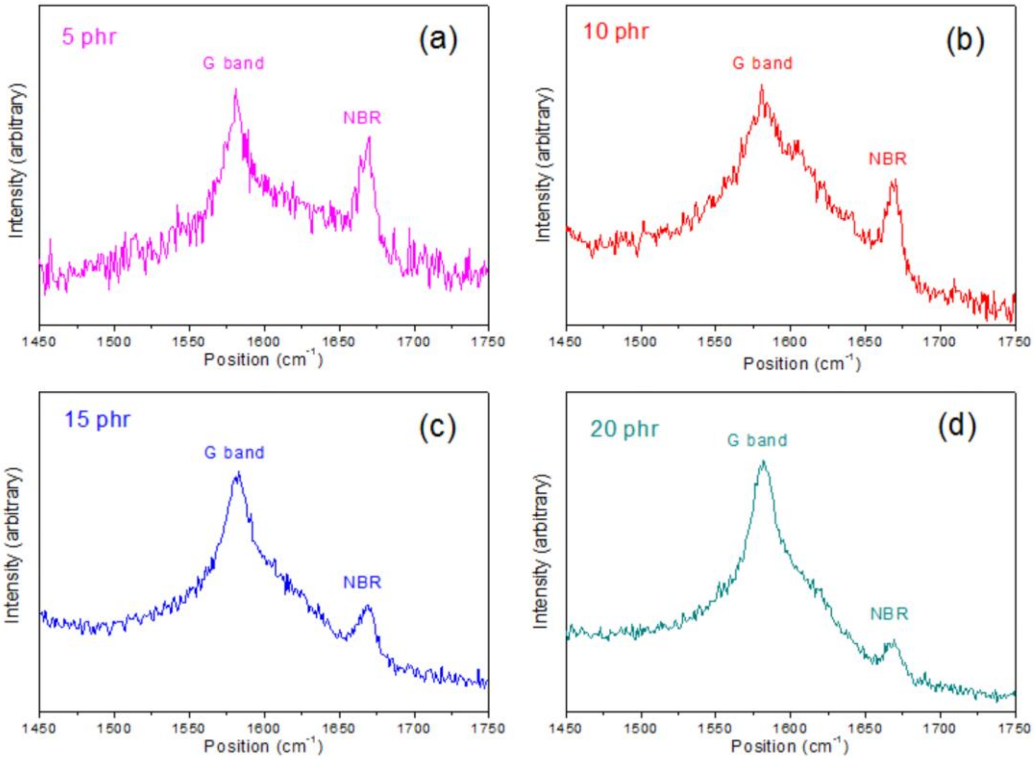

Figure 5.4 Raman spectra of the GNP NBR nanocomposites at 5, 10, 15, 20 phr loadings ranging from 1450 to 1750 cm^{-1} (laser excitation: 633 nm).

5.3. Characterisation of the nanocomposites

5.3.1. Thermogravimetric analysis (TGA)

Thermogravimetric analysis was undertaken to analyze the thermal stability of the NBR composites and determine the actual compositions of the composites since the processing method employed inevitably involves some loss of filler material. The TGA curves of the composites can be seen in Figure 5.5 and 5.6 and a small range of the curves is shown in the inset. As can been seen in the TGA curves, with the addition of graphene flakes, the T_{50} (temperature at 50% weight loss, indicated by the dash line in the inset) increases more and more significantly. What is more, the $T_{\max}$ (temperature of the maximum weight loss, indicated by the gradient dashed line at around 500 ℃) also shows an improvement with the incorporation of graphene flakes. It is clear that the thermal stability of the nitrile butadiene rubber is enhanced by the addition of the GNPs. The reason may be attributed to the strong interaction (π-π bonding) between the GNP flakes and the rubber matrix that delays the degradation of the rubber polymers.

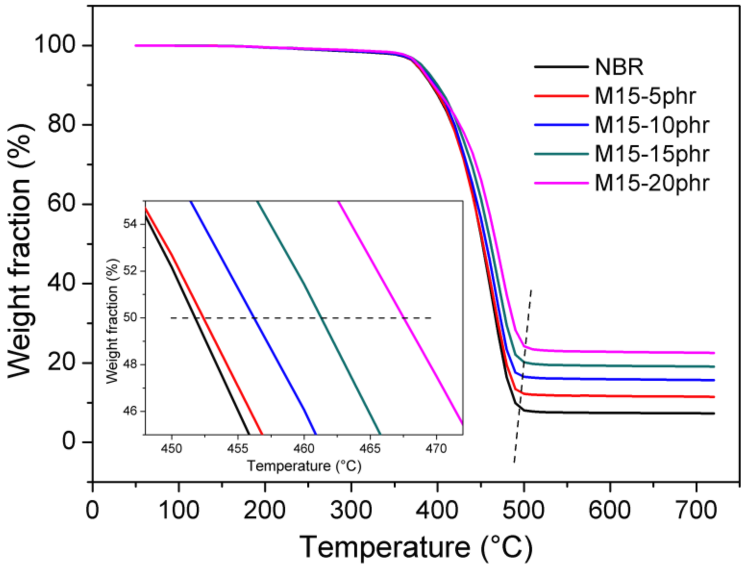

Figure 5.5 TGA curves of the GNP NBR composites. Each curve shows the typical one out of three results. (Inset shows the small range to highlight the T_{50})

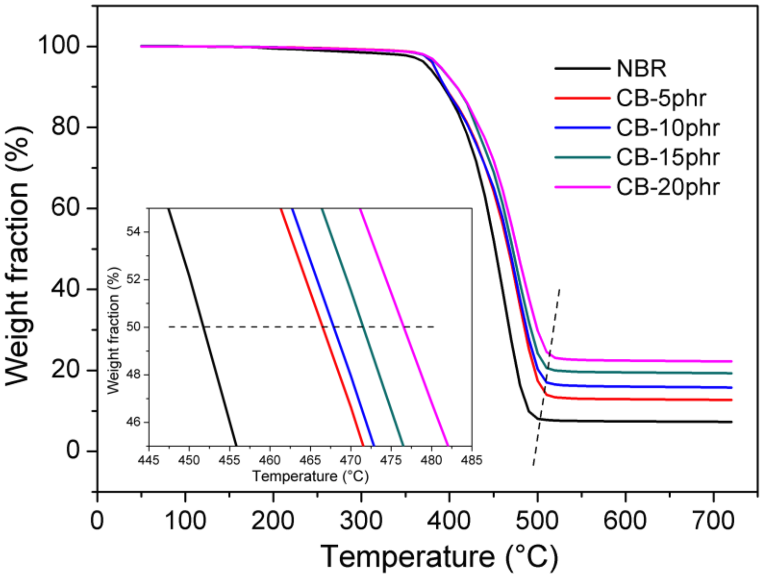

Figure 5.6 TGA curves of the CB NBR composites. Each curve shows the typical one out of three results. (Inset shows the small range to highlight the T_{50})

Similar enhancement of thermal stability is also observed in CB NBR composites as shown in Figure 5.6. The improvement by carbon black is even higher than that by the GNPs. Specifically, the T_{50} of the CB composites at 20 phr is roughly 10 ℃ higher than that of the GNP composites where the $T_{\max}$ of CB composites at 20 phr is slight higher than that of the GNP composites. This can be explained by the strong interface bonding between the carbon black particles and the rubber matrix and the much poorer heat transfer of the carbon black compared with that of the GNP, which can be seen in detail in Chapter 6.

Table 5.1 Mass fractions of the GNP and carbon black in the natural rubber determined from thermogravimetric analysis, along with the estimated volume fractions.

Material	Mass fraction (%)	Volume fraction (%)
NR	0	0
M15 5phr	3.18 ± 0.19	2.00 ± 0.10
M15 10phr	7.34 ± 0.32	4.06 ± 0.09
M15 15phr	10.76 ± 0.17	5.89 ± 0.07
M15 20 phr	13.31 ± 0.58	7.64 ± 0.14
CB 5phr	3.64 ± 0.14	3.10 ± 0.06
CB 10ohr	7.44 ± 0.18	5.07 ± 0.08
CB 15phr	11.27 ± 0.12	7.46 ± 0.21
CB 20phr	14.67 ± 0.08	9.10 ±0.05

*Density of the materials used for the calculation are, NBR[4]: 0.98 g/cm^3, zinc oxide[5]: 5.61 g/cm^3, TMTD[6]: 1.36 g/cm^3, CBS accelerator[6]: 1.29 g/cm^3, sulphur[7]: 2.06 g/cm^3 and GNP[8]: 2.2 g/cm^3; CB[9]: 1.8 g/cm^3.

Apart from the thermal stability, the weight loss from the TGA curves can also be used to determine the actual composition of the composites. Basically, the filler mass fraction is calculated by deducting the residual mass in the pure rubber (contains the mass of the non-degraded rubber and the additives) from the composites residual mass. The mass fractions of the GNP and carbon black in the nitrile butadiene rubber determined from TGA are summarized in Table 5.1. The volume fractions, calculated using the appropriate densities of the rubber, filler and additives are also given in the Table. The assumptions and the calculation method is the same as illustrated for Table 4.1.

5.3.2. Scanning electron microscopy

The distribution and orientation of the GNP and carbon black in the nitrile butadiene rubber was evaluated firstly using SEM of samples fractured rubber sheets after immersion in liquid nitrogen. Images of the fracture surfaces for the materials with all loadings of the fillers are given in Figure 5.7 and 5.8. The M15 GNP flakes can clearly be seen to be well dispersed in the nitrile butadiene rubber matrix and being pulled out from the fracture surfaces for NBR composites whereas the fracture surfaces for the NBR composites containing the N330 carbon black is much smoother and sub-micron-sized clusters of carbon black agglomerates can just about be resolved in the surface features.

Preferred alignment of the GNP in the plane of the sheets (horizontal) can also be seen in Figure 5.7. The orientation of the GNP flakes can be most easily seen in the fracture surfaces of the composites with 5 and 10 phr loadings, from the white straight lines, linear holes and pulled out flakes parallel to horizontal direction. The lengths of straight lines, holes and pulled-out flakes are consistent with the lateral size of the M15 GNP as given in Figure 4.1b. Similar to the SEM images of the fractured surfaces of carbon black NR composites, the 15 phr carbon black NBR composite shows the most visible particles, which can be attributed to the high loading of fillers but not high enough to generate aggregation of the carbon black in the rubber matrix.

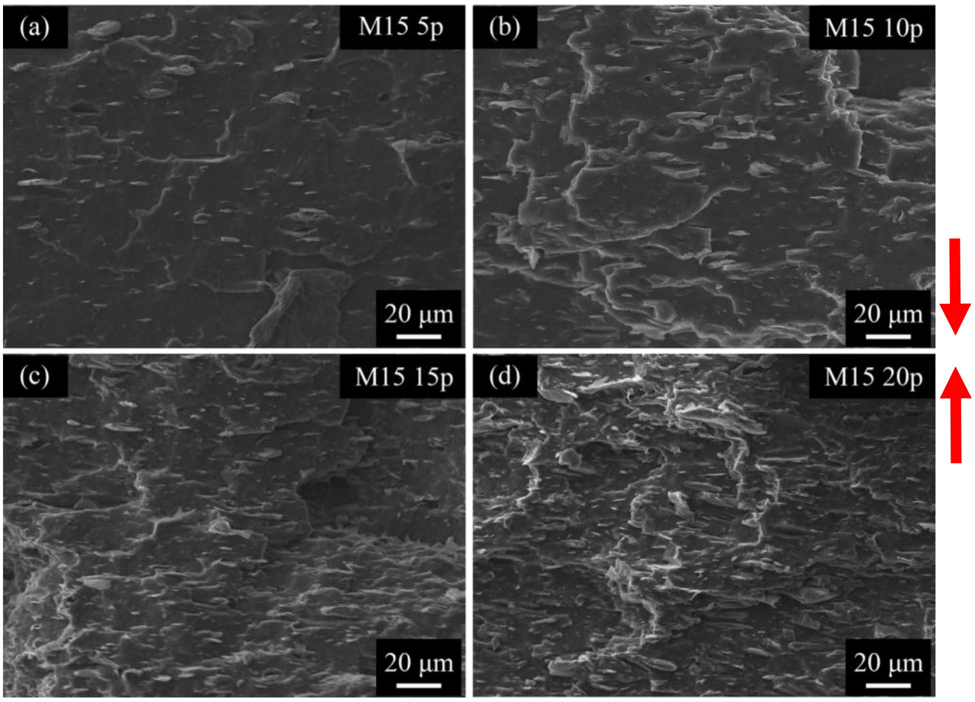

Figure 5.7 SEM micrographs of fracture surfaces of the M5 NBR nanocomposites. Specimen thickness: 1mm. The red arrows indicate the hydraulic pressure direction in the hot press.

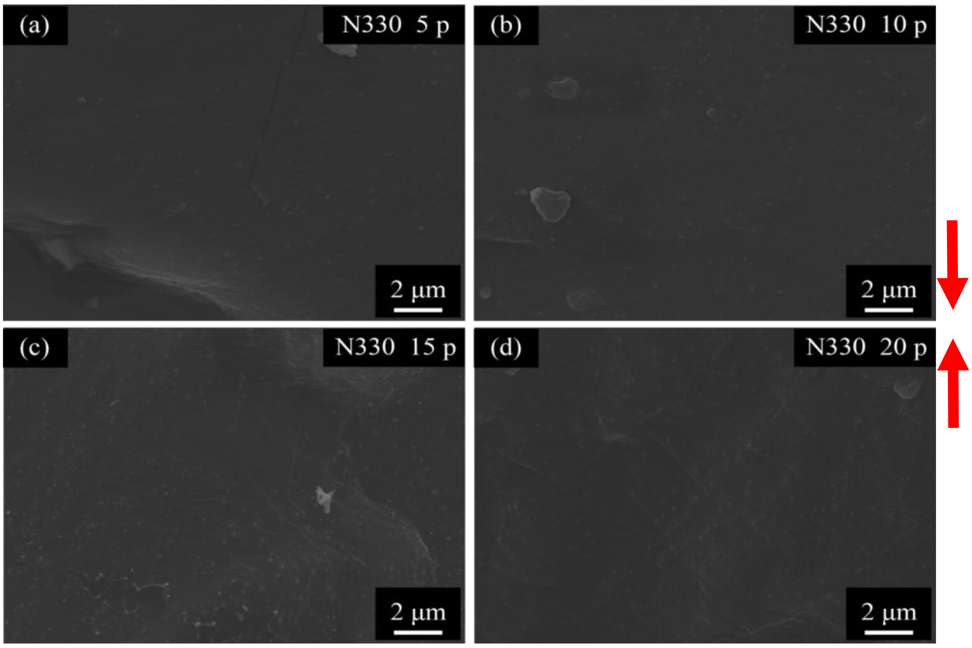

Figure 5.8 SEM micrographs of fracture surfaces of the carbon black (N330) NBR nanocomposites. Specimen thickness: 1mm. The red arrows indicate the hydraulic pressure direction in the hot press.

5.3.3. Polarized Raman spectroscopy

Since the fracture surfaces of the GNP nanocomposites showed preferred alignment of the GNP, polarized Raman spectroscopy was employed to quantify the level of orientation of the GNP in the nanocomposites. The results of this analysis are shown in Figure 5.9 where the measurements of the intensity of the G band as a function of orientation rotating each specimen around the *Z* and *X* axes are presented for the nitrile butadiene rubber with 5, 10, 15 and 20 phr of the M15 GNP. It can be seen that in each case there is no change intensity (red dots in Figure 5.9) during rotation of the specimen about the *Z* axis (perpendicular to the sheet), implying no preferred orientation of the GNP in the *X* or *Y* directions. In contrast, it case be seen that in each case the intensity of the G band decreases (black dots in Figure 5.9) with increasing angle of rotation when the specimens were rotated about the *X* axis (similar behaviour was found for rotation about the *Y* axis). This implies that GNPs tends to be aligned in-plane within the nitrile butadiene rubber sheets.

It is possible to quantify this level of orientation from the values of $\langle P_2(\cos\theta)\rangle$ and $\langle P_4(\cos\theta)\rangle$[10] fitted to the data in Figure 5.9 and they are also given on the plots ($\langle P_2(\cos\theta)\rangle$ = 1 for perfect alignment and $\langle P_2(\cos\theta)\rangle$ = 0 for random orientation[11]). The value of $\langle P_2(\cos\theta)\rangle$ was found to be in the range 0.16-0.42 for the all the loadings of M15 GNP nanocomposite samples studied, showing a general preferred in-plane alignment of the nanoplatelets. No systematic trend could, however, be found with either the level of loading. This is most likely due to the fact that the size of the Raman laser spot (~2 μm) is of the same order of magnitude as the lateral size of the GNP. The reason to cause the in-plane alignment of the flakes in the rubber matrix can be attributed to the processing in the hot press. No matter how the masticated rubber compounds of any shape were put into the mould (one piece, multiple pieces, flat-like, sphere-like, folded or unfolded), it always showed a similar orientation of flakes.

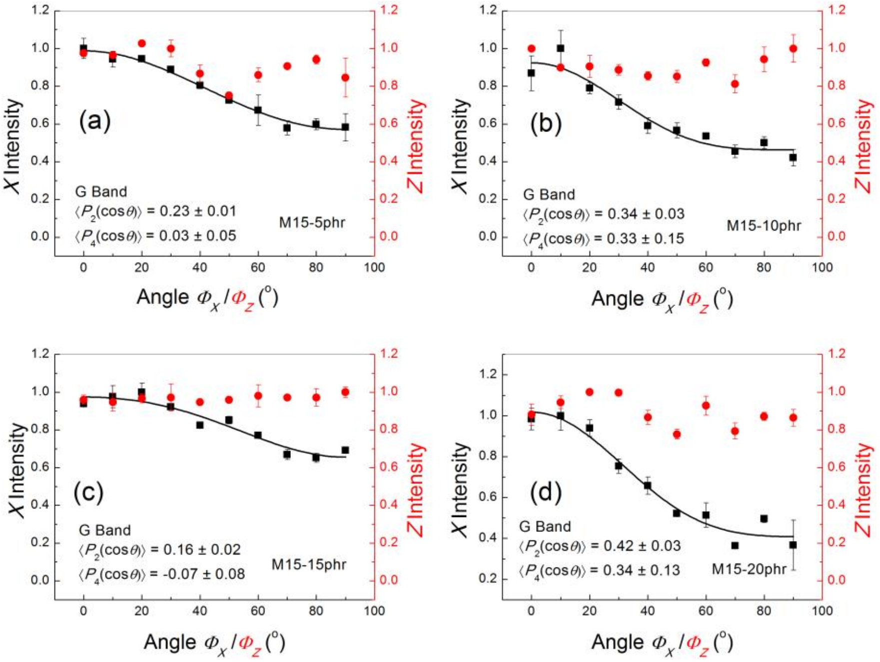

Figure 5.9 Polarized Raman measurements of the intensity of the G band as a function of orientation around the *Z* and *X* axes for the nitrile butadiene rubber with M15 GNP at (a) 5, (b) 10, (c) 15 and (d) 20 phr loadings. Each curve set (black and red) are from one sample and each data point is from 3 scanning. Error bars represent the standard errors (laser excitation: 633 nm).

5.3.4. X-ray diffraction

The X-ray diffraction patterns of the GNPs and pure natural rubber can be seen Figure 5.10. The M15 GNP basically exhibits the sharp typical graphitic peak at 26.4 °, which is corresponding to a lattice spacing of 0.334 nm. In contrast, the nitrile butadiene rubber only shows a broad band at around 20.2 ° with other several sharp peaks that can be attributed to the additives incorporated during the mixing and are much more significant than those in NR.

After the fabrication by incorporation of GNP into the nitrile butadiene rubber matrix, the XRD patterns of the composites show a combination of each component. As can be seen in Figure 5.11, the XRD patterns of the GNP NBR composites remain the sharp typical graphitic peak, the short broad rubber band and the minor peaks from the additives. The positions of the graphitic peak are slightly shifted to 26.6 °, which can be considered is identical to those of the GNPs. Apart from that, when the intensity of the graphitic material is normalized, the intensity of the broad rubber band and the peaks from the additives show a decrease upon increasing GNP loading. The reason of this evolution is similar to the change of the Raman peak intensity ratio.

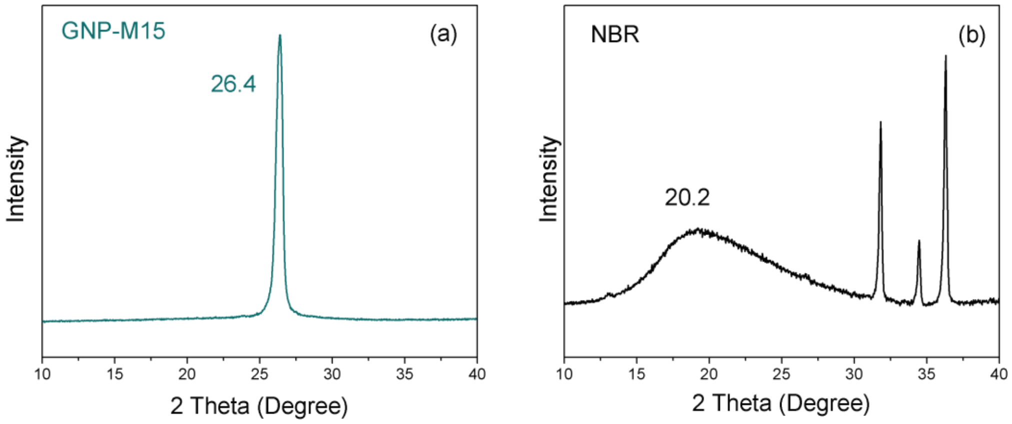

Figure 5.10 XRD patterns of (a) M15 GNP and (b) pure NBR.

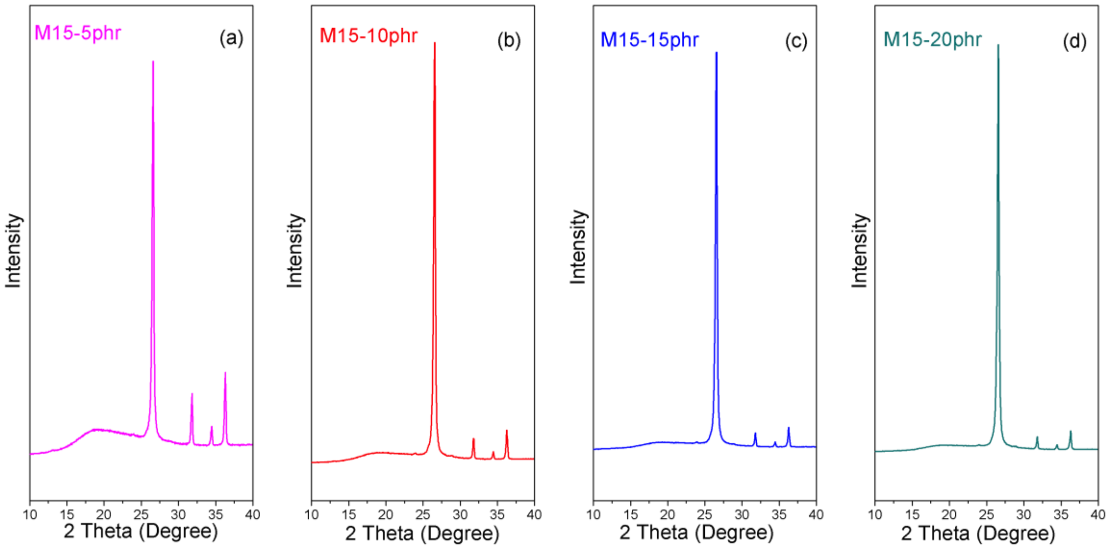

Figure 5.11 XRD patterns of the M15-GNP NBR composites at 5 to 20 phr.

5.4. Mechanical properties

5.4.1. Stress-strain behavior

Stress strain curves for the M15 GNP and N330 carbon black NBR composites studied are given in Figure 5.12. Five stress-strain curves were obtained for each loading level for each type of filler, and representative ones are presented. Overall the addition of the M15 GNP and carbon black can be seen to increase the stiffness of the mterials significantly. Nitrile butadiene rubber has a relatively low inherent strength compared with that of natural rubber (NR) because it has no tendency to strain crystallise and none of the fillers appear to increase the tensile strength of NR. The strength of the NBR composites appears to increase much more for the carbon black than the M15 GNP. For the two highest loadings (15 phr and 20 phr), the strength of carbon black composites is even nearly twice that of GNP composites. In all cases the strain at failure appears to be enhanced and once the fillers are added in it remains almost unchanged upon increasing loadings.

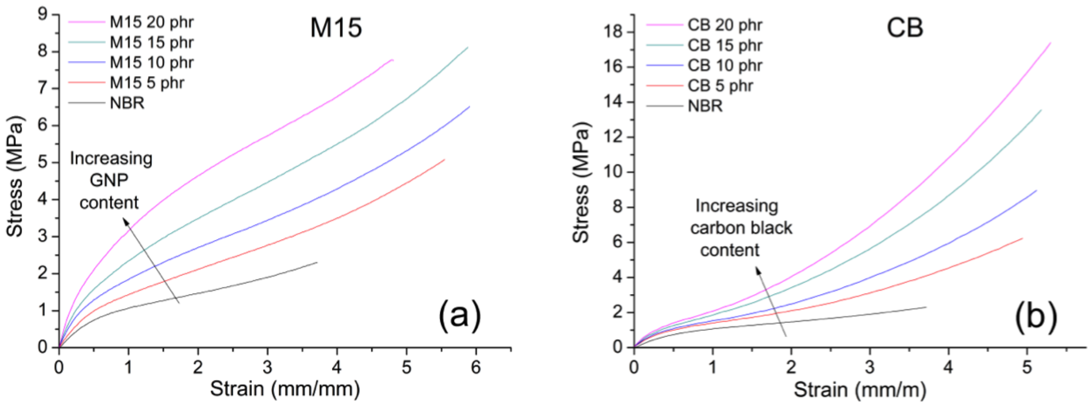

Figure 5.12 Stress-strain curves for the nitrile butadiene rubber containing 5, 10, 15 and 20 phr of (a) M15 and (b) N330 carbon black. Each curve is the typical one out of 5 results. Specimen thickness: 2 mm.

5.4.2. Modulus values

Although from Figure 5.12, it can be seen that the addition of the M15 GNP and carbon black leads to stiffer materials compared with the pure NBR, the reinforcement has not been shown in detail. Specifically, the stress-strain curves at low strain (<300%) of the pure NBR and the composites of each filler of highest loading are shown in Figure 5.13a. The addition of the GNP leads to a significantly higher initial slope for the stress-strain curve than for the rubber reinforced with carbon black, so that the modulus at 100% strain is nearly twice that of the carbon black loaded material. Similar behaviour was found for the other levels of filler loading. The interesting thing is when the strain is higher than 2.4, the stress of the CB composite become higher than that of the GNP composite.

The tensile moduli at 100% and 200% strain are plotted as a function of the volume fraction of fillers (Table 5.1) in Figures 5.13b and 5.13c respectively. Since the modulus appears linearly increasing upon the loading of the fillers, the significance analysis is conducted by comparing the slopes obtained from the linearly fitted data and the values are tabulated in Table 5.2. The higher levels of reinforcement achieved with the addition of the GNP compared with that obtained for the CB at a given volume fraction can be clearly seen. Another way of looking at the data in Figures 5.13b and 5.13c is in terms of the volume fraction of filler needed for a particular level of modulus. It can be seen that for a particular modulus value, up to twice (more straightforwardly seen in Table 5.2) the volume fraction of carbon black is needed to match that of natural rubber reinforced with the GNP materials, which is lower than that of the NR composites.

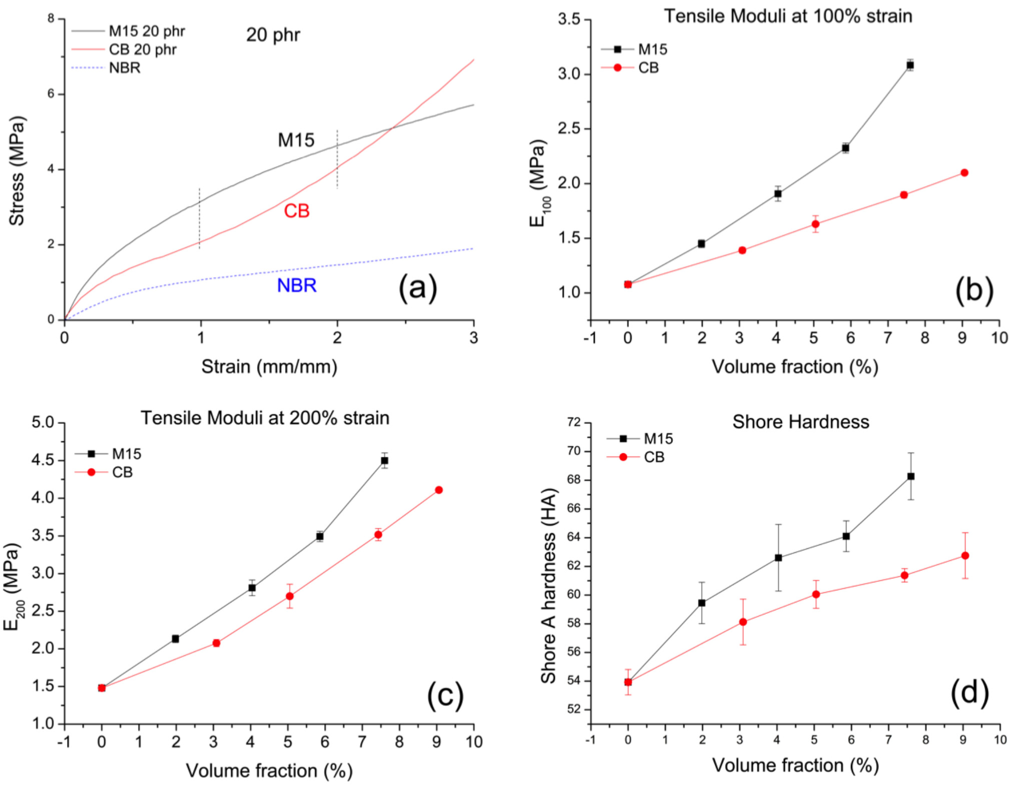

Figure 5.13 Mechanical properties of the nanocomposites. (a) Comparison of the stress-strain curves for the different nanofillers at 20 phr loading. (b) Tensile modulus at 100% strain as a function of filler volume fraction. (c) Tensile modulus at 200% strain as a function of filler volume fraction. (d) Shore A hardness as a function of filler volume fraction ((5 specimens for each point)). Error bars represent the standard deviation. Specimen thickness: 2 mm for tensile tests and 6 mm for hardness tests.

Table 5.2 Slope of the linear fitting of the curves in Figure 5.13b, c and d. (units: 10^{-2} MPa/vol% fillers for E_{100} and E_{200}; 10^{-2} HA/vol% fillers for hardness)

Sample	E100	E200	Hardness
NBR-M15	24.1 ±0.6	36.3 ±0.9	178 ±19
NBR-CB	11.4 ±0.2	29.4 ±0.3	97 ±13

Finally, the Shore hardness of sheets of the natural rubber and all materials with different filler loadings was determined as shown in Figure 5.13d. The significance analysis follows the same procedure for the modulus as tabulated in Table 5.2. It can be seen that the measured values of Shore hardness of GNPs composites exhibit nearly doubly increasing rates compared with the rubber filled with CB.

5.4.3. Ultimate properties

It was aforementioned that nitrile butadiene rubber cannot crystallize under stress like natural rubber does, which makes it break at a relatively low strain. Figure 5.14a shows that the tensile strength is highly affected by the addition of all the loadings but tends to increase more significantly on the addition of the carbon black, with the smaller particles giving rise to the higher level of strength enhancement. Figure 5.14b shows the effect of the addition of the M15 GNP and the carbon black upon the ultimate failure strain of the natural rubber. It increases with low loadings of both fillers, and trends to lever upon higher loadings. Apart from that, the addition of the M15 GNP gives more enhancements in failure strain than carbon black among all the loadings. The improvement of the strain at break at small loadings may be attributed to the void formation, the delamination or the pullout of the flakes which absorb energy and increase the toughness of the composites. Figure 5.15 shows the change of the tear strength of the rubber incorporated with the M15 GNP and the carbon black. At small loadings of the M15 GNP and the carbon black, the tear strength shows a linear increase whereas at high loadings the increasing rate tends to grow for GNPs and fall away for carbon black.

The effect of the different nano-fillers upon the ultimate properties of the nitrile rubber appears to be related to the size of the particles. This implies that the larger particles give rise to an easier crack initiation. Hence, the larger M15 GNP particles, causes the lower enhancement in tensile strength with increasing volume fraction (Figure 5.14a), whereas the tensile strength appears to be improved much more significantly upon the addition of the small carbon black particles. Unlike natural rubber, and the larger flat M15 GNP particles in nitrile butadiene rubber seems to give a higher resistance to the crack propagation due to a stronger bonding at the interfaces with the rubber, which leads to a higher tear strength than that of the carbon black.

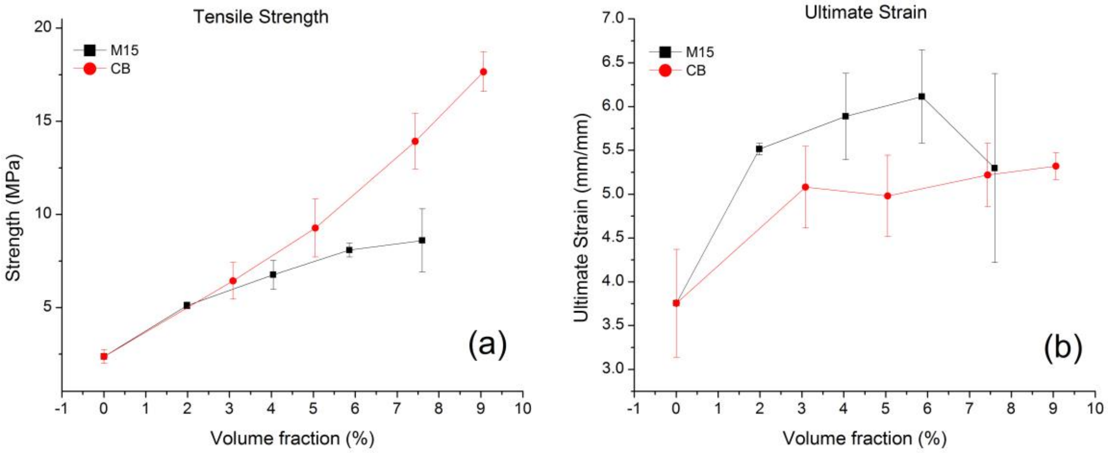

Figure 5.14 Mechanical properties of the nanocomposite as a function of filler volume fraction. (a) Tensile strength and (b) ultimate strain. Error bars represent the standard deviation.

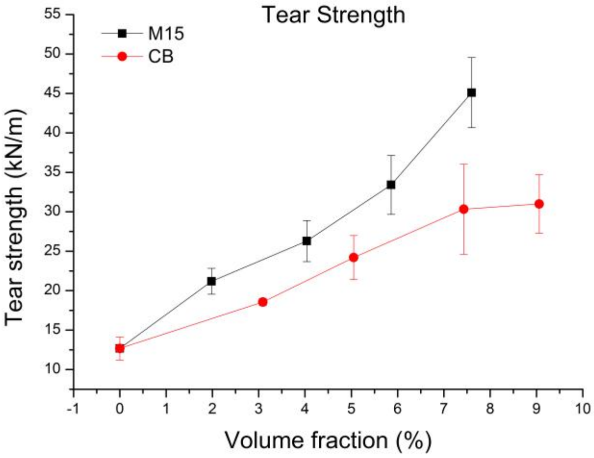

Figure 5.15 Tear strength of the nanocomposite as a function of filler volume fraction ((5 specimens for each point)). Error bars represent the standard deviation. Specimen thickness: 2 mm.

Overall, the parameters of the mechanical properties of the GNPs NR composites can be tabulated in Table 5.3 as below.

Table 5.3 Parameters of the mechanical properties

	E_{100} (MPa)	E_{200} (MPa)	σ_u (MPa)	ε_u (mm/mm)	H (HA)	σ_t (MPa)
NBR	1.08 ±0.02	1.48 ±0.02	2.38 ±0.37	3.76 ±0.62	53.9 ±0.9	12.6 ±1.5
M15-5phr	1.45 ±0.03	2.13 ±0.05	5.11 ±0.18	5.52 ±0.07	59.5 ±1.4	21.2 ±1.6
M15-10phr	1.91 ±0.07	2.81 ±0.10	6.77 ±0.78	5.89 ±0.49	62.6 ±2.3	26.3 ±2.6
M15-15phr	2.33 ±0.05	3.50 ±0.07	8.09 ±0.37	6.12 ±0.53	64.1 ±1.1	33.4 ±3.7
M15-20phr	3.09 ±0.05	4.50 ±0.10	8.60 ±1.70	5.30 ±1.08	68.3 ±1.6	45.1 ±4.4
CB-5phr	1.39 ±0.03	2.08 ±0.05	6.44 ±1.00	5.08 ±0.47	58.1 ±1.6	18.6 ±1.5
CB-10phr	1.63 ±0.08	2.70 ±0.16	9.27 ±1.56	4.98 ±0.47	60.1 ±1.0	24.2 ±2.8
CB-15phr	1.90 ±0.03	3.52 ±0.08	13.93 ±1.49	5.22 ±0.36	61.4 ±0.5	30.3 ±5.7
CB-20phr	2.10 ±0.01	4.11 ±0.02	17.67 ±1.06	5.32 ±0.15	62.8 ±1.6	31.0 ±3.7

* E_{100}, E_{200}, σ_u, ε_u, H and σ_t are the Young's modulus at 100% strain, Young's modulus at 200% strain, tensile strength, ultimate strain, Shore A hardness and tear strength, respectively.

5.4.4. Stress-induced Raman band shifts

Shifts in the position of the 2D Raman band with strain were determined for the nitrile butadiene rubber filled with the M15 GNP materials, as shown in Figure 5.16. This was a particularly difficult experiment to undertake as the 2D band is rather ill-defined in the spectrum as a result of fluorescence from the rubber matrix, as found in Figure 5.3, and the shifts were relatively small. Hence only the materials with the highest loading of 20 phr of the M15 GNP were employed as they had the strongest 2D band. Another difficulty of this experiment is to fix the microscope and laser spot at one particular point on one particular individual micron-sized flake while large extensions (a few centimeters) were applied to stretch the specimen. Additionally, as the result of the small band shifts and scatter in the data, the experiments were undertaken upon at least 16 different specimens for each composition and the data points in Figure 5.16 represent the mean value for all the specimens used for the M15 GNP.

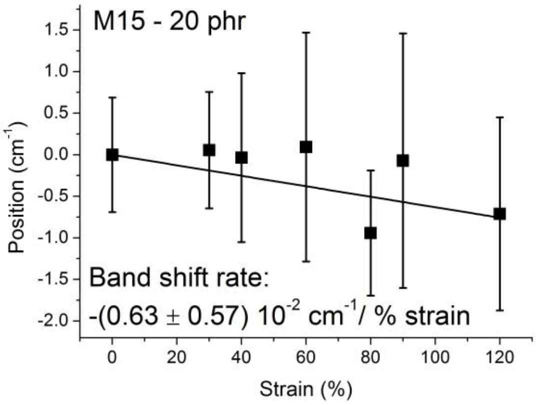

Figure 5.16 Shift of the 2D Raman band with strain for the nanocomposites with 20 phr M15 GNP (laser excitation: 633 nm). Each data point represents the average of 16 repeated scanning of 16 specimens at one particular strain. Specimen thickness: 2 mm.

Although there is considerable scatter in the data in Figure 5.16 relatively larger error bars than the energy error of the instrument (±1 cm^{-1}), but the data of each figure were obtained from numerous data points and it appears that there is a small but significant downshift in the position of the 2D band with tensile strain. the data were linearly fitted that shows a band shift rate in an order of magnitude of 10^{-2} cm^{-1}/% strain. The band shift rate will be further discussed in Chapter 7.

5.5. Conclusion

From the SEM images, the good dispersion of GNPs can be observed. The orientation of the flakes was determined to be in-plane alignment by the SEM images and was quantified by polarized Raman spectroscopy. The addition of the M15 GNPs was found to suppress the fluorescence background of the Raman spectrum of the nitrile butadiene rubber. The addition of the fillers was confirmed to enhance the thermal stability. The M15 GNPs imparted a higher reinforcement to the nitrile butadiene rubber compared with the carbon black. Stress transfer between the GNPs and the rubber was detected by the deformation experiment under Raman spectroscopy.

References

1. Hendra, P. J.; Jackson, K. D. O., Applications of Raman spectroscopy to the analysis of natural rubber. *Spectrochim. Acta A* **1994,** *50*, 1987-1997.
2. Xie, L.; Ling, X.; Fang, Y.; Zhang, J.; Liu, Z., Graphene as a substrate to suppress fluorescence in resonance Raman spectroscopy. *J. Am. Chem. Soc.* **2009,** *131*, 9890-9891.
3. Pakjamsai, S.; Suwanprateeb, J., Using FT-Raman spectroscopy for quantitative determination of high filler content in particulated composites. *J. Appl. Polym. Sci.* **2000,** *78*, 1947-1954.
4. Mahmoud, W. E.; El-Eraki, M. H. I.; El-Lawindy, A. M. Y.; Hassan, H. H., A novel application of ADC/K-foaming agent-loaded NBR rubber composites as pressure sensor. *J. Phys. D Appl. Phys.* **2006,** *39*, 541-546.
5. Derenzo, S. E.; Weber, M. J.; Klintenberg, M. K., Temperature dependence of the fast, near-band-edge scintillation from CuI, HgI2, PbI2, ZnO:Ga and CdS:In. *Nucl. Instr. Meth. Phys. Res. A* **2002,** *486*, 214-219.
6. Janković, B.; Marinović-Cincović, M.; Jovanović, V.; Samaržija-Jovanović, S.; Marković, G., The comparative kinetic analysis of non-isothermal degradation process of acrylonitrile–butadiene/ethylene–propylene–diene rubber blends reinforced with carbon black/silica fillers. Part II. *Thermochim. Acta* **2012,** *543*, 304-312.
7. Dorfler, S.; Hagen, M.; Althues, H.; Tubke, J.; Kaskel, S.; Hoffmann, M. J., High capacity vertical aligned carbon nanotube/sulfur composite cathodes for lithium-sulfur batteries. *Chem. Commun.* **2012,** *48*, 4097-9.
8. Centeno, A.; Rocha, V. G.; Alonso, B.; Fernández, A.; Gutierrez-Gonzalez, C. F.; Torrecillas, R.; Zurutuza, A., Graphene for tough and electroconductive alumina ceramics. *J. Eur. Ceram. Soc.* **2013,** *33*, 3201-3210.
9. Tunnicliffe, L. B.; Kadlcak, J.; Morris, M. D.; Shi, Y.; Thomas, A. G.; Busfield, J.

J. C., Flocculation and Viscoelastic Behaviour in Carbon Black-Filled Natural Rubber. *Macromol. Mater. Eng.* **2014,** *299*, 1474-1483.

10. Li, Z.; Young, R. J.; Kinloch, I. A.; Wilson, N. R.; Marsden, A. J.; Raju, A. P. A., Quantitative determination of the spatial orientation of graphene by polarized Raman spectroscopy. *Carbon* **2015,** *88*, 215-224.

11. Li, Z. L.; Young, R. J.; Wilson, N. R.; Kinloch, I. A.; Valles, C.; Li, Z., Effect of the orientation of graphene-based nanoplatelets upon the Young's modulus of nanocomposites. *Compos. Sci. Technol.* **2016,** *123*, 125-133.

6. Transport properties: solvent diffusion and thermal conductivity

6.1. Introduction

In this chapter, the transport behavior of the filled elastomers will be investigated. The diffusion of toluene into the pure rubbers and particle-filled composites will be presented. Both mass swelling and dimensional swelling of the specimens were conducted. Heat transfer was also investigated for all types of composites. There will be comparison between the three grades of GNP flakes (M5, M15 and M25) in the natural rubber and between the two types of rubber matrices only with the M15 GNP flakes and carbon black.

Since the specimens in the swelling test were made into flat sheets with a high aspect ratio (~25), the penetration of the solvent molecules predominantly occurred through the flat surfaces rather the side surfaces. The flat surfaces are parallel to the planes where the flakes were known to be aligned as observed by SEM images of fracture surfaces, angular-dependent intensity from polarized Raman spectroscopy and rotation videos from X-ray CT-scanning. Hence, the effect of the flake orientation was expected to observe in the transport properties.

6.2. Mass uptake of solvent

The mass uptake M_t of the toluene by each composite specimen was measured at certain intervals, calculated by the mass of the soaked specimen minus the original mass M_0 of the dried specimen. The sorption of the composites is defined as $S = M_t/M_0$. The mass uptake at equilibrium is defined as M_∞. As can be seen in Figure 6.1, the sorption of all the composites increases at a relatively high rate from the beginning of the test and tends to slow down and approach the equilibrium at the end. It takes basically 48 hours for all the NR composites to reach the equilibrium, and the curves share the same form all long the whole absorption process. For all the composites, the sorption is suppressed by the addition of all types of fillers. However, the GNP flakes exhibit better resistance of the uptake of the solvent compared with carbon black, with up to a ~43 % drop of the uptake at equilibrium.

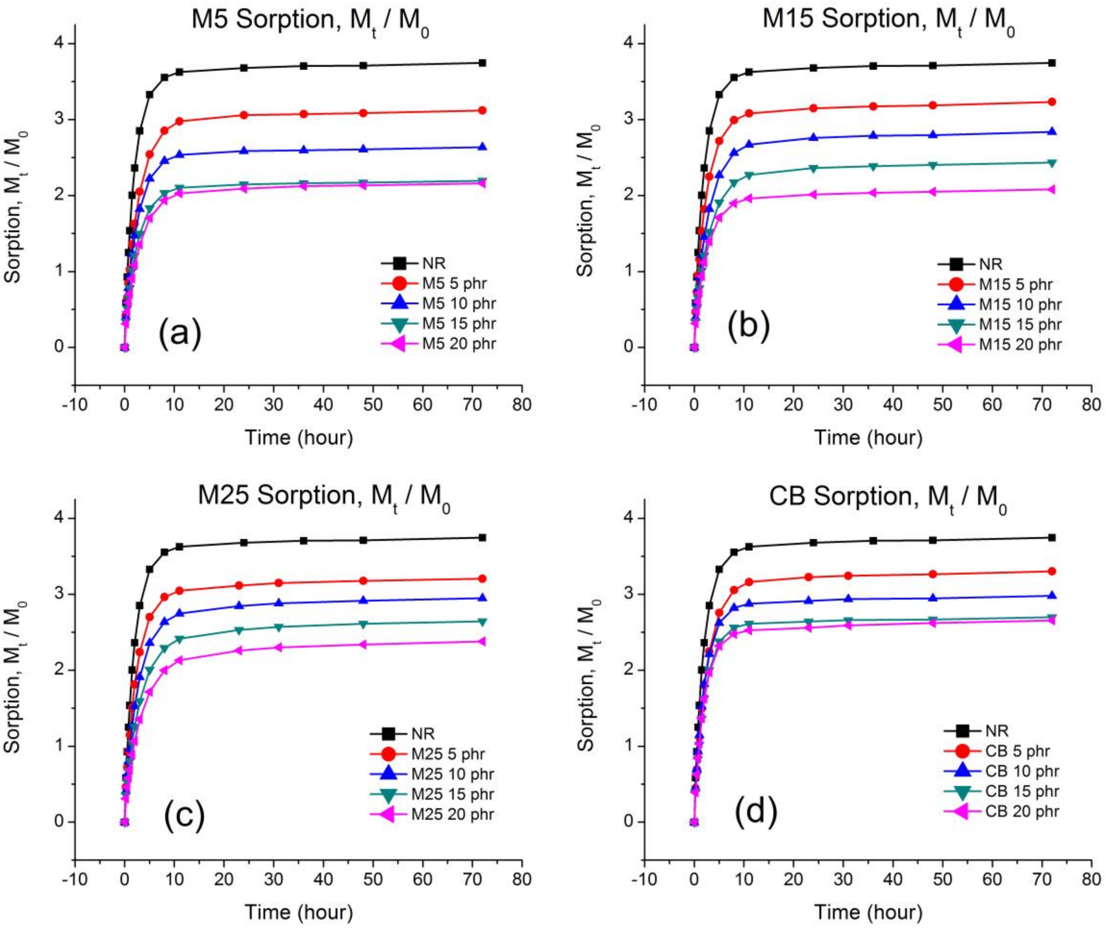

Figure 6.1 Sorption of the NR composites against time. (a) M5; (b) M15; (c) M25 and (d) CB. Each curve represents the result of one specimen. Specimen thickness: 2 mm. Solvent: toluene.

The relative mass increment (M_∞/M_0) of the NR composites at equilibrium is presented in Figure 6.2, giving a comparison between the different fillers. All the GNPs exhibit superiority to the carbon black upon the resistance to the solvent uptake. For the three types of GNP, M5 shows the highest resistance to the solvent molecules, whereas M25 gives rise to a highest solvent uptake. Specifically, compared with the swelling of the pure NR, the M5 and M15 GNPs nearly halve the mass swelling at 20 phr loading, whereas the carbon black basically decreases by ~30% at 20 phr.

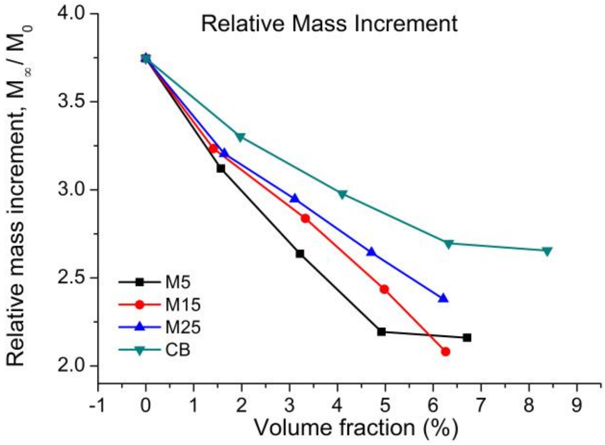

Figure 6.2 Relative mass increment of the NR composites at equilibrium. Each data point represents the result of one specimen.

Compared with the NR composites, the sorption of the NBR composites shows a much less uptake of the toluene and the similar characteristics can be observed as presented in Figure 6.3. The sorption is highly reduced by the addition of the fillers, and it reaches the equilibrium after the same time for the composites filled with the same filler at all loadings. The sorption of the M15 GNP in NBR shows a better resistance of solvent uptake compared with the carbon black composites, with up to ~30% decreasing at equilibrium.

The relative mass increment of the NBR composites is presented in Figure 6.4. Due to the high intrinsic chemical resistance as reviewed in Chapter 2, the NBR composites give rise to a much less swelling compared with the NR composites. The GNP NBR composites basically show a linear decrease, which is much faster than that of the carbon black NBR composites. The gap between them is very close to those of the NR composites.

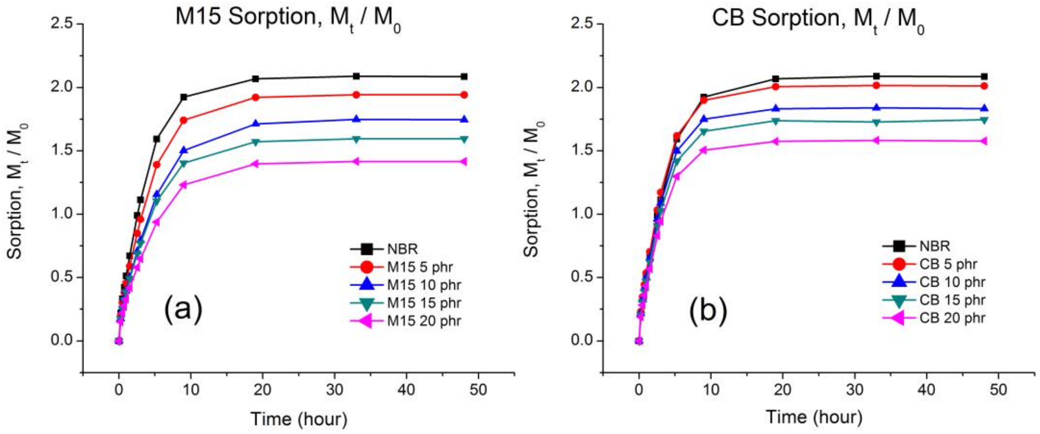

Figure 6.3 Sorption of the NBR composites against time. (a) M15 and (b) CB. Each curve represents the result of one specimen. Specimen thickness: 2 mm. Solvent: toluene.

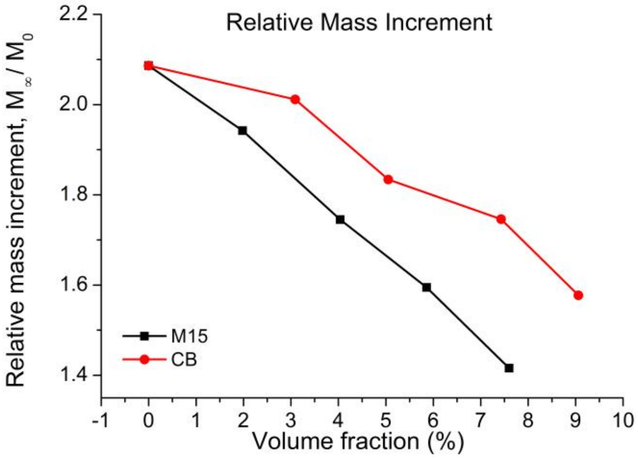

Figure 6.4 Relative mass increment of the NBR composites at equilibrium. Each data point represents the result of one specimen.

6.3. Dimensional swelling

After the specimens were soaked in toluene and reached the equilibrium, the first conspicuous change was the dimensional change. As can be seen in Figure 6.5, the thickness swelling ratios (H_∞/H_0, H_∞ - the swollen thickness at the equilibrium, H_0 - the original thickness) and the width swelling ratios (L_∞/L_0, L_∞ - the swollen width at the equilibrium, L_0 - the original width) are all higher than 1, which implies that specimens were elongated in both vertical and horizontal directions.

However, with the loading of the fillers increases, they show different trends. Specifically, for all types of GNP NR composites, the thickness of the composites swelled more with increasing GNP loading, whereas the width swelled less with higher GNP content. For the carbon black nanocomposites, the thickness and width swelling ratio both slightly decreases with the increasing loading. It seems that the addition of the GNP flakes restrains (~26 % at 20 phr) the swelling in the horizontal direction and boosts (~ 26 % at 20 phr) it in the vertical direction while the addition of the carbon black particles weakens the swelling in both directions. A clearer way to understand that behaviour is to plot the thickness swelling ratio divided by the width swelling ratio against the loading as presented in Figure 6.6. The pure natural rubber shows a value extremely close to 1, which represents an isotropic swelling process (as notated by the red dash line). The carbon black composites maintain this characteristic, with a value close to 1 at all loadings. On the other hand, all the GNP composites exhibit significant anisotropic swelling, with a linearly increasing value upon the increasing loading. The reason why they show different degrees of anisotropy can be attributed to the combination of the intrinsic structure of the fillers and the orientation of the fillers distributed in the matrix.

For the pure natural rubber, the structure is uniform within the whole materials in all directions so that the isotropic swelling is expected. For the carbon black particles, with a shape of sphere, the structure of the composites should be homogeneous in all directions as well. For the GNP flakes with a two-dimensional structure, if they are randomly oriented in the three-dimensional matrix, the structure and the swelling of the composites should be isotropic as well. Nevertheless, the orientation of the GNP flakes in the as-made composites has been determined to be in-plane alignment, which leads to an anisotropic structure of the composites. Hence, the bonding between the flakes and the rubber matrix is anisotropic, which results in an overall anisotropic swelling of the whole composites.

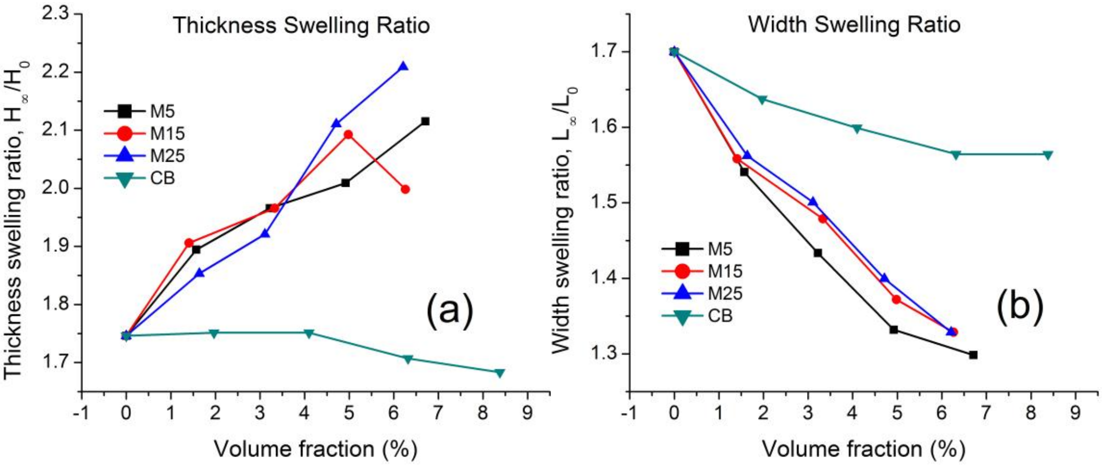

Figure 6.5 (a) Thickness swelling ratio and (b) width swelling ratio of the NR composites at equilibrium. Each data point represents the result of one specimen.

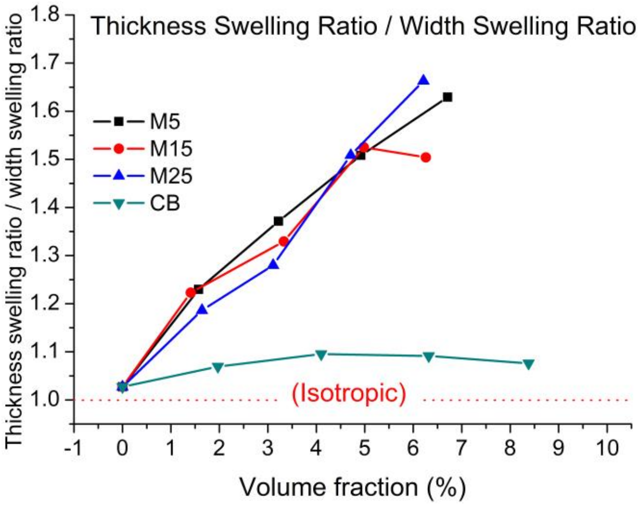

Figure 6.6 Thickness swelling ratio / width swelling ratio of the NR composites at equilibrium. Each data point represents the result of one specimen.

Furthermore, the relative volume increment at equilibrium ($\Delta V/V_0$, ΔV – volume increment at equilibrium, V_0 – original volume) after the swelling can be calculated by the thickness swelling ratio and the square of the width swelling ratio (as the specimens are square sheets). As seen in Figure 6.7, all types of fillers reduce the volume swelling, and the effect grows with increasing loading of the fillers. Compared to all types of GNP, carbon black shows the poorest restraining effect on the volume swelling. Among all the GNP composites, the M5 GNP composites exhibit the best resistance to the penetration of the solvent, whereas the M25 GNP composites give rise to the highest uptake of the solvent. Specifically, the M5 and M15 GNP almost halve the volume swelling at 20 phr loading, whereas the carbon black decreases the swelling less. The shape of the relative volume increment curves basically mirrors that of the relative mass increment as presented in Figure 6.2.

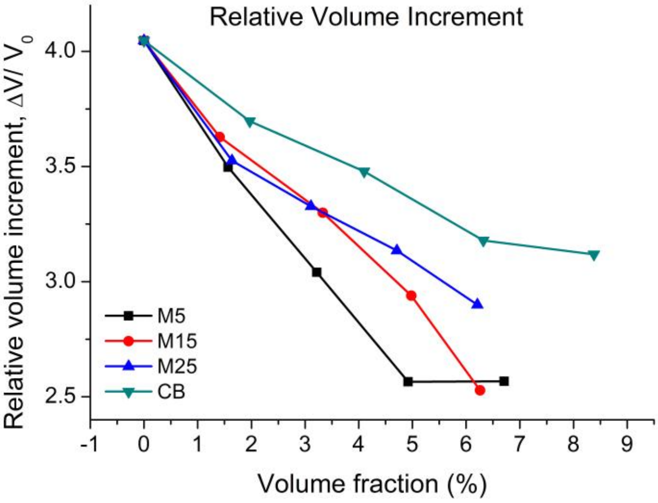

Figure 6.7 Relative volume increment of the NR composites at equilibrium. Each data point represents the result of one specimen.

On the other hand, the NBR composites filled up with the M15 GNP mimics the anisotropic characteristic from all the GNP NR composites upon dimensional swelling as can be seen in Figure 6.8 and 6.9. However, their boosting effect (~16% at 20 phr) of the thickness swelling and the restraining effect (~16% at 20 phr) of the width swelling are both less significant than those (both ~23 % at 20 phr) in NR composites. Since both the boosting and the restraining effects are on the same level in either rubber system, the quatification of the ability of the GNP flakes to resist the solvent is more related to the retraining effect of the width swelling rather than the effect of the thickness swelling as the volume calculation is obtained by the width^2 × the thickness (as the specimens are square sheets). Hence, the ability of the GNP flakes to resist the solvent in NR is better than that in NBR. Additionally, the trend of anisotropy in the M15 GNP composites is also less than that in the NR composites. Nevertheless, the pure NBR and the carbon black NBR composites exhibit their isotropic swelling features similar to the pure NR and the carbon black NR composites.

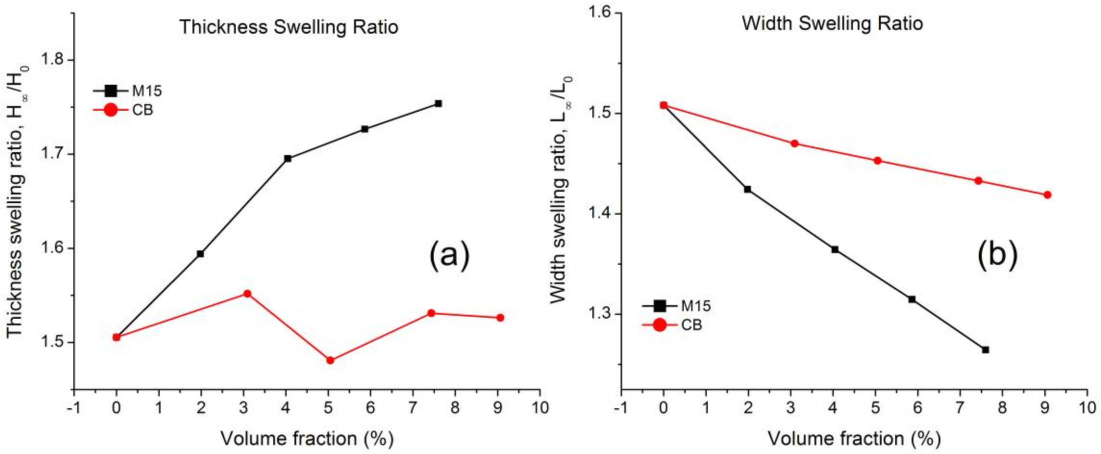

Figure 6.8 (a) Thickness swelling ratio and (b) width swelling ratio of the NBR composites at equilibrium. Each data point represents the result of one specimen.

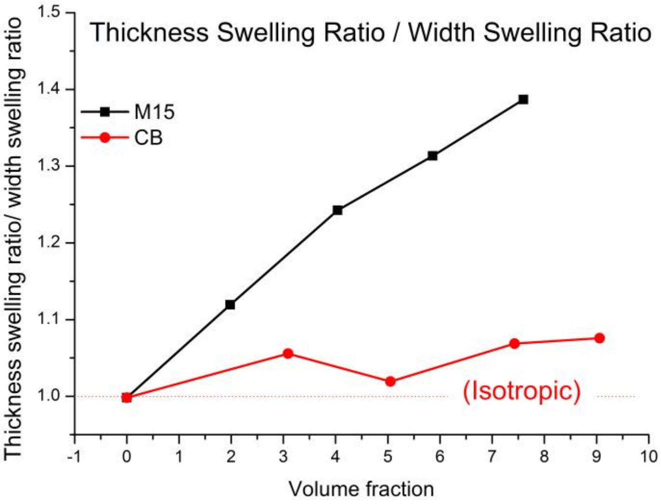

Figure 6.9 Thickness swelling ratio / width swelling ratio of the NBR composites at equilibrium. Each data point represents the result of one specimen.

In term of volume swelling, as can be seen in Figure 6.10, the M15 GNP NBR composites shows a lower solvent uptake than that in the NR composites at small loadings but a higher uptake at high loadings. The reason is the solubility of the toluene molecules in NBR is intrinsically lower than in NR due to the polar group (-C≡N), but the ability of the GNP in NBR to resist the toluene molecules is also lower than that in NR (as demonstrated above), which leads to a lower value for the NBR composites compared with the NR composites at the zero loading, with a slower decreasing rate resulting in a higher value of the NBR composites compared with the NR composites at the highest loading. Additionally, the carbon black in the NBR composites shows no significant difference in the volume swelling from that in the NR composites.

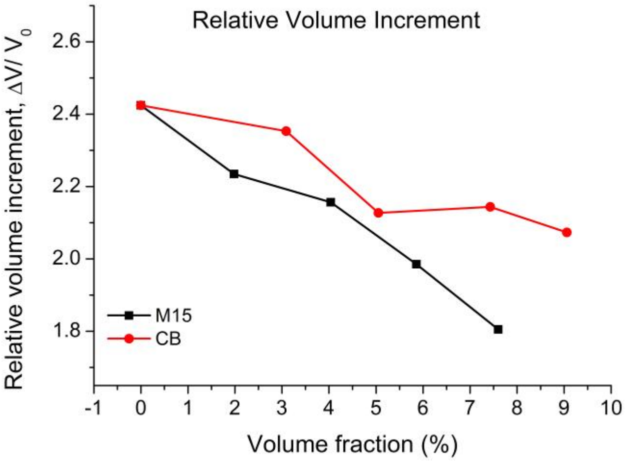

Figure 6.10 Relative volume increment of the NBR composites at equilibrium. Each data point represents the result of one specimen.

6.4. Degree of saturation and diffusion coefficient

The mechanism of the solvent transport of the nanocomposites is analysed by the empirical relationship,[1-8]

$$\log\left(\frac{M_t}{M_\infty}\right) = \log k + n\ \log t \tag{6.1}$$

where k is a constant that depends on the microstructure of the polymer and relates to the interaction between the polymer and the solvent and n indicates the mechanism of the diffusion. M_t/M_∞ is defined herein as degree of saturation.

Table 6.1 Parameters n and k for NR composites

Sample	n	k (h^{-n})
NR	0.65	2.51
M5 5 phr	0.65	3.02
M5 10 phr	0.62	2.82
M5 15 phr	0.60	2.82
M5 20 phr	0.60	3.02
M15 5 phr	0.64	2.82
M15 10 phr	0.63	3.09
M15 15 phr	0.60	3.09
M15 20 phr	0.60	2.88
M25 5 phr	0.65	2.82
M25 10 phr	0.63	3.02
M25 15 phr	0.61	3.24
M25 20 phr	0.60	3.39
CB 5 phr	0.66	2.95
CB 10 phr	0.66	2.63
CB 15 phr	0.67	2.69
CB 20 phr	0.67	2.63

When $n = 0.5$, the diffusion is classified as Case I or Fickian diffusion and this occurs when the rate of the solvent diffusion is much less than the relaxation rate of the polymer chains and the solvent molecules diffuse in a random walk motion. When $n = 1$, the diffusion is termed Case II or non-Fickian, and this occurs when the rate of the solvent diffusion is much larger than the relaxation rate of the polymer chains. When $0.5 < n < 1$, the diffusion rate of the solvent into the polymer is close to the relaxation rate of the polymer chains.[9-10] By plotting log (M_t/M_∞) against log t, the values of n and k can be obtained, which are tabulated in Table 6.1 and 6.2.

As can be seen in Table 6.1 and 6.2, the n value of the NR nanocomposites ranges from 0.60 to 0.67 whereas that of the NBR nanocomposites ranges from 0.59 to 0.66. The n values are closer to 0.5 than 1.0, which makes the diffusion of the toluene into the composites closer to Fickian diffusion.

Table 6.2 Parameters n and k for NBR composites

Sample	n	k (hour^{-n})
NBR	0.66	3.98
M15 5 phr	0.63	4.17
M15 10 phr	0.60	4.37
M15 15 phr	0.60	4.07
M15 20 phr	0.59	4.27
CB 5 phr	0.66	3.63
CB 10 phr	0.65	3.55
CB 15 phr	0.65	3.55
CB 20 phr	0.65	3.55

Therefore, the diffusion coefficient of the composites can be calculated by the initial soaking at short exposure time using Fickian theory.[2, 7] A relation can be used as below,

$$\frac{4M_\infty}{H\sqrt{\pi}}\sqrt{D} = \frac{M_2 - M_1}{\sqrt{t_2} - \sqrt{t_1}} \tag{6.2}$$

where D is the diffusion coefficient, M_1 and M_2 are the solvent uptake at times t_1 and t_2. The equation can be transformed to another version as follow,

$$D = \left(\frac{H}{4}\,\theta\right)^2 \tag{6.3}$$

where θ is the initial slope of degree of saturation, M_t/M_∞, plotted against the square root of time. The degree of saturation of all the composites plotted against $t^{1/2}$ can be seen in Figure 6.11 and 6.12. In Figure 6.11, for carbon black NR composites, the slopes of the curves of all the loadings are similar whereas the GNP NR composites exhibit the dependence of the slope upon the loading. For all the three types of GNP NR composites, the M25 GNP NR composites shows a biggest gap between the curves at different loadings, whereas the M5 GNP composites exhibit the smallest difference between all the curves. Similar behaviour can be observed for the NBR composites in Figure 6.12 as well.

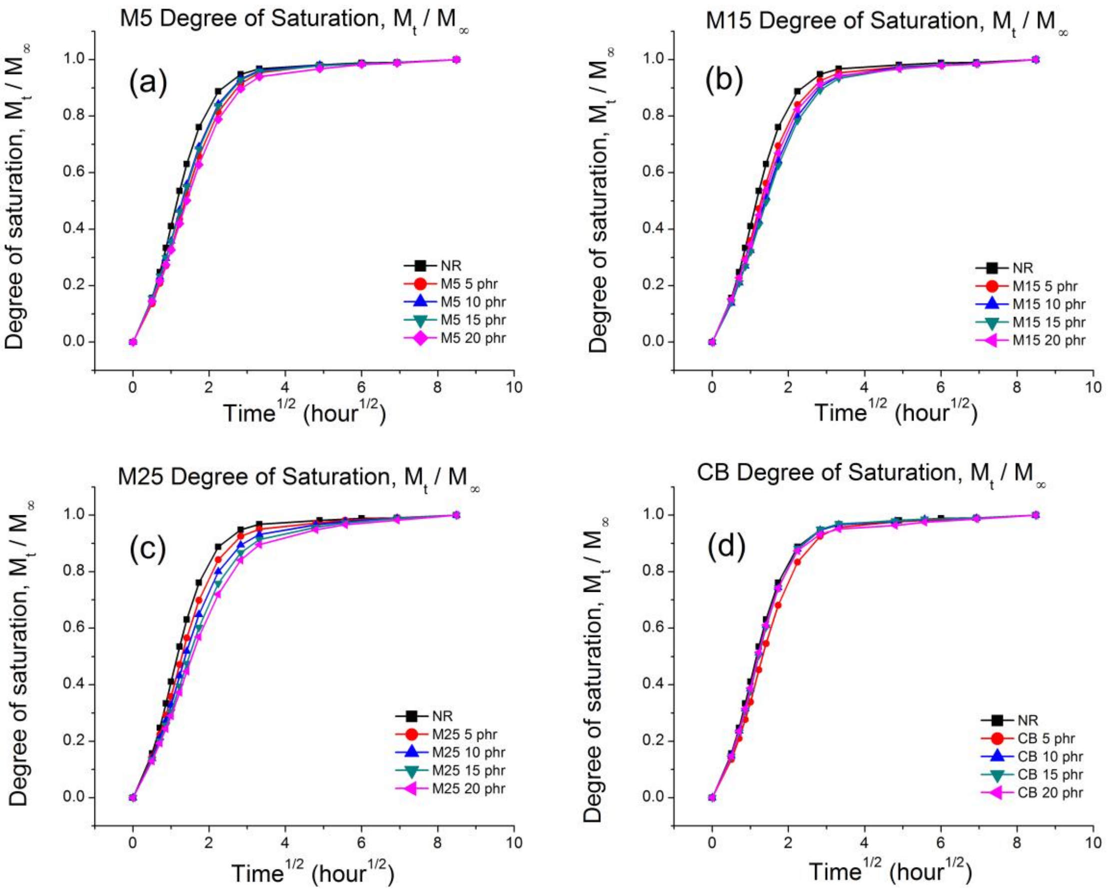

Figure 6.11 Degree of saturation of the NR composites against square root of time. (a) M5; (b) M15; (c) M25 and (d) CB. Each curve represents the result of one specimen. Specimen thickness: 2 mm.

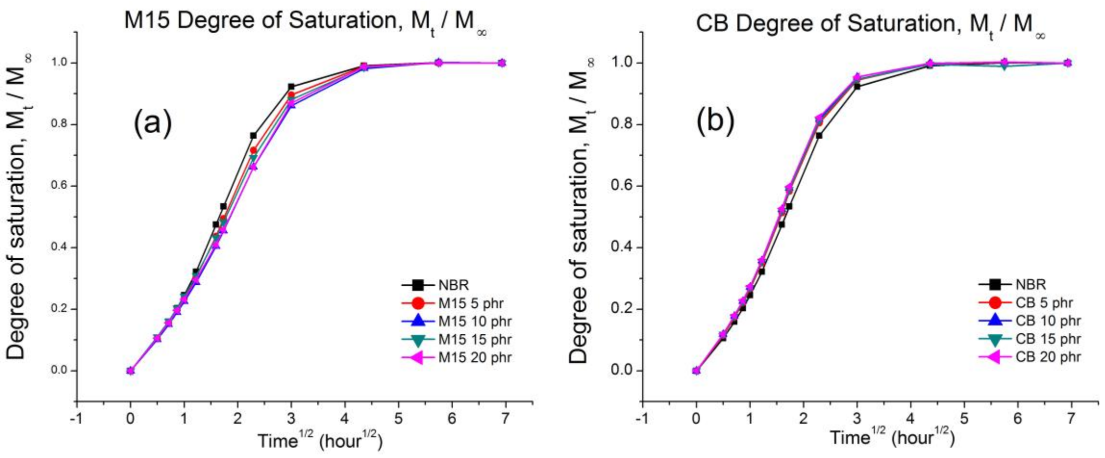

Figure 6.12 Degree of saturation of the NBR composites against square root of time. (a) M15; (b) CB.

Each curve represents the result of one specimen. Specimen thickness: 2 mm.

According to Equation (6.3), the diffusion coefficient is proportion to the initial slope of the degree of saturation curves against $t^{1/2}$. An example of M25 NR composites showing the early stages of the swelling can be seen in Figure 6.13. It is easy to find that the initial slope decreases with the increasing content of the GNP flakes. The diffusion coefficient of all composites can be calculated by Equation 6.3 and plotted as presented in Figure 6.14.

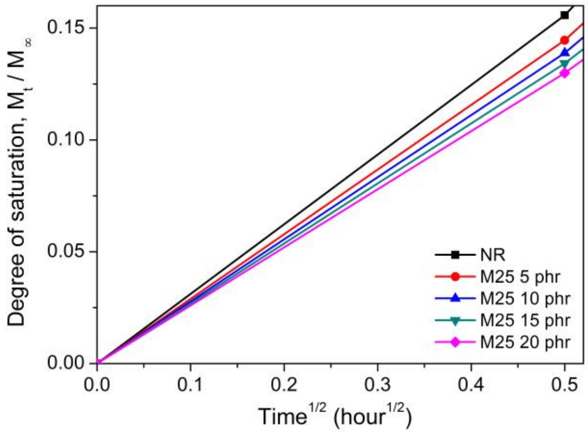

Figure 6.13 Degree of saturation of the M25 NR composites against square root of time at initial stage.

Each curve represents the result of one specimen.

As can be seen in Figure 6.14, with the addition of carbon black, the diffusion coefficient basically remains as the same as the pure rubbers. However, when the GNP flakes are incorporated in, the diffusion coefficient of the composites shows a significant decrease. For the M15 GNP, both NR and NBR composites show a ~30% decrease at 20 phr. For the GNP NR composites, the M25 GNP gives arise to the slowest diffusion whereas the M5 GNP provides the least resistance to the solvent diffusion. This may be due to size effect that the larger particles create a longer penetration path (tortuous path[11-12]) of the solvent molecules through the composites.

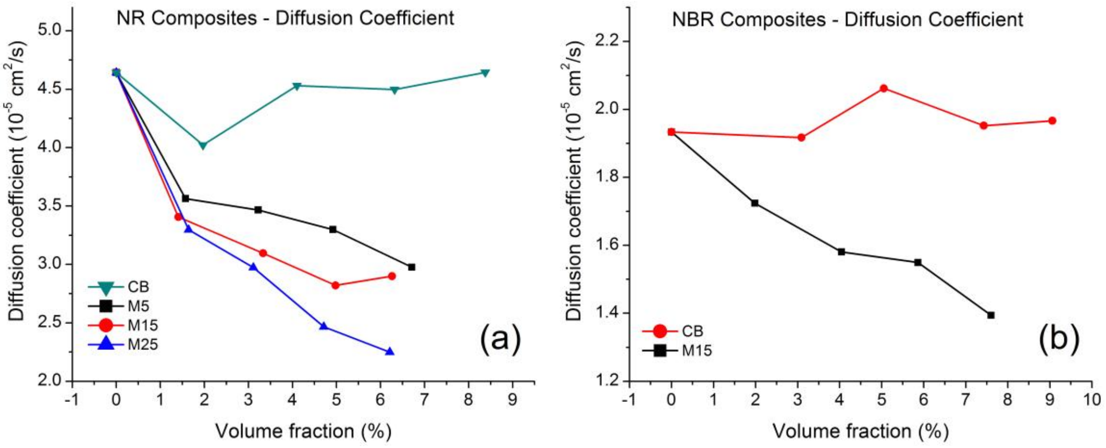

Figure 6.14 Diffusion coefficients of (a) NR and (b) NBR composites. Each data point represents the result of one specimen.

6.5. Thermal conductivity

Heat transfer and thermal conductivity are crucial properties of rubbers, as they usually have influence on other properties during work life. During the experiment, the heat flux transfers from the top surface to the bottom surface, and the thermal conductivity can be calculated by the Fourier's heat conduction equation,[13-14]

$$k = \frac{QH}{tA\Delta T} \tag{6.4}$$

where k is the thermal conductivity, Q is the heat flux, H is the thickness, A is the cross-sectional area that the heat is flowing through, ΔT is the temperature difference between the upper and bottom platens and t is the duration of the heat flow.

As can be seen in Figure 6.15a, for the natural rubber, all the fillers enhance the thermal conductivity of the rubber. The carbon black gives rise to a slight increase, whereas the GNP flakes impart a large improvement to the conductivity, with up to a two times higher value of the pure NR. Among the three types of GNP, the effect of particle size is significantly seen in this experiment. The sudden enhancement of the conductivity can be found in the composites filled with the larger flake (M15 and M25) at a lower loading (M25 at ~ 3 vol% and M15 at ~ 5vol%). This can be explained by the mechanism that the larger particles can form the thermally conductive network more easily at even small loadings as demonstrated in Section 2.6. A conclusion can be made in the NBR composites as presented in Figure 6.15b that the M15 GNP flakes result in a higher improvement of thermal conductivity of the NBR matrix compared with the carbon black.

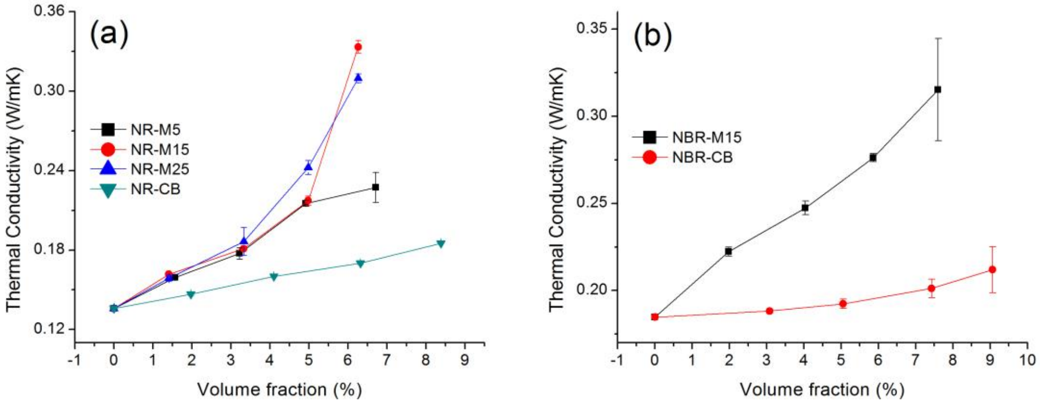

Figure 6.15 Thermal conductivity of (a) NR composites and (b) NBR composites. Each data point is from three specimens. Error bars represent the standard deviation. Specimen thickness: 2 mm.

Furthermore, graphene has an in-plane thermal conductivity (~2000 to 5000 W/mK[15-19]) up to one thousand times higher than the out-of-plane conductivity (~6W/mK[20-21]). In consideration of the experiment setting combined with the orientation determined of the GNP flakes, the thermal conductivity was not conducted in the preferred direction of the GNP flakes, so that the heat flux travels mostly through the flakes rather than parallel to the flakes. A higher enhancement would be expected to be obtained if the heat flux transferred along the top or bottom surfaces of the specimens.

6.6. Conclusion

For the solvent molecular transport, the pure nitrile butadiene rubber shows a lower sorption than the pure natural rubber, and the addition of the fillers highly suppressed the solvent uptake of both the natural rubber and the nitrile butadiene rubber. The swelling of the GNPs rubber composites was boosted in thickness and constrained in width while the swelling of the carbon black composites and the pure rubbers was constrained in all directions. Moreover, the GNPs composites were anisotropically swollen whereas the carbon black composites and the pure rubbers were isotropically swollen. The size effect can also be observed in the sorption at equilibrium and the diffusion coefficient. The composites filled with the smaller flakes show a less solvent uptake and a higher diffusion coefficient.

References

1. Wei, C., Thermal expansion and diffusion coefficients of carbon nanotube-polymer composites. *Nano Lett.* **2002,** *6*, 647-650.
2. Cervenka, A. J.; Young, R. J.; Kueseng, K., Gravimetric determination of the diffusion characteristics of polymers using small specimens. *J. Polym. Sci. Pol. Phys.* **2004,** *42*, 2122-2128.
3. Geethamma, V. G.; Thomas, S., Diffusion of water and artificial seawater through coir fiber reinforced natural rubber composites. *Polym. Composite.* **2005,** *26*, 136-143.
4. Obasi, H. C.; Ogbobe, O.; Igwe, I. O., Diffusion Characteristics of Toluene into Natural Rubber/Linear Low Density Polyethylene Blends. *Int. J. Polym. Sci.* **2009,** *2009*, 1-6.
5. Yin, H.; Ma, Q.; Zhou, Y.; Ai, S.; Zhu, L., Electrochemical behavior and voltammetric determination of 4-aminophenol based on graphene–chitosan composite

film modified glassy carbon electrode. *Electrochim. Acta* **2010,** *55*, 7102-7108.

6. Unnikrishnan, G.; Thomas, S., Diffusion and transport of aromatic hydrocarbons through natural rubber. *Polymer* **1994,** *35*, 5504-5510.
7. Visakh, P. M.; Thomas, S.; Oksman, K.; Mathew, A. P., Cellulose nanofibres and cellulose nanowhiskers based natural rubber composites: Diffusion, sorption, and permeation of aromatic organic solvents. *J. Appl. Polym. Sci.* **2012,** *124*, 1614-1623.
8. Gwaily, S. E.; Badawy, M. M.; Hassan, H. H.; Madani, M., Influence of thermal aging on crosslinking density of boron carbide:natural rubber composites. *Polym. Test.* **2003,** *22*, 3-7.
9. Alfrey, T.; Gurnee, E. F.; Lloyd, W., Duffusion in glassy polymers. *J. Polym. Sci.* **1966,** *12*, 249-261.
10. Crank, J., *The mathematics of diffusion*. 2nd ed.; Clarendon Press: Oxford, 1975.
11. Cui, Y.; Kumar, S.; Rao Kona, B.; van Houcke, D., Gas barrier properties of polymer/clay nanocomposites. *RSC Adv.* **2015,** *5*, 63669-63690.
12. Cui Y; Kundalwal S I; Kumar S, Gas barrier performance of graphene:polymer nanocomposites. *Carbon* **2016,** *98*, 313-333.
13. Hahn, D. W.; Özişik, M. N., *Heat conduction*. John Wiley & Sons: 2012.
14. Bacon, D. H., *Basic heat transfter*. Butterworth & Co. Ltd.: 1989.
15. Chen, S.; Moore, A. L.; Cai, W.; Suk, J. W.; An, J.; Mishra, C.; Amos, C.; Magnuson, C. W.; Kang, J.; Shi, L.; Ruoff, R. S., Raman measurements of thermal transport in suspended monolayer graphene of variable sizes in vacuum and gaseous environments. *ACS Nano* **2011,** *5*, 321-328.
16. Chen, S.; Wu, Q.; Mishra, C.; Kang, J.; Zhang, H.; Cho, K.; Cai, W.; Balandin, A. A.; Ruoff, R. S., Thermal conductivity of isotopically modified graphene. *Nat. Mater.* **2012,** *11*, 203-7.
17. Balandin, A. A.; Ghosh, S.; Bao, W.; Calizo, I.; Teweldebrhan, D.; Miao, F.; Lau, C. N., Superior thermal conductivity of single-layer graphene. *Nano Lett.* **2008,** *8*, 902-907.

18. Ghosh, S.; Calizo, I.; Teweldebrhan, D.; Pokatilov, E. P.; Nika, D. L.; Balandin, A. A.; Bao, W.; Miao, F.; Lau, C. N., Extremely high thermal conductivity of graphene: Prospects for thermal management applications in nanoelectronic circuits. *Appl. Phys. Lett.* **2008,** *92*, 151911.

19. Nika, D. L.; Pokatilov, E. P.; Askerov, A. S.; Balandin, A. A., Phonon thermal conduction in graphene: Role of Umklapp and edge roughness scattering. *Phys. Rev. B* **2009,** *79*, 155413.

20. Ho, C. Y.; Powell, R. W.; Liley, P. E., Thermal conductivity of the elements: a comprehensive review. *J. Phys. Chem. Ref. Data* **1974,** *3*, 1.

21. Sun, K.; Stroscio, M. A.; Dutta, M., Graphite C-axis thermal conductivity. *Superlattice. Microst.* **2009,** *45*, 60-64.

7. Discussion

7.1. Raman spectra and XRD intensity dependence

The Raman spectra of the GNP elastomer composites were obtained for more than ten scans for each specimen, and the laser beam was focused on the low-temperature fractured surfaces. As notated in Figure 4.5 and 5.4, the G bands from GNPs and the rubber peaks show an evolution upon the increasing content of GNPs. The ratio of these two peaks I_G/I_R can be plotted against the loading of the GNPs determined from TGA as presented in Figure 7.1. It should be noticed that the unit of the loading is "phr", which is calculated by the "ratio of the volume fraction of the GNPs to that of the elastomers in each case" × 100. The I_G/I_R ratio exhibits a clear increasing dependence on the loading of the GNPs, and the relationship is also reported by Pakjamsai and Suwanprateeb.[1] The scattering intensity (I) of the Raman peak can be expressed as the equation as below,

$$I = K \cdot S \cdot C \cdot I_0 \tag{7.1}$$

where I_0 is the intensity of the exciting radiation, S is the volume illuminated by the laser beam, C is the concentration of the sample, and K is the constant for each band. The similar linear correlation and the trend of size dependence are also observed in the ratio of the graphene G peak to the rubber band in the XRD patterns as well (see in Figure 7.2). The reason is similar to that in the Raman spectra except the GNP/NBR basically owns the summit. The linear dependence of the intensity upon the loadings of the fillers can be calibrated and utilized to determine the volume fraction of the fillers. What is more, the correlation between the intensity and the loading is better in Raman spectra than the XRD patterns. Furthermore, the dispersion of the GNPs in the elastomers can be quantified as demonstrated in Section 2.4.2.2 by Equation (2.1), and the dispersion parameters, D, can be calculated as shown in

Figure 7.3. It shows that the dispersion trends to be poorer with the increasing loading for all GNP composites (a value of 0.18 to 0.30 for GO/epoxy composites at loading < 1wt% can be used as a comparison[2]), which can be attributed to the aggregation formation of the GNPs at higher loadings.

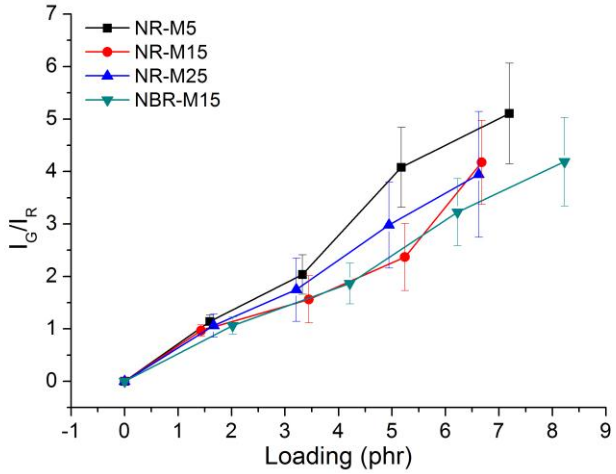

Figure 7.1 Intensity ratios of G band to rubber Raman band in Raman spectra (30 scanning for each point). Laser excitation: 633 nm.

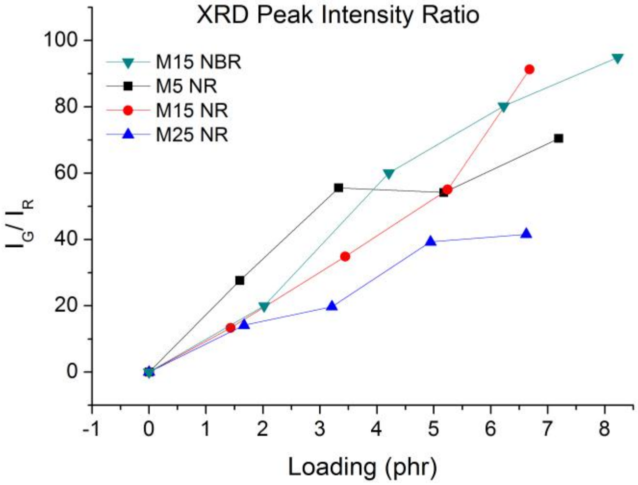

Figure 7.2 Intensity ratios of graphene G peak to broad rubber band in XRD spectra

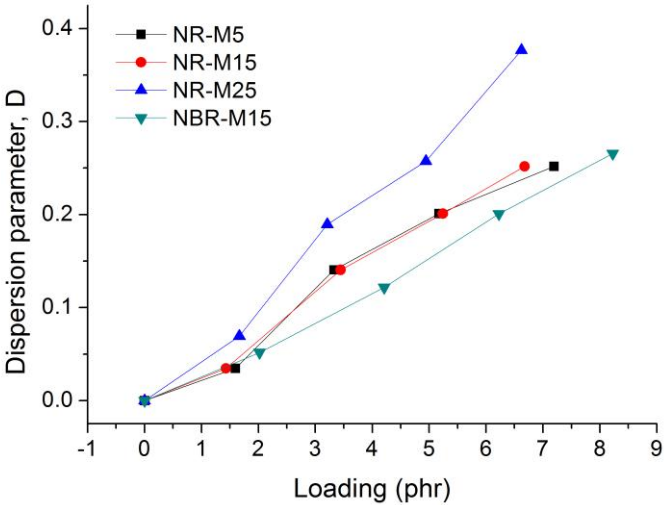

Figure 7.3 Dispersion parameters of the composites calculated from Raman results.

Another intensity change of the XRD pattern occurs when the position of the specimens alters which was schematically illustrated in Figure 3.3. As can be seen in Figure 3.3a, the specimen was placed with the top surface reflected by the X-ray beam whereas in Figure 3.3b the specimens were rotated by 90 ° with edge surface exposed to the X-ray beam. The X-ray diffraction patterns of the M15 NR composites at 10 and 20 phr can be seen in Figure 7.4. In Figure 7.4a and 7.4c, for the diffraction on the top surface which the GNP flakes were determined to be parallel to by the SEM images and polarized Raman spectroscopy, the XRD patterns of the composites both exhibit a sharp graphitic peak at 26.5 ° with a broad rubber band at around 19 °. For the diffraction on the edge surface which the GNP flakes were determined to be perpendicular to, the XRD patterns can be seen in Figure 7.4b and 7.4d. The graphitic peaks become much weaker and even weaker than the rubber peaks.

This can be explained by the reason that the preferred alignment imparts the intrinsic feature of the GNP flakes into the composites, which leads to the anisotropic intensity characteristics of the composites upon the X-ray diffraction. To be more specific, the X-ray diffraction on the top surface is a good diffraction that follows the Bragg's law whereas a poor diffraction is obtained on the edge surface. On the other hand, if the

GNP flakes are 3D randomly oriented in the rubber matrix, the intensity ratio of the graphitic peak to the rubber peak should be the same no matter how the specimen is positioned.

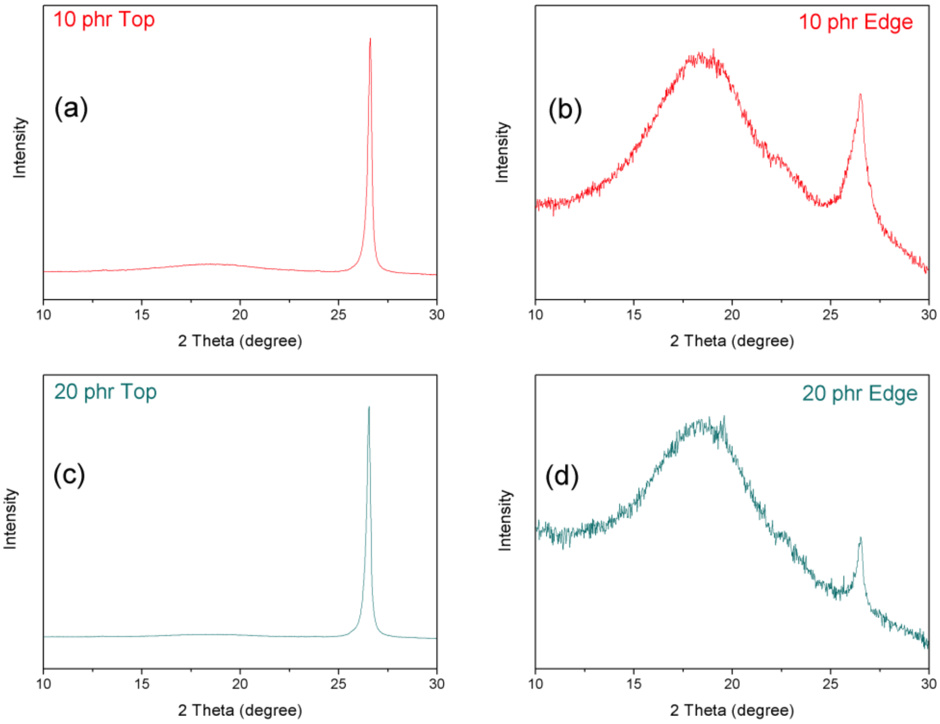

Figure 7.4 The X-ray diffraction patterns of M15 10 phr and 20 phr natural rubber composites. (a) (c) Top reflection; (b) (d) edge reflection.

7.2. Crosslink density

The crosslink density can be determined by the swelling experiment of rubbers using the Flory-Rehner equation[3-12],

$$-[\ln(1-v_r) + v_r + \chi v_r{}^2] = V_0\, n\left(v_r{}^{1/3} - v_r/2\right) \qquad (7.2)$$

where v_r is the volume fraction of the rubber in the swollen mass and calculated by the mass and densities. V_0 is the molar volume of the solvent (106.2 cm^3 for toluene[11]). n is the crosslink density (the number of active network chain segments per unit of volume), and χ is the Flory-Huggins polymer-solvent interaction parameter. The value of χ for NR-toluene and NBR-toluene are taken as 0.393[11] and 0.435[12]. The crosslink densities of all the composites can be calculated using Equation 7.2 and plotted as in

Figure 7.5. It is clear that the addition of all fillers enhances the crosslinking for both elastomers whereas the GNPs show superiority over carbon black. For NR GNP composites as seen in Figure 7.5a, the enhancement effect of the GNPs can be ranked in order as M25 < M15 < M5, which is similar to the ranking of their mechanical reinforcement as described in Chapter 4. The reason of this ranking can be explained by deficiency of the larger particle morphology in the matrix that tend to be rippled, folded or in shape of “U” or “O”. These characteristics reduce the interface areas between the GNPs and the rubber matrix that leads to a smaller possibility to form physical crosslinking.

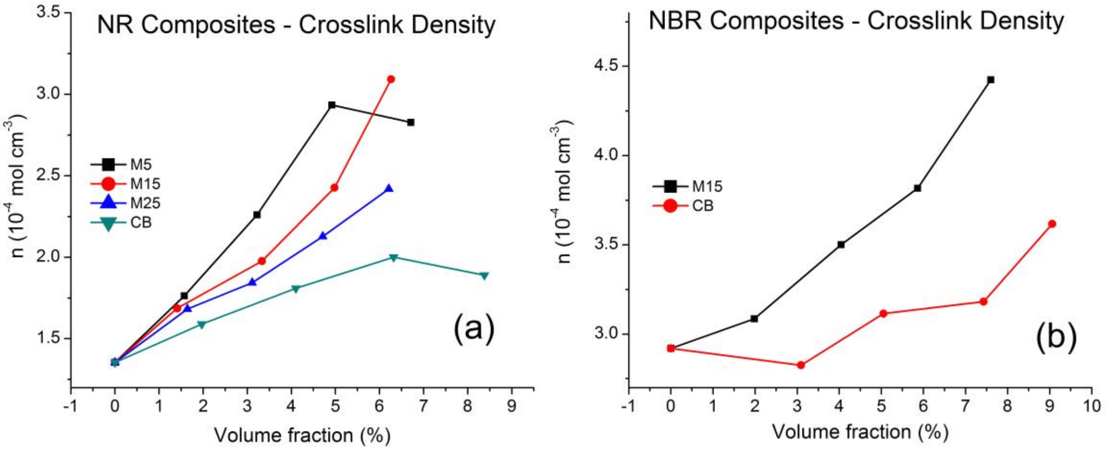

Figure 7.5 Crosslink density of the (a) NR and (b) NBR nanocomposites. Each data point represents the result of one specimen.

On the other hand, to further understand the mechanical behavior and calculate crosslink density of the GNP elastomer composites in another way, the stress-strain curves are converted into Mooney-Rivlin curves. Specifically, the reduced stress $\sigma^* = (\sigma / (\alpha - \alpha^{-2}))$ is plotted against the reciprocal of the extension ratio α ($\alpha = \varepsilon + 1$) as represented in Figure 7.6 and 7.7. Particularly, for filled rubber composites, the extension ratio should be substituted by the intrinsic extension ratio α' that is involved with the stretching of the rubber matrix as follow[6]

$$\alpha' = (\alpha - 1)x + 1 \tag{7.3}$$

$$x = 1 + 2.5V_{\mathrm{f}} + 14.1{V_{\mathrm{f}}}^{2} \tag{7.4}$$

where x is the amplication factor. It can be seen that at small extension ratio (high α^{-1} values), the reduced stress undergoes a decrease at the starting of the stretching, which is attributed to the Payne effect. On the other hand, when the specimens were stretched to a high extension ratio ($\alpha^{-1} < 0.2$), an abrupt upturn shows up, which was explained by controversial reasons including entanglement of the molecular segments that perform like effective crosslinking,[13] finite extensibility of the polymer chains[14-15] and the most popular, stress-induced crystallization.[16-18] Moreover, with increasing content of GNP and carbon black particles, the upturn of the curves occurs at smaller strains, which implies that the addition of the fillers encourages the stress-induced crystallization.

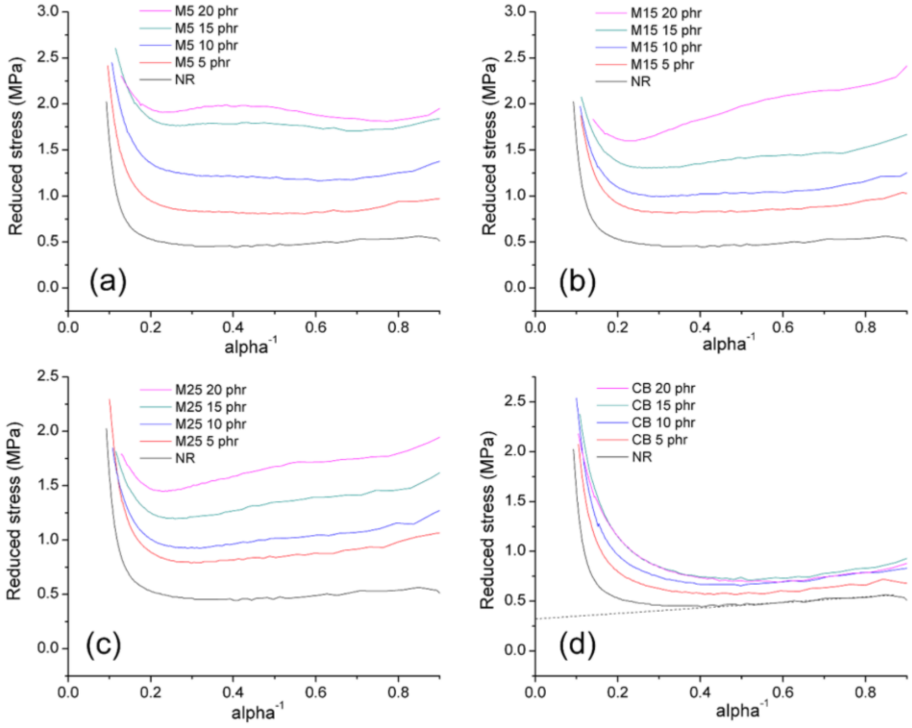

Figure.7.6 Mooney-Rivlin plots of NR composites. (a) M5; (b) M15; (c) M25; (d) CB.

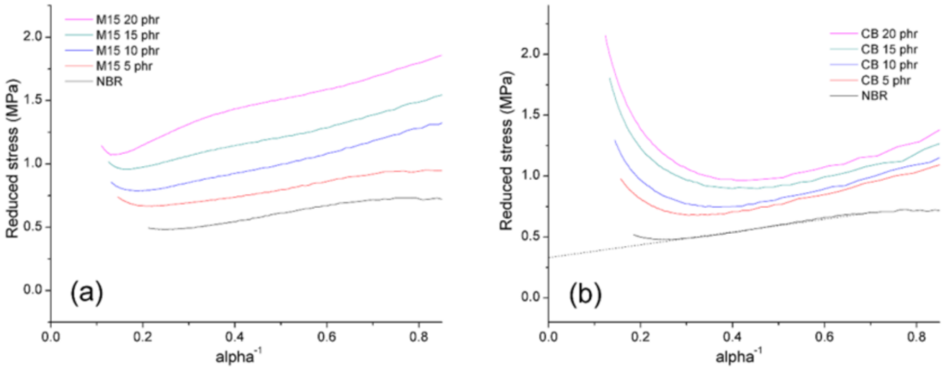

Figure 7.7 Mooney-Rivlin plots of NBR composites. (a) M15; (b) CB.

Apart from the mechanical behavior analysis, the crosslinking density can also be acquired from the Mooney-Rivlin curves. Specifically, according to *Tube Model Theory of rubber elasticity,*[19-21] a relationship involved the reduced stress σ^* can be given as follow

$$\sigma^* = G_\mathrm{c} + G_\mathrm{e}\,\alpha^{-1} \tag{7.5}$$

where G_c refers to the elastic modulus regarding the crosslinking constraints and G_e is related to the entanglement modulus involved with the topological tube-like constraints. These two parameters can be determined from the Mooney-Rivlin curves by the y-axis intercept and the gradient of the linear part as presented by the dash lines in Figure 7.6 and 7.7. G_c is involved with the crosslinking density and the relationship can be expressed as follow

$$G_\mathrm{c} = A_\mathrm{c} v_\mathrm{c} k_\mathrm{B} T \tag{7.6}$$

where A_c is the microstructure factor depending on the fluctuations of the effective crosslinking junctions and the values is normally taken as 0.67;[22] v_c is the crosslinking density; k_B is the Boltzmann constant; T is the absolute temperature of curing.

Based on the Mooney-Rivlin Curves and the Equation (7.5) and (7.6), the crosslinking density can be calculated and compared with those obtained from Flory-Rehner equation (see in Figure 7.8 and 7.9). As presented in Figure 7.8 for NR composites, the crosslinking density of NR composites acquired by two methods exhibit great consistence with each other and all increase with the addition of fillers implying the additional chemical and physical crosslinking created by the fillers and the rubber matrix. In details, GNP shows a higher promotion than carbon black particles that can be attributed the larger interactive interfaces of GNP imparted by the high aspect ratio. For NBR composites shown in Figure 7.9, the crosslinking density calculated from two methods shows a similarly increasing trend with the addition of fillers, but of different amplitudes. Particularly, the CB NBR composites exhibit much higher values of crosslink density calculated from Flory-Rehner equation. The big differentiation in NBR composites is probably due to the difficulty in calculating the correct value of the Flory-Huggins polymer-solvent interaction term χ. As NBR is a co-polymer, the molecular structure such as monomer ratio and sequence, and chain linearity can be complicated which is highly depending on the processing history, which affects the interaction of the polar groups -C≡N with the organic solvent.

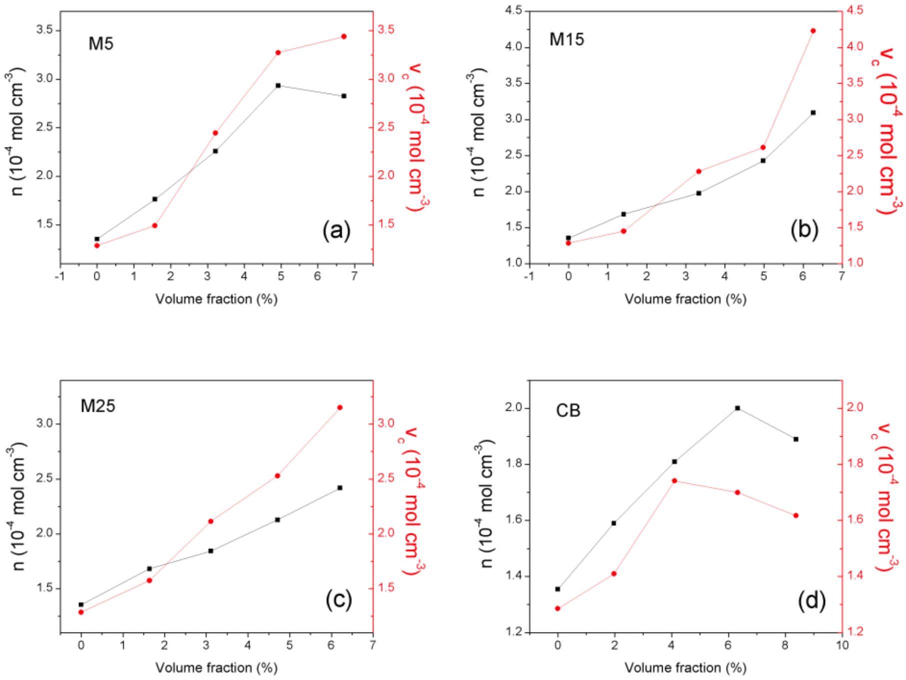

Figure 7.8 Crosslinking densities of the NR composites calculated by Flory-Rehner equation (black curves) and Mooney-Rivlin plots (red curves). (a) M5; (b) M15; (c) M25; (d) CB.

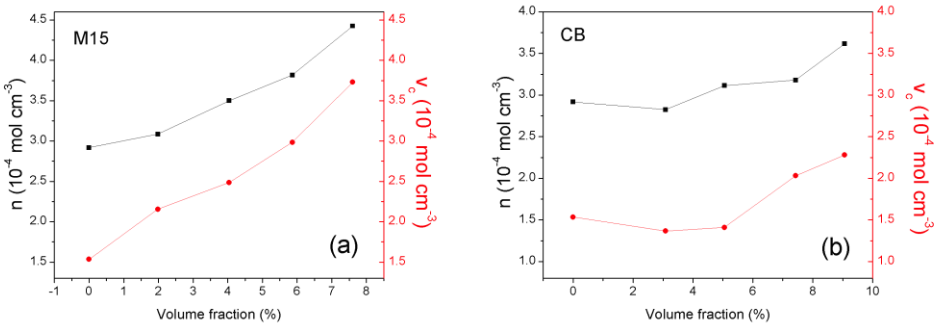

Figure 7.9 Crosslinking densities of the NR composites calculated by Flory-Rehner equation (black curves) and Mooney-Rivlin plots (red curves). (a) M15; (b) CB.

7.3. Mechanisms of reinforcement

7.3.1. Rule of mixture

One of the simplest methods of evaluating the reinforcement achieved in nanocomposites is the "*rule of mixtures*"[23] whereby the Young's modulus of the nanocomposite E_c is given by the relationship

$$E_c = E_f V_f + E_m V_m \tag{7.7}$$

where E_f, E_m are the effective modulus of the filler and the modulus of the matrix, while V_f and V_m are the volume fractions of the filler and the natural rubber matrix. The value of the effective modulus of the fillers can be determined directly from the slopes of the lines in Figure 4.24b and 5.13b for the modulus values at 100% strain. The derived values of E_f for the different GNPs and carbon black are given in Table 7.1 and it can be seen that E_f is significantly higher for the GNPs than the carbon black.

As mentioned earlier, the orientation and size of a platelet-like filler plays a major role in the reinforcement, and for this reason a modified rule of mixtures has been proposed[24]:

$$E_c = E_{eff} V_f \eta_o \eta_l + E_m V_m \tag{7.8}$$

where E_{eff} is now the effective modulus of the GNPs and η_o is the Krenchel orientation factor which depends on the average orientation of the filler with respect to the applied stress. The parameter η_l is the length distribution factor and takes values between 0 and 1. It is possible to take into account the effect of orientation to determine the effective modulus of the GNPs by dividing E_f by η_o determined from the orientation parameters in Figures 4.12-4.14 and 5.9[24]. The values of E_{eff} determined (assuming at this stage η_l = 1) are of the order of 60 MPa as shown in Table 7.1.

Table 7.1 Modulus at 100% strain for the NR nanocomposites and NBR nanocomposites for a volume fraction of 5% filler.

	E_{100} at V_f = 5% (MPa)	E_f (MPa)	η_o	E_{eff} (MPa)
NR*	0.81 ±0.02	-	-	-
NR-N330	1.36 ±0.03	11.8 ±1.0	-	-
NR-M5	3.55 ±0.07	55.6 ±1.8	0.825	67.4 ±2.2
NR-M15	2.78 ±0.05	40.2 ±1.4	0.725	55.4 ±1.9
NR-M25	2.74 ±0.07	39.4 ±1.8	0.670	58.8 ±2.7
NBR*	1.08 ±0.02	-	-	-
NBR-N330	1.62 ±0.04	11.8 ±1.2	-	-
NBR-M15	2.12 ±0.05	21.8 ±1.4	0.720	30.2 ±1.9

E_f is the modulus of the filler determined using the rule, η_o is the Krenchel orientation factor determined from the parameters by polarized Raman data, E_{eff} is the effective modulus of the GNP determined using Equation (7.8), and errors of the E_{100} are given by the mean values of the error bars of each curve in Figure 4.16b and 5.10b.

* Data for unfilled NR and NBR.

This shows that even though the values of E_f are different for different composites, once the orientation factor is taken into account, similar vales of E_f are obtained for the NR composites filled with the three types of GNPs. This also confirms the validity of the Equation. (7.8).

7.3.2. Raman band shifts

The effective modulus of the GNPs can also be estimated completely independently from the stress-induced Raman band shifts shown in Figure 4.27 and 5.16. It is well established[25] that the 2D bands of a graphene monolayer with a Young's modulus 1050 GPa[26] will undergo a shift of -60 cm^{-1} when deformed to a strain of 1%. This observation allows the effective modulus of any type of graphene under tensile stress to be determined in a variety of microstructures, including nanocomposites, from stress-induced shifts of the 2D band. The effective modulus of the GNPs in the nanocomposites is therefore given by

$$E_{\text{eff}} = - \frac{\mathrm{d}\omega_{2\mathrm{D}}}{\mathrm{d}\varepsilon} \frac{1050}{60} \text{ GPa} \tag{7.9}$$

where $-\mathrm{d}\omega_{2\mathrm{D}}/\mathrm{d}\varepsilon$ is the shift rate of the 2D Raman band in the nanocomposite in cm^{-1}/%. The shift rates measured for the nanocomposites in this present study were very small as can be seen in Figure 4.27 and 5.16, typically around -1 cm^{-1} for 100% strain (E_{eff} ~ 175 MPa), indicating that the effective modulus of the GNPs in the NR is relatively small compared with that of pristine graphene (1050 GPa). The 2D band shifts for the GNPs measured for the nanocomposites with 20 phr of GNPs are listed in Table 7.2 and the values of E_{eff} calculated using Equation (7.9) are given in the Table. It can be seen that the derived values of E_{eff} are in the range 110-204 MPa but there is considerable scatter in the data.

It is interesting to consider why the Raman analysis gives a higher value of effective Young's modulus of the GNPs in the NR than the mechanical testing data, and why both values are many orders of magnitude lower than the value of 1050 GPa for pristine graphene.[26] The Raman measurements were made upon individual exposed

GNP flakes under stress in the nanocomposites, whereas the mechanical data were obtained for the deformation the whole nanocomposite. We have not so far taken into account any length effects that will reduce the effectiveness of the reinforcement by the GNPs ($\eta_l < 1$). The difference between the values of E_{eff} determined using the two techniques could be rationalised through using a value of η_l of the order of 0.3 in Equation (7.8) for the values determined by mechanical testing. Another possible reason for the difference can be that the stress determined from the stress-strain curves is the nominal stress, which did not consider the Poisson's contraction that narrows the cross-section area of the specimens. Hence, the values of E_{eff} determined from the mechanical testing were smaller than the actual moduli.

Table 7.2 Shift of the 2D Raman band determined for each of the GNP nanocomposites and the calculated effective modulus at 100% strain

	Band shift rate (10^{-2} cm^{-1}/ %strain)	E_{eff} (MPa)
NR-M5	-1.17 ± 0.27	204 ± 48
NR-M15	-1.17 ± 0.53	204 ± 93
NR-M25	-0.93 ± 0.31	163 ± 54
NBR-M15	-0.63 ± 0.57	110 ± 100

7.3.3. Shear lag theory

In any case, both effective modulus values obtained by *the rule of mixture* and the Raman band shifts are 4 orders of magnitude lower than that of the pristine graphene. This indicates that although impressive levels of reinforcement can be obtained through the use of GNPs in the rubbers, stress transfer from the rubbers to the GNPs that takes place through the rubbers/GNP interface by shear of the low modulus rubber matrix[27] is relatively inefficient. This means that the full potential of reinforcement by the GNPs is difficult to achieve in such soft systems.

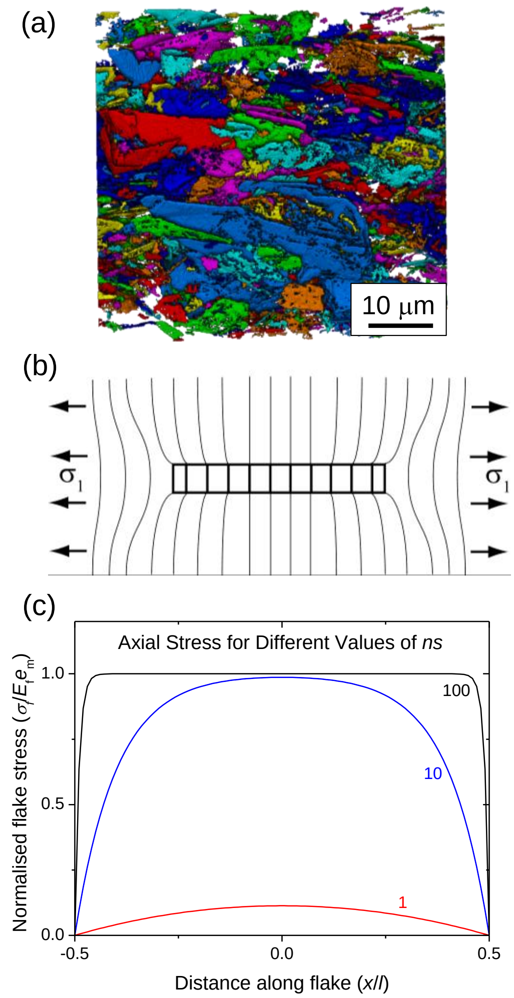

Figure 7.10 (a) Artificially-coloured image of a CT scan of in natural rubber nanocomposite containing M25 GNPs nanoplatelelets. (b) Deformation patterns for a discontinuous nanoplatelet in a polymer matrix under stress. (c) Predicted variation of normalized axial stress with distance along the nanoplatelet for a short nanoplatelet in a matrix. (The values of the product *ns* are indicated.)

To explain the deficiency, we have developed a comprehensive theory for the mechanisms of reinforcement of polymers by nanoplatelets that enables us to predict the effect of how reinforcement is controlled by factors such as matrix modulus, particle geometry and the strength of the filler-matrix interface. The basis of the theory is shown in Figure 7.10. The individual nanoplatelets are assumed to be well dispersed in the polymer matrix without interacting with each other as shown in the CT scan in Figure 7.10a.

Stress transfer from the matrix to the individual aligned nanoplatelet shown in Figure 7.10b is assumed to take place through a shear stress at the nanoplatelet/matrix interface.[28-29] Before deformation, parallel lines perpendicular to the nanoplatelet can be drawn from the matrix through the nanoplatelet. When the system is subjected to axial stress, σ_1, parallel to the nanoplatelet axis, the lines become distorted as shown in Figure 7.10b since the Young's modulus of the matrix is much less than that of the nanoplatelet. This induces a shear stress at the nanoplatelet/matrix interface. The axial stress in the nanoplatelet will build up from zero at the nanoplatelet ends to a maximum value in the middle of the nanoplatelet and shown in Figure 7.10c. The uniform strain assumption means that, if the nanoplatelet is long enough, the strain in the middle of the nanoplatelet equals that of the matrix. Since the nanoplatelets have a much higher Young's modulus than the matrix the nanoplatelets carry most of the load in the composite.

The behavior of a single discontinuous nanoplatelet in a matrix can be modelled using shear lag theory[28, 30-33] in which it is assumed that the nanoplatelet of length l and thickness t is surrounded by a layer of resin with an overall thickness of T.[28] It is also assumed that both the nanoplatelet and matrix deform elastically and the nanoplatelet-matrix interface remains intact. The final equation for the distribution of nanoplatelet stress as a function of distance, x along the nanoplatelet at a given level of matrix strain, e_{m}, was determined and is given by[28]

$$\sigma_{\mathrm{f}}(x) = E_{eff}\, e_{\mathrm{m}} \left[\ 1 - \frac{\cosh(nx/t)}{\cosh(nl/2t)}\ \right] \tag{7.10}$$

where $n = \sqrt{\dfrac{2G_{\mathrm{m}}}{E_{\mathrm{eff}}}\ \dfrac{t}{T}}$,

E_{eff} is the effective Young's modulus of the nanoplatelet and G_{m} is the shear modulus of the matrix. It is convenient to use the concept of nanoplatelet aspect ratio, $s = l/t$ so that the above equation can be rewritten as

$$\sigma_{\mathrm{f}}(x) = E_{\mathrm{eff}}\, e_{\mathrm{m}} \; [1 - \frac{\cosh\left(ns\frac{x}{l}\right)}{\cosh(ns/2)}] \tag{7.11}$$

for the axial nanoplatelet stress. The effect of the different parameters upon the build-up of stress in a nanoplatelet is demonstrated in Figure 7.10c for different values of the product *ns*. It can be seen that the nanoplatelet is most highly stressed, i.e. the most efficient reinforcement is obtained, when the product *ns* is high.

The mean stress along an aligned individual nanoplatelet can be determined from the integral

$$\bar{\sigma}_{\mathrm{f}} = \frac{1}{l}\int_{-l/2}^{+l/2} \sigma_{\mathrm{f}}(x)\,\mathrm{d}x \tag{7.12}$$

Substitution of Equation (7.11) into this integral gives

$$\bar{\sigma}_{\mathrm{f}} = E_{\mathrm{eff}}\, e_{\mathrm{m}} [\; 1 - \frac{\tanh(ns/2)}{ns/2} \;] \tag{7.13}$$

This equation again shows that the best reinforcement is obtained when E_{eff} is high and the product *ns* is very large.

The Young's modulus of the nanoplatelet E_{f} in the nanocomposite is given by the mean stress $\bar{\sigma}_{\mathrm{f}}$ divided by the nanoplatelet strain e_{f} (= e_{m} for uniform strain). Hence for an aligned individual nanoplatelet Equation (7.13) gives

$$E_{\mathrm{f}} = E_{\mathrm{eff}} \; [1 - \frac{\tanh(ns/2)}{ns/2} \;] \tag{7.14}$$

This shows that the value of E_f for an aligned graphene nanoplatelet in the nanocomposite is controlled by the effective Young's modulus of the nanoplatelet, E_{eff}, and the value of *ns*. It also follows that the length factor is given by

$$\eta_l = 1 - \frac{\tanh(ns/2)}{ns/2} \tag{7.15}$$

If the nanoplatelets are not aligned then the Krenchel orientation factor[34-35] needs to be taken into account and Equation (7.14) becomes

$$E_f = E_{eff}\,\eta_o \; [1 - \frac{\tanh(ns/2)}{ns/2} \;] \tag{7.16}$$

In the case where *ns* is small this equation can be recast since the hyberbolic function can be represented by a Taylor series as

$$\tanh x = x - \frac{x^3}{3} + \frac{2x^5}{15} - \frac{17x^7}{315} + ... \tag{7.17}$$

If *ns* is small Equation (7.16) then becomes

$$E_f \approx E_{eff}\,\eta_o \frac{(ns/2)^2}{3} \tag{7.18}$$

Substituting the value of *n* given in Equation (7.10), this gives for small values of *n*

$$E_f \approx \eta_o \frac{s^2}{6} \frac{t}{T} G_m \tag{7.19}$$

The shear modulus of the matrix is related to its Young's modulus through the relation[31]

$$G_m = \frac{E_m}{2(1+\nu)} \tag{7.20}$$

where ν is Poisson's ratio (typically $\nu \sim 0.35 – 0.5$ for rigid polymers and elastomers). Combining Equation (7.19) and (7.20) gives the final equation

$$E_f \approx \eta_o \frac{s^2}{12} \frac{t}{T} \frac{E_m}{(1+\nu)} \tag{7.21}$$

Hence it is predicted that $E_f \propto E_m$ when ns is small corresponding, for a fixed aspect ratio s, to low values of G_m and hence E_m. Moreover the slope of unity on a log-log plot of E_f versus E_m is predicted, as found from the analysis of literature data[36] (see Figure 7.11).

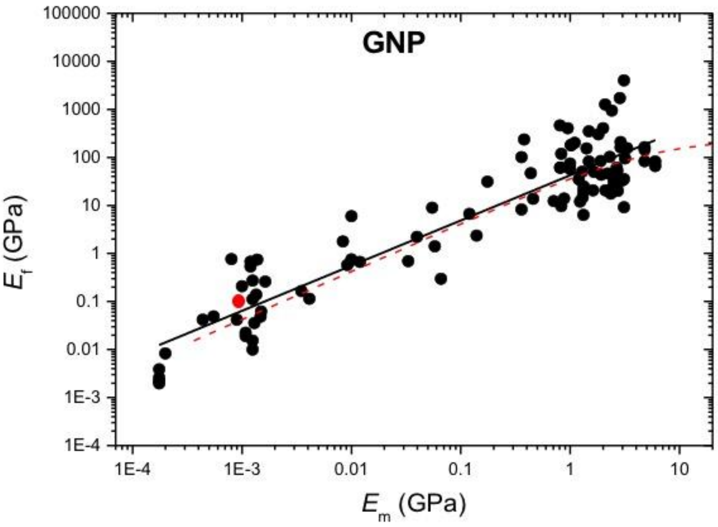

Figure 7.11 Comparison of literature values of the Young's modulus of the filler, E_f, as a function of matrix Young's modulus, E_m, with the behavior predicted using Equation (7.16) for graphite nanoplatelets (GNPs) in a range of different polymers (broken red line). The solid black line is the best fit of the data to a straight line.[36] (The red dot indicates the E_f and E_m of our GNP elastomer composites)

Varying the parameters in Equation (7.16) reveals some interesting findings as shown in Figure 7.12. The effect of varying the value of the effective filler modulus E_{eff} is shown in Figure 7.12a. A higher value of E_{eff} leads to a higher value of E_f for rigid matrix materials ($E_m > 1$ GPa) but for flexible matrices, E_f is independent of E_{eff} as predicted by Equation (7.21). The value of E_f depends upon the degree of orientation of the nanoplatelets as shown in Figure 7.12b; it is reduced by a factor of 8/15 for randomly oriented nanoplatelets compared with perfectly-aligned ones.[34-35] Figure 7.12c shows that E_f depends strongly upon the aspect ratio, s, highlighting that the aspect ratio of the nanofiller is of vital importance. Finally Figure 7.12d shows that E_f

depends strongly upon the ratio, t/T. This parameter essentially depends upon how rapidly the stress decays into the matrix away from the nanofiller and is controlled by the strength of the filler-matrix interface. Hence this ratio, t/T, can be thought of as an indication of the quality of the interface[28] and E_f will be higher for stronger interfaces.

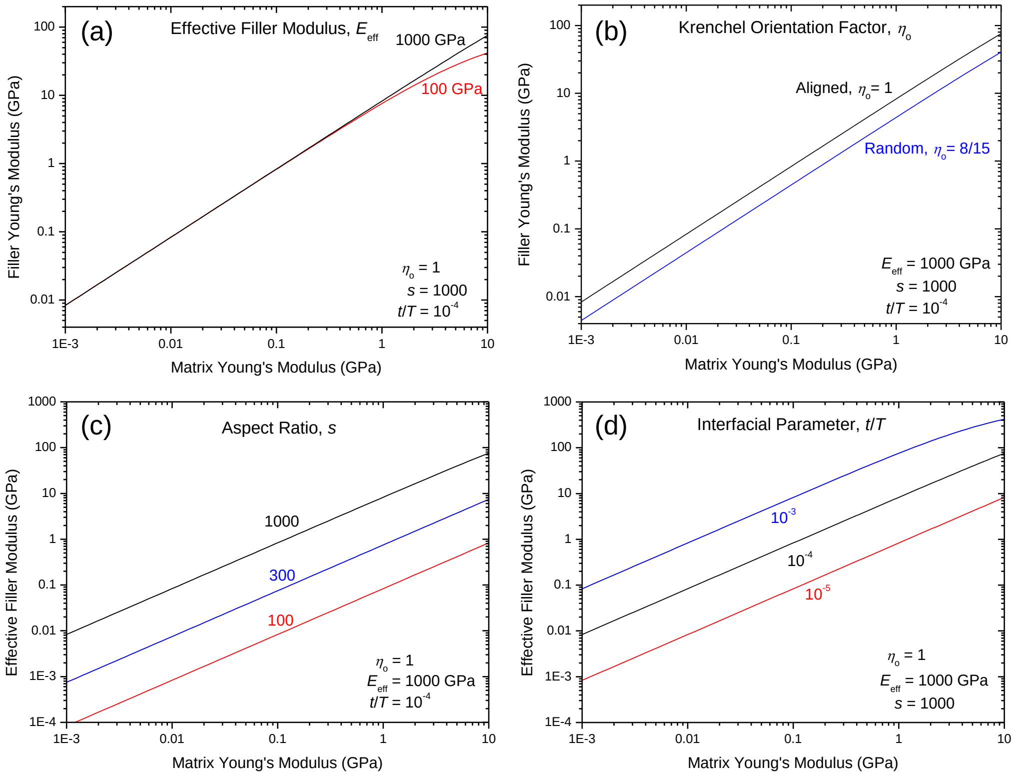

Figure 7.12 Filler Young's modulus as a function of matrix Young's modulus predicted using Equation (7.16). (a) Effect of different graphene Young's modulus, E_{eff}. (b) Effect of different Krenchel orientation factor $\eta_{o.}$ (c) Effect of different nanoplatelet aspect ratio, s. (d) Effect of different interfacial parameter, t/T. (The parameters used are listed in each case).

It is clear that the development of our simple but comprehensive theory has enabled the effective Young's modulus of graphite nanoplatelets in polymer-based nanocomposites to be modelled with a high degree of precision. The importance of different structural parameters is clearly highlighted. The theory gives a convincing explanation of why it is not possible to realise the promised 1 TPa Young's modulus of the graphene in low modulus polymeric matrices. In fact, it predicts, perhaps rather surprisingly, that the Young’s modulus of such a nanocomposite will be independent of the Young’s modulus of the nanofiller and more correlated to the modulus of the soft matrix.

This theory does have its limtations, however. It is only concerned with the elastic deformation of the nanocomposites at relatively low levels of loading before any agglomeration or restacking effects occur. It is also not related directly to other important mechanical properties such as fracture strength, tear resistance or toughness. Nevertheless, the ability of nanofillers such as graphene to increase the stiffness of a polymer is of major technological importance and our theoretical approach represents a significant step forward towards a full understanding of the mechanical properties of polymer-based nanocomposties reinforced with nanoplatelets.

References

1. Pakjamsai, S.; Suwanprateeb, J., Using FT-Raman spectroscopy for quantitative determination of high filler content in particulated composites. *J. Appl. Polym. Sci.* **2000,** *78*, 1947-1954.

2. Li, Z.; Young, R. J.; Wang, R.; Yang, F.; Hao, L.; Jiao, W.; Liu, W., The role of functional groups on graphene oxide in epoxy nanocomposites. *Polymer* **2013,** *54*, 5821-5829.

3. Araby, S.; Zhang, L.; Kuan, H.-C.; Dai, J.-B.; Majewski, P.; Ma, J., A novel approach to electrically and thermally conductive elastomers using graphene. *Polymer* **2013,** *54*, 3663-3670.

4. Lin, Y.; Liu, K.; Chen, Y.; Liu, L., Influence of graphene functionalized with zinc dimethacrylate on the mechanical and thermal properties of natural rubber nanocomposites. *Polym. Composite.* **2015,** *36*, 1775-1785.

5. Yang, G.; Liao, Z.; Yang, Z.; Tang, Z.; Guo, B., Effects of substitution for carbon black with graphene oxide or graphene on the morphology and performance of natural

rubber/carbon black composites. *J. Appl. Polym. Sci.* **2015,** *132,* 41832.

6. Xing, W.; Wu, J.; Huang, G.; Li, H.; Tang, M.; Fu, X., Enhanced mechanical properties of graphene/natural rubber nanocomposites at low content. *Polym. Int.* **2014,** *63*, 1674-1681.

7. Zhang, X.; Xue, X.; Yin, Q.; Jia, H.; Wang, J.; Ji, Q.; Xu, Z., Enhanced compatibility and mechanical properties of carboxylated acrylonitrile butadiene rubber/styrene butadiene rubber by using graphene oxide as reinforcing filler. *Compos. Part B - Eng.* **2017,** *111*, 243-250.

8. Araby, S.; Meng, Q.; Zhang, L.; Kang, H.; Majewski, P.; Tang, Y.; Ma, J., Electrically and thermally conductive elastomer/graphene nanocomposites by solution mixing. *Polymer* **2014,** *55*, 201-210.

9. Kang, H.; Tang, Y.; Yao, L.; Yang, F.; Fang, Q.; Hui, D., Fabrication of graphene/natural rubber nanocomposites with high dynamic properties through convenient mechanical mixing. *Compos. Part B- Eng.* **2017,** *112,* 1-7.

10. Yaragalla, S.; A.P, M.; Kalarikkal, N.; Thomas, S., Chemistry associated with natural rubber–graphene nanocomposites and its effect on physical and structural properties. *Ind. Crop. Prod.* **2015,** *74*, 792-802.

11. Wu, J.; Xing, W.; Huang, G.; Li, H.; Tang, M.; Wu, S.; Liu, Y., Vulcanization kinetics of graphene/natural rubber nanocomposites. *Polymer* **2013,** *54*, 3314-3323.

12. Yang, J.; Tian, M.; Jia, Q.-X.; Shi, J.-H.; Zhang, L.-Q.; Lim, S.-H.; Yu, Z.-Z.; Mai, Y.-W., Improved mechanical and functional properties of elastomer/graphite nanocomposites prepared by latex compounding. *Acta Mater.* **2007,** *55*, 6372-6382.

13. López-Manchado, M. A.; Valentín, J. L.; Carretero, J.; Barroso, F.; Arroyo, M., Rubber network in elastomer nanocomposites. *Eur. Polym. J.* **2007,** *43*, 4143-4150.

14. Treloar, L. R. G., The photoelastic properties of short-chain molecular networks. *Trans. Faraday. Soc.* **1954,** *50*, 881-896.

15. Isihara, A.; Hashitsume, N.; Tatibana, M., Statistical theory of rubber‐like elasticity. IV. (two‐dimensional stretching). *J. Chem. Phys.* **1951,** *19*, 1508-1512.

16. Nie, Y.; Huang, G.; Qu, L.; Wang, X.; Weng, G.; Wu, J., New insights into thermodynamic description of strain-induced crystallization of peroxide cross-linked natural rubber filled with clay by tube model. *Polymer* **2011,** *52*, 3234-3242.

17. Flory, P. J., Effects of molecular structure on physical properties of butyl rubber. *Ind. Eng. Chem.* **1946,** *38*, 417-436.

18. Mark, J. E., *Physical properties of polymers*. 2nd ed.; Springer: Cincinnati, Ohio, 2007.

19. Edwards, S. F.; Vilgis, T. A., The tube model theory of rubber elasticity. *Rep. Prog. Phys.* **1988,** *51*, 243.

20. Klüppel, M., Finite chain extensibility and topological constraints in swollen networks. *Macromolecules* **1994,** *27*, 7179-7184

21. Heinrich, G., Contribution of entanglements to the mechanical properties of carbon black filled polymer networks. *Macromolecules* **1993,** *26*, 1109-1119.

22. Klüppel, M., Network structure and mechanical properties of sulfur-cured rubbers. *Macromolecules* **1994,** *27*, 3596-3603.

23. Young, R. J.; Loverll, A. P., *Introduction to polymers*. 3rd ed.; CRC Press: Boca Raton, 2011.

24. Li, Z.; Young, R. J.; Wilson, N. R.; Kinloch, I. A.; Vallés, C.; Li, Z., Effect of the orientation of graphene-based nanoplatelets upon the Young's modulus of nanocomposites. *Compos. Sci. Technol.* **2016,** *123*, 125-133.

25. Young, R. J.; Kinloch, I. A.; Gong, L.; Novoselov, K. S., The mechanics of graphene nanocomposites: A review. *Compos. Sci. Technol.* **2012,** *72*, 1459-1476.

26. Lee, C.; Wei, X.; Kysar, J. W.; Hone, J., Measurement of the elastic properties and intrinsic strength of monolayer graphene. *Science* **2008,** *321*, 385-8.

27. Gong, L.; Kinloch, I. A.; Young, R. J.; Riaz, I.; Jalil, R.; Novoselov, K. S., Interfacial stress transfer in a graphene monolayer nanocomposite. *Adv. Mater.* **2010,** *22*, 2694-7.

28. Gong, L.; Kinloch, I. A.; Young, R. J.; Riaz, I.; Jalil, R.; Novoselov, K. S.,

Interfacial Stress Transfer in a Graphene Monolayer Nanocomposite. *Adv. Mat.* **2010,** *22* (24), 2694-2697.

29. Young, R. J.; Kinloch, I. A.; Gong, L.; Novoselov, K. S., The mechanics of graphene nanocomposites: a review. *Compos. Sci. Technol.* **2012,** *72* (12), 1459-1476.

30. Hull, D.; Clyne, T. W., *An introduction to composite materials*. 2nd ed.; Cambridge University Press: Cambridge ; New York, 1996.

31. Young, R. J.; Lovell, P. A., *Introduction to Polymers, Third Edition*. CRC Press: Boca Baton, Florida, USA, 2013.

32. Cox, H. L., The Elasticity and Strength of Paper and Other Fibrous Materials. *Brit. J. Appl. Phys.* **1952,** *3*, 72-79.

33. Nairn, J. A., On the use of shear-lag methods for analysis of stress transfer unidirectional composites. *Mech. Mater.* **1997,** *26*, 63-80.

34. Li, Z. L.; Young, R. J.; Kinloch, I. A.; Wilson, N. R.; Marsden, A. J.; Raju, A. P. A., Quantitative determination of the spatial orientation of graphene by polarized Raman spectroscopy. *Carbon* **2015,** *88*, 215-224.

35. Li, Z. L.; Young, R. J.; Wilson, N. R.; Kinloch, I. A.; Valles, C.; Li, Z., Effect of the orientation of graphene-based nanoplatelets upon the Young's modulus of nanocomposites. *Compos. Sci. Technol.* **2016,** *123*, 125-133.

36. Papageorgiou, D. G.; Kinloch, I. A.; Young, R. J., Mechanical Properties of Graphene and Graphene-based Nanocomposites. *Prog. Mater. Sci.* **2017,** *in press*.

8. Conclusions and suggestion for future works

8.1. Conclusions

The good dispersion of the GNPs and carbon black in the elastomers through melt mixing was proven by SEM images, Raman spectra and XRD intensity ratio and CT scanning imaging. The morphology of the GNPs in the rubber shows dependence on the size of the particles. The particles of larger sizes tend to give smaller interface areas between the GNPs and the matrix due to the rippling, folding and various distortions. Hence, the composites with smaller GNP particles were imparted with better interfacial bonding (physical crosslinking), which gives rise to stiffer characteristics in the mechanical properties.

The orientation of the GNPs in the elastomers was characterization by SEM images, polarized Raman spectroscopy, XRD patterns and CT scanning imaging, which showed that GNPs trend to be oriented in an in-plane alignment. This preferred orientation imparts the anisotropic characteristics of the GNPs into the elastomers, which results in the distinction of anisotropy in mechanical behaviour, solvent diffusion and possibly heat transfer.

The properties of the elastomer nanocomposites show high dependence on the size and orientation of the fillers. The mechanical properties are greatly reinforced by the addition of the GNPs, and the M5 composites exhibit the highest stiffness, which can be explained by their high crosslink densities. The solvent diffusion is highly suppressed by the incorporation of the GNPs, and the M5 GNP composites give rise to the highest resistance to the solvent uptake due to their high crosslink density whereas M25 composites exhibit the lowest diffusion coefficients due to the longest penetration path. The thermal stability is slightly improved by the addition of the GNPs. The thermal conductivity is greatly enhanced by the incorporation of the GNPs with the largest GNP particle giving the highest conductivity. In additionally, the GNP particles exhibit the superior improvement in nearly all kinds of properties investigated compared to the carbon black particles.

The stress transfer from the matrix to the GNP particles was estimated from the tensile properties using *the rule of mixture* and stress-induced Raman band shifts. Even although the reinforcement of the GNPs is significant, the effective moduli of the GNPs in the elastomer is still 4 orders of magnitude lower than the intrinsic modulus of pristine graphene. A comprehensive theory was developed to explain the deficiency of the stress transfer in these soft matrix systems and this showed that the effective modulus of the GNP is related to the modulus of the soft matrix rather than the filler modulus.

8.2. Future work

As demonstrated in Chapters 4 and 5, the fluorescence ground of the elastomers can be suppressed by the addition of GNP flakes. The rubber peaks were overwhelmed by the significant background and exposed by the addition of the GNPs. The mechanism is not clearly known, which may be due to the phonon interaction between the GNP flakes and the rubber molecules. A deeper study should be undertaken to explain the phenomenon.

In Chapter 5, as presented in Figure 5.14a, the stress of the CB NBR composite becomes higher than that of the M15 GNP NBR composite at 20 phr. The mechanism is not well known and should be investigated. This behaviour may probably be correlated to the particular structure of the NBR polymer chains. Since NBR is a copolymer, the fractions of the monomers and the processing conditions need to be considered.

In Chapter 6, the thermal conductivity testing was undertaken. However, due to the experimental setting, the conductivity could only be tested from the heat flux that transfers through the specimen plane, in the direction perpendicular to the preferred orientation plane of the GNPs. The enhancement can be possibly caused by the out-of-plane conductivity of the GNPs, which is much lower than the in-plane conductivity. Another technique could be employed to determine the conductivity from the heat flux that transfers parallel to the preferred alignment plane of the GNPs in the elastomer such as Laser-Flash Method[1] or Non-contact Raman Spectra Shift Method[2] and a higher enhancement will be expected.

In Chapter 6, the swelling tests of the GNPs composites were undertaken. Actually, the anisotropic swelling occurs upon the thickness and the length direction. In the top surface plane, the swelling is biaxial and isotropic. The swelling of the rubber polymers is involved with a mechanical process, and the stress-transfer can be much different than the uniaxial stretch. The Raman band shifts of the specimens under swelling (or the evaporation of the swollen specimens) can be measured and used for investigation.

References

1. Shahil, K. M.; Balandin, A. A., Graphene-multilayer graphene nanocomposites as highly efficient thermal interface materials. *Nano. Lett.* **2012,** *12,* 861-7.
2. Li, Q.; Liu, C.; Wang, X.; Fan, S., Measuring the thermal conductivity of individual carbon nanotubes by the Raman shift method. *Nanotechnology* **2009,** *20,* 145702.